

ISSN 0938-5177

# Validation of Clouds in the ECHAM4 Model Using a Dynamical Adjustment Technique

Dissertation zur Erlangung des Doktorgrades  
der Naturwissenschaften im Fachbereich  
Geowissenschaften  
der Universität Hamburg

vorgelegt von

**Hans-Stefan Bauer**

aus Hamburg

Hamburg  
2000

Als Dissertation angenommen vom Fachbereich Geowissenschaften der Universität Hamburg

aufgrund der Gutachten von Herrn Prof. Dr. Lennart Bengtsson

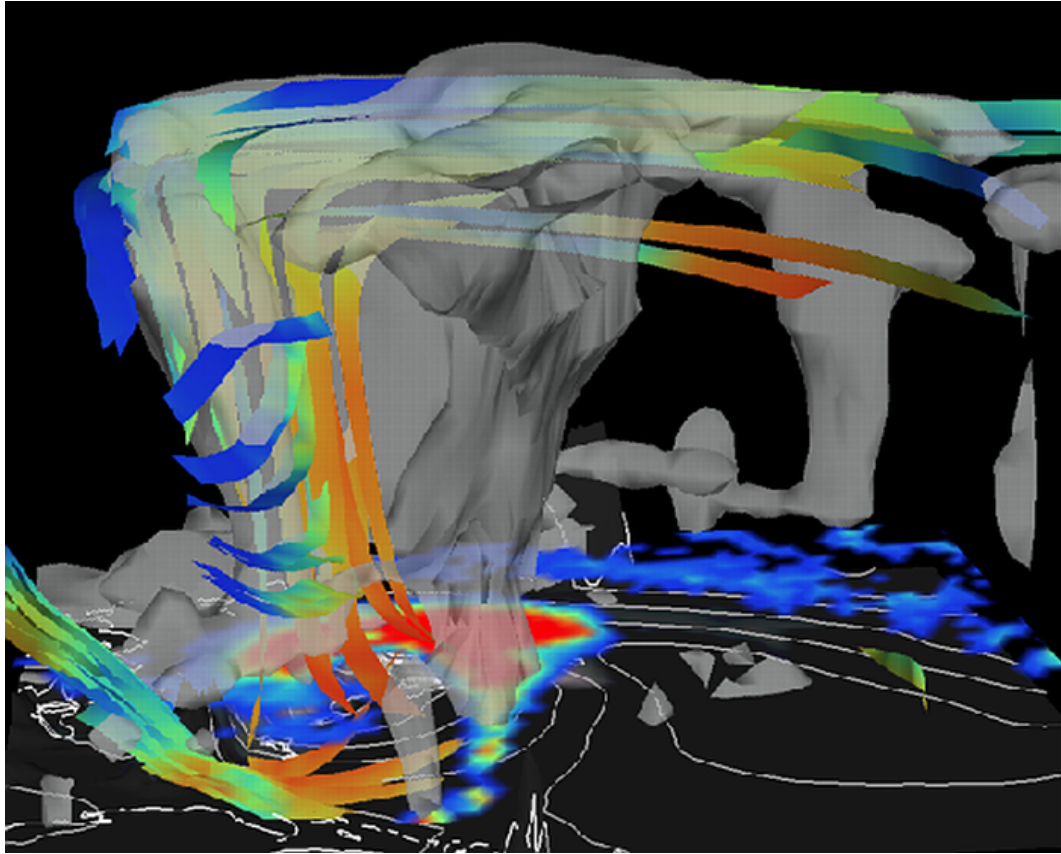
und Herrn Prof. Dr. Hartmut Graßl

Hamburg, den 2.5.2000

Prof. Dr. U. Bismayer

Dekan

des Fachbereichs Geowissenschaften



Rows and flows of angel hair  
And ice cream castles in the air  
And feather canyons ev'rywhere  
I've looked at clouds that way

But now they only block the sun  
They rain and snow on ev'ryone  
So many things I would have done  
But clouds got in my way

I've looked at clouds from both sides now  
From up and down, and still somehow  
It's cloud illusions I recall  
I really don't know clouds at all

(Joni Mitchell)

# Contents

<b>Abstract</b>	<b>6</b>
<b>Zusammenfassung</b>	<b>7</b>
<b>1 Introduction</b>	<b>9</b>
<b>2 Technical introduction</b>	<b>15</b>
2.1 Model . . . . .	15
2.1.1 The convection scheme . . . . .	16
2.1.2 The stratiform cloud scheme . . . . .	18
2.1.3 Cloud optical properties . . . . .	20
2.2 Dynamical adjustment . . . . .	21
2.2.1 Introductory remarks . . . . .	21
2.2.2 Method . . . . .	22
2.2.3 Influence on the model balance . . . . .	23
2.3 Observational data . . . . .	25
2.3.1 ISCCP satellite data . . . . .	25
2.3.2 Other observations . . . . .	29
<b>3 Synoptic situations</b>	<b>31</b>
3.1 Introductory remarks . . . . .	31
3.2 Cyclone at the East Coast of the U.S.A. . . . .	32
3.2.1 General features . . . . .	32
3.2.2 The "Storm of the Century" . . . . .	34
3.3 Atlantic blocking situation . . . . .	41
3.3.1 General features . . . . .	41
3.3.2 The case from the 15th to the 23rd of February 1993 . . . . .	44

<b>4</b>	<b>Cloud validation</b>	<b>47</b>
4.1	Introductory remarks . . . . .	47
4.2	Brief summary of a climatological validation . . . . .	47
4.3	Case study validation . . . . .	50
4.3.1	Cloud cover . . . . .	50
4.3.2	Relative humidity . . . . .	57
4.3.3	Cloud top pressure . . . . .	62
4.3.4	Cloud optical thickness . . . . .	67
4.3.5	Cloud types . . . . .	71
4.3.6	Brightness temperature . . . . .	74
4.4	Summary of the cloud validation . . . . .	81
<b>5</b>	<b>Sensitivity studies</b>	<b>83</b>
5.1	Introductory remarks . . . . .	83
5.2	Description of the experiments . . . . .	84
5.2.1	PCI - A new stratiform cloud scheme . . . . .	84
5.2.2	Vertical profile of the critical relative humidity . . . . .	85
5.2.3	Spitfire - A new advection scheme . . . . .	86
5.2.4	AMIP2 - A step forward to the new model version ECHAM5 . . . . .	87
5.3	Results of the experiments . . . . .	89
5.3.1	Introductory remarks . . . . .	89
5.3.2	Cloud cover . . . . .	89
5.3.3	Cloud water path (CWP) . . . . .	104
5.3.4	Cloud optical thickness . . . . .	107
5.3.5	Detrainment and precipitation efficiency . . . . .	111
5.3.6	Brightness temperature . . . . .	116
<b>6</b>	<b>Conclusions</b>	<b>122</b>
6.1	Discussion of the results . . . . .	122
6.2	Future work . . . . .	127
	<b>References</b>	<b>130</b>

## Abstract

Clouds are an important regulator of the Earth’s radiation budget and represent a major link between radiation and the hydrological cycle. In contrast to the “standard” method of comparing the model results with long-term climatologies, a different approach to validate clouds and cloud systems in ECHAM4 T106 is used by investigating the representation of synoptic-scale cloud systems. The aim is to explore whether the realistically reproduced mean cloud amounts are the result of a realistic representation of clouds in a higher temporal resolution. To enable a validation against observations, a dynamical adjustment approach based on the so-called Newtonian relaxation technique (nudging) is used, which relaxes the model state towards reanalysis data by adding a non-physical relaxation term to the model equations. In the simulations vorticity, divergence, temperature and the logarithm of surface pressure are adjusted to ECMWF reanalysis fields. The strength of the forcing is controlled by an adjustment time scale which is different for each adjusted variable.

The development of an extraordinary strong cyclone along the East Coast of the U.S.A. and a North Atlantic blocking situation are chosen as case studies. The synoptic systems have been selected to cover a large range of typical phenomena. A third situation, namely tropical convection in the western Pacific warm pool region, has been excluded from the cloud validation, since the Newtonian relaxation cannot force the model to the observed state for single convective events.

Compared to observations, the synoptic-scale features are well reproduced by the model. This is true even for variables which are not adjusted to the observed state. The general features of the horizontal and vertical cloud distribution are well reproduced for both synoptic systems. Nevertheless, systematic differences occur. The model underestimates clouds in low and middle levels of the troposphere and therefore total cloud amounts. Low-level clouds are most obviously underestimated in the blocking situation and behind the cold front of the developing cyclone, while the underestimation of mid-level cloudiness seems to be a more general feature which appears in both cases. On the other hand, thin upper-level cirrus anvils in pre-frontal regions seem to be overestimated. For the blocking situation, in addition, the horizontal distribution of clouds is different compared to ISCCP observations.

Sensitivity studies are carried out to confirm the findings of the cloud validation in order to study the effects of changes in the description of clouds and other processes, which will be included into the upcoming model version ECHAM5. Such experiments are an AMIP2 simulation, a more sophisticated stratiform cloud scheme PCI, developed by [Lohmann and Roeckner \(1996a\)](#), and the new advection scheme SPITFIRE ([Rasch and Lawrence, 1997](#)). With an experiment using a changed profile of the “critical relative humidity”, the effect of small changes on the representation of clouds is investigated. All experiments lead to larger cloud amounts in the lower troposphere and a slight increase in mid-level cloud amounts. Small changes occur in the upper troposphere, except for the PCI scheme, which clearly reduces the upper-level cloudiness. Encouraging is that the changed condensation profile in the experiment RHCRIT, which is only a small modification compared to the other experiments, clearly improves the representation of clouds in the blocking situation and even slightly improves the cloud distribution in the extratropical cyclone. In short, the modified profile of the critical relative humidity and the more sophisticated stratiform cloud scheme PCI lead to considerable improvements in the blocking situation, while the representation of frontal cloudiness in the East Coast storm is mainly improved by AMIP2 and SPITFIRE.

## Zusammenfassung

Wolken beeinflussen stark den Strahlungshaushalt der Erde und stellen eine wichtige Verbindung zwischen der Strahlung und dem Hydrologischen Zyklus dar. Im Gegensatz zur “Standard-Methode” der Validierung eines Klimamodelles, bei der die Modellergebnisse mit langjährigen Klimatologien verglichen werden, wurde ein anderer Weg gewählt. Hier wurde die Darstellung einzelner synoptischer Systeme in einer höheren räumlichen und zeitlichen Auflösung untersucht. Eines der Ziele war es, herauszufinden, ob der im Mittel realistisch wiedergegebene Bedeckungsgrad das Ergebnis der realistischen Darstellung von Wolken in einer höheren zeitlichen Auflösung ist – oder anders gesagt, ob das realistisch dargestellte Klima die Ursache eines realistisch wiedergegebenen Wetters ist.

Um eine Validierung dieser Systeme gegenüber Beobachtungen zu ermöglichen, wurde eine dynamische Anpassung basierend auf der sogenannten “Newton’schen Relaxations Technik” (“nudging”) benutzt. Diese passt die Modellgleichungen (Modell-Dynamik) durch das Addieren eines “nicht-physikalischen” Anpassungsterms der Reanalyse des Europäische Zentrums für mittelfristige Wettervorhersage (EZMW) an. In den hier durchgeführten Simulationen wurden Vorticity, Divergenz und Temperatur aller Schichten der Modellatmosphäre sowie der Logarithmus des Bodendrucks angepasst. Die Stärke der Anpassung wird dabei durch eine für jede Variable unterschiedliche Anpassungszeit bestimmt. Außerdem geht die Meeresoberflächen-Temperatur als untere Randbedingung ein.

Die Entwicklung eines außergewöhnlich starken außertropischen Tiefdruckgebietes entlang der Ostküste der USA und ein blockierendes Hochdruckgebiet über dem Nordatlantik wurden als Fallstudien verwendet. Die beiden Systeme wurden ausgesucht, um einen möglichst großen Bereich von synoptischen Systemen zu erfassen. Eine dritte Situation, tropische Konvektion über den Warmwassergebieten des westlichen Pazifiks, wurde in der Validierung von Wolken nicht berücksichtigt, da die Anpassungsmethode das Modell für einzelne konvektive Ereignisse nicht auf die Beobachtung zwingen kann.

Für die Vergleiche wurden Beobachtungen aus verschiedenen Quellen herangezogen. Die synoptischen Merkmale wurden mit den tatsächlichen Beobachtungen aus anderen Veröffentlichungen verglichen, während für die Validierung der Wolken Sattelitebeobachtungen (ISCCP) verwendet wurden. Im Vergleich zu den Beobachtungen werden die synoptischen Merkmale vom Modell sehr gut wiedergegeben. Das gilt auch für die Variablen, die nicht direkt angepasst werden. Die allgemeinen Merkmale der horizontalen und vertikalen Wolkenverteilung werden ebenfalls für beide synoptischen Systeme realistisch wiedergegeben. Dennoch treten Unterschiede zu den Beobachtungen auf. Das Modell unterschätzt den Bedeckungsgrad in niedrigen und mittleren Schichten der Troposphäre und deswegen auch den Gesamtbedeckungsgrad. Wolken in der unteren Troposphäre werden am deutlichsten im Bereich des blockierenden Hochdruckgebietes und hinter der Kaltfront des sich entwickelnden Tiefdruckgebietes unterschätzt. In mittleren Schichten scheint die unterschiedliche Bewölkung dagegen ein allgemeines Problem zu sein, das durchweg in beiden untersuchten Systemen auftritt. Andererseits werden Cirrus Wolken in der oberen Troposphäre vor allem in prä-frontalen Bereichen überschätzt. Bei der Blocking-Situation ist auch die grobe Struktur der Wolkenverteilung im Modell anders als bei den Beobachtungen von ISCCP.

Weiterhin sind Sensitivitäts-Experimente durchgeführt worden, um die in der Validierung angenommenen Ursachen für die Schwächen bei der Darstellung von Wolken zu bestätigen oder zu widerlegen und um die Wirkung anderer Veränderungen in den Parametrisierungen auf die Darstellung von Wolken zu testen, die in die neue Modellversion ECHAM5 eingebaut werden sollen. Solche Experimente sind z.B. eine AMIP2 Simulation, ein verbessertes stratiformes Wolkenschema, entwickelt von [Lohmann and Roeckner \(1996a\)](#), und das neue Advektionsschema SPITFIRE ([Rasch and Lawrence, 1997](#)).

Außerdem wird mit einem weiteren Experiment (RHCRIT), in dem ein verändertes Vertikalprofil der “kritischen relativen Feuchte” verwendet wurde, stellvertretend der Einfluß kleiner Veränderungen untersucht, die zu einer verbesserten Darstellung von Wolken führen könnten.

Alle Experimente führen zu einer stärkeren Bewölkung in der unteren Troposphäre und einem leicht verstärkten Bedeckungsgrad in mittleren Schichten. Geringere Unterschiede treten dagegen in der oberen Troposphäre auf, abgesehen von der PCI-Simulation, die die Bewölkung in der oberen Troposphäre deutlich reduziert. Interessant ist, daß es durch die, im Vergleich zu den anderen Experimenten, geringe Modifikation im RHCRIT Experiment zu einer deutlichen Verbesserung der Darstellung von Wolken im Bereiche des blockierenden Hochdruckgebietes kommt und auch die Wolkenverteilung in der außertropischen Zyklone verbessert wird. Während das PCI und das RHCRIT Experiment vor allem zu einer verbesserten Darstellung des blockierenden Hochdruckgebietes führen, wird die Darstellung des außertropischen Tiefdruckgebietes am deutlichsten von AMIP2 und SPITFIRE verbessert.

# Chapter 1

## Introduction

About 60% of the Earth's surface is covered by clouds. They are a major regulator of the Earth's climate by being a dominant modulator of radiation. This cloud-related spatial variation of the radiation induces changes in the general circulation which alter the hydrological cycle. On the other hand, clouds themselves depend in a non-linear way on climate and the cloud optical properties are related to each other non-linearly. The cloud albedo for example depends strongly on the number and size of aerosol particles, which serve as cloud condensation nuclei.

The spatial scales which are involved in the formation of clouds range from tenths of a micrometer for cloud condensation nuclei to a few hundred kilometres for large-scale cloud systems. Even single clouds appear on spatial scales ranging from a few hundred metres for a cumulus cloud to hundreds of kilometers for frontal clouds.

To demonstrate the importance of clouds for the climate system, one result of the ERBE<sup>1</sup> (Barkstrom et al., 1990) experiment is cited. On average the net-radiation of the Earth-atmosphere-system is reduced by  $18 \text{ Wm}^{-2}$  due to the effect of clouds (Collins et al., 1994). This is four times as much as the radiation gain due to  $\text{CO}_2$  doubling (Cess et al., 1993). These numbers suggest, that an increase of the cloud effect by 25% would theoretically cancel the effect of  $\text{CO}_2$  doubling. This compensating influence could be induced by a 4% larger region covered with stratocumulus clouds in subtropical subsidence regions, a cloud type which is systematically underestimated in most climate models (Randall et al., 1984).

Furthermore, cloud amount, cloud type, cloud height or the cloud microphysical properties may change in a warmer climate. Cess et al. (1996) investigated the response of 19 general circulation models to a changed climate. Therefore they used changes of the sea surface temperature as a surrogate for climate changes and found that most of the variations between the models are attributable to differences in the description of the cloud-climate feedback in the models.

Water is a unique substance. Under the climatic conditions occurring on Earth, it can exist in the solid, the liquid and the gaseous phase. Phase changes associated with energy conversions, and the transport of water vapour are important mechanisms for the redistribution of energy in the atmosphere. The release of latent heat, for example, represents a major component for the heating of the atmosphere. Figure 1.1 shows schematically the global and annual mean hydrological cycle for the marine and continental hemisphere.

Atmospheric and ocean circulations are driven by temperature differences resulting from differential heating from the sun. Figure 1.2 shows the observed annual and global mean of the energy cycle in the Earth-atmosphere-system.

---

<sup>1</sup>ERBE = Earth Radiation Budget Experiment

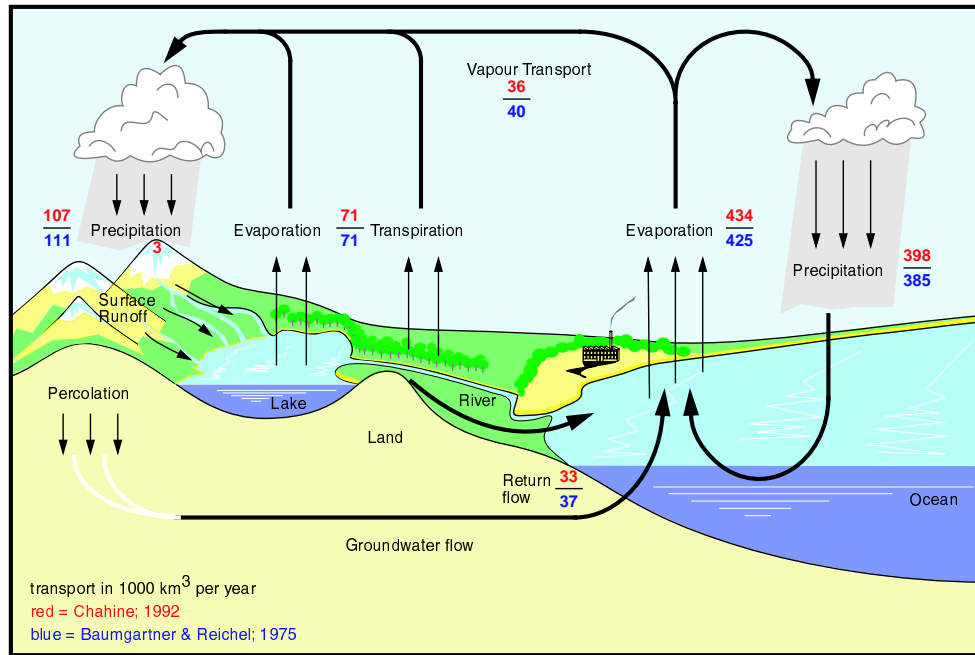


**Figure 1.1:** Schematic description of the hydrological cycle for the marine and the continental area. The values were obtained from different sources like routine meteorological observations, hydrological records or energy balance calculations. Upper numbers show empirical estimates from Chahine (1992) and lower numbers are from Baumgartner and Reichel (1975). Snow accumulation follows Bromwich (1990). Units are given in  $1000 \text{ km}^3 \text{ year}^{-1}$ .

In spite of major improvements in measurement technology and observational systems in recent years, there are still substantial inaccuracies in the knowledge of the three-dimensional hydrological cycle and radiative forcing. For precipitation this is due to its fine, almost fractal structure which cannot be sampled from synoptic stations (Bergeron, 1970). The inaccuracies of most energy fluxes in Figure 1.2 are of the order  $5 \text{ Wm}^{-2}$ , a large value if one bears in mind that globally averaged only  $3 \text{ Wm}^{-2}$  of the incoming solar radiation is transferred to kinetic energy, responsible for the whole atmospheric general circulation.

Even if the optical properties and spatial distribution of clouds are known, there is an uncertainty in their radiative effect. The most uncertain component of radiation is the absorption of shortwave radiation by clouds. Recent observational studies supported the existence of an additional shortwave absorption by clouds of  $25\text{-}30 \text{ Wm}^{-2}$  [e.g. Cess et al. (1995), Ramanathan and Vogelmann (1997) or Kondratyev et al. (1998)]. The cause for this additional short-wave absorption, which is not supported by model experiments (Kiehl and Trenberth, 1997), is unknown. But it may be associated with processes which are largely ignored in state of the art climate models (e.g. pollution or 3-d effects) [e.g. Ramanathan and Vogelmann (1997) or Kondratyev et al. (1998)].

In the solar spectrum clouds mainly reflect radiation back to space and reduce the amount of energy reaching the surface (albedo effect). The amount of reflection is governed by the total cloud liquid water and mean droplet size. Low-level clouds, which contain higher amounts of liquid water, have a strong effect in the solar spectrum. On the other hand their effect in the terrestrial spectrum is small due to the small difference between cloud top and surface temperatures. Marine stratiform clouds, which cover a third of the Earth's ocean area, are the most prominent example of this type of clouds.

In the terrestrial spectrum the radiation coming from the surface is mostly absorbed by the clouds and then radiated back depending on cloud temperature. Clouds therefore strengthen the backward radiation towards the surface, reduce emission to space and lead to a net warming

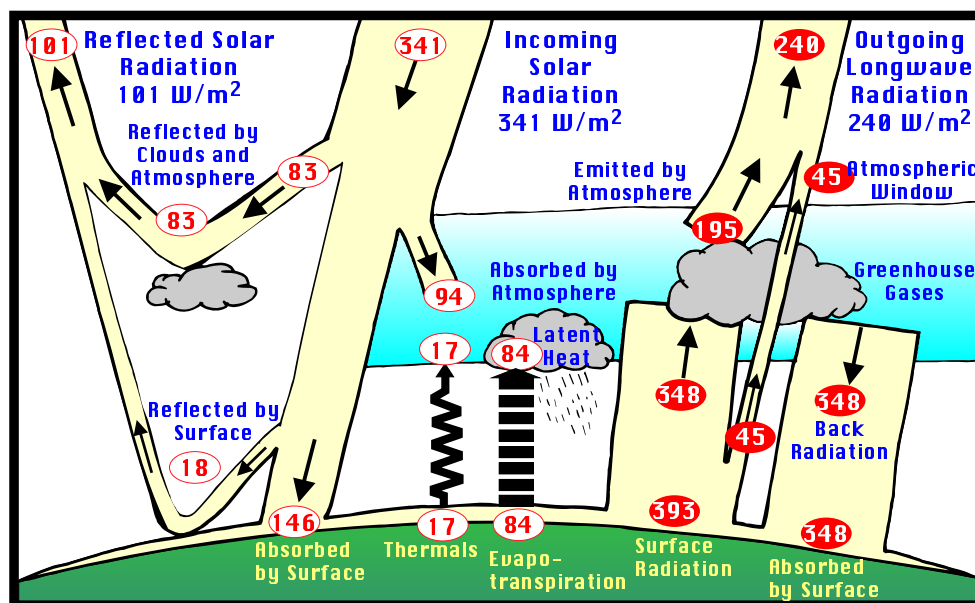


**Figure 1.2:** Schematic description of the global energy balance based on recent estimates of different components of the radiational cycle, e.g. from Hartmann (1993), Ohmura and Gilgen (1993), Hahn et al. (1994a) or Giorgetta and Wild (1995). Units in  $Wm^{-2}$ .

of the Earth and atmosphere in the terrestrial spectrum. Cirrus clouds typically have low values of the optical thickness. Their influence in the solar spectrum is small, since the largest part of the solar radiation passes the cloud unimpeded. On the other hand cirrus cloud top temperature is much lower than the surface temperature so that less infrared radiation coming from below is emitted to space. This traps a large portion of the longwave radiation in the atmosphere.

Due to the appearance of clouds over a wide range of spatial scales, many of them smaller or even much smaller than the normal grid boxes of today's climate models, it is necessary to parameterize clouds and their effects in climate models. Although the horizontal resolution is going to be higher in future model versions due to more powerful computers, microphysical processes as well as the radiative effects of clouds will remain highly parameterized. Therefore the continuous development of parameterization schemes is one of the main targets in climate modeling.

In recent years different parameterization schemes of increasing complexity have been introduced into the models. Previously, clouds were described diagnostically, as for example by Slingo (1987). In such schemes the fractional cloudiness in a grid box is calculated from empirical relationships using one or more model predictors such as vertical velocity or static stability. Nowadays prognostic schemes are more advanced. One of the first approaches which described stratiform clouds was developed by Sundqvist (1978). It uses one prognostic equation for cloud liquid water and cloud ice and calculates sub-grid scale cloud cover diagnostically as a function of the relative humidity. A method of increasing the accuracy of a scheme is to increase the number of prognostic variables. Lohmann and Roeckner (1996a) used different prognostic equations for cloud liquid water and cloud ice, which introduces more physical processes into the model. Tiedtke (1993) on the other hand adds to the prognostic equation for cloud water (liquid and ice) an equation which calculates cloud cover prognostically.

During the past two decades, modeling studies as well as observational studies have demonstrated the importance of convective moisture transport for an accurate representation of the general circulation. Current schemes use the so-called mass flux approach, in which the contribution of cumulus convection to the large-scale budgets of heat, moisture and momentum is represented by an ensemble of clouds consisting of updrafts and downdrafts in a steady state. Mass flux schemes

have been developed for example by [Tiedtke \(1989\)](#) or [Gregory et al. \(1997\)](#) and [Kershaw and Gregory \(1997\)](#). The former is the basis of the convection scheme in the ECHAM4 model, in which modifications by [Nordeng \(1994\)](#) have been taken into account.

To simplify the calculations, convective and stratiform processes are treated separately in climate models. This is possible because different processes as well as different temporal and spatial scales are responsible for the different cloud formation processes. Nevertheless, this is a crude simplification of the reality, where the two processes interact non-linearly. For example, regions of convectively enhanced precipitation are often embedded into regions of large-scale rising motion along warm fronts. Thus improved cloud parameterizations have to be linked to improvements of other parameterizations and the schemes have to be built on a better physical basis with a more elaborate treatment of the sub-grid scale processes ([Roeckner and LeTreut, 1996](#)).

The major goal for this study is to identify the causes of the errors in the representation of clouds. This task leads to an important question: **How can we validate a climate model ?**

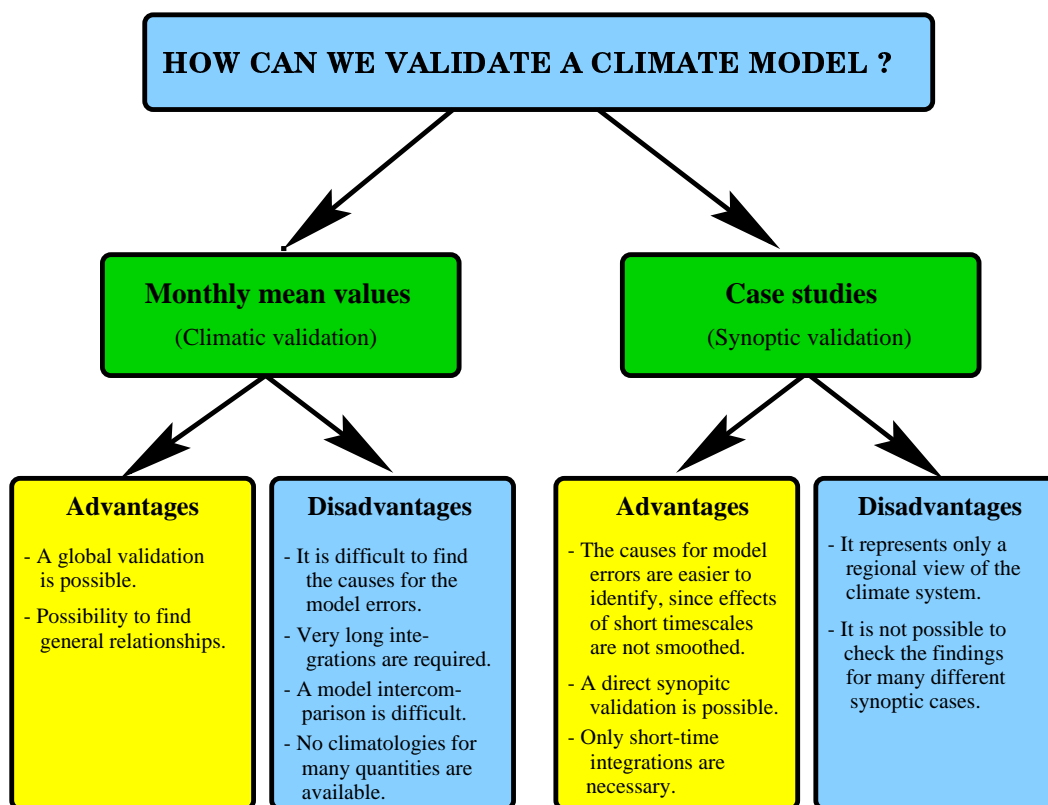


**Figure 1.3:** Advantages and disadvantages of the two different methods of validation.

In most cases validation is only done for long-term means, for example by comparing to a monthly mean value of cloud cover and liquid water. The disadvantages with this approach are highlighted in [Figure 1.3](#). This is particularly true for the validation of climate models, where much effort is involved in the "tuning" of the parameterization schemes in order to obtain a satisfactory large-scale response ([Moncrieff, 1995](#)). This tuning and the temporal averaging hide model weaknesses occurring on shorter time scales. In a numerical weather prediction model on the other hand, the forecast quality is the most important subject. Changes which would improve the physical representation of synoptic systems but decrease the forecast quality due to non-linear interactions with other parameterizations could not be introduced into the model.

In recent years some very important field experiments have been carried out in order to improve the knowledge and understanding of the physical processes which are important for the life-cycle of synoptic-scale weather systems. Some of those campaigns were for example ERICA<sup>2</sup> ([Hadlock](#)

<sup>2</sup>ERICA = Experiment on Rapidly Intensifying Cyclones over the Atlantic

and Kreitzberg, 1988) or FASTEX<sup>3</sup> (Joly et al., 1997). During ERICA Neiman and Shapiro (1993) and Neiman et al. (1993) accurately documented a cyclogenesis of January 4-5 1989 off the East Coast of the U.S.A..

One of the first who discussed the evolution of an Atlantic cyclone in a general circulation model was Gilchrist (1971). He used a five layer model with a horizontal resolution of 5° longitude and 3° latitude which covered the northern hemisphere. Despite the crude resolution many of the typical synoptic features during the life-cycle were reproduced realistically. Another study was performed by Bengtsson (1991a), who described the development of a cyclone in the ECMWF<sup>4</sup> numerical weather prediction model.

Chen and Roeckner (1999) compiled a representative cyclone from an ensemble of cyclones in ECHAM4 T42. They found that the simulated features were in good agreement with recent observational studies using the ISCCP<sup>5</sup> (Rossow and Schiffer, 1991) cloud climatology, operational analyses or conceptual models. This work is based on the approach of Lau and Crane (1995), who associated cloud patterns and different cloud types observed from ISCCP satellite data with typical circulation patterns of the ECMWF reanalysis (Gibson et al., 1997). In Lau and Crane (1997) the ISCCP satellite data was compared with an independent dataset compiled from surface observations (Hahn et al., 1994b). They found an overall consistency of the propagation characteristics and the spatial cloud structures deduced from the two different datasets in spite of their complementary nature.

In this study the temporal evolution of distinct synoptic systems in the climate model ECHAM4 will be investigated in a high temporal and spatial resolution focusing on the evolution of cloud systems. From Figure 1.3 it is concluded that for an appropriate validation of the climate model, in addition to a climatological validation, detailed case studies are necessary. Therefore three typical systems, namely the development of an extratropical cyclone along the East Coast of the U.S.A, a blocking situation over the Atlantic ocean and tropical convection in the western Pacific warm pool region are chosen. It is not the aim of this study, to develop a new scheme. Instead, a diagnostic method should be developed, which allows a fast and efficient diagnostic validation of physical parameterization schemes. Clouds are used as an example, because they represent a central problem in model development. One interesting question is whether the reasonable representation of the climatological cloud patterns in the model is based on a realistic representation of the "model weather" or whether it is the result of error compensation. For the validation of the model weather an approach has to be developed which allows the comparison with "real" synoptic systems. It has been decided to use a dynamical adjustment based on the "Newtonian relaxation technique" (nudging) [e.g. Anthes (1974), Hoke and Anthes (1976), Krishnamurti et al. (1991) or Jeuken et al. (1996)], which forces the model dynamics to the observed state by adding a non-physical relaxation term to the model equations. The decision is based on the following arguments:

- The dynamical adjustment provides the model with excellent spin-up characteristics compared to standard data assimilation schemes, since it takes place every time step rather than every six hours, as for example in the ECMWF reanalysis. This ensures a more gradual forcing of the model dynamics.
- There exists no standard data assimilation scheme for ECHAM.
- Forcing only the model dynamics to the observed state allows the physical processes to develop freely. Thus, the model errors, occurring despite nudging, can more easily be associated with their causes in the parameterization schemes used.

Other studies using this initialization method have been carried out by Brill et al. (1991), Krishnamurti et al. (1991) or Krishnamurti et al. (1993). The former initialized a forecast

---

<sup>3</sup>FASTEX = Fronts and Atlantic Storm-Track EXperiment

<sup>4</sup>ECMWF = European Centre for Medium Range Weather Forecasting

<sup>5</sup>ISCCP = International Satellite Cloud Climatology Project

model with observations collected during the GALE<sup>6</sup> experiment (Dirks et al., 1988). They concluded that the use of this approach made the model a powerful tool for the synoptic analysis. Krishnamurti et al. (1991) and Krishnamurti et al. (1993) used the initialization to improve tropical forecasts. In addition to the dynamics they initialized precipitation with SSM/I<sup>7</sup> rain rates, which led to improvements in the predicted circulation and precipitation patterns.

In chapter 2 a brief description of the main parts of the model is given. The stratiform and convective schemes are described in more detail, because this work focuses on the representation of clouds. Furthermore the adjustment technique, its quality and influence on the model dynamics and the observational datasets used for the validation are described.

Chapter 3 describes the synoptic systems investigated in this work. Every system is first introduced by the typical features for this kind of system and thereafter the investigated situation is described as it occurred in reality and how it is represented in the model simulation. In chapter 4 a more accurate validation of the cloud related processes is carried out.

In chapter 5 sensitivity studies using ECHAM4 T106 are described. They are of different complexity, ranging from small changes in some physical constants determining the cloud microphysics to alternative parameterization schemes. The aims are threefold. Firstly, the effects of some changes, which will be introduced in the upcoming model version ECHAM5, are diagnosed. Secondly, the experiments might help to identify the causes for the model errors and thirdly, small changes which might lead to a better description of clouds in the model (e.g. a changed vertical profile of the critical relative humidity) are tested.

Conclusions are given in chapter 6 containing a summary of the main results and an outlook on future work.

---

<sup>6</sup>GALE = Genesis of Atlantic Lows Experiment

<sup>7</sup>SSM/I = Special Sensor Microwave/Imager

# Chapter 2

## Technical introduction

### 2.1 Model

The model used in this study is the 4th generation of the Max Planck Institutes general circulation model ECHAM<sup>1</sup> (Roeckner et al., 1996). It is available at various horizontal resolutions from T21 to T106 triangular truncation, which determines the number of waves explicitly resolved on the globe. For this investigation the T106 horizontal resolution with 19 vertical hybrid levels up to a height of 30 km (10 hPa) is used. The boundary layer is resolved by 5 levels, corresponding with heights of  $\sim 30, 150, 390, 800,$  and  $1400$  m. The time step is 12 minutes for the dynamics and physics and 2 hours for the radiation. ECHAM is based on the primitive equations and uses vorticity, divergence, temperature, the logarithm of surface pressure, water vapour and cloud water as prognostic variables. In order to reduce truncation errors the advection of water vapour, cloud water and chemical substances is calculated using a semi-Lagrangian transport scheme [Williamson and Rasch (1989) and Williamson and Rasch (1994)]. The time integration is carried out using a semi-implicit "leap frog" method. Orography, land-sea mask and glacier mask are calculated from the high resolution US Navy data set.

The radiation scheme is a modified version of the ECMWF scheme. It is separated into two parts. The shortwave part, developed by Fouquart and Bonnel (1980), solves the radiative transfer equation by integrating the fluxes between 0.2 and  $4 \mu\text{m}$ . During the integration the visible part from 0.2 to  $0.68 \mu\text{m}$  and a near-infrared part from  $0.68$  to  $4 \mu\text{m}$  are treated differently. In the clear sky fractions the scheme accounts for scattering and absorption by molecules and aerosols. The single scattering properties of cloud droplets and ice crystals are calculated from Mie-theory with a suitable adaptation to a broad-band model (Rockel et al., 1991).

The longwave part of the scheme is based on the Morcrette scheme (Morcrette, 1991b) used in the ECMWF forecast model. The longwave spectrum is divided into 6 spectral bands. In addition to  $\text{CO}_2$  the greenhouse gases  $\text{CH}_4$ ,  $\text{N}_2\text{O}$ ,  $\text{O}_3$  and different *CFCs* have been introduced. The water vapour continuum is modified following Giorgetta and Wild (1995) to include temperature weighted band averages of e-type absorption and a band dependent ratio of (p-e)-type to e-type continuum absorption. The latter changes are of particular importance since they have increased the downward longwave radiation at the surface by  $10\text{-}15 \text{ W/m}^2$  in agreement with observations.

The vertical turbulent transfer of momentum, heat, water vapour and cloud water is based on the Monin-Obukhov similarity theory for the surface layer and the eddy diffusivity approach in the layers above. As closure a turbulent kinetic energy approach is used with the Prandtl-Kolmogorov parameterization of eddy diffusivity (Brinkop and Roeckner, 1995).

---

<sup>1</sup>ECHAM = ECMWF model HAMburg version

The effect of orographically excited gravity waves is parameterized on the basis of a linear theory and dimensional considerations following Palmer et al. (1986) and Miller et al. (1989). The vertical structure of the momentum flux induced by the gravity waves is calculated from a local Richardson number, which describes the onset of turbulence due to convective instability.

The land surface model considers the budget of heat and water in the soil, snow cover over land and the heat budget of permanent land and sea ice (Dümenil and Todini, 1992). The heat transfer equation is solved in a five-layer model assuming vanishing heat fluxes at the bottom. Vegetation effects such as the interception of rain and snow in the canopy and the stomatal control of evaporation are grossly simplified. The local runoff scheme is based on catchment considerations and takes into account sub-grid scale variations of the field capacity over inhomogeneous ground.

### 2.1.1 The convection scheme

The cumulus convection is parameterized using the mass flux approach (Tiedtke, 1989). The scheme includes the effects of deep, shallow and midlevel convection in the budget equations of heat, water vapour and momentum. After the initialization of the scheme, the cloud base is determined. This separates midlevel from shallow and penetrative convection as the former originates at higher levels in the troposphere. The next step is the calculation of the total moisture convergence, separating shallow from penetrative convection, because the former occurs in undisturbed situations with small amounts of moisture convergence compared to evaporation from the surface in the atmospheric column.

Cumulus clouds are represented by a bulk model including the effect of entrainment and detrainment on the updraft and downdraft convective mass fluxes.

$$\frac{\partial M_u}{\partial z} = E_u - D_u \quad (2.1)$$

$$\frac{\partial}{\partial z} (M_u s_u) = E_u \bar{s} - D_u s_u + L \bar{\rho} c_u \quad (2.2)$$

$$\frac{\partial}{\partial z} (M_u q_u) = E_u \bar{q} - D_u q_u - \bar{\rho} c_u \quad (2.3)$$

$$\frac{\partial}{\partial z} (M_u l_u) = -D_u l_u + \bar{\rho} c_u - \bar{\rho} P_u \quad (2.4)$$

$$\frac{\partial}{\partial z} (M_u u_u) = E_u \bar{u} - D_u u_u \quad (2.5)$$

$$\frac{\partial}{\partial z} (M_u v_u) = E_u \bar{v} - D_u v_u \quad (2.6)$$

where the subscript  $u$  denotes updraft variables and the overbar denotes large-scale variables.  $E$  is entrainment,  $D$  is detrainment,  $s = c_p T + gz$  is dry static energy,  $\rho$  is the density of air,  $q$  is specific humidity,  $l$  is the cloud water mixing ratio,  $c$  is the release of latent heat from condensation,  $P_u$  is the conversion of cloud water to precipitation and  $u$  and  $v$  are the components of the horizontal wind vector.

A corresponding set of equations is used for the cumulus downdrafts. They are assumed to originate from mixing of cloudy air with environmental air which has been cooled to its wet bulb temperature by evaporation of precipitation generated in the updrafts (Tiedtke, 1989).

For entrainment and detrainment the scheme differentiates between an organized part through the cloud top and the cloud base and a turbulent part through the lateral cloud boundaries.

The total values of entrainment and detrainment are the sum of the appropriate parts. The turbulent parts are parameterized as functions of the updraft mass flux inside the cloud.

$$E_u^{(1)} = \varepsilon_u^{(1)} M_u \quad (2.7)$$

$$D_u^{(1)} = \delta_u^{(1)} M_u \quad (2.8)$$

The turbulent entrainment ( $\varepsilon_u^{(1)}$ ) and detrainment ( $\delta_u^{(1)}$ ) rates are functions of the cloud radii, but are kept constant to keep the scheme simple. Different values are assumed for the different types of convection.

Organized entrainment is assumed to take place as inflow of air into the cloud when cloud parcels are accelerated upward, i.e. where the buoyancy is positive (Nordeng, 1994). The organized entrainment rate of an ensemble of clouds is calculated by

$$\varepsilon^{(2)} = \frac{b}{2 \cdot (w_0^2 + \int_0^z b dz)} + \frac{1}{\bar{\rho}} \frac{\partial \bar{\rho}}{\partial z} \quad (2.9)$$

with the vertical velocity  $\omega$  and the ensemble buoyancy  $b$ .

$$b = \frac{g}{T_v} (T_v - \bar{T}_v) - gl \quad (2.10)$$

where  $T_v$  is the virtual temperature,  $g$  the gravitational force and  $l$  the cloud water mixing ratio.

Organized detrainment, on the other hand, takes place where the air decelerates, i.e. where the buoyancy is negative. It is equal to the change of mass flux with height. Since the in-cloud vertical velocities are primarily functions of height above cloud base and due to the assumption that individual clouds do not change their area fraction before they start to detrain, the organized detrainment can be parameterized as

$$D = -\frac{M}{\sigma} \frac{\partial \sigma}{\partial z} \quad (2.11)$$

with the spectrum of clouds  $\sigma(z)$  realized as

$$\sigma(z) = \sigma_0 \cos \left[ \frac{\pi (z - z_d)}{2 (z_t - z_d)} \right] \quad (2.12)$$

This spectrum of clouds (Nordeng, 1994) allows detrainment within a deeper layer of the troposphere as compared to the scheme of Tiedtke (1989) which only allows detrainment from the highest cloud layer in the grid box. The detrained fraction of the convectively generated cloud water, from anvils of deep tropical convection as well as from non-precipitating shallow cumuli, is used as a source term in the stratiform cloud water equation. This is the reason why the convection is calculated before the stratiform condensation.

Using this formalism, organized entrainment and detrainment are related to the cloud activity itself and not to large-scale moisture convergence as assumed by Tiedtke (1989).

As closure for deep convection, Nordeng (1994) relates the cloud base mass flux to the convective instability CAPE.

$$CAPE = \int_{base}^{top} \left( \frac{g}{T_v} [T_v - \bar{T}_v] - gl \right) dz \quad (2.13)$$

where cloud ensemble values for the virtual temperature  $T_v$  and the cloud water content  $l$  are used. The change of CAPE<sup>2</sup> due to convective heating/moistening is approximated by

$$\frac{\partial}{\partial t}CAPE \approx - \int_{base}^{top} \frac{g}{\bar{T}_v} \frac{\partial \bar{T}_v}{\partial t} dz = -M_B \int_{base}^{top} \left( \frac{[1 + \delta \bar{q}]}{c_p \bar{T}_v} \frac{\partial}{\partial z} \bar{s} + \delta \frac{\partial}{\partial z} \bar{q} \right) \eta \frac{g}{\bar{\rho}} dz \quad (2.14)$$

with the normalized mass flux  $\eta$  defined as  $M = M_B \eta(z)$  where  $M_B$  is the cloud base mass flux. Then a relaxation time  $\tau$  is introduced during which the convective system should remove the instability, so that

$$\frac{\partial}{\partial t}CAPE = -\frac{CAPE}{\tau} \quad (2.15)$$

and the cloud base mass flux can be computed from (2.14).

In ECHAM4 the stratocumulus regime is considered as a part of the boundary layer scheme, which includes the effect of clouds on vertical transport, such as the downward transfer of turbulent kinetic energy generated by radiative cooling at cloud top, the impact of cloud water on the buoyancy flux, as well as cloud top entrainment processes represented by the turbulent diffusion of cloud liquid water (Brinkop and Roeckner, 1995).

### 2.1.2 The stratiform cloud scheme

The scheme is based on an approach of Sundqvist (1978) who includes the fractional cloud cover ( $b$ ) in a prognostic scheme. The governing equations for water vapour ( $q_v$ ) and cloud water ( $l$ , liquid and ice) are

$$\frac{\partial q_v}{\partial t} = R(q_v) - bC_c - (1-b)C_0 + (1-b)E_0 \quad (2.16)$$

$$\frac{\partial l}{\partial t} = R(l) + bC_c + (1-b)C_0 - bP_c \quad (2.17)$$

where  $R(q_v)$ ,  $R(l)$  are the sum of all transport terms of  $q_v$  and  $l$  including advection, turbulence and convection. The latter represents water vapour and cloud water detrained from the top of the cumulus clouds. The subscripts  $c$  and  $0$  refer to the cloudy and cloud-free part of the grid box. The cloud microphysical terms are condensation of water vapour in the cloudy part ( $C_c > 0$ ), evaporation of cloud water ( $C_c < 0$ ), evaporation of cloud water transported into the cloud-free part of the grid box ( $C_0 > 0$ ), formation of precipitation by coalescence of cloud droplets and sedimentation of ice crystals ( $P_c$ ), and evaporation of precipitation falling into the unsaturated part of the grid box ( $E_0$ ).

The fractional cloud cover  $b$  is parameterized as a non-linear function of the grid-mean relative humidity  $r$  (Sundqvist et al., 1989). For this purpose a sub-grid scale condensation threshold, the so-called "critical relative humidity"  $r_0$  is defined. Its value is smaller than the saturation relative humidity  $r_{sat}$  (=1 in general). For  $r > r_0$  the partial cloud cover is defined as

$$b = 1 - \sqrt{1 - b_0} \quad (2.18)$$

with

$$b_0 = \frac{r - r_0}{r_{sat} - r_0} \quad (2.19)$$

---

<sup>2</sup>CAPE = Convective Available Potential Energy

Condensational growth of cloud droplets occurs if  $r > r_0$ , while an existing cloud is diluted by evaporation if  $r < r_0$ . The condensation threshold is specified as a function of height (or pressure), fitted to the result obtained by [Xu and Kruger \(1991\)](#) from experiments with a high-resolution cumulus ensemble model.

$$r_0(p) = r_{0,top} + (r_{0,surf} - r_{0,top}) e^{\left[1 - \left(\frac{p_s}{p}\right)^n\right]} \quad (2.20)$$

where  $p$  is pressure,  $p_s$  is surface pressure,  $r_{0,top} = 0.6$  and  $r_{0,surf} = 0.99$  are the values at the uppermost and lowest model level and  $n = 4$  is a fitting parameter. The profile described in (2.20) is used for all cloud types except for marine stratus under a low-level inversion. In such cases, the value of  $r_0$  is reduced to 0.6 below the inversion and  $r_{sat}$  is reduced to 0.9, so that according to (2.18) and (2.19)  $b = 1$  is reached before the whole layer is saturated. Those settings allow the formation of thin stratus clouds under a subsidence inversion which otherwise would not be captured by the model due to an insufficient vertical resolution. Total cloud cover is calculated using the maximum overlap assumption for adjacent cloud layers and random overlap otherwise.

The mechanism of precipitation development depends strongly on cloud phase. Therefore the total cloud water content computed by equation (2.17) is split into a liquid and an ice phase using probability functions  $f_{liq}$  and  $f_{ice}$ , derived by [Rockel et al. \(1991\)](#) empirically fitted to aircraft measurements by [Matveev \(1984\)](#).

$$f_{liq} = a + (1 - a) e^{-b(T-T_0)^2} \quad (2.21)$$

with  $a = 0.0059$  and  $b = 0.003102$ .  $f_{liq} = 1$  is assumed for  $T \geq T_0 = 273.16$  K and

$$f_{liq} + f_{ice} = 1 \quad (2.22)$$

Accordingly, the liquid and ice fractions of the in-cloud water content  $q_c = l/b$  are given by

$$q_c = q_{cl} + q_{ci} \quad (2.23)$$

where

$$q_{cl} = f_{liq} \cdot q_c \quad (2.24)$$

$$q_{ci} = f_{ice} \cdot q_c \quad (2.25)$$

represent the in-cloud liquid and ice water content.

The autoconversion of cloud droplets to rain drops is parameterized using an exponential form ([Sundqvist, 1978](#)). In addition, collision of cloud droplets with rain drops and snow flakes is taken into account ([Smith, 1990](#)), so that the total coalescence rate is given by

$$P_{cl} = q_{cl} \cdot \left( C_0 \left[ 1 - e^{-\left(\frac{q_{cl}}{q_{cr}}\right)^2} \right] + C_1 [P] \right) \quad (2.26)$$

where  $P$  is the rain flux density at the top of the respective cloud layer, and  $C_0$ ,  $C_1$  and  $q_{cr}$  are microphysical constants which determine the efficiency of rain formation and therefore the cloud lifetime.

Ice crystals sedimentate at a rate which depends on their form and size. Both parameters are not available in the model. According to an observational study by [Heymsfield \(1977\)](#) the terminal velocity  $v_t$  of ice crystals can be parameterized in terms of the ice water content.

$$v_t = \alpha (\rho_a \cdot q_{ci})^\beta \quad (2.27)$$

where  $\rho_a$  is the density of air and  $\alpha$  and  $\beta$  are empirical constants. The loss of ice crystals due to sedimentation is given by the divergence of the ice water flux density.

$$P_{ci} = g \frac{\partial}{\partial p} (v_t \cdot \rho_a \cdot q_{ci}) \quad (2.28)$$

where  $p$  is the pressure and  $g$  the gravitational force. The total precipitation formation is the sum of the two components for the warm precipitation formation (2.26) plus the sedimentation of ice crystals (2.28)

$$P_c = P_{cl} + P_{ci} \quad (2.29)$$

Precipitation falling into the cloud-free part of the grid box is assumed to evaporate or sublimate which is parameterized in terms of the saturation deficit. Melting of snow is assumed whenever the temperature of the respective layer exceeds 2°C (Roeckner et al., 1992).

### 2.1.3 Cloud optical properties

For the solar part of the spectrum the single scattering properties are calculated on the basis of high-resolution Mie calculations using idealized size distributions for both cloud droplets and spherical ice crystals (Rockel et al., 1991). For each spectral region (0.2 to 0.68  $\mu m$  and 0.68 to 4.0  $\mu m$ ) the optical depth of a cloud layer is calculated from the cloud liquid water path ( $LWP$ ) or ice water path ( $IWP$ ) and the effective radii of cloud droplets ( $r_{el}^{a1}$ ) and ice crystals ( $r_{ei}^{a1}$ ).

$$\delta_l = a_0 r_{el}^{a_1} \cdot LWP \quad (2.30)$$

$$\delta_i = a_0 r_{ei}^{a_1} \cdot IWP \quad (2.31)$$

with  $a_0$  and  $a_1$  being coefficients used in the polynomial fit to the Mie calculations (Roeckner et al., 1996). The total cloud optical thickness then is

$$\delta = \delta_l + \delta_i \quad (2.32)$$

The effective radius of cloud droplets is parameterized from the in-cloud liquid water content  $q_{cl}$ .

$$r_{el} = \left( \frac{3q_{cl} \cdot \rho_a}{4\pi\rho_w k N} \right)^{\frac{1}{3}} \quad (2.33)$$

with the shape parameter  $k$  (0.67 in continental clouds and 0.8 in maritime clouds) and the number of cloud droplets  $N$ . The largest uncertainty is due to  $N$  which may vary by orders of magnitude in time and space. In the standard version of the model specified values are used. 100 and 220  $cm^{-3}$  are assigned to the low-level maritime and continental clouds. These values are gradually reduced to 50  $cm^{-3}$  in higher layers. The effective radius of ice crystals is a function of the ice water content based on empirical data [Heymsfield (1977) and McFarlane et al. (1992)].

$$r_{ei} = \alpha \chi^\beta \quad (2.34)$$

The mean crystal length  $\chi$  is an empirical function of the model calculated in-cloud ice water content  $q_{ci}$  (Heymsfield, 1977).

$$\chi = \gamma \sum_{n=0}^3 \delta_n (\log q_{ci})^n \quad (2.35)$$

with  $\gamma = 0.001$ ,  $\delta_0 = 0.698$ ,  $\delta_1 = 0.366$ ,  $\delta_2 = 0.122$  and  $\delta_3 = 0.0136$

## 2.2 Dynamical adjustment

### 2.2.1 Introductory remarks

It is necessary to force the model to the observed state to be able to validate simulations for specific synoptic situations against observations. The reason for the necessity to compare with short observation periods (field studies) is, that many meteorological quantities calculated by the model, like cloud liquid water or number of cloud droplet, are not available as long term observations (Lohmann et al., 1999). For this purpose two common approaches exist: data assimilation and dynamical adjustment.

An issue which is not yet solved satisfactorily in the process of initializing numerical models is the so-called spin-up effect. Numerical weather prediction models are usually initialized using a data-assimilation scheme. During this procedure an estimate (first guess) of the actual initial stage is provided by a short-range forecast from a previous initial state. The first guess is then modified by new observations and the analysis increment is added to the first guess. This new state is no longer in balance with the model equations because of the increments of the observations. This imbalance is dissipated as gravity waves after some time (hours to days) but in the meantime the model contains noise which can significantly disturb the three dimensional divergence and associated fluxes. The effect of this spin-up is illustrated in Figures 2.1 and 2.2 showing differences of the ECMWF's 24 h and 6 h forecast valid for the same time 00Z<sup>3</sup>, 14th of March 1993.

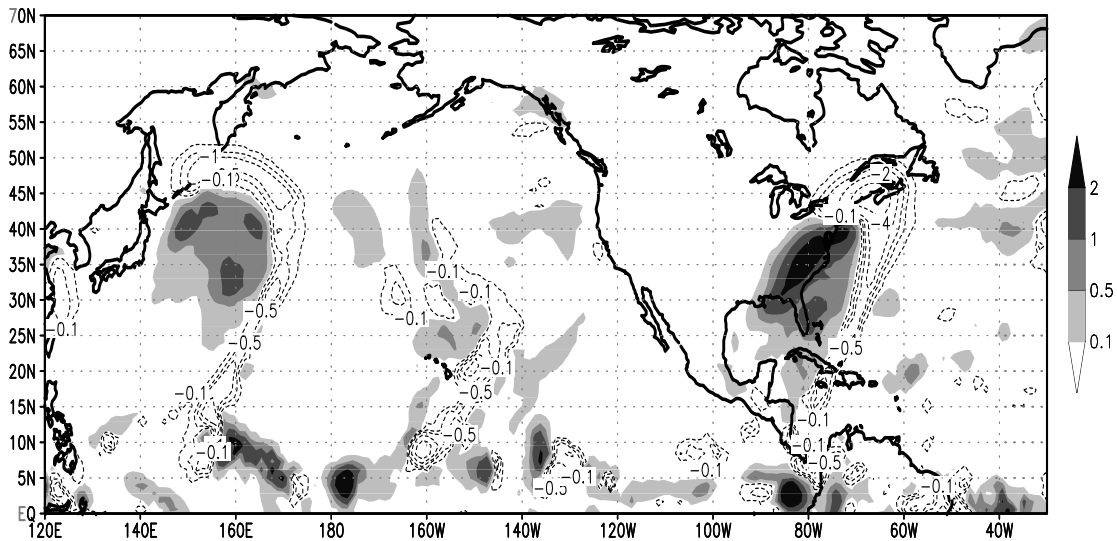


**Figure 2.1:** Difference 24h-6h forecast of the ECMWF forecast system for the total precipitation [ $mmh^{-1}$ ] at 00Z, 14th of March 1993. In shaded regions stronger precipitation is predicted by the 24h forecast, while weaker precipitation is predicted in contoured regions. Contours are plotted for: -4.0, -2.0, -1.0, -0.5 and -0.1  $mmh^{-1}$ .

The 6 h forecast predicts too much precipitation in frontal areas (up to 5  $mmh^{-1}$ ) and too little behind the cold front. A good example is the developing system along the East Coast of the U.S.A., which will be investigated in more detail in the following sections. Large differences also occur in the representations of total cloud cover (Figure 2.2). Because of this spin-up problem, the direct validation with the ECMWF reanalysis is avoided.

Although the dynamical adjustment also disturbs the model balance it has advantages compared to the standard data assimilation. Since the non-physical relaxation term is added at every

<sup>3</sup>00Z = 00 UTC = 00 GMT (Greenwich Mean Time)

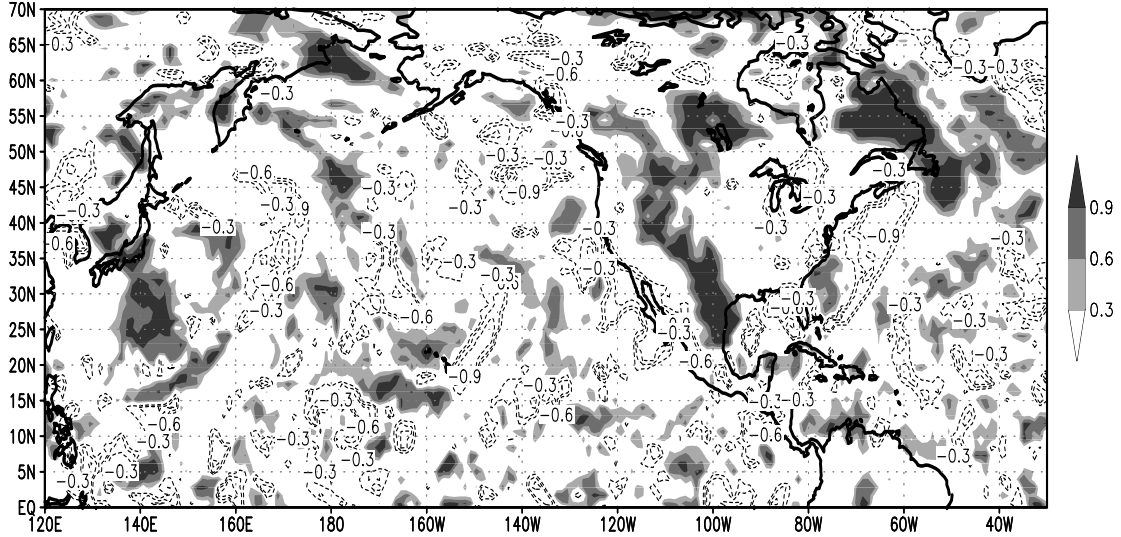


**Figure 2.2:** Same as Figure 2.1 but for the total cloud cover [fract.]. Contours are plotted for -0.9, -0.6 and -0.3.

model time step (every 12 minutes in this case), this more gradual adjustment to the observed state, compared to the standard data assimilation, reduces largely the production of noise and maintains the full dynamical and physical interactions of the climate model to generate its own, internally consistent, evolution of the physical processes.

Another advantage is that, once a control simulation is available, changes in the parameterization schemes can be tested very quickly, even in higher horizontal resolutions, as compared to a validation in a climatological sense. Furthermore it is important to note, that this method cannot be used in regions where the forcing reanalysis does not reproduce the observations. This might be the case in the tropics, at least for situations which are only weakly dependent on the large-scale circulation.

### 2.2.2 Method

The dynamical adjustment used in this study is based on the "Newtonian relaxation technique" or "nudging" [e.g. Anthes (1974), Hoke and Anthes (1976), Krishnamurti et al. (1991) or Jeuken et al. (1996)], which relaxes the model dynamics to the observed state by adding a non-physical relaxation term to the model equations.

$$\frac{\partial X}{\partial t} = F_m(X) + G(X_{Obs} - X) \quad (2.36)$$

where  $X$  is the prognostic variable,  $F_m$  is the model forcing and  $G(X_{Obs} - X)$  is the relaxation term. The latter is a product of the relaxation coefficient  $G$  and the difference between the observation and the value calculated by the model.

In the ECHAM4 model the relaxation is carried out in two steps. First the model forcing  $F_m$  is calculated yielding a new value for the prognostic variable. Afterwards the new model value is calculated with the observation. Discretization of equation (2.36) into the "leap frog" scheme of the model leads to

$$\frac{X_{new} - X_{old}}{2\Delta t} = G(X) [X_{obs} - X_{new}] \quad (2.37)$$

Defining an adjustment weight  $C(X) = 2\Delta t \cdot G(X)$  and solving the equation for the new model time step  $X_{new}$  leads to the equation which is finally implemented into the model. The new

model value is calculated as a linear combination of the old model value  $X_{old}$  and the observation  $X_{obs}$ , both depending on the adjustment weight.

$$X_{new} = \left( \frac{1}{1 + C(X)} \right) \cdot X_{old} + \left( \frac{C(X)}{1 + C(X)} \right) \cdot X_{obs} \quad (2.38)$$

The main difficulty is the choice of variables to be adjusted and the appropriate relaxation coefficients. A large relaxation term would dominate the model forcing and would therefore suppress characteristic features (and errors) of the model. Furthermore errors in the observation can be spuriously amplified. On the other hand a small relaxation term would not force the model to the observed state, so that a validation with observational data is not meaningful (Jeuken et al., 1996).

Since observational data is neither available at every model time step (12 minutes) nor at every grid point on the globe, the ECHAM4 model is adjusted to the ECMWF reanalysis. As the latter is only available every six hours, it is necessary to interpolate to the time steps in-between. For that purpose a simple linear interpolation is used. According to Jeuken et al. (1996) and Kirchner (1999) a more sophisticated cubic spline interpolation does not lead to significant improvements of the results.

nudged variable	G
vorticity	1.0E-4
divergence	5.0E-5
temperature	1.0E-5
surface pressure	1.0E-4

**Table 2.1:** Adjusted variables and their relaxation coefficients.

Different approaches exist for the choice of variables to be adjusted. Kuo and Guo (1989) concluded that a simultaneous assimilation of both, wind and mass field leads to the best result. According to Brill et al. (1991) the adjustment of the surface pressure is necessary as well, because adapting the atmosphere only can lead to an accumulation of errors at the surface. For this investigation the approach of Jeuken et al. (1996) is used and vorticity, divergence, temperature at each model level and the logarithm of surface pressure are adjusted with the relaxation coefficients shown in Table 2.1. They represent

a good compromise between a too large forcing, which would dominate the model physics and a too weak forcing, which will worsen the agreement with observations.

The time scale for the adjustment term is of the same order of magnitude as the time scale for the geostrophic adjustment. The largest weights are put on the surface pressure and vorticity with smaller values used for the temperature and the divergent part of the wind. Reason for this choice is, that the model performs better with relatively small coefficients for temperature and divergence, which directly influence diabatic processes in the model (Jeuken et al., 1996). Furthermore the daily observed SST serves as a lower boundary condition. The moisture field is not adjusted because of large spin-up errors occurring in the moisture field of the ECMWF reanalysis (Figure 2.1 and 2.2),

The ECMWF reanalysis, from which the necessary forcing files are calculated, uses the same horizontal resolution as the version of ECHAM4 used in this study, so that a horizontal interpolation is not necessary. A vertical interpolation of the forcing files is necessary, because the reanalysis uses a higher vertical resolution of 31 levels up to 10 hPa as compared to 19 levels in the standard ECHAM4 version.

### 2.2.3 Influence on the model balance

The dynamical adjustment approach is not perfect. The initialized field is not in balance due to the weak but steady forcing. Furthermore, not only the dynamical quantities like wind and temperature are influenced by the relaxation. The adjustment also modifies diabatic processes indirectly. The advantage of the method is demonstrated by comparing the adjusted fields with

the results of a short 24 h forecasts. This comparison is shown in Figures 2.3 and 2.4 for the adjusted model simulation at 00Z 14 March 1993 and for the 24 h forecast, initialized at 00Z 13 March 1993. After an integration of 24 h in forecast mode, the model is assumed to be in reasonable balance. The differences between the two simulations are small. This confirms that the adjusted simulation shows the nearly balanced state.

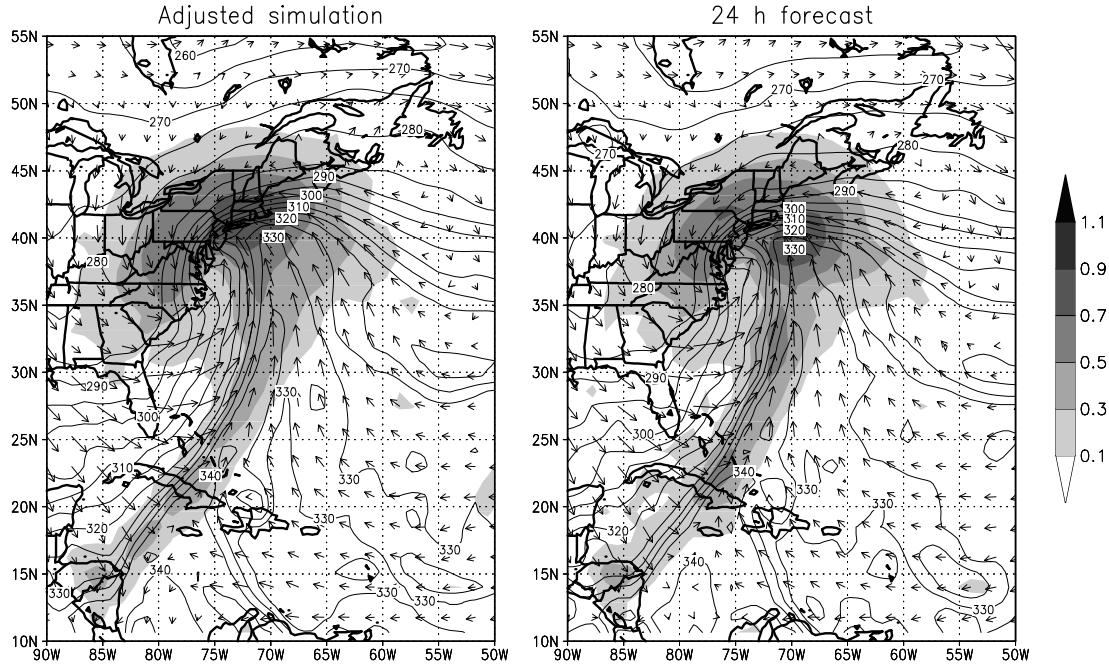


**Figure 2.3:** Comparison of the dynamically adjusted simulation (left) and the 24h forecast (right) at 00Z, 14th of March 1993. The vector field shows the 10m wind field and it is coloured by the 2m temperature. Grey-shaded is the cloud water path [ $kg/m^2$ ] and contoured the near surface equivalent potential temperature [ $K$ ].

This raises the question why the dynamical adjustment is used when the forecast mode is able to reproduce the observed features. However, this is true only for short range forecasts. The longer the forecast, the larger the differences to the observed field. Therefore only series of short forecasts are possible ending in inconsistent representations of the life cycles of the investigated systems. Furthermore the forecasts are restarted from the adjusted CONTROL simulation. The adjustment is therefore not only necessary to force the model to the observed state, but also to enable forecast simulations by producing the necessary initial files.

For a validation study it is necessary to know how large the adjustment of the forced variables is compared to the physical and dynamical tendencies. Therefore accumulated tendencies of the adjustment are calculated for each relaxed variable. It is important that the tendencies of the adjustment are small compared to the dynamical tendencies. Otherwise the influence of the forcing is too large to allow a validation of the parameterization schemes.

The CONTROL simulation was started at the first of January 1993 from a restart file of a climate run. While the adjustment tendencies are large at the beginning of the simulation, they are becoming smaller during the course of the simulation. To minimize the influence of the adjustment, synoptic situations occurring at least one month after the start of the simulation are chosen. This spin-up time is long enough for the atmospheric fields to reach a nearly balanced state, but probably not long enough for surface fields like soil moisture.

Figure 2.5 demonstrates that the tendencies from the adjustment are in fact small compared to the dynamical tendencies. It shows time series of the dynamical and adjustment tendencies, which have been averaged over the region in which the extratropical cyclone occurs. Even if single grid points are compared the adjustment tendencies are some orders of magnitude smaller

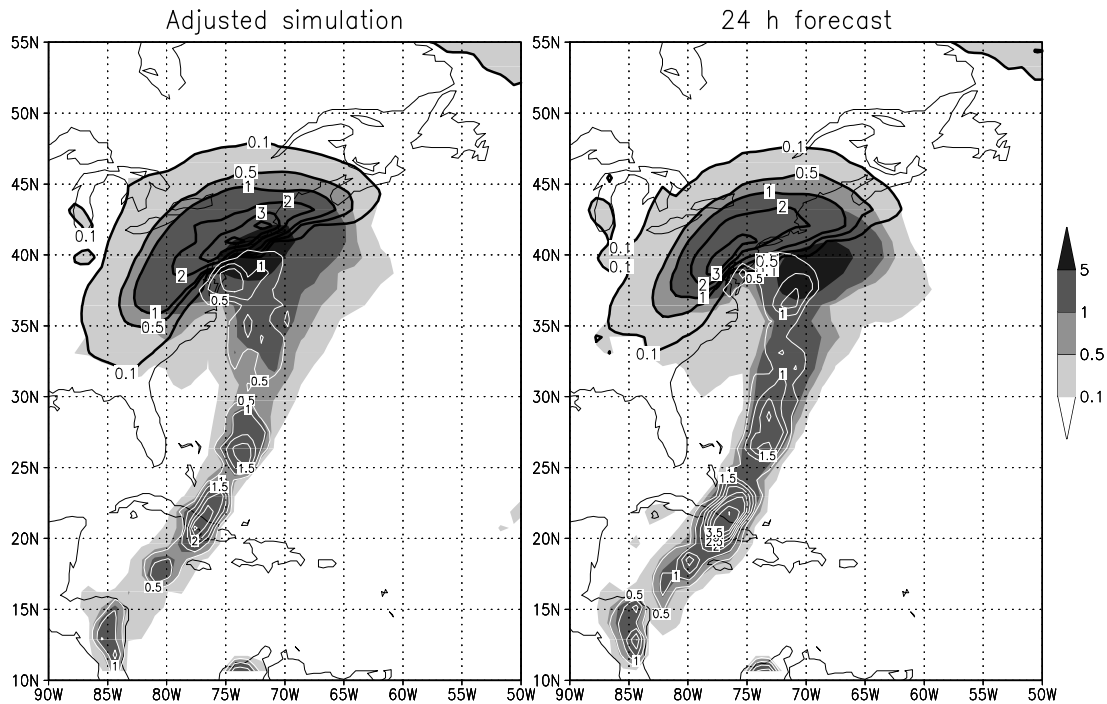


**Figure 2.4:** Same as Figure 2.3 for the different precipitation fields [ $mm/h$ ]. The color shaded field shows the snow fall. Grey-shaded is the total precipitation, red contoured the convective precipitation and black contoured the near surface equivalent potential temperature [ $K$ ].

than the dynamical tendencies. This is illustrated in Figure 2.6 which shows the horizontal distribution of the adjustment tendencies at one single time step as compared to the corresponding dynamical tendencies.

## 2.3 Observational data

### 2.3.1 ISCCP satellite data

The ISCCP<sup>4</sup> project [e.g. Rossow and Schiffer (1991), Rossow and Garder (1993a) or Rossow et al. (1996b)] was established in 1982. Its primary focus is the improvement of the understanding of the role of clouds in the radiation budget and the global hydrological cycle. For this purposes the ISCCP analysis combines satellite-measured radiances (stage B3 data) (Rossow et al., 1996a) with the TOVS<sup>5</sup> (Kidwell, 1995) atmospheric temperature-humidity data and ice/snow correlative datasets to obtain a hierarchy of data products. The ISCCP cloud analysis consists of three main parts, namely cloud detection, radiance analysis and statistical analysis. This is schematically illustrated in Figure 2.7.

The cloud detection procedure analyses the B3 radiance data in four steps during which several threshold tests are carried out to separate cloudy pixels from cloud-free pixels. In the first step a first estimate of the radiances for cloud-free pixels is retrieved at each point and time, while in the second step any pixel with a radiance sufficiently different from the clear sky value is declared cloudy (first threshold test). In the third step additional tests are carried out to remove infrequent errors occurring in clear sky radiances. The last step, the so-called final threshold test, identifies cloudy conditions by those radiances that are sufficiently different from the clear sky values in any spectral channel.

<sup>4</sup>ISCCP = International Satellite Cloud Climatology Project

<sup>5</sup>TOVS = TIROS Operational Vertical Sounder

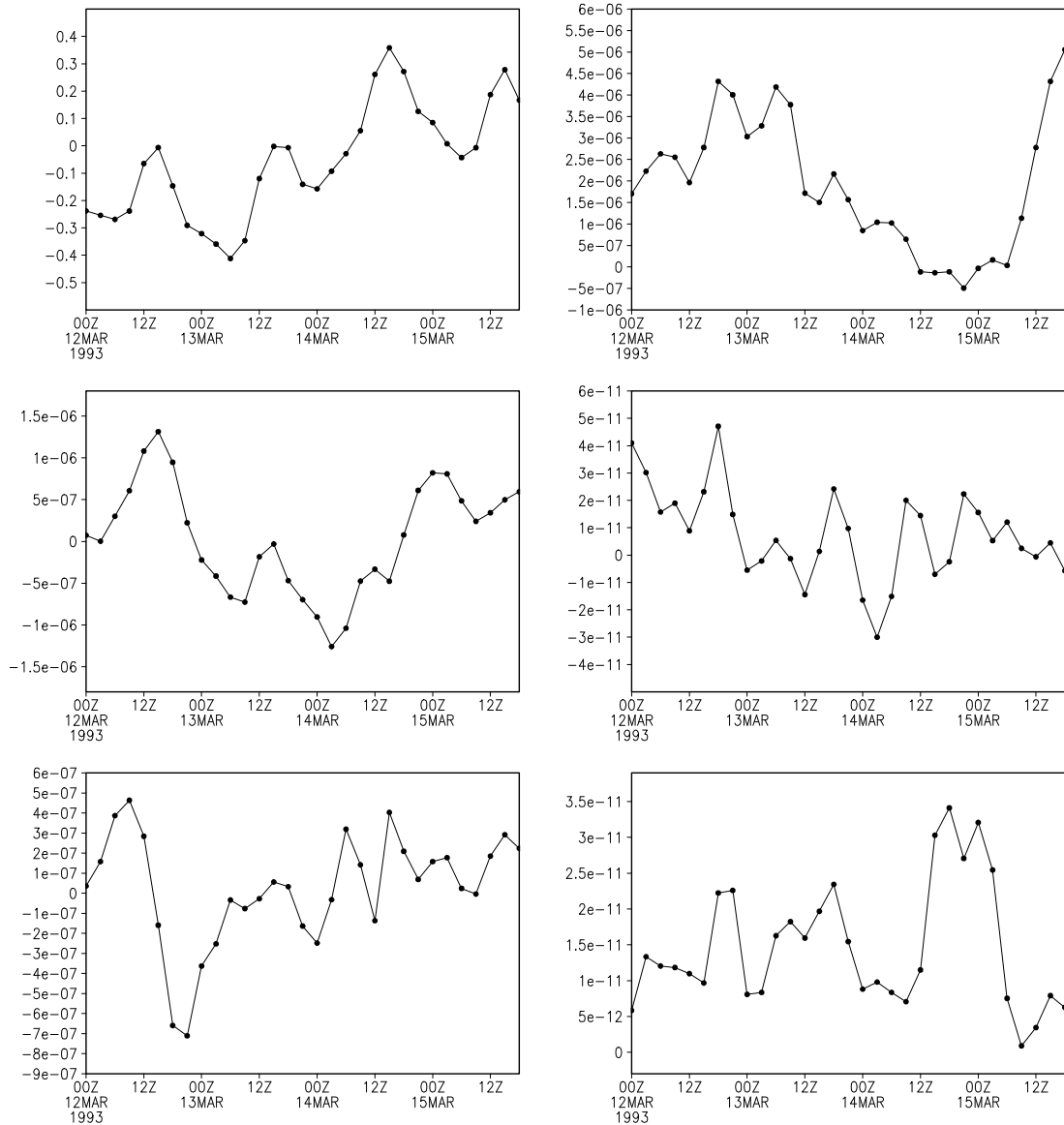


**Figure 2.5:** Temporal development of the dynamical tendency (left) and the adjustment tendency (right) averaged over the region  $100^{\circ}\text{W}$  to  $40^{\circ}\text{W}$  and  $15^{\circ}\text{N}$  to  $70^{\circ}\text{N}$ . **Upper row:** Temperature at model level 15 ( $\sim 850$  hPa)[K/3h]. **Middle row:** Vorticity at model level 11 ( $\sim 500$  hPa) [1/3h]. **lower row:** Divergence at model level 8 ( $\sim 250$  hPa) [1/3h].

Clear sky, IR and VIS radiances are determined independently and all threshold decisions are recorded separately. The pixel analysis is done separately for each satellite radiance dataset and the results are reported in the stage DX dataset with a nominal resolution of 30 km and 3 h.

Once pixels are classified as cloudy or clear, the radiances are compared with radiative model transfer calculations designated to simulate the measurements of the AVHRR<sup>6</sup> channels, to which all the radiometers have been normalized (Brest and Rossow, 1992). Comparisons of observed radiances to simulated values are used to retrieve the surface reflectance and temperatures from clear sky radiances, and the cloud optical thickness and cloud top temperature from cloudy radiances. All retrieved parameters are model-dependent quantities. The accuracy with which they represent real quantities depends on the effect of other cloud and surface characteristics, which are neglected or kept constant in the model such as for example the assumed optical homogeneity at pixel spatial scales.

<sup>6</sup>AVHRR = Advanced Very High Resolution Radiometer

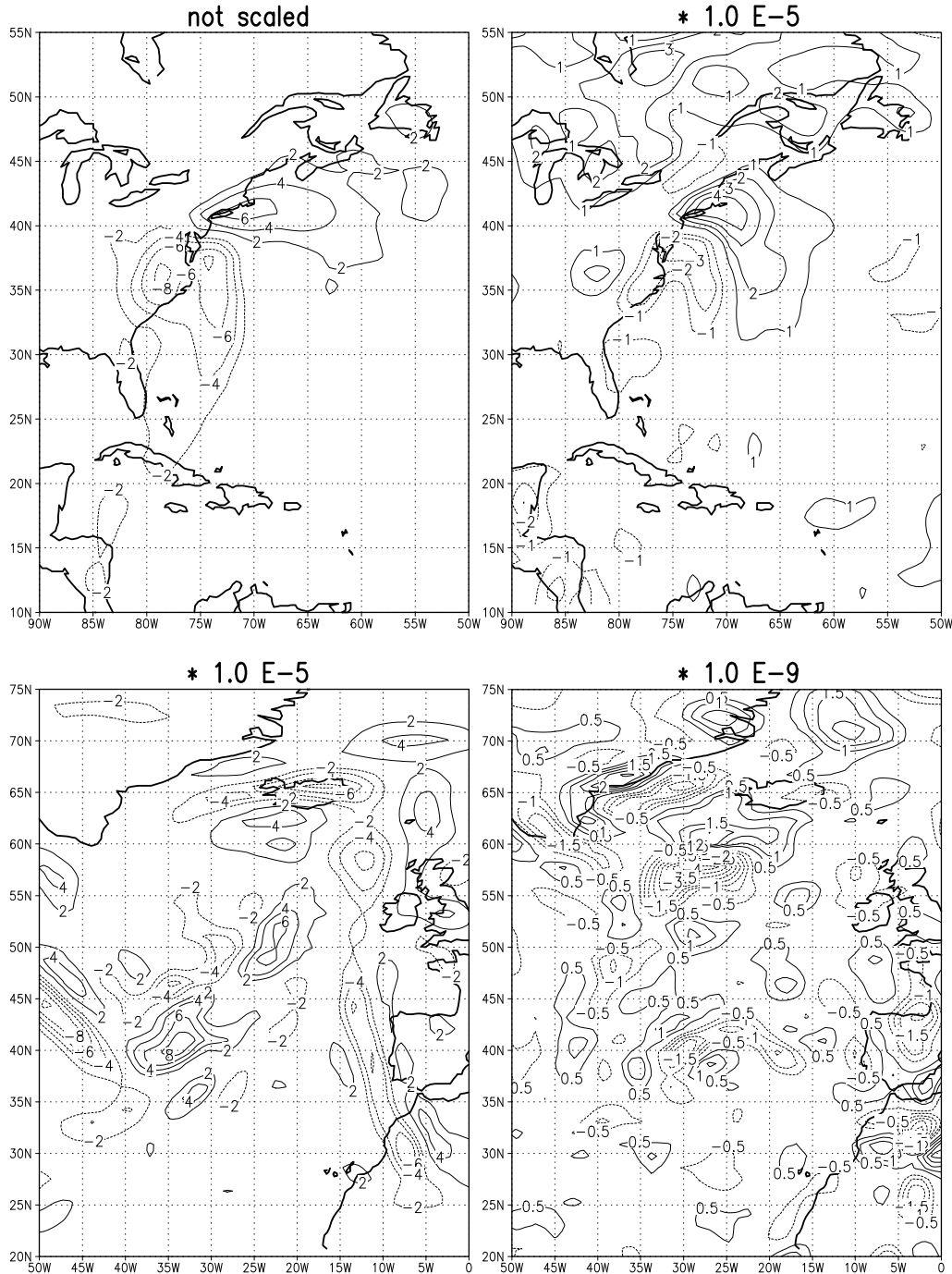


**Figure 2.6:** Dynamical tendency (**left**) and adjustment tendency (**right**) of ECHAM4 for the temperature at model level 15 ( $\sim 850$  hPa) [K/3h] (**top**) and the vorticity at model level 11 ( $\sim 500$  hPa) [1/3h] (**bottom**) (at 00Z, 14 March 1993).

The validation of the ISCCP cloud analysis involves three steps, cloud detection, cloud amount determinations and retrieval of cloud radiative properties. One of the most straightforward checks of the clear sky IR radiances is to compare the retrieved SST with other measurements. At the same time this is a test for the radiation models used (Rossow and Schiffer, 1991). A problem with all comparisons of ISCCP clear sky IR or VIS radiances with other datasets is the comparability. This is true for SST observations as well as for cloud observations. While surface temperatures measured by ISCCP represent the skin temperature of ocean and land surfaces, other datasets are mostly compiled from weather reports (2m temperatures). Furthermore the ISCCP surface temperatures are brightness temperatures for which the emissivity is assumed

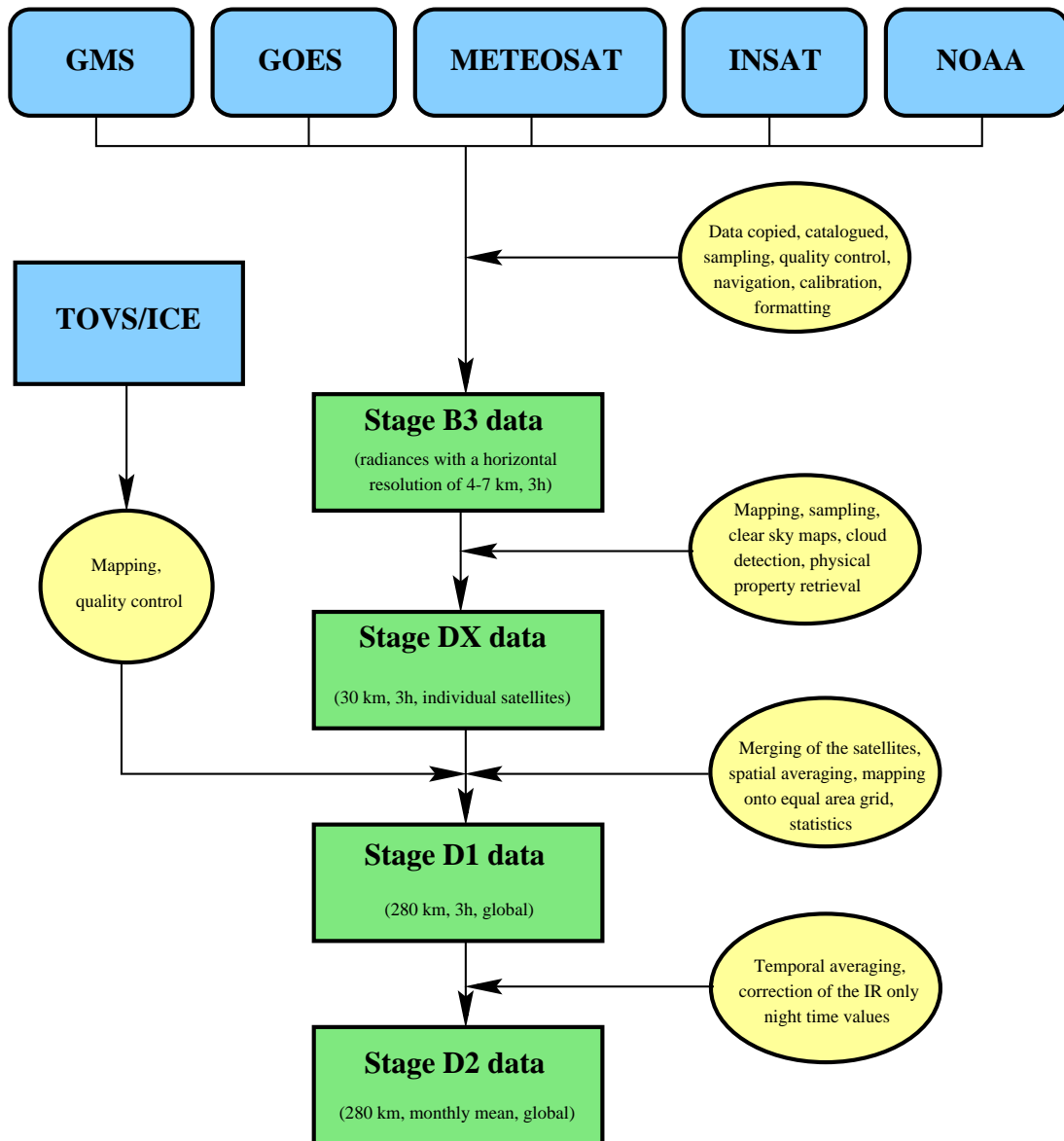


**Figure 2.7:** Product hierarchy of the ISCCP satellite data and main steps carried out to produce the different products.

to be 1. Therefore they underestimate physical temperatures by about 0.3 to 0.7 K since real emissivities have values between 0.98 and 0.99. Further problems occur due to different detection procedures, the much smaller area size (5-10%) observed by a surface observer compared to an ISCCP pixel, untrained observers on non-scientific ships (observer bias) and due to the “weather bias” caused by ships avoiding bad weather (Warren et al., 1986). Comparisons of satellite measurements with values from land stations is much more difficult since the emissivity is much more variable with location and time than over water. The averaged errors of the ISCCP analysis for distinct regions on the globe are summarized in Table 2.2.

The main sources of errors in the cloud detection are systematic and random errors in the retrieval of the clear sky radiances. But, as long as the magnitude of the clear radiance errors is smaller than the value assumed by the algorithm detection threshold, no systematic effect is introduced in the representation of cloud amounts. Overall, the uncertainties in the clear sky radiances over land are smaller than the thresholds used in the detection algorithm. Problems appear in coastal regions where large changes in cloud cover occur or in snow melt as well as

Surface type	VIS reflectance [%]	Cloud error [%]
Open ocean (ice free)	$\sim 0$ [3]	$\sim 0$ [10]
Coastal water	$\sim 0$ [3]	-5 [15]
Subtropical marine stratus	$\sim 0$ [3]	-(5-10) [20]
High-latitude storm tracks	+3 [3]	-(5-10) [20]
Ocean glint	[>20]	No VIS threshold
Sea ice	$\sim 0$ [10]	-(20-30) [20]
Land (snow free)	$\sim 0$ [3-5]	-(3-6) [10]
High-latitude land	$\sim 0$ [3-5]	-(6-10) [10]
Snow-/ice-covered land	$\sim 0$ [10]	-(15-25) [15]

**Table 2.2:** Summary of bias and [rms] errors of visible reflectances [%] derived from ISCCP clear-sky radiances and the implied bias and [rms] errors in cloud detection expressed as percentage cloud amounts. Rms cloud amount errors are estimated from the amount of marginally cloudy pixels (pixels with radiances close to the dividing line between clear and cloudy categories) (Rossow and Garder, 1993b).

strong cooling events, which are associated with large changes of surface temperature (Rossow and Garder, 1993b).

On average, the ISCCP results are lower than individual surface observations by about 11% with a standard deviation of almost 40%. This negative bias changes with season, being 8% more negative in winter than in summer (Rossow et al., 1993). The large standard deviations are caused by a small number of cases with large differences. Major problems with the accurate determination of the clear sky visible radiances are associated with few regions of persistent cloud cover and small time-space scale variations of the reflectances of snow and sea-ice covered areas (Rossow and Garder, 1993b). Moreover, surface as well as satellite observations are expected to underestimate cloud amounts at night. The results of ISCCP are biased by about 3-6% more than daytime results due to the decreasing surface temperature (Rossow et al., 1993).

ISCCP analyses underestimate cloud amount at both poles by about 10% in winter and by at least 25% in summer. This general underestimation is not only caused by an overall decrease in contrast between clear sky and cloudy IR and VIS radiances, but also by an increase in the frequency of occurrence of optically thin, low-level, persistent cloud types that do not alter radiances at  $0.65 \mu m$  or  $11 \mu m$  sufficiently to be detected (Rossow et al., 1993).

Lau and Crane (1997) compared the ISCCP dataset with observations compiled from surface stations. In spite of the complementary nature of the two datasets, an overall consistency is noted between the propagation characteristics and the spatial structure of cloud cover. Nevertheless several discrepancies are noted. The most striking example is the underestimation of low-level clouds in the satellite composite under high cloud shields east of the extratropical cyclone centre. In the tropics the broad pattern of precipitation, based on surface observations, is in good agreement with the shield of deep convective clouds, as deduced independently from the satellite dataset (Lau and Crane, 1997).

### 2.3.2 Other observations

Other types of observations are occasionally used to support the results of the comparisons with ISCCP DX or in situations where no observations by ISCCP are available. This is the case for the climatological cloud validation at the beginning of chapter 4, where different climatologies for total cloud cover [Rossow and Schiffer (1991), Hahn et al. (1994a)], liquid water path [Greenwaldt et al. (1993), Weng and Grody (1994)] and precipitable water [Greenwaldt et al. (1993), Liu and Curry (1993)] are used.

The liquid water path and precipitable water datasets are calculated from SSM/I<sup>7</sup> observations. The SSM/I is a passive remote sensing radiometer which measures the upwelling radiation in 4 spectral channels: 19.235, 22.235, 37 and 85.5 GHz. All frequencies are received in both horizontal and vertical polarization except the 22.235 GHz channel which only measures in vertical polarization. The studies mentioned above do not agree, because the results depend strongly on the retrieval algorithm used and can be affected by many input factors (e.g. SST, cloud temperature or surface wind). Therefore different datasets are used to estimate the possible range of the observed cloud properties.

GOES<sup>8</sup> satellite observations from the COMET<sup>9</sup> 001<sup>10</sup> dataset are used for illustration of the developing extratropical cyclone along the East Coast of the U.S.A.. Relative humidity is validated against radiosonde measurements.

ISCCP DX brightness temperatures are partly replaced by data from the CLAUS<sup>11</sup> project, because ISCCP stores data as integer counts. They are re-translated into physical values using lookup tables with the consequence that only distinct temperature values are used. This would lead to large scattering in the histograms used for validation as well as for the comparison with the sensitivity studies.

CLAUS uses the ISCCP B3 radiance data (Rossow et al., 1996a) and stores the brightness temperatures in a  $0.5^\circ$  rectangular grid. Due to the use of special data processing techniques, the problems caused by assimilating data from multiple satellites are reduced. The method separates the processing into a spatial stage with different levels of smoothing to preserve details wherever the data density warrants it, but to fill in small holes ( $< 1^\circ$ ) caused by missing data. The spatial stage is followed by a linear temporal interpolation of adjacent images to fill in the remaining holes. More information about CLAUS can be found on the project web page <http://clus.nrsc.co.uk/introduction.html>.

---

<sup>7</sup>SSM/I = Special Sensor Microwave/Imager. Web page: <http://www.ssmi.com>

<sup>8</sup>GOES = Geostationary Orbiting Environmental Satellite

<sup>9</sup>COMET = Cooperative Program for Operational Meteorology, Education and Training

<sup>10</sup>More information can be found on the web page <http://www.joss.ucar.edu/cometCases/>

<sup>11</sup>CLAUS = Cloud Archive User Service

# Chapter 3

## Synoptic situations

### 3.1 Introductory remarks

While a climatological validation of monthly mean values has the advantage of retaining the global view of the system, it is more difficult to identify the errors in the representation of distinct synoptic systems, because the cloud climatology of the model may not originate from well represented weather episodes.

Synoptic systems occur in many different types. Not only do different systems occur in different regions of the globe. Differences occur in the same region between systems over land and ocean. Therefore it is not feasible to validate every single system which could occur on the globe. The first and important task is the restriction on a few systems which are thought to be representative for a wide range of synoptic systems.

In this thesis three systems have been chosen. As an example of extratropical cyclones in midlatitudes an intense cyclone development along the East Coast of the U.S.A. between the 12th and 14th of March 1993 is investigated. Anticyclones in subtropics and midlatitudes are represented by an Atlantic blocking situation which developed between 15th and 23rd of February 1993.

As a representative of tropical systems, cloud clusters in the western Pacific warm pool region are investigated. Mesoscale convection is an important process on scales from a few to many hundreds of kilometres. It plays a major role as an energy source for the climate system. Furthermore, it represents the major heat and moisture source for the upper layers in the tropics and strongly influences the radiation budget ([Moncrieff, 1995](#)).

However, it is questionable, whether the pure dynamical adjustment, being used in this study, is able to force the model to the observed track for the tropical case, due to the much stronger dependence of the convection on local conditions like SST or surface heat fluxes. [Figure 3.1](#) compares the cloud optical thickness simulated by the model with observations of ISCCP at 21Z, 9th of February 1993 during the TOGA COARE<sup>1</sup> ([Webster and Lukas, 1992](#)) experiment.

It demonstrates that the model, although able to reproduce tropical convection in general, cannot reproduce the observed cloud distribution. This is true in spite of the larger amounts of observations assimilated into ERA during the TOGA COARE experiment. Therefore the third case is excluded from the investigation.

In the following sections the two remaining cases are described in more detail. Each section is subdivided into a general introduction into the type of system and a description of the distinct case which has been investigated. In the latter, the system, as it has been observed, is described as well as its representation in the adjusted model simulation.

---

<sup>1</sup>TOGA COARE = Tropical Ocean Global Atmosphere Coupled Ocean Atmosphere Response Experiment

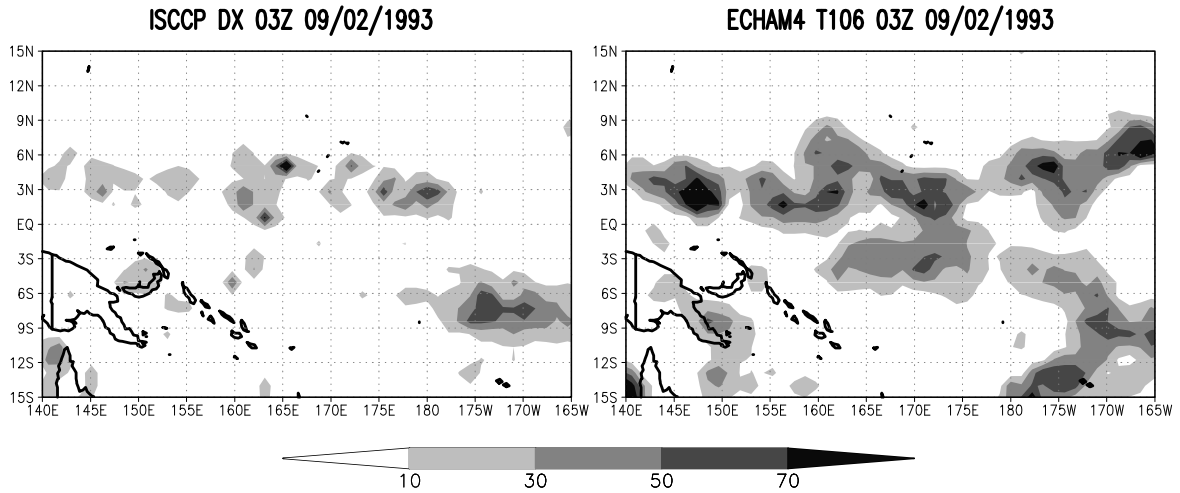


**Figure 3.1:** Comparison of the cloud optical thickness  $\tau$  at 21Z, 9th of February 1993 of the adjusted ECHAM4 T106 (right) simulation and observed by ISCCP DX (left).

## 3.2 Cyclone at the East Coast of the U.S.A.

### 3.2.1 General features

Severe snow storms are a major weather concern for the East Coast of the U.S.A. Such storms are usually marked either by a primary surface low that propagates northeastward along the Gulf of Mexico and Atlantic coast or a primary low that tracks towards the Appalachian mountains and subsequently weakens as a secondary surface low develops along the southeast or Middle Atlantic coast. The former develops in the Gulf of Mexico, typically along the leading edge of an Arctic anticyclone centred over the southern Great Plains (Uccellini and Kocin, 1987). Cyclogenesis is triggered by the outbreak of Arctic air moving southward from the Canadian prairies, which meets warm air over the Gulf of Mexico and develops a baroclinic zone.

The rapid deepening of the cyclones off the Carolina coast, which often occur, is the result of the tight thermal gradient that forms between the cold continental air and the relative warm air over the Gulf stream (Cione et al., 1993).

In general heavy snowfall occurs to the north and northwest of the coastal surface low. It is located downwind of an upper-level

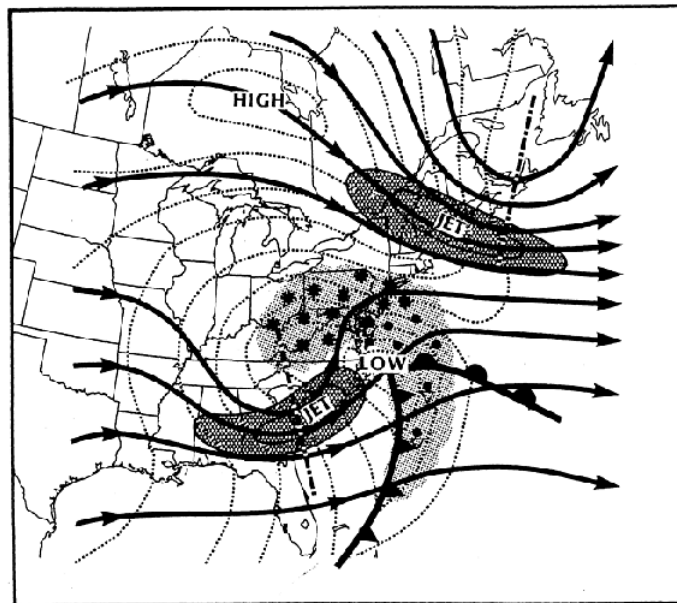


**Figure 3.2:** Schematic view of surface cold and warm fronts, high and low pressure centers, sea level isobars (dotted), precipitation (light shaded with distinguishing symbols for rain and snowfall), upper-level flow (arrows), upper-level trough axis (dot-dashed) and jet streaks (cross-hatched shading) associated with a typical heavy snow event along the East Coast (Uccellini and Kocin, 1987).

trough approaching the East Coast, characterized by diffluent height contours, and within the exit region of an upper-level jet streak. The cyclone interacts with a strong surface anticyclone to the north of New York or New England which provides a low-level source of cold air. The high is typically located beneath confluent height contours within the entrance region of a separate jet streak located upwind of a trough axis over southeastern Canada. Upper-level confluence is an important precursor for many East Coast snowstorms, since it acts to maintain the cold air in middle levels, an important requirement for precipitation falling as snow (Kocin and Uccellini, 1990). Those common features are illustrated by the conceptual model presented in Figure 3.2 (Uccellini and Kocin, 1987).

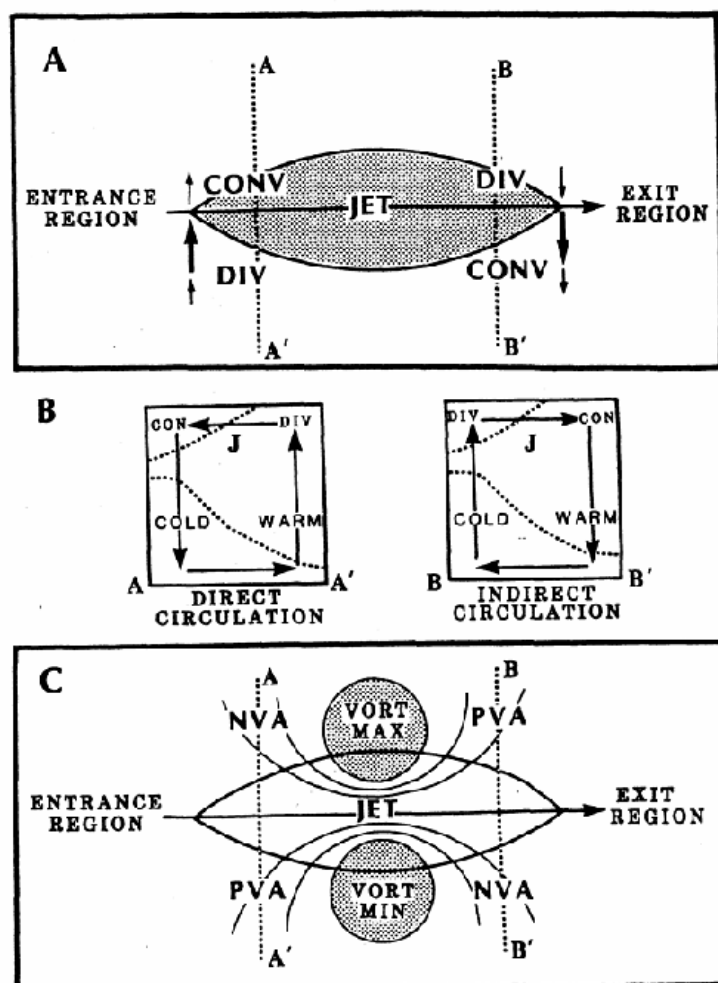


**Figure 3.3:** (A) Schematic view of ageostrophic wind components and patterns of divergence associated with the entrance and exit regions of a straight jet streak [after Bjerknes (1951)]. (B) Vertical cross sections illustrating direct and indirect circulations in the entrance region (A-A') and exit region (B-B') of a jet streak. The cross sections included two representative isentropes (dotted), upper-level jet location (marked by a J), relative position of cold and warm air, upper-level convergence and divergence, horizontal ageostrophic components and vertical motions (arrows) within the plane of each cross section. (C) Schematic view of maximum (cyclonic) and minimum (anticyclonic) relative vorticity centers and advection patterns associated with a straight jet streak (NVA = negative or anticyclonic vorticity advection, PVA = positive or cyclonic vorticity advection) (Uccellini and Kocin, 1987).

The secondary circulations as well as temperature and vorticity advections associated with an idealized jet streak are illustrated in Figure 3.3 (Bjerknes, 1951). The entrance region of the jet streak is marked by an ageostrophic component directed towards the cyclonic-shear side of the jet. This component represents the upper branch of a direct circulation that converts

available potential energy into kinetic energy for parcels accelerating into the jet. It is marked by rising motion on the anticyclonic (warm) side of the jet and sinking motion on the cyclonic (cold) side. Conversely, in the exit region, the ageostrophic component in the upper troposphere is directed towards the anticyclonic-shear side of the jet, representing the upper branch of an indirect circulation pattern that converts kinetic energy to available potential energy as parcels decelerate upon exiting the jet. Associated with this circulation pattern is rising motion on the cyclonic (cold) side of the jet and sinking motion on the anticyclonic (warm) side of the jet (e.g. Bjerknes (1951) or Uccellini and Johnson (1979)).

The rising branches of the ageostrophic circulations in the exit region of the jet streak approaching the East Coast from the southwest and the entrance region of the jet streak located over the northeastern U.S.A. appear to merge, contributing to a widespread region of ascent that produces clouds and precipitation (Uccellini and Kocin, 1987). The advection of Canadian air southward in the lower branch of the direct circulation across the northeastern U.S.A. maintains cold lower-tropospheric temperatures needed for snowfall along the East Coast. The northward advection of warm, moist air in the lower branch of the indirect circulation across the southeastern U.S.A. ascends over colder air to the north of the surface low and transports moisture into the region of the largest ascent. Those circulations additionally strengthen the thermal gradients in the middle and lower troposphere (Sanders and Bosart, 1985).

Furthermore the presence of the Rocky Mountains is crucial for the cyclogenesis, because the development of a lee through favours a poleward advection of warm moist unstable air from the Gulf of Mexico into southeastern Texas (Dickinson et al., 1997). Often those snow storms are associated with strong cold air outbreaks into the tropics, increasing the strength of the easterly trades resulting in stronger convective activity in the ITCZ (Schultz et al., 1997).

### 3.2.2 The "Storm of the Century"

Between the 12th and 14th of March 1993 one of the most intense East Coast storms of the 20th century paralyzed much of the eastern U.S.A. (thereafter referred to as "blizzard case"). It was the deepest cool season storm which affected the Gulf of Mexico during the period 1957-1996 (Dickinson et al., 1997). Figure 3.4 shows four time steps during the development of the storm between the 12th and 14th of March 1993.

Figure 3.5 compares the simulated and observed track of the cyclone and shows the ability of the model to represent the general synoptic situation. The simulated cyclone crosses the Gulf of Mexico and Florida and moves, further deepening, along the East Coast of the U.S.A.. The reason for the different tracks in ECHAM4 and the observation over the Gulf of Mexico might be a lower amount of observational data fed into the ECMWF reanalysis, from which the forcing data for the relaxation is calculated.

The cyclone developed along a stationary front from the western Gulf of Mexico to southern Georgia, which separated cold dry continental air from warm moist air over the Gulf of Mexico. South of this front the winds were mostly weak with values below  $15 \text{ ms}^{-1}$ , while to the north of the front values of  $25 \text{ ms}^{-1}$  were reached. A rapid intensification took place as the cyclone crossed the Gulf of Mexico and moved into Florida with hurricane-force winds and high tides. The rate of intensification is slightly weaker in the ECHAM4 model simulation compared to the observation in the developing stage and slightly stronger when the cyclone reaches the southeastern U.S.A. (Figure 3.6). This corresponds to the findings of Gilhousen (1994) that hardly any forecast model was able to predict the strong deepening of the system earlier than 24h in advance of the development, although buoy measurements in the Gulf of Mexico provided several indications of a more rapid deepening on the 12th of March 1993. The simulated cyclone reaches its lowest core pressure of 963 hPa on the 14th of March at 6 UTC, slightly higher than the observed 960 hPa.

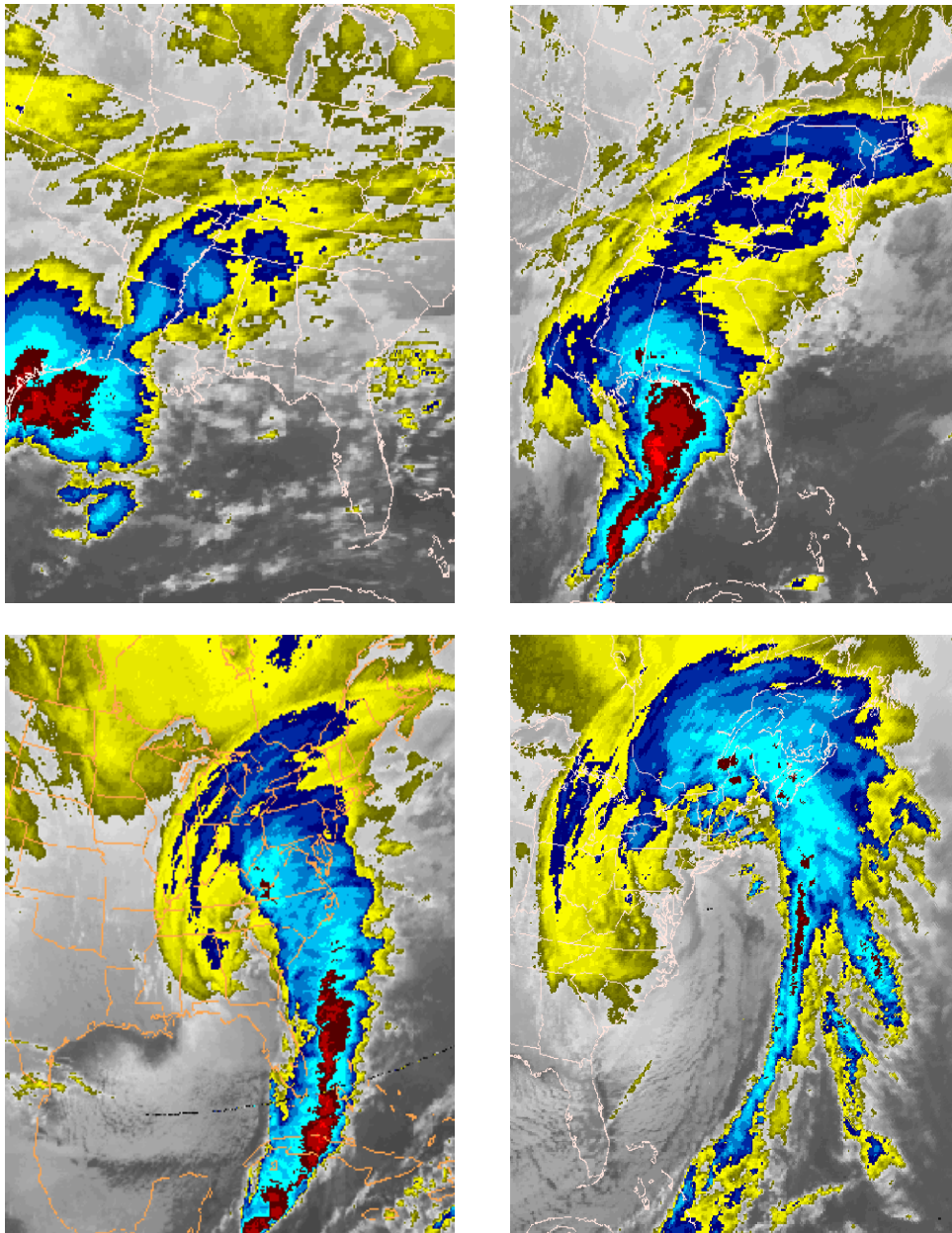


**Figure 3.4:** GOES7 images from 12Z, 12th of March 1993 to 00Z, 14th of March 1993 in the infrared channel with a horizontal resolution of 8 km (Source: COMET 001 data).

During the development, record-low surface temperatures and sea level pressures were measured in many regions of the southeastern and Middle Atlantic parts of the U.S.A. (Kocin et al., 1995). For example Dover (Delaware) reported the remarkable pressure drop of 58 hPa between 01 and 19 EST<sup>2</sup> on the 13th of March 1993. Equally remarkable was the pressure rise of 78 hPa within 37 hours after the passage of the storm. Since the track of the storm remained slightly inland, it prevented the urban corridor along the East Coast from receiving large accumulations of snow due to the change from snow to ice pellets or rain (Kocin et al., 1995).

The temperature advection fields are well reproduced in the adjusted simulation. This is illustrated by the equivalent potential temperature field, which combines information from the temperature and moisture fields (Figure 3.7). Moreover it emphasizes the frontal structures as

---

<sup>2</sup>EST = Eastern Standard Time

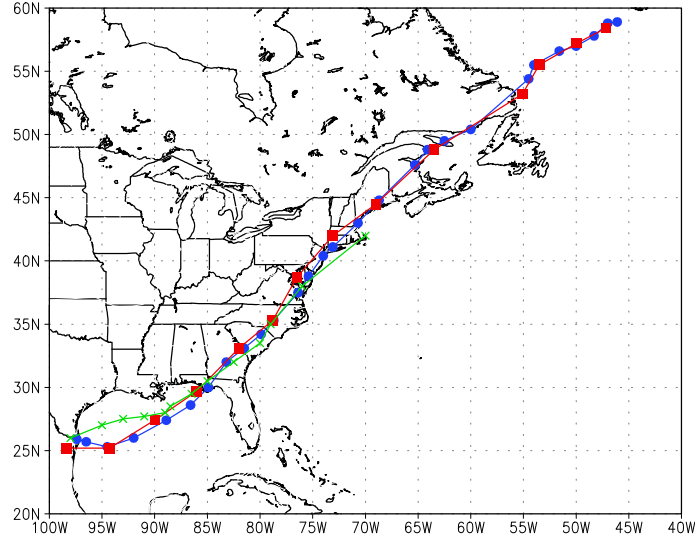


**Figure 3.5:** Path of the cyclone between the 12th and 15th of March 1993 in the adjusted ECHAM4 simulation (filled circle) compared to the ECMWF reanalysis (filled square) and an observation (crosses) (Kocin et al., 1995).

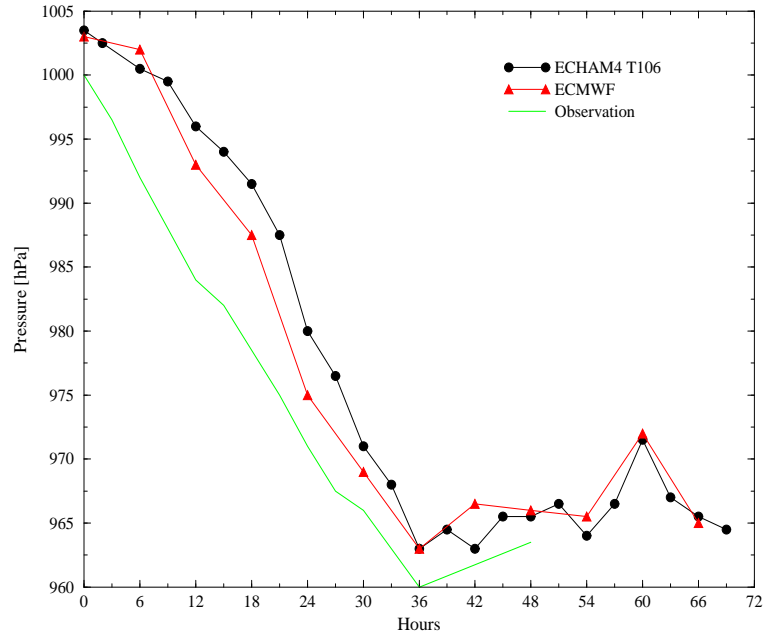


**Figure 3.6:** Temporal development of the surface pressure [hPa] of the developing cyclone between the 12th and 15th of March 1993 of the adjusted ECHAM4 simulation compared to the ECMWF reanalysis and an observation (Kocin et al., 1995).

sharp gradients and is calculated by:

$$\theta_e = \frac{1}{\exp\left[-\frac{g}{R_L T} \cdot Z\right]^{\frac{L}{c_p}}} \cdot \left[T + \frac{L}{c_p} \cdot q_v\right] \quad (3.1)$$

with the gravitational force  $g = 9.81 \text{ ms}^{-2}$ , the gas constant of dry air  $R_L = 287.07 \text{ Jkg}^{-1}\text{K}^{-1}$ , the geopotential height  $Z$ , the temperature  $T$ , the specific humidity  $q_v$ , the heat of vaporization  $L = 2.5 \cdot 10^6 \text{ Jkg}^{-1}$  and the specific heat capacity at constant pressure  $c_p = 1005 \text{ Jkg}^{-1}$ .

For a long time the cyclone model developed by Bjerknes (1919) and Bjerknes and Solberg (1922) formed the conceptual basis for describing the evolution of fronts during the life-cycle

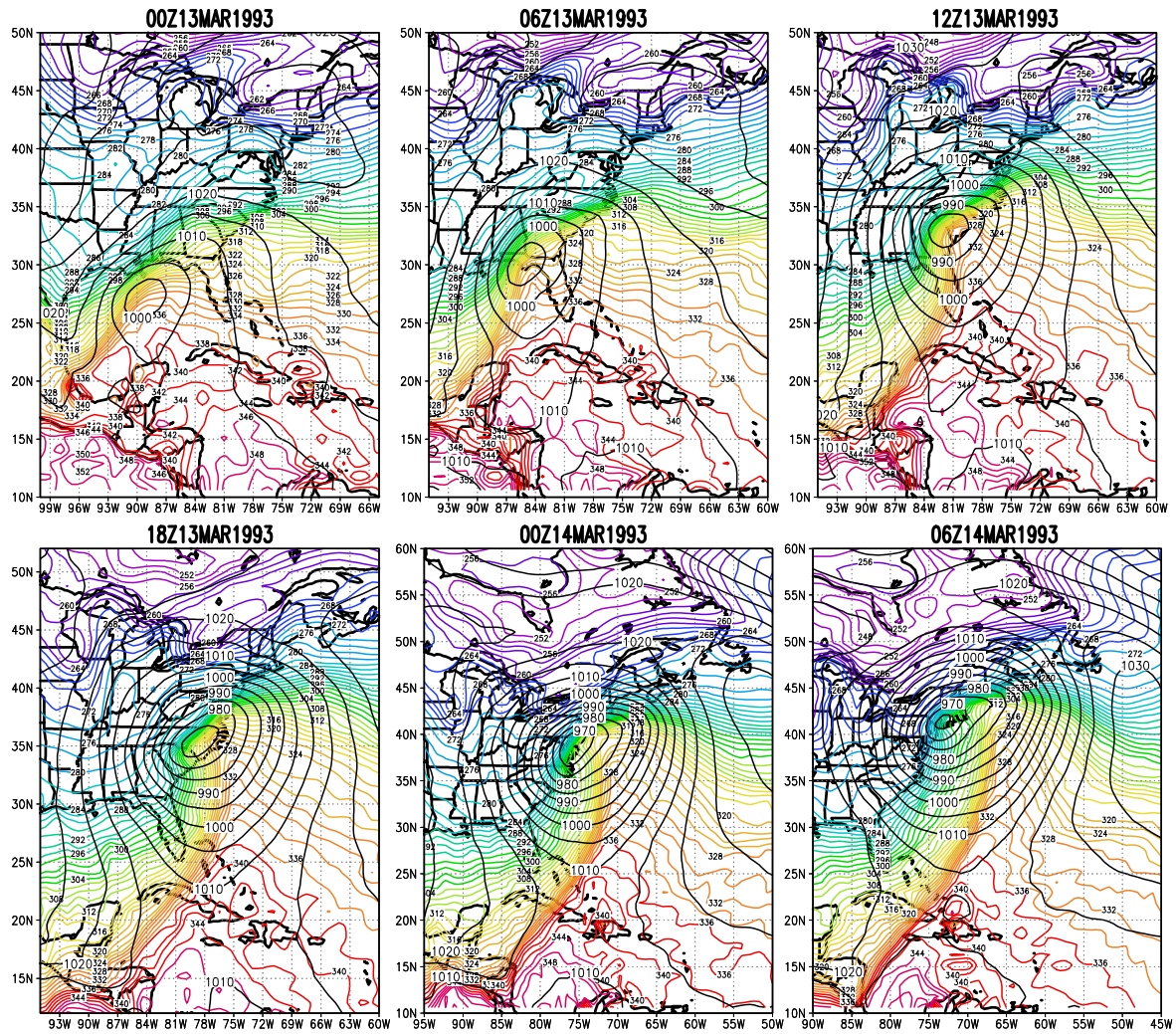


**Figure 3.7:** Mean sea level pressure [hPa] and equivalent potential temperature [K] (lowest model level) of the adjusted ECHAM4 simulation between the 13th and 14th of March 1993.

of extratropical cyclones. This model was derived primarily from the analysis of cyclones over the eastern Atlantic and Europe. Recent studies (e.g. [Neiman and Shapiro \(1993\)](#) and [Neiman et al. \(1993\)](#) among others) in other regions on the globe suggested some modifications to the Norwegian model in particular for cyclones which develop over the ocean:

- Loss of frontal baroclinicity (frontolysis) near the cyclone centre during the early phases of cyclogenesis (frontal fracture).
- Subsequent migration of warm frontal structure back into the northerly flow to the west of the intensifying cyclone (T-bone structure and bent-back warm front).
- Formation of a warm-core frontal occlusion in the polar air behind the cold front in the fully developed cyclone.

The modified conceptual model is illustrated in [Figure 3.8 \(Shapiro and Keyser, 1990\)](#). However, it is important to note, that the detailed flow during the development of an extratropical cyclone is far more complex than suggested by any conveyor belt model.

In ECHAM4 behind the cold front, as observed in typical extratropical cyclones, stratospheric air is mixed downward into the troposphere. This so-called "tropopause fold" is clearly seen in the potential vorticity (thereafter PV)<sup>3</sup> field ([Figure 3.9](#)). This important mechanism associated

<sup>3</sup>e.g. [Holton \(1992\)](#), [Hoskins et al. \(1985\)](#)

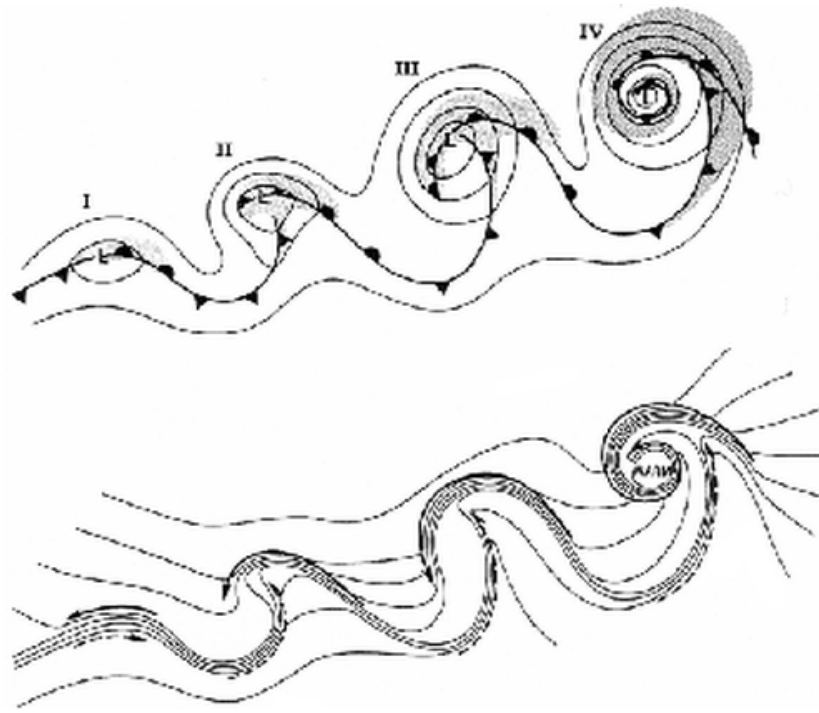


**Figure 3.8:** The life-cycle of a marine extratropical frontal cyclone (Shapiro and Keyser, 1990). (I) incipient frontal cyclone; (II) frontal fracture; (III) bent-back warm front and frontal T-bone; (IV) warm-core frontal seclusion. **Upper panel:** sea level isobars, fronts and cloud signatures. **Lower panel:** temperature, cold and warm air currents.

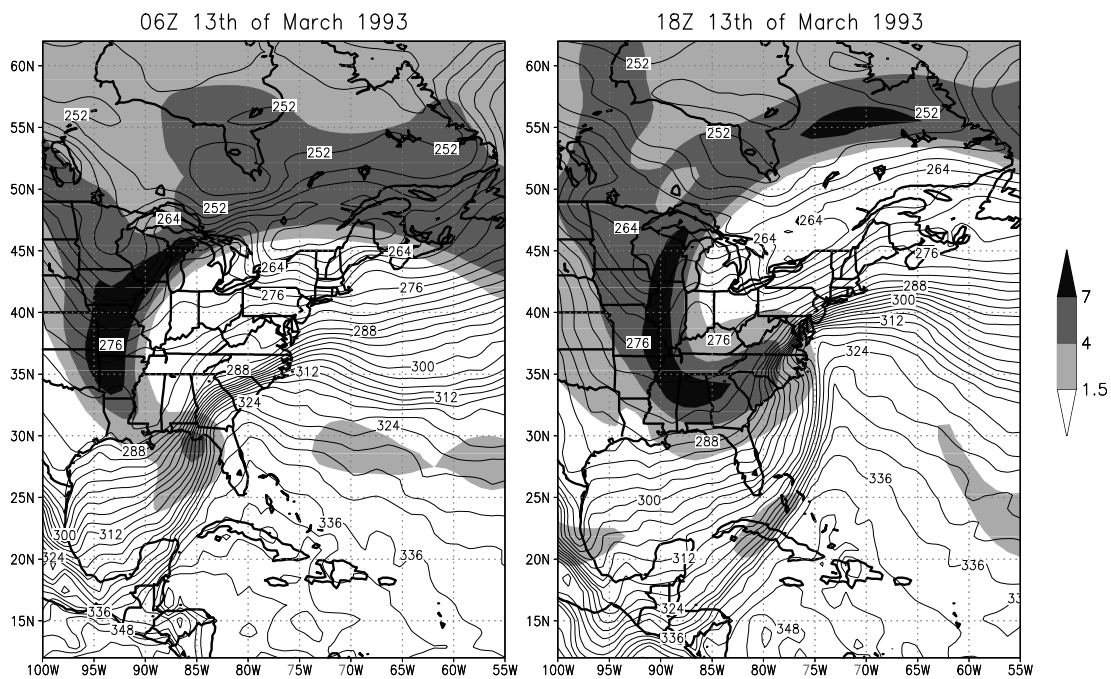


**Figure 3.9:** Equivalent potential temperature [K] (lowest model level) and potential vorticity larger than 1.5 PVU of the adjusted ECHAM4 simulation at model level 9 ( $\sim 300$  hPa) for two time steps during the blizzard case.

with the exchange of air between the troposphere and the stratosphere is well reproduced and is further pronounced by a cross frontal vertical section of the equivalent potential temperature and

the PV (Figure 3.10). A PV of 1.5 PVU<sup>4</sup> represents roughly the boundary between tropospheric and stratospheric air [Dickinson et al. (1997), Hoskins et al. (1985)]. In pre-frontal regions on the other hand, tropospheric air with lower values of PV is lifted caused by widespread condensation in lower levels. The contours of the equivalent potential temperature show the tilt of the cold front. It is nearly vertical in the lowest 2 km suggesting a well-mixed lower troposphere which is expected in the cold continental air above the warm Gulf Stream.

The storm drew much of its energy from the strong thermal contrast. Many stations across the northern U.S.A. experienced a 500 hPa temperature of  $-40^{\circ}\text{C}$  or colder in the morning of the 12th of March. The Gulf coast on the other hand experienced a period of near record warmth (Forbes et al., 1993). Figure 3.11 shows the temperature distribution at 500 hPa in the adjusted model simulation.

The thermal contrast was accompanied by very strong jet stream winds exceeding  $45\text{ m s}^{-1}$  at many stations across the northeastern U.S.A. (Forbes et al., 1993). A jet stream with maximum winds of  $60\text{ m s}^{-1}$  at 300 hPa was associated with the confluent flow over the northeastern U.S.A.. During the development a second jet streak over the southeastern U.S.A. developed and merged with the existing northern one. This feature is again well represented by the model as illustrated by Figure 3.12.

In addition the vertical velocity at 500 hPa is plotted in Figure 3.12. As suggested by Uccellini and Kocin (1987), strong upward motion is located in the region between the two jet streaks. It is the result of the opposite secondary circulations in their entrance and exit regions and is associated with the heavy precipitation.

Huo et al. (1995) investigated the importance of different mechanisms for the development of the East Coast storm with a mesoscale forecast model. They found that the jet-induced circulation described above was important during the cyclone's incipient stage, whereas the final intensity of the storm was mainly determined by the latent heating in the rapid development phase of the system. Once the latent heating became dominant, the jet-induced circulation provided a favorable environment within which warm and moist air was transported into the warm-frontal zone.

The distribution of the vertical circulation is reproduced realistically in the ECHAM4 simulation with upward motion in the cloud head and in frontal regions and downward motion behind the cold front in the "dry intrusion" area ("dry slot") and in the environment of the system (Figure 3.13). As expected from the conceptual model developed by Uccellini and Kocin (1987) the strongest vertical velocity occurs to the north and northeast of the surface low in the region of large-scale uplift of moist Atlantic air.

The strong temperature gradient between the arctic air over land and the warm and moist air over the Gulf of Mexico and the warm Gulf stream led to heavy rainfall in frontal regions over

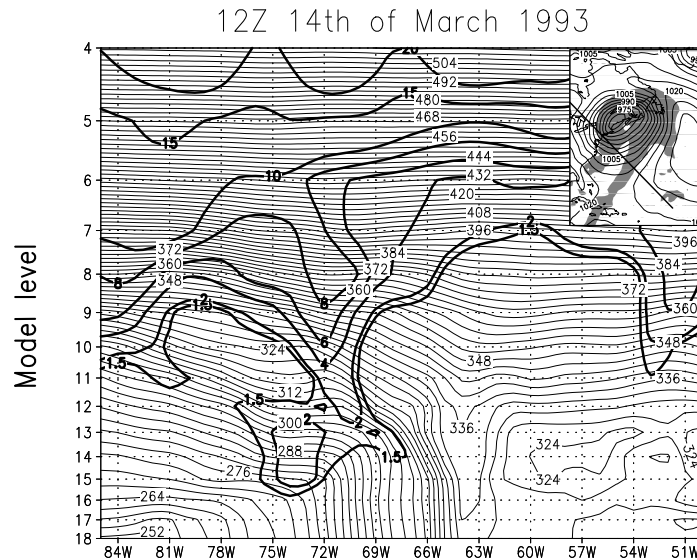


**Figure 3.10:** Cross section of the potential vorticity larger than 1.5 PVU (strong contours) and the equivalent potential temperature [K] (light contours) of the adjusted ECHAM4 simulation at 12Z, 14th of March 1993.

<sup>4</sup>PVU = Potential Vorticity Unit =  $10^{-6}\text{ K m}^2\text{ kg}^{-1}\text{ s}^{-1}$

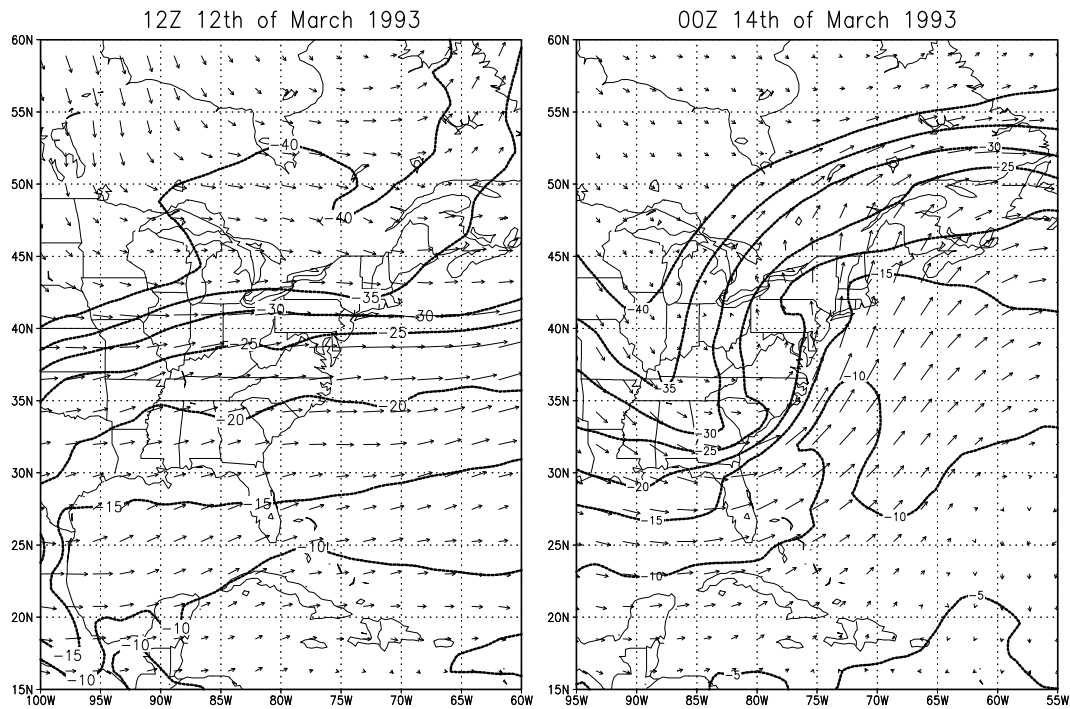


**Figure 3.11:** Temperature [ $^{\circ}\text{C}$ ] and wind vectors at model level 11 ( $\sim 500$  hPa) of the adjusted model simulation for two time steps during the development of the cyclone.

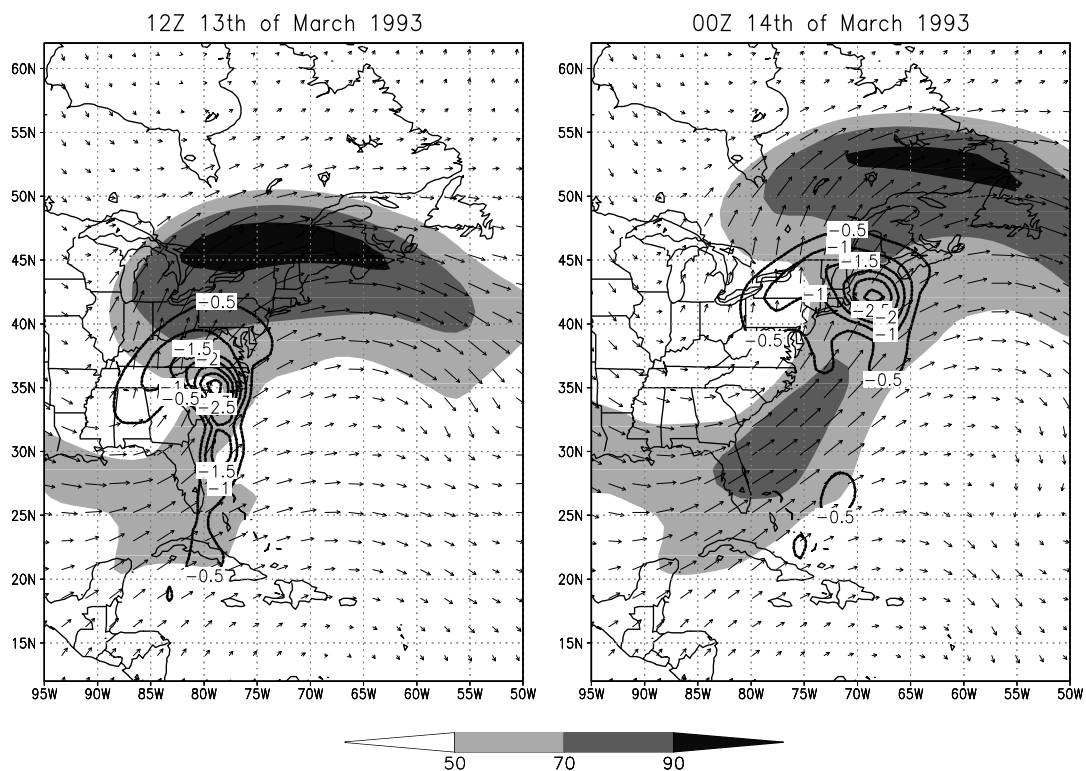


**Figure 3.12:** Wind field at model level 8 ( $\sim 250$  hPa) of the adjusted ECHAM4 simulation. Velocities larger than  $50 \text{ m s}^{-1}$  are shaded. Black contours represent upward motion larger than  $0.5 \text{ Pa s}^{-1}$  at model level 11 ( $\sim 500$  hPa).

the warm sea. Associated with the cyclone was a heavy line of thunderstorms (“squall line”) which crossed Florida and spawned a tornado outbreak. Precipitation rates across the Florida

Panhandle, Mississippi, Alabama and Georgia averaged to  $10\text{--}20\text{ mmh}^{-1}$ . The development of the different precipitation patterns is well represented in the model simulation as illustrated in Figure 3.14.

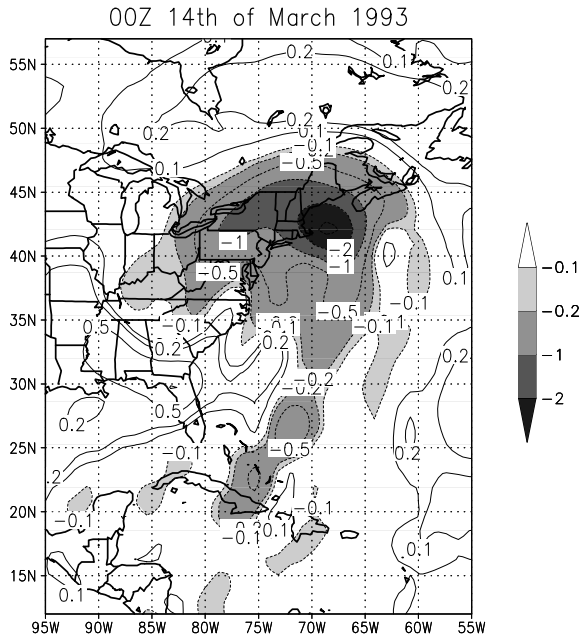


**Figure 3.13:** Vertical wind velocity [ $\text{Pas}^{-1}$ ] at model level 11 ( $\sim 500\text{ hPa}$ ) of the adjusted ECHAM4 T106 simulation in the mature stage of the cyclone.

The areal coverage of snowfall was among the largest of any storm in the recorded history (Kocin et al., 1995). There were significant accumulations of snow extending from northern Louisiana and Alabama in the south into Canada to the north. Most locations within the heavy snow area experienced a period of snow falling at a rate in excess of  $20\text{ mmh}^{-1}$ , with maximum rates of  $70\text{ mmh}^{-1}$ . Strong surface winds created snow drifts of more than  $3\text{ m}$  in places (Forbes et al., 1993). In the model simulation the snowfall is first expanded southward west of the Appalachian mountain range in the cold continental air. The region of strongest snowfall with values between  $20$  and  $50\text{ mmh}^{-1}$  is located to the north and west of the surface low, the region where moist warm air from the Atlantic is lifted above the cold continental air.

During the following days the cyclone moved to the southern tip of Greenland and further to Iceland, where it became stationary for a few days. As a classic “Icelandic low” it steered the following disturbances over the Atlantic before it dissipated slowly after the 19th of March off the western coast of Norway.

### 3.3 Atlantic blocking situation

#### 3.3.1 General features

Blocking anticyclones are large-scale phenomena that have long been of interest because of their profound effect on local and regional climate [e.g. Bengtsson (1991b) or Anderson (1993)]. There are mainly two features that have been related to blocking situations. Those are extratropical cyclones [Tsou and Smith (1990a) and Tsou and Smith (1990b)] that precede blocking events and low-frequency planetary waves (Lejenäs and Madden, 1992). Experiments show that the two precursors occur simultaneously but only the synoptic-scale baroclinic wave train is necessary to trigger Euro-Atlantic blocking (Michelangeli and Vautard, 1998).

Although the migrating cyclones and the blocking anticyclones are of different spatial and temporal scales and have generally different characteristics, they are dynamically linked. By investigating the relative importance of the various forcing mechanisms during the whole life-cycle of an Atlantic blocking situation Lupu and Smith (1994) confirmed results of Tsou and Smith (1990a) that upper-tropospheric anticyclonic vorticity advection is the most important contributor to block formation and maintenance. However, adiabatic warming and vorticity tilting are also important. Those primary contributors are provided by the extratropical cyclone occurring upstream of the developing block. On the other hand a deep layer of upper-tropospheric warm

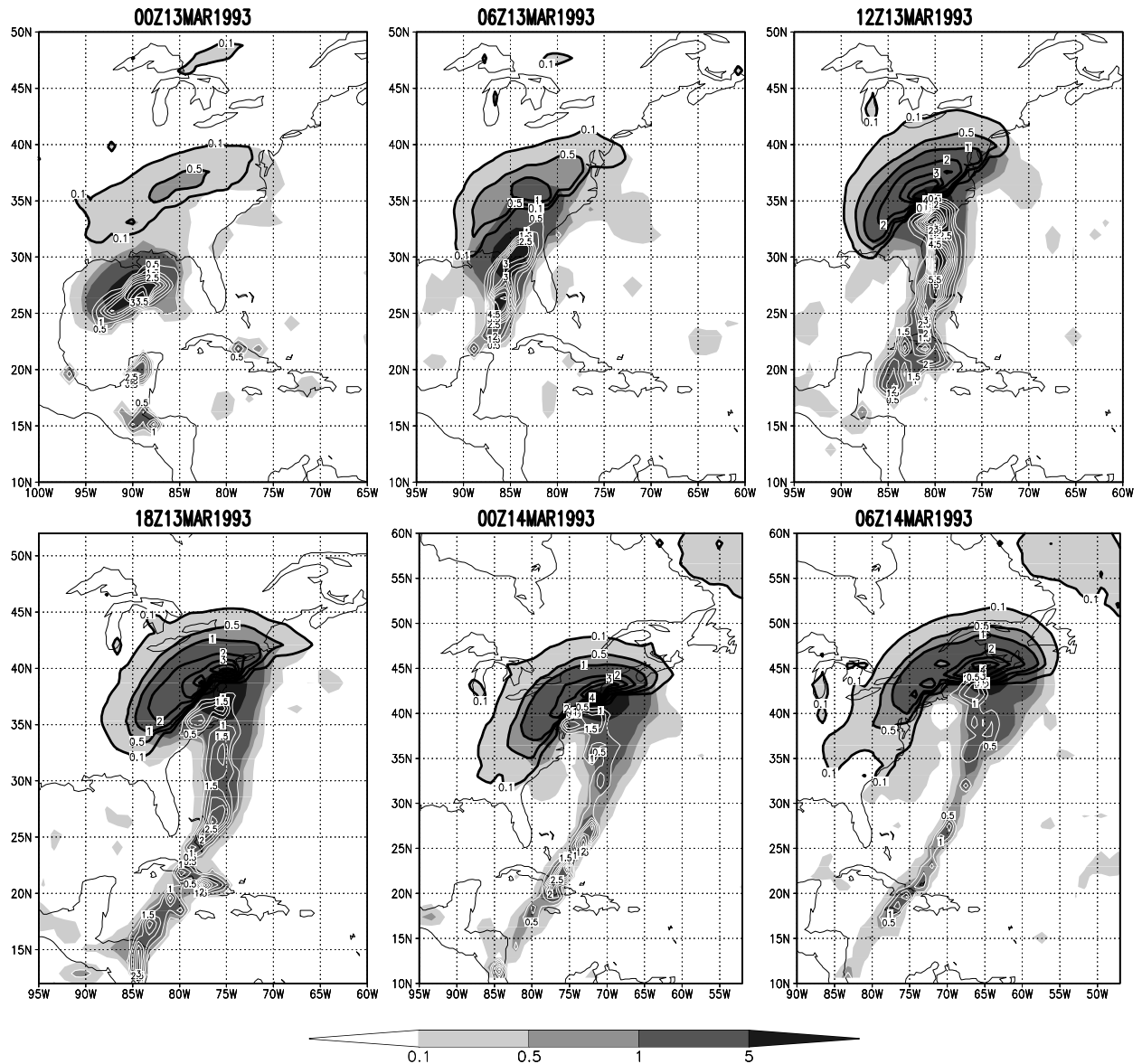


**Figure 3.14:** Development of the different precipitation fields [ $mmh^{-1}$ ] between the 13th and 14th of March 1993 of the adjusted ECHAM4 T106 simulation. Snowfall (color shaded), total precipitation (grey-scale shaded) and convective precipitation (red contours).

air advection associated with an advancing trough contributes to height falls in the dissipating stage of the system.

In addition non-quasigeostrophic processes, like baroclinic or barotropic energy exchanges, are crucial for the development of the blocking high and the preceding cyclone. They systematically strengthen the eddy circulation associated with the developing block and its precursor cyclone (Tsou and Smith, 1990b).

In the following some climatological features of blocking highs derived from situations between July 1985 and June 1988 (Lupo and Smith, 1994) are summarized. In the Northern Hemisphere blocking occurs most often over the Atlantic during the winter season. The average duration of a blocking event is approximately 9 days with more persistent systems occurring in winter than in summer. The Atlantic situations are generally stronger and larger than blocking events over the Pacific. Furthermore more intense blocks are also larger. In winter the majority of the preceding cyclones develop explosively, that is, they experience a pressure drop of  $1 hPa h^{-1}$  or more for at least 24 h. In spring and summer this is the case for only half of them.

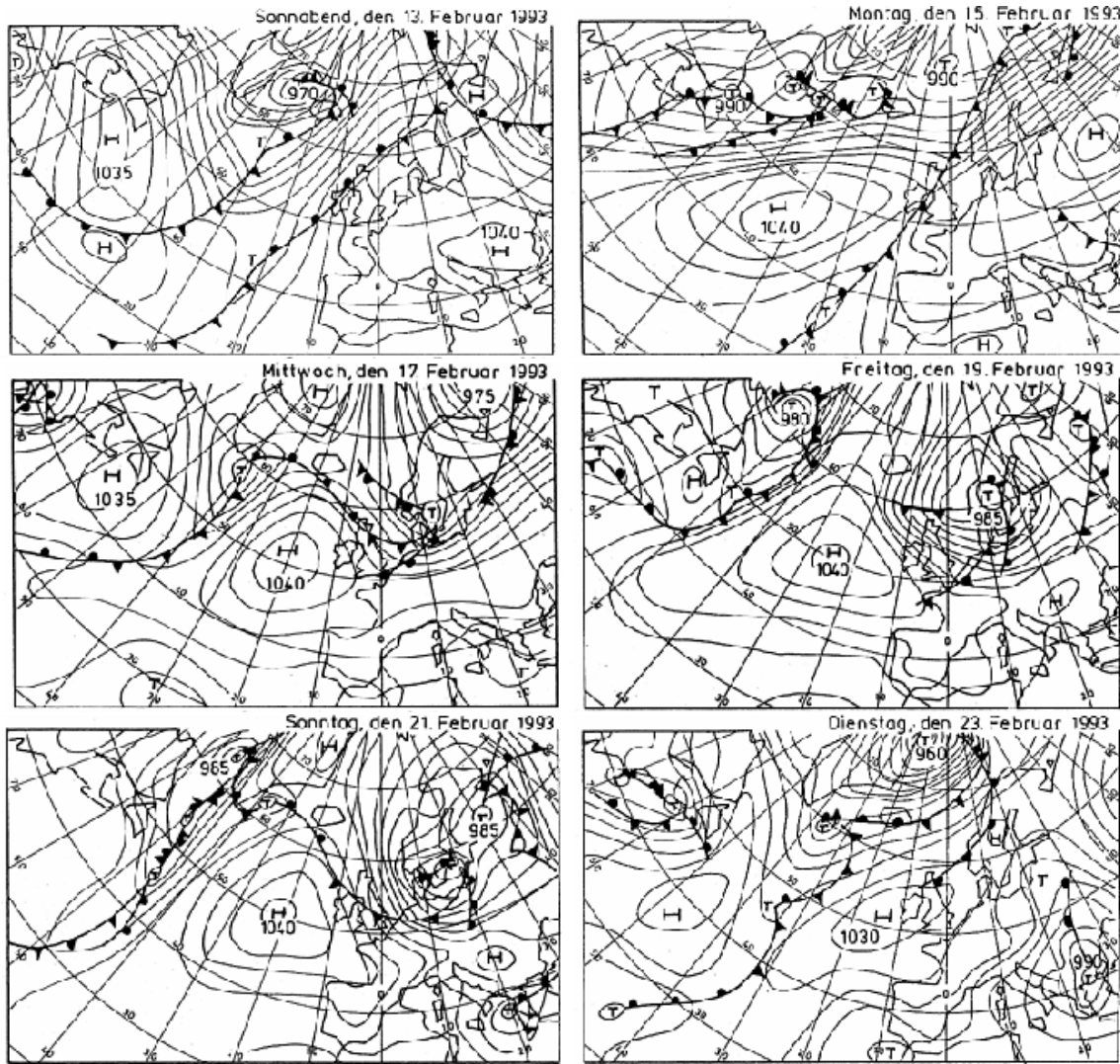


**Figure 3.15:** Maps containing mean sea level pressure [hPa] and frontal structures for the period 13th to 23rd of February 1993 (Source: Weather maps of the German Weather Service (DWD)).

The formulation of an appropriate blocking definition itself is an intriguing problem. No common definition of blocking exists and almost all definitions contain some subjectivity (Lupo and Smith, 1994). An important index to identify blocking situations is the one developed by Lejenäs and Okland (1983):

$$LO = Z_{40^\circ} - Z_{60^\circ} \quad (3.2)$$

$Z$  represents the 500 hPa geopotential height. Main criteria necessary for a blocking anticyclone are:

- The basic midlatitude flow has to be split into two branches from which each has to transport an appreciable amount of mass. This split should lead to a sharp change from a more zonal to a more meridional flow in the region.
- The double-jet system has to exist over at least  $45^\circ$  longitude and for at least 5 days.
- A negative or small positive LO index (Lejenäs and Okland, 1983) has to be present.
- The centre of the anticyclone has to be located north of  $35^\circ\text{N}$ .

Tibaldi et al. (1997) investigated the climatology of blocking in ECHAM3 with simulations of different configurations of horizontal spectral truncation and oceanic surface temperatures. They concluded that all versions of the model show a tendency to underestimate blocking occurrence.

As part of AMIP<sup>5</sup> (Gates, 1992), the behaviour of 15 general circulation models have been anal-

<sup>5</sup>AMIP = Atmospheric Model Intercomparison Project

used in order to diagnose and compare the ability of the different models to simulate midlatitude atmospheric blocking (D'Andrea et al., 1998). The models involved in this comparison represent a wide spectrum of model complexity, with different horizontal and vertical resolutions, numerical techniques and physical parameterizations, and exhibit large differences in blocking behaviour. Nevertheless, a few common features can be found, as the general tendency to underestimate both blocking frequency and average duration. However, it is impossible to relate the weaknesses to precise parts of the model formulation (D'Andrea et al., 1998).

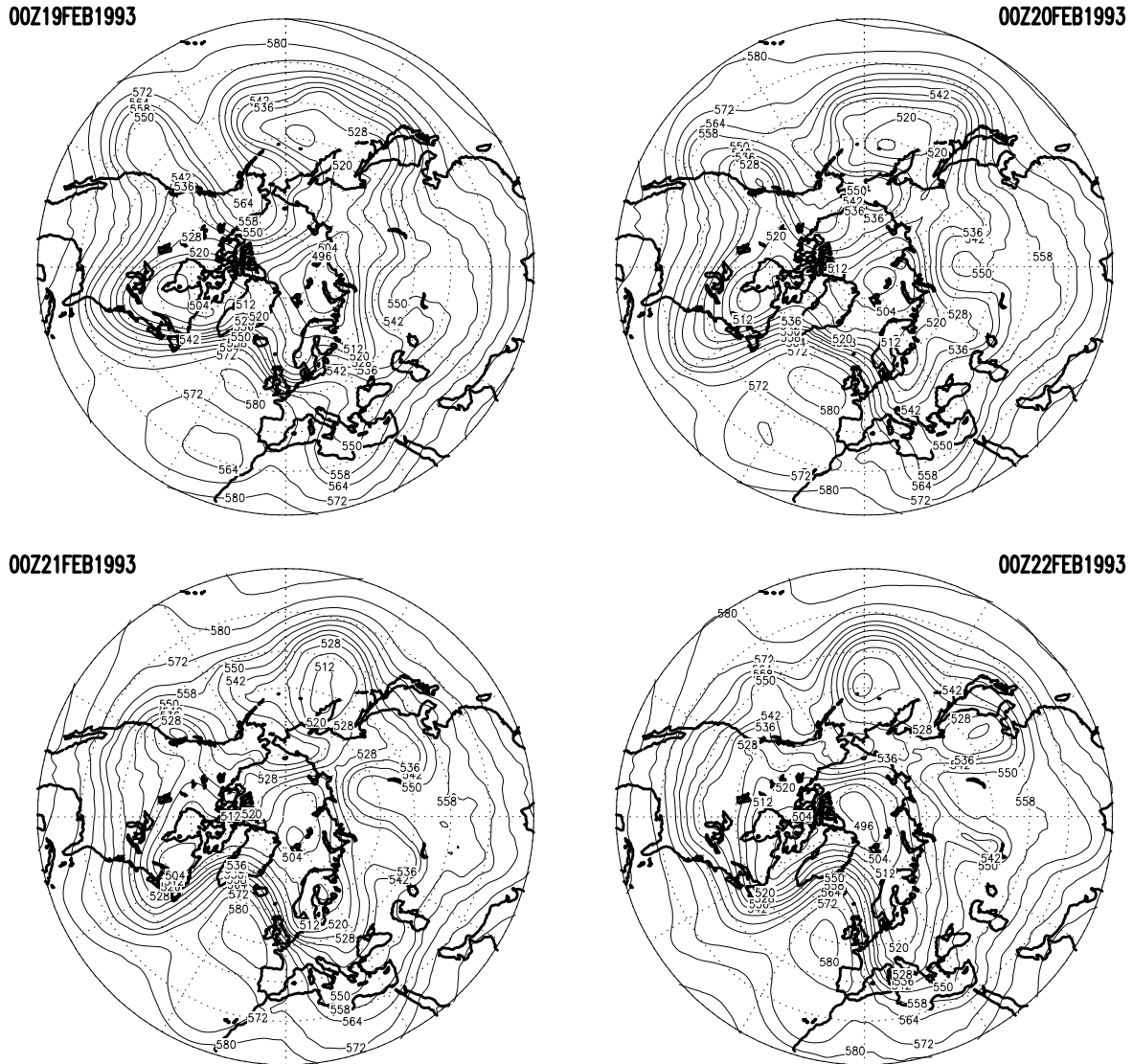


**Figure 3.16:** Temporal development of the 500 hPa geopotential height field [*gpdm*] (geopotential deca metres) between the 19th and 22nd of February 1993 in the adjusted model simulation.

Tschuck (1998) investigated in detail the capability of ECHAM3 and ECHAM4 to simulate blocking situations and the mechanisms necessary for a reasonable simulation of these phenomena. For the Atlantic-European sector he found that ECHAM4 T106 underestimates the blocking frequency in winter. The simulation recovers from this weakness in spring, when the model is able to capture the main peak at 20°E.

### 3.3.2 The case from the 15th to the 23rd of February 1993

From a cloud point of view a blocking situation is very important because a climatological cloud validation by Chen and Roeckner (1997) revealed that the ECHAM4 model is not able to

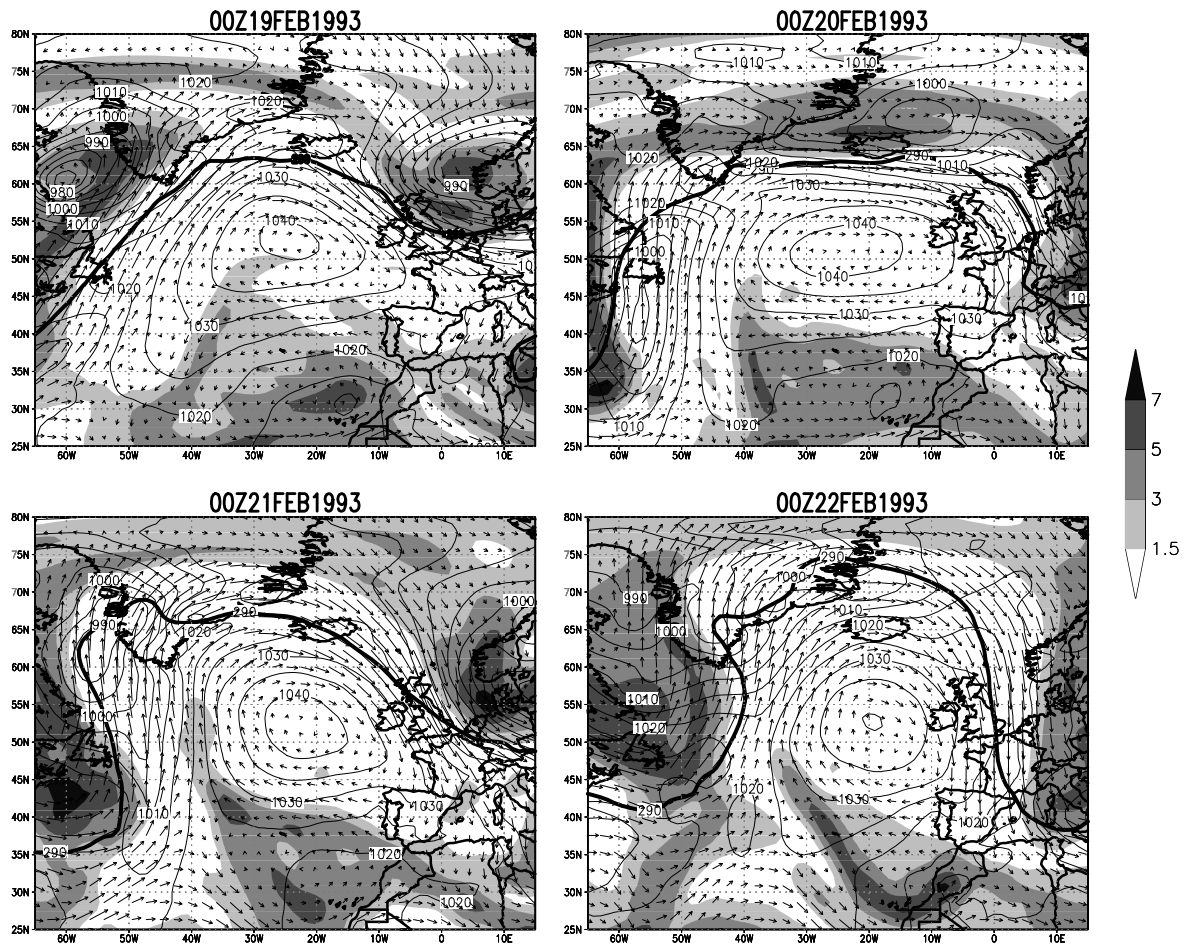


**Figure 3.17:** Mean sea level pressure [hPa], 500 hPa wind field and 300 hPa PV (larger than 1.5 PVU shaded) of the adjusted model simulation. In addition the strong black contour line marks a potential temperature of 290 K at 700 hPa.

reasonably reproduce low-level boundary clouds in regions of large-scale subsidence.

Figure 3.15 shows the weather maps from the German Weather Service (DWD) from 00Z 13th of February to 00Z 23rd of February 1993 for every 48 h illustrating the life-cycle of the system. The anticyclone developed on the 14th of February over the central Atlantic at about  $42^\circ$  N. During the following days it moved to the east with a slight displacement to the north. On the 19th of February, it disrupted the chain of cyclones and shifted its core to a more northerly position of about  $50^\circ$  N. During the following three days the cyclone track was strongly shifted to the north, so that the cyclones reached Europe from a northerly direction.

These features are well represented by the adjusted model simulation. Furthermore, the criteria mentioned in the last subsection are fulfilled. The system leads to a significant split of the large-scale zonal circulation, it lasts longer than 5 days and is centered mainly between  $40$  and  $50^\circ$  N. The split large-scale circulation extends roughly over  $50^\circ$  longitude.

Following the analysis procedure from Tschuck (1998) a sequence of 500 hPa geopotential height plots is shown in Figure 3.16 starting at 00Z, 19th of February 1993 with a 24h time increment. It clearly illustrates the development of the block over the north Atlantic. An interesting detail is the strong southward extension of the trough to the west of the developing block over eastern North America during the first days of the development, a feature associated with a strong precursor cyclone.

At the same time the ridge is extended far to the north indicating a strong northward advection of warm air. The synoptic situation is further illustrated by Figure 3.17, which shows the

potential vorticity at 300 hPa, the circulation in the middle troposphere at 500 hPa and the position of the 290 K potential temperature isoline at 700 hPa.

It is clearly seen that low values of upper-tropospheric PV and wind speed are extended far to the north, indicating warm air advection even in the upper troposphere. The same is true in the lower troposphere where the isoline of the 290 K potential temperature at 700 hPa is extended to 75°N, leading to equal temperatures over Iceland and Spain on the 22nd of February. To the west and east the system is flanked by high PV values associated with cold air advection over Newfoundland and Europe.

# Chapter 4

## Cloud validation

### 4.1 Introductory remarks

Prior to the validation of clouds for different case studies a short summary of a validation in a climatological sense is given. Therefore monthly mean total cloud amounts, cloud liquid water path (CLWP) and precipitable water are compared with observations.

The following validation for the two case studies is restricted to quantities which can be validated against ISCCP satellite or radiosonde data: total cloud cover, relative humidity, visible cloud optical thickness, cloud top pressure, cloud types calculated following the ISCCP cloud classification algorithm and the influence of clouds on the infrared (IR) brightness temperature.

### 4.2 Brief summary of a climatological validation

As observational datasets monthly mean total cloud cover from ISCCP (C2 data set) ([Rossow and Schiffer, 1991](#)) and from a climatology based on surface observations ([Hahn et al., 1994a](#)) are used. The former is provided in  $2.5^\circ \times 2.5^\circ$  resolution while the latter is available in  $5^\circ \times 5^\circ$  resolution. In the following only climatologies for January are shown, while July conditions are partly referred to in the text. [Figure 4.1](#) compares monthly mean total cloud cover of the different datasets.

The general distribution of clouds from ISCCP and from the surface climatology agrees reasonably well, except over the continents on the Northern Hemisphere, where larger cloud amounts are found in the surface climatology. The lower cloud amounts over the continents in the ISCCP observation are explained by the wide occurrence of low-level stratiform clouds with similar cloud top than surface temperatures, impeding the separation between snow-covered surfaces and clouds. Furthermore, frequently occurring low-level inversions lead to higher cloud top than surface temperatures, which also confuses the cloud recognition algorithm [[Rossow and Garder \(1993a\)](#), [Rossow and Garder \(1993b\)](#)].

Although ECHAM4 reproduces the main pattern of the cloud distribution rather well, systematic differences to the observations occur. The differences between ECHAM4 T106 and observations are comparable to the findings of [Chen and Roeckner \(1997\)](#), who validated the representation of clouds in ECHAM4 in the lower horizontal resolution T42. In subtropical subsidence regions, the total cloud cover is underestimated apart from a narrow belt along the eastern coasts of South Africa, South America and Australia. Furthermore, ECHAM4 T106 simulates smaller cloud amounts over midlatitude oceans on both hemispheres. Over the continents on the Northern Hemisphere the total cloud cover is overestimated compared to ISCCP, while the differences

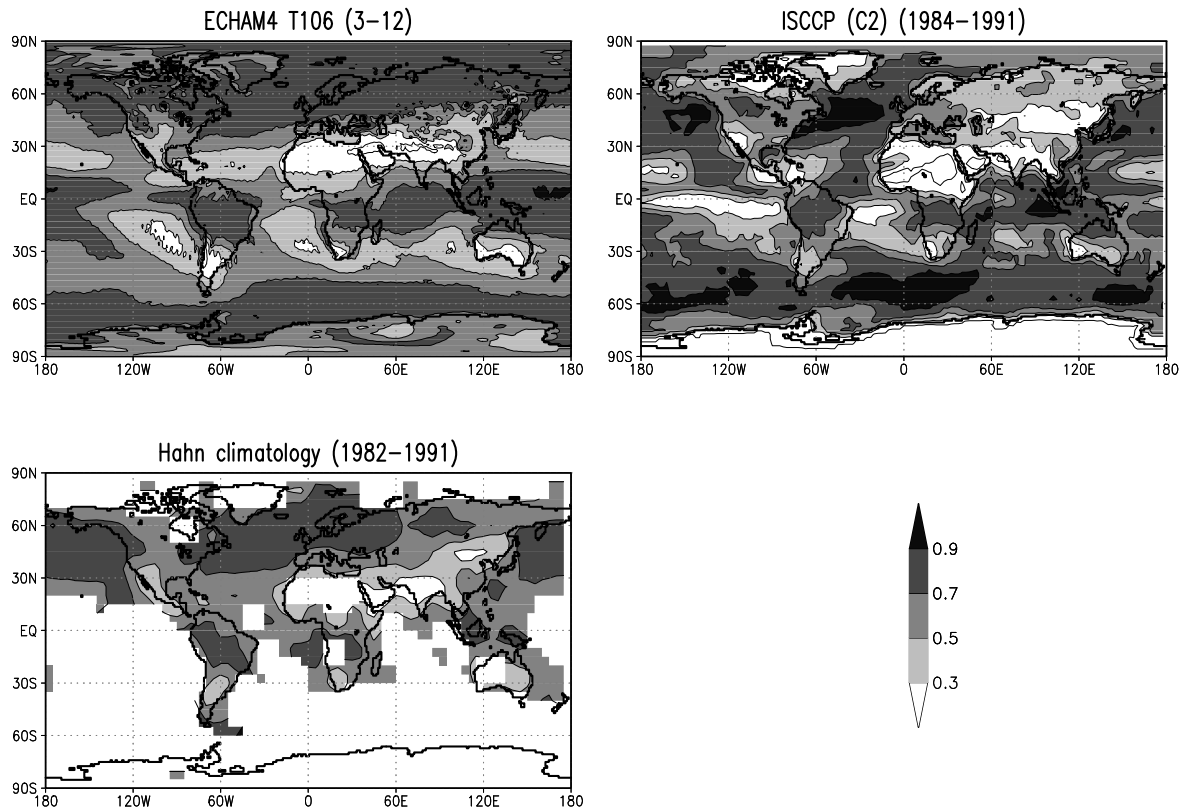


**Figure 4.1:** Monthly mean total cloud cover [fract.] of ECHAM4 T106 (January)(AMIP), ISCCP C2 satellite observations (Rossow and Schiffer, 1991) and a cloud climatology based on surface observations (Hahn et al., 1994a). Contours are drawn for 0.1, 0.3, 0.5, 0.7 and 0.9 (shaded for values larger than 0.3).

are smaller compared to the surface climatology. Moreover, the ITCZ<sup>1</sup> is stronger pronounced in ECHAM4 as compared to ISCCP observations. This might be caused by weaknesses in the parameterization of deep convection. They lead to redistributions between the convective and large-scale parts of precipitation with larger amounts of large-scale precipitation using the modifications of Nordeng (1994) (Roeckner, 1999). This is associated with larger areas covered by anvil clouds and a broader representation of the ITCZ. It might also be the reason for the underestimated convection (OLR<sup>2</sup>) over tropical continents (Dümenil and Bauer, 1998), whereas the differences in total precipitation are small.

ECHAM4 underestimates total cloud amounts over midlatitude ocean regions also in July (not shown). According to Chen and Roeckner (1996b) these underestimations lead to underpredicted shortwave cloud radiative forcing over the regions. The cloud amounts over subtropical subsidence areas are again underestimated although the agreement is better in July than in January. Furthermore, the differences to ISCCP observations over continental regions on the Northern Hemisphere are smaller in July than in January (Chen and Roeckner, 1997).

These results are supported by a comparison of the 10-year monthly mean cloud liquid water path (CLWP) simulated by ECHAM4 T106 with climatologies derived from SSM/I microwave measurements (Figure 4.2). Here the two climatologies calculated by Greenwaldt et al. (1993) and Weng and Grody (1994) are used. It is important to note that the results of the satellite measurements depend strongly on the retrieval algorithm used. Furthermore, many input factors can influence the microwave measurements (as e.g. total precipitable water, SST, cloud surface

<sup>1</sup>ITCZ = Inter Tropical Convergence Zone

<sup>2</sup>OLR = Outgoing Longwave Radiation

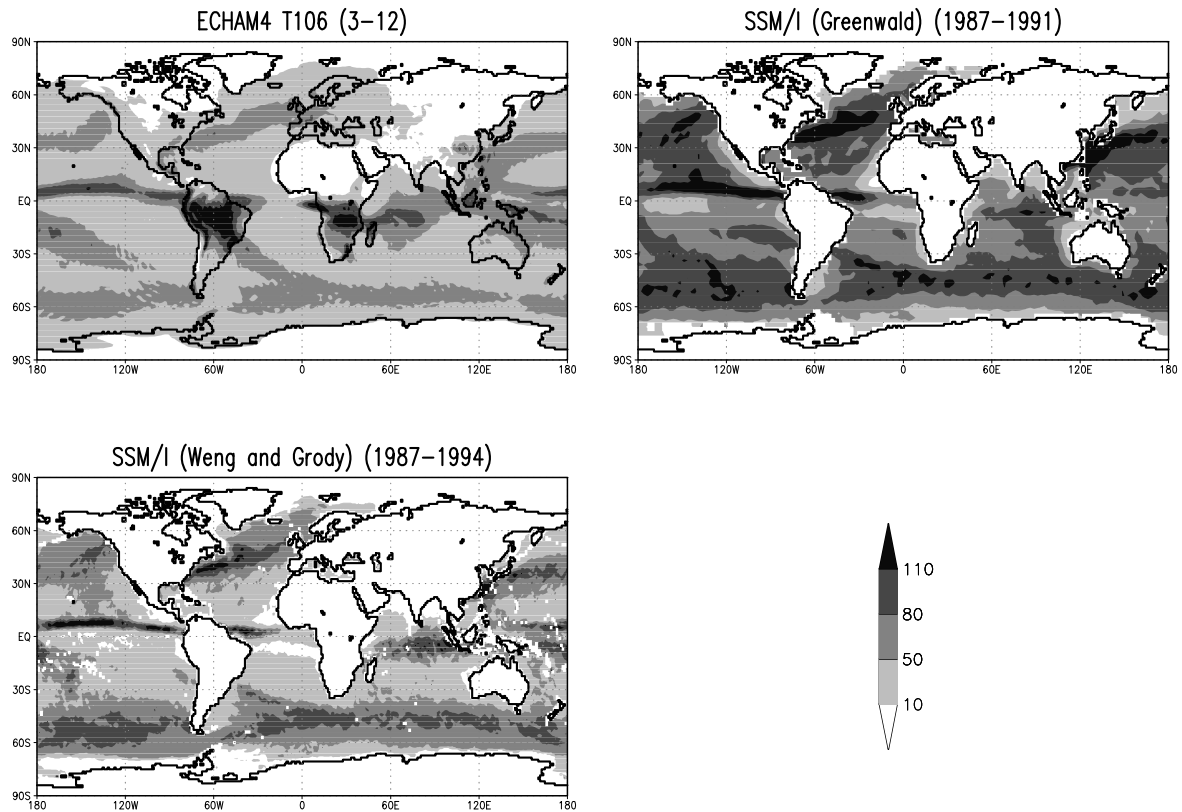


**Figure 4.2:** Monthly mean cloud liquid water path (CLWP) [ $gm^{-2}$ ] of ECHAM4 T106 (January)(AMIP) and climatologies based on SSM/I microwave measurements from [Greenwaldt et al. \(1993\)](#) ( $2.5^\circ$  horizontal resolution) and [Weng and Grody \(1994\)](#) ( $1^\circ$  horizontal resolution).

temperature or surface wind). Therefore two datasets are used to illustrate the range of CLWP observations. Despite the large range this is currently the best way to estimate the near global distribution of CLWP as long as no ground truth is available.

ECHAM4 separates cloud water diagnostically into liquid and ice using an empirical relationship based on cloud temperature as described in section 2.1.2 (equations (2.21) and (2.24)). To make the comparison as fair as possible, only the liquid part is compared to SSM/I observations. However, because of the crude empirical method of calculating CLWP from the model results, the different horizontal resolutions of the SSM/I observations and the differences occurring between the two observations, only main patterns can be compared.

In January, the observed local maxima of CLWP associated with the ITCZ and midlatitude storm tracks are captured by the model, although the occurring amounts of CLWP appear to be underestimated. A systematic underestimation of CLWP in the model simulation occurs over subtropical eastern ocean basins associated with an underestimation of marine stratocumulus clouds. In July, the observed local maxima of CLWP are again represented by the model (not shown). However, the negative biases over subtropical eastern oceans are even stronger compared to January conditions ([Chen and Roeckner, 1997](#)).

Figure 4.3 compares the vertically integrated specific humidity (total precipitable water) of ECHAM4 T106 with climatologies derived from SSM/I measurements [[Greenwaldt et al. \(1993\)](#), [Liu and Curry \(1993\)](#)]. As for the CLWP only main patterns can be compared due to the strong dependence on the used retrieval algorithm and the different horizontal resolutions.

The main patterns are reasonably represented in ECHAM4 compared to the observations. Main differences are an underestimated precipitable water in the model simulation along the ITCZ,

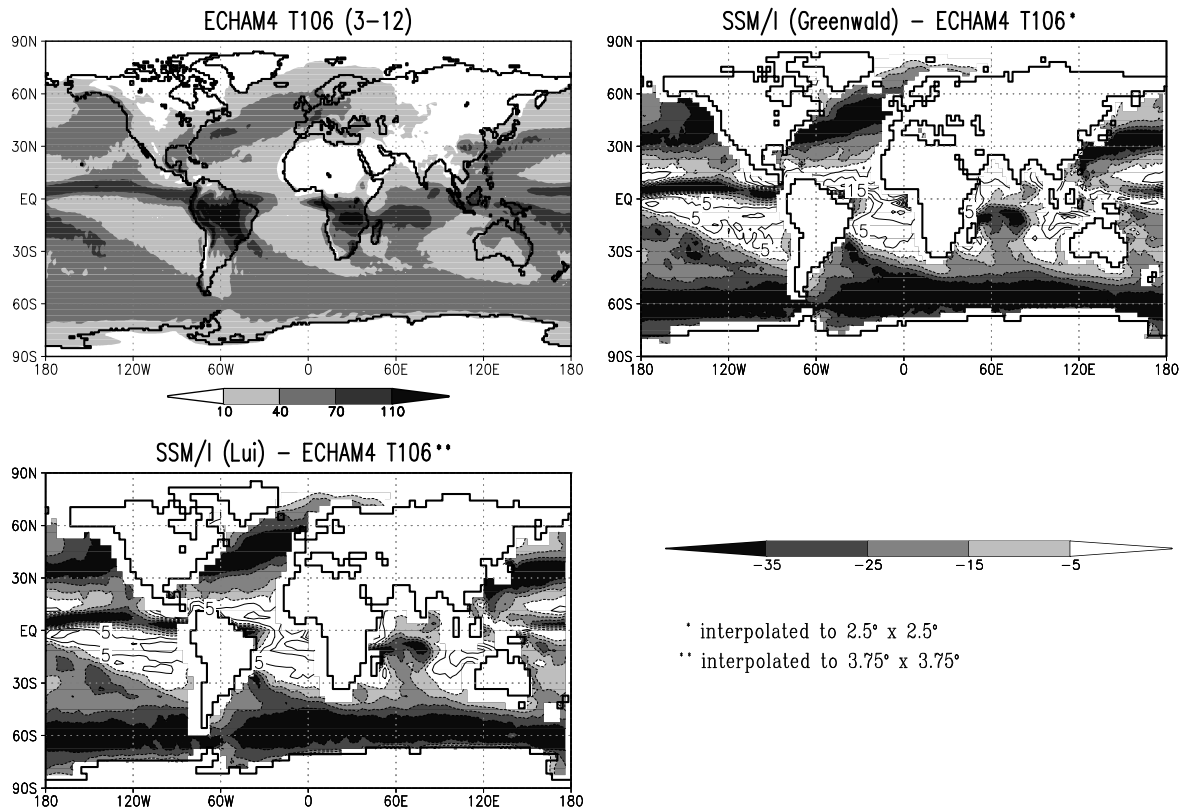


**Figure 4.3:** Monthly mean vertically integrated specific humidity (precipitable water) [ $kgm^{-2}$ ] of ECHAM4 T106 (January)(AMIP) and climatologies based on SSM/I microwave measurements from [Greenwaldt et al. \(1993\)](#) and [Liu and Curry \(1993\)](#).

particularly over the Atlantic and in the Indonesian region and in subtropical subsidence regions on the Southern Hemisphere. On the other hand, larger values occur in the regions of the storm tracks, along the Pacific ITCZ and in subtropical subsidence regions on the Northern Hemisphere. The latter suggests a too weak or too slow condensation in ECHAM4, because cloud cover and CLWP are underestimated despite larger amounts of precipitable water. The underestimated precipitable water in the tropics on the other hand indicates a stronger removal of moisture from the troposphere in the model simulation. Possible causes are stronger precipitation or moisture transport by convection, stronger evaporation, stronger turbulent mixing or dynamical problems as for example too strong subsidence ([Chen and Roeckner, 1996a](#)).

## 4.3 Case study validation

### 4.3.1 Cloud cover

The only information ISCCP DX provides is whether a pixel is cloudy or clear. During the interpolation to the coarser T106 grid this is transferred to a cloud cover which is comparable with the value ECHAM4 or ECMWF calculates. But no information about the 3D-distribution of clouds is available. The latter is provided by the lower resolution ( $2.5^{\circ} \times 2.5^{\circ}$ ) ISCCP D1 dataset which combines information from ISCCP DX and temperature and humidity data from TOVS. This enables the retrieval of cloud amounts in 7 atmospheric layers. But the coarse horizontal as well as vertical resolution does not allow to use the data for an investigation of the representation of clouds along fronts. Moreover it is important to note that the reliability of the

ISCCP data is different depending on the channels available for the cloud recognition, with a better dataset quality during daytimes where additional information from the visible channel is available. Therefore only time steps are compared for which all three threshold values (infrared, near-infrared and visible) are available. Furthermore, the quality of the observation depends on the satellite geometry with larger cloud amounts observed in cases of larger satellite zenith angles (Rossow and Garder, 1993b).

To stress that the ECMWF reanalysis is not applicable for the validation of clouds, Figure 4.4 compares the total cloud cover simulated by ECHAM4 T106 with the distributions simulated by the ECMWF reanalysis and observed by ISCCP.

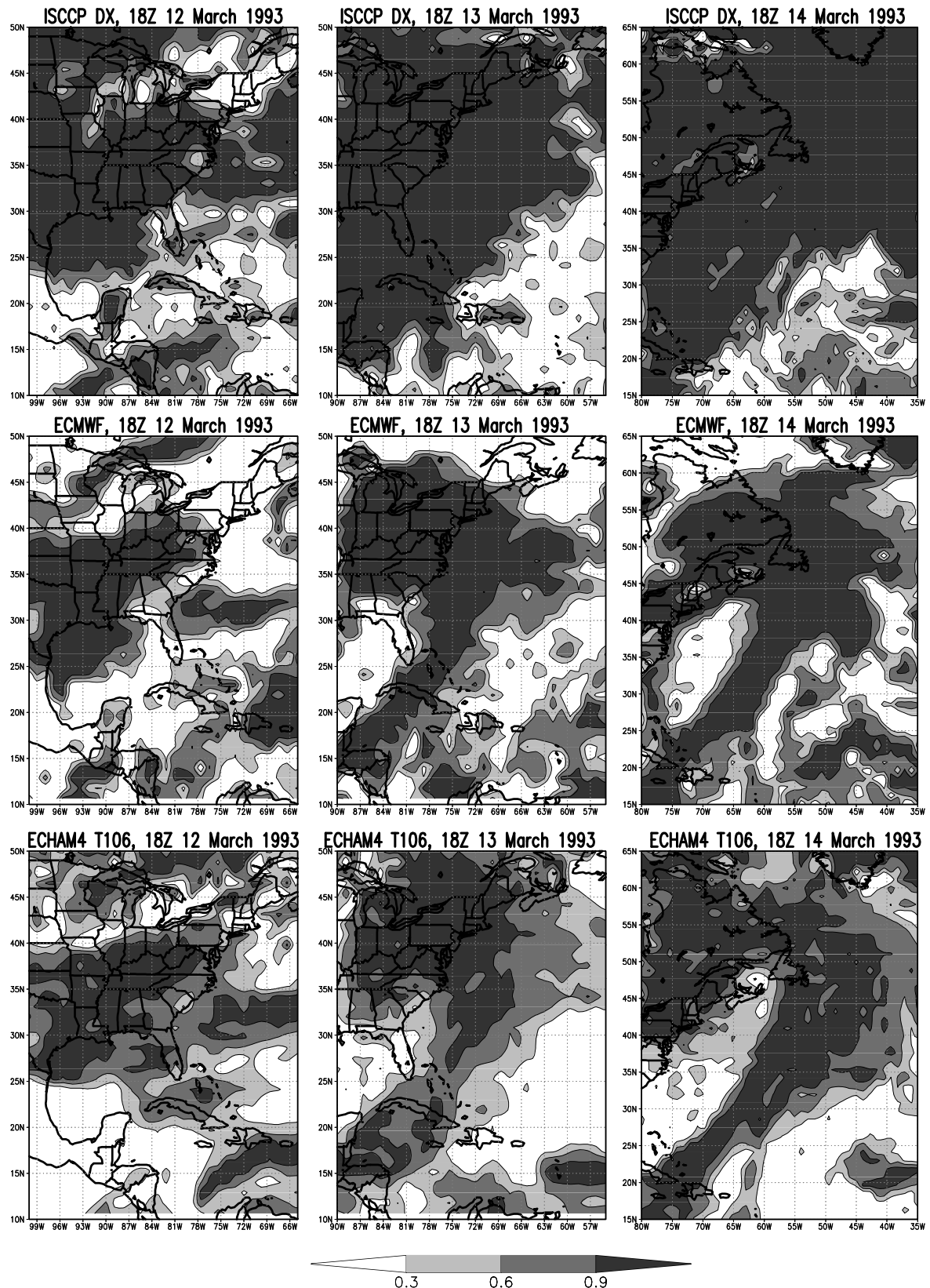
At first glance the cloud cover observed by ISCCP appears to be too large. The typical structure of an extratropical cyclone, as it is seen in a satellite image, is not visible. Even behind the cold front, where at least broken cloud cover is expected due to the subsiding dry stratospheric air in the dry slot, overcast sky is observed. However, one has to note that the satellite only reports cloudy or clear, independent of cloud height. In contrast to an IR satellite image, where low-level clouds are nearly invisible, they appear in the same way as high-level clouds here. Nevertheless, in northern regions of the cyclone the satellite observes the system with a large satellite zenith angle, which might lead to overestimated cloud amounts [Rossow and Garder (1993a), Rossow and Garder (1993b)]. Another possible reason for an overestimation might be the interpolation of the satellite data to the coarser horizontal resolution T106. However, a comparison of cloud cover in T106 and  $0.5^\circ$  resolution (not shown) reveal no systematic differences for the developing system.

The cloud schemes used in the ECMWF reanalysis and ECHAM4 use different approaches to calculate the partial cloud cover. While it is calculated diagnostically from the relative humidity in ECHAM4 following equations (2.18) to (2.20), a prognostic approach is used in the ECMWF reanalysis (Tiedtke, 1993). In the latter the transport of cloud area, the formation of cloud area by convection, stratiform condensation and turbulence and the evaporation of cloud area are taken into account in the prognostic equation.

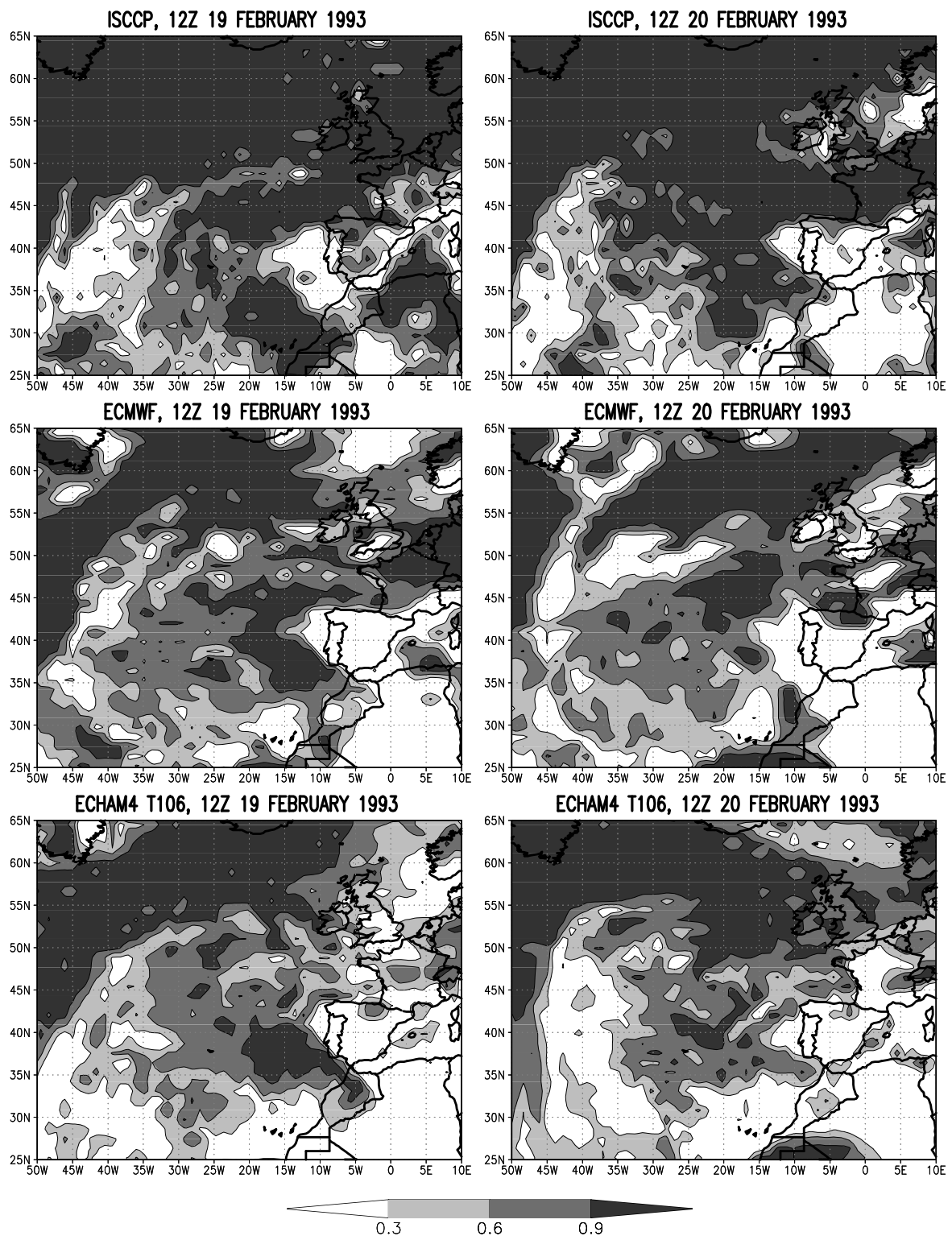
Figure 4.4 illustrates that both model simulations clearly underestimate total cloud cover. This is true for large regions in the environment of the developing system. Most striking differences occur behind the cold front where the satellite detects overcast sky while total cloud cover is less than 30% in both model simulations. Only at the 14th of March off the East Coast of the U.S.A., ECHAM4 is able to simulate at least partly the expected cloud amounts. Here the underestimation is even stronger in the ECMWF reanalysis.

Figure 4.5 compares the total cloud cover for the blocking situation. Again the two models behave similarly in underestimating total cloud cover. The result, that ECHAM4 and the reanalysis simulate similar cloud distributions, which are clearly different to the observation, confirms that the ECMWF reanalysis should not be used for the validation of clouds. This is consistent with results from van Meijgaard et al. (1999). They compared the 3D-representation of clouds by the stratiform cloud schemes of ECHAM4 and ECMWF with an observation based on surface radiation measurements for three different synoptic situations over the Netherlands. They concluded that the schemes are more in accordance with each other than with observations although the approaches used in the two schemes are completely different. This similarity suggests that other parameterizations in the model are also very important for the representation of clouds (van Meijgaard et al., 1999).

The general underestimation of total cloud amounts might partly be caused by the overlap assumption which is used to calculate total cloud cover from partial cloud amounts at the model levels. Petch and Edwards (1999) investigated the effect of different overlap assumptions in 2D and 3D model simulations using a large-eddy simulation as a surrogate for an observation. They concluded from their test case, that the maximum-random overlap, which is used in ECHAM4,



**Figure 4.4:** Comparison of total cloud cover [fract.] for three time steps during the blizzard case. They represent the developing (left column), mature (middle column) and dissipating stage (right column) of the development. The upper row shows the ISCCP DX satellite observation, the middle row the ECMWF reanalysis and the lower row the adjusted ECHAM4 T106 simulation.



**Figure 4.5:** Same as Figure 4.4 but for two time steps during the blocking situation.

leads to most realistic results. This indicates, that the overlap assumption is not the cause for the underestimation of total cloud cover. However, it is important to note, that they investigate only one case in the western Pacific. The situation might be different in midlatitudes.

Typical cloud types occurring behind a cold front are cumulus clouds of different height and size. Low-level cumulus clouds are represented by the shallow convection scheme. It is fed by turbulence present in the sub-cloud layer in cases where the large-scale moisture convergence

in the atmospheric column is small compared to the evaporation. If this is not the case, the deep convection scheme is switched on. For the activation of the midlevel convection three requirements have to be fulfilled. Firstly, large-scale ascent has to be present at lower levels. Secondly, the environment has to be sufficiently moist and thirdly, a convectively unstable layer is necessary above.

Figure 4.6 shows the distribution of the different types of convection for two time steps representing the mature and dissipating stage of the development in the blizzard case.

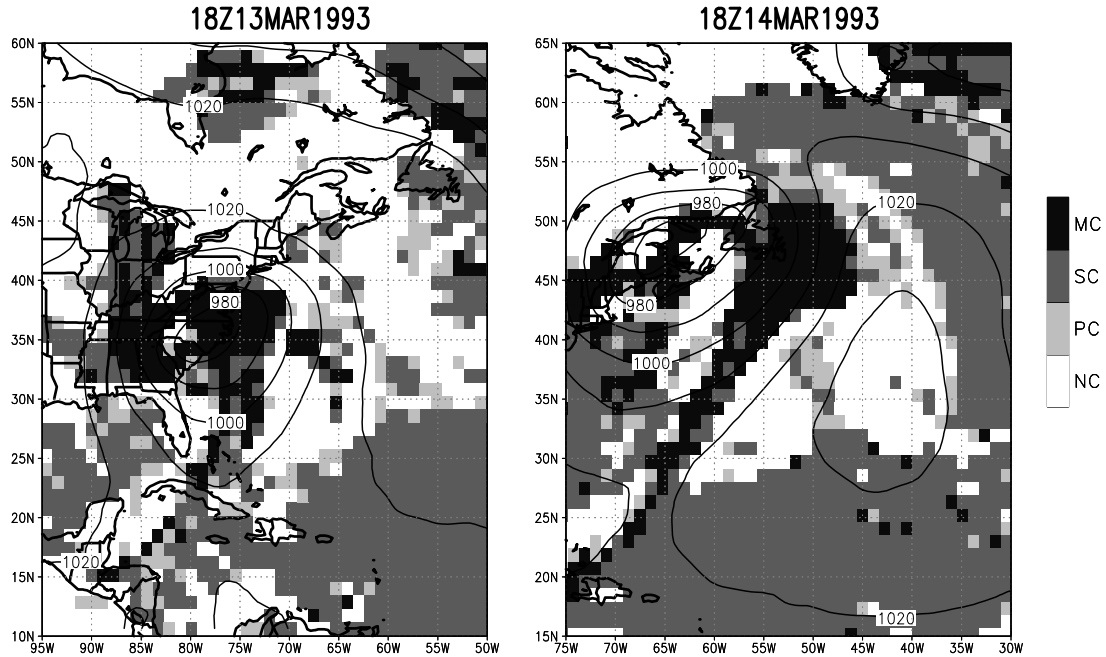


**Figure 4.6:** Horizontal distribution of the different types of convection for the mature and dissipating stage of the developing cyclone. [NC = no convection, PC = penetrative convection, SC = shallow convection, MC = midlevel convection]

In regions of strongest convection, midlevel instead of penetrative convection dominates. Behind the cold front, mainly shallow convection occurs with some scattered grid boxes containing penetrative convection. In later stages some grid points in which midlevel convection occur, are present. However, the upward convective mass flux behind the cold front is confined to the lower troposphere, as shown in Figure 4.7.

An important restriction in the mass flux scheme is, that only one kind of convection can exist in the grid box during one time step. When the shallow convection scheme is switched on, the midlevel scheme cannot be switched on to enhance convective mass fluxes. Another problem could be, that the subsidence behind the cold front is too strong in the model simulation, suppressing the penetration of convective mass flux into higher levels of the troposphere and the exchange of moisture by large-scale vertical advection.

Further insight into the 3D representation of clouds is given by vertical cross sections along and perpendicular to the cold front (Figure 4.8). The left section crosses the cold front and the bent-back warm front. It shows the well represented "dry intrusion" behind the cold front in which dry stratospheric air is mixed downward into the troposphere (see also Figure 3.10). Furthermore the cirrus anvil to the east of the cold front is visible.

Observational studies of cyclones suggest that cirrus clouds appear some 500 to 800 km in advance of the surface front (Kurz, 1990). In the model the anvil covers an area up to 1500 km in advance of the front suggesting an overestimation of upper-tropospheric cloudiness. However, it is important to note that only cloud cover is plotted here. No information about the optical

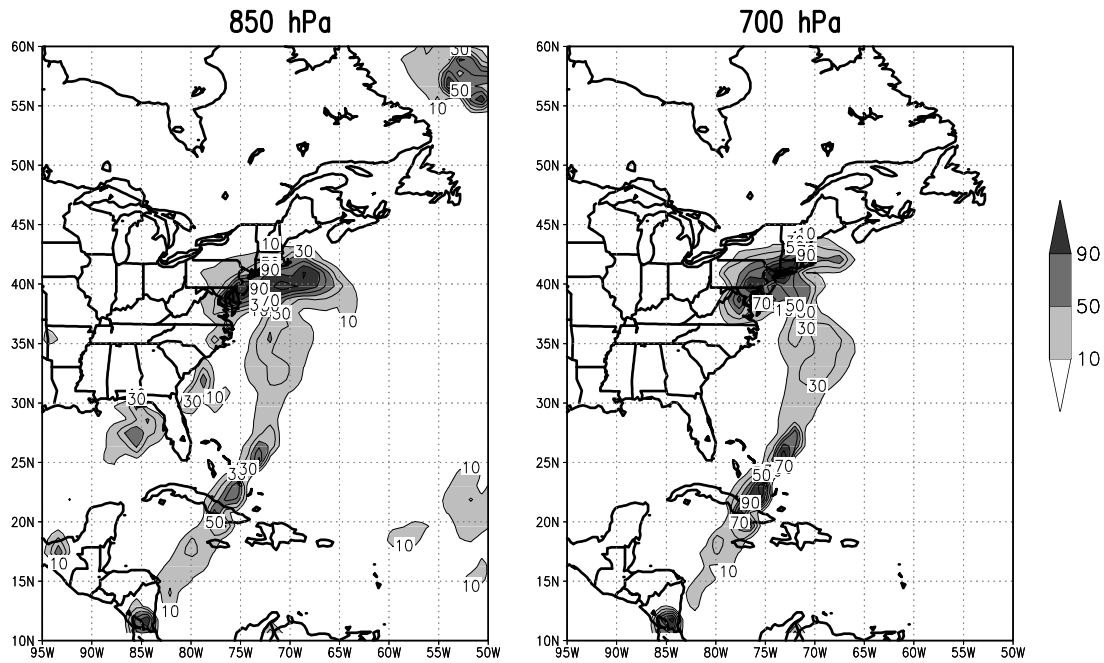


**Figure 4.7:** Upward convective mass flux [ $gm^{-2}s^{-1}$ ] at two atmospheric levels at 00Z 14th of March 1993 of the adjusted ECHAM4 simulation.

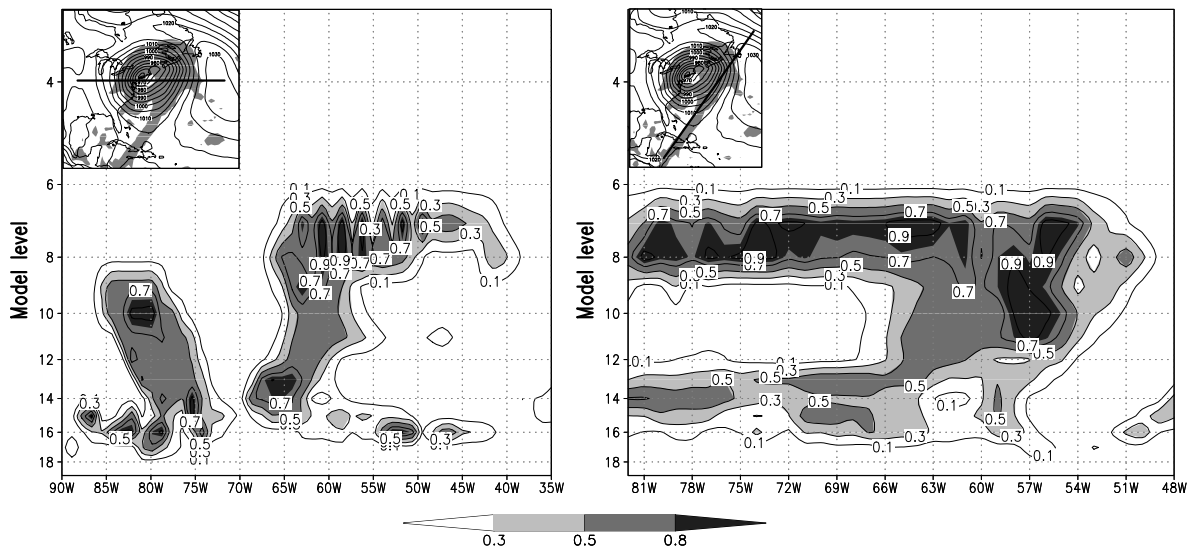


**Figure 4.8:** Vertical cloud cover section [fract.] for the adjusted model simulation at 40N (left) and along the cold front (right) for 06Z, 14th of March 1993. The small figures show the course of the section in relation to the system.

thickness is given. This overestimation is likely caused by a too weak removal of ice crystals from the cirrus level. The sedimentation of ice crystals is parameterized in terms of the ice water content with higher sedimentation rates occurring at higher amounts of cloud ice, causing an accumulation of thin cirrus clouds.

On the other hand, as mentioned above, the total cloud cover simulated by ECHAM4 in pre-frontal regions of the cold front, is in accordance with ISCCP observations. An explanation could be that the clouds, which are recognized by ISCCP, leading to an extended cloudy region in advance of the cold front, are low or mid-level clouds which are underestimated in the model simulation. This point will be clarified by a comparison of cloud top pressures in subsection

## 4.2.3.

Moreover, from real cyclones, it is expected that in the “core regions” of the fronts large cloud amounts occur continuously from the lower to the upper troposphere [e.g. [Browning \(1985\)](#) or [Houze \(1993\)](#)]. This is not the case in the model simulation. Generally, largest cloud amounts are simulated in the upper troposphere by the model. It is expected, that a more sophisticated diagnostic calculation of cloud cover, using additional predictors together with the relative humidity and stability or even a prognostic calculation, will lead to higher cloud amounts in frontal regions.

The right plot in [Figure 4.8](#) shows a section along the cold front. It reveals a cloud-free middle troposphere, in particular in southern parts of the cold front, suggesting that the model cannot reproduce the vertical cloud distribution along the narrow front. Likely reasons are an underestimated advection of moisture (vertical as well as horizontal), a too weak evaporation of precipitation or a too weak detrainment of convective cloud water and water vapour in the middle troposphere. Furthermore, a higher horizontal resolution would improve the representation of clouds by enhancing the convective activity.

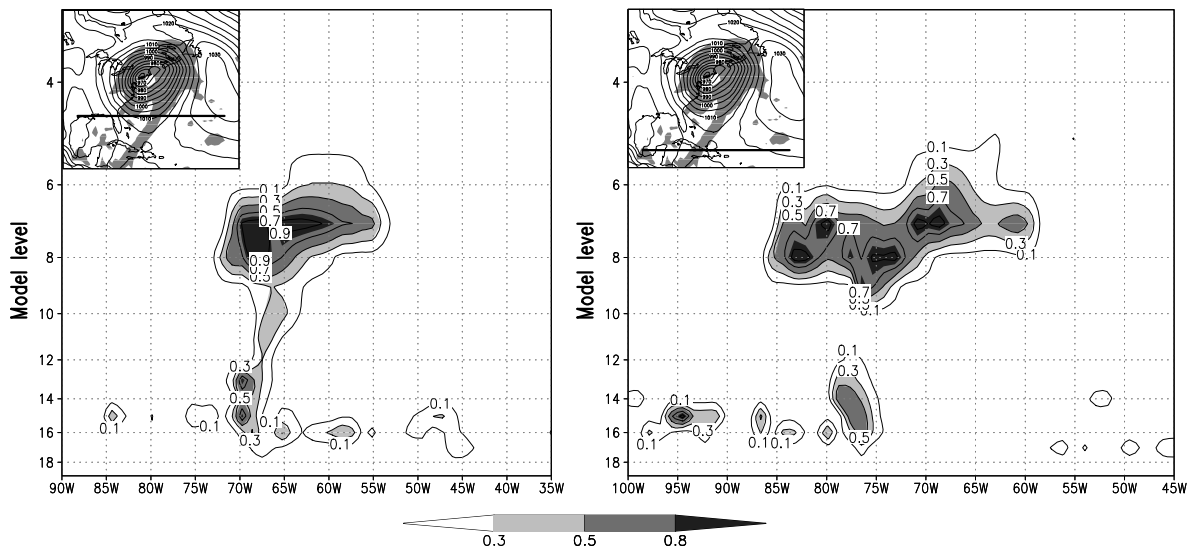


**Figure 4.9:** Same as [Figure 4.8](#) for two zonal sections through the cold front at 30°N (left) and 20°N (right) in the adjusted model simulation.

The problem of underestimating cloud fraction in the middle troposphere is stressed in [Figure 4.9](#), which shows zonal cross sections through the cold front at two different latitudes. It is realistic that the cloud amounts are lower in middle levels than in the upper and lower troposphere. Furthermore, it is realistic that highest cloud amounts occur in the upper troposphere, although the right panel suggests an overestimation of upper tropospheric cloudiness. Nevertheless, the values in the middle troposphere appear to be underestimated in the model simulation compared to observations from typical cold fronts [e.g. [Browning \(1985\)](#) or [Houze \(1993\)](#)]. This is especially true in the southern part of the cold front where no mid-level cloud cover is simulated at all. The zonal sections further illustrate that low-level clouds behind the cold front are represented by the model simulation. But they are confined to the boundary layer and are not partly extended into higher levels of the troposphere as expected from the weather occurring behind cold fronts of typical cyclones [e.g. [Browning \(1985\)](#) or [Houze \(1993\)](#)].

[Figure 4.10](#) shows a zonal and a meridional cross section for the blocking case. Here the frontal system to the west of the blocking high is much better represented than the southern part of the cold front in the blizzard case with large cloud amounts occurring from the lower to the upper troposphere. This is also true for a section located 10° further south (not shown), indicating

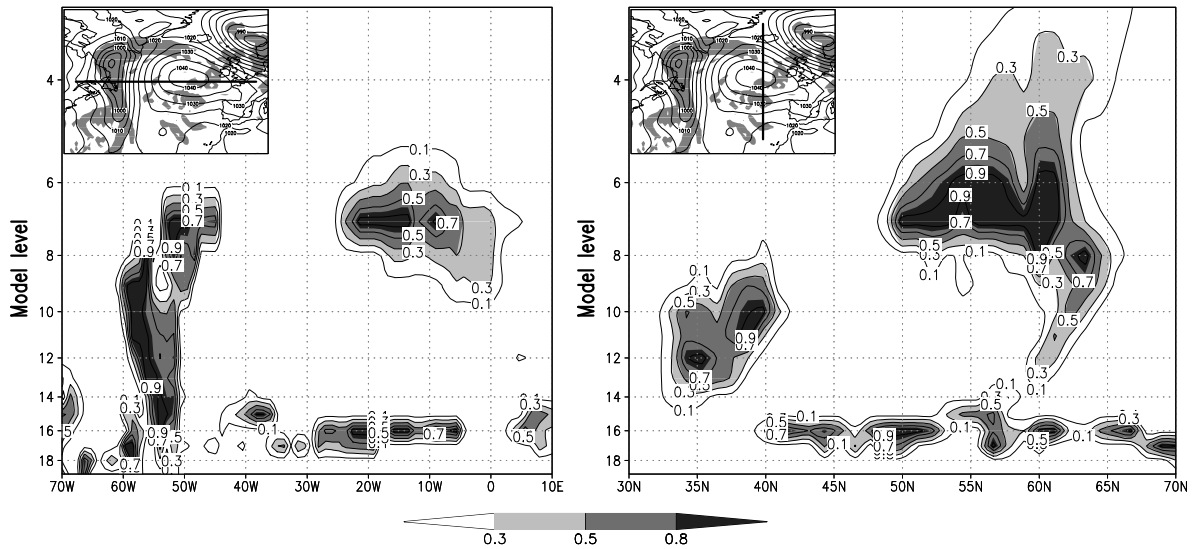


**Figure 4.10:** Same as Figure 4.8 but for the blocking case for the adjusted model simulation.

that frontal boundaries are better represented in later stages of the cyclone development. Again the low-level cloud cover is reproduced by the model and again it is confined to the boundary layer. The sharp cloud top indicates the presence of an inversion as it often occurs in blocking highs caused by large-scale subsidence. Both sections in Figure 4.10, in particular the meridional section to the east of Greenland, show the tendency of the model to simulate persistent cloud cover in the upper troposphere and suggest that the sedimentation of ice crystals, which is the main sink of upper level clouds, is too weak or too slow in the stratiform cloud scheme of ECHAM4.

The layer cloud fraction depends on a threshold value, the so-called “critical relative humidity” (equation (2.20)). Changing its profile would change the condensation characteristics of the model. In the next chapter a sensitivity experiment with a changed profile of the critical relative humidity will be described. It will be changed in a way which should lead to larger cloud amounts in the lower and middle troposphere and smaller cloud cover in the upper troposphere.

Smaller cloud amounts in lower and middle levels and larger cloud amounts in the upper troposphere are also supported by Lohmann et al. (1995), who performed a cloud study during the CEPEX<sup>3</sup> experiment in the Pacific warm pool region.

### 4.3.2 Relative humidity

Since the partial cloud cover in ECHAM4 is a non-linear function of the relative humidity and the stability of the atmosphere, a comparison of the 3D structure of the relative humidity with observations might reveal the reason for the shortcomings in cloud cover.

The ISCCP satellite dataset does not provide any information about relative humidity. Therefore the model results could be compared with the ECMWF reanalysis. On the other hand, the use of the reanalysis should be avoided because of the spin-up problem, which largely influences the representation of moisture and therefore the distribution of clouds (Figure 2.1 and 2.2). Another source of observations are radiosonde measurements. They are available for the U.S.A. to validate the blizzard case, but hardly available over the Atlantic ocean. The quality of the reanalysis is checked by comparing single radiosonde ascents with corresponding grid point

<sup>3</sup>CEPEX = Central Equatorial Pacific EXperiment

profiles of the reanalysis and the adjusted ECHAM4 simulation (Figure 4.11). The datasets are strictly speaking not comparable because the simulated relative humidity represents a mean value of a grid box of 100 by 100 km, while radiosonde measurements are "point" measurements (the drift with the horizontal circulation is usually neglected).

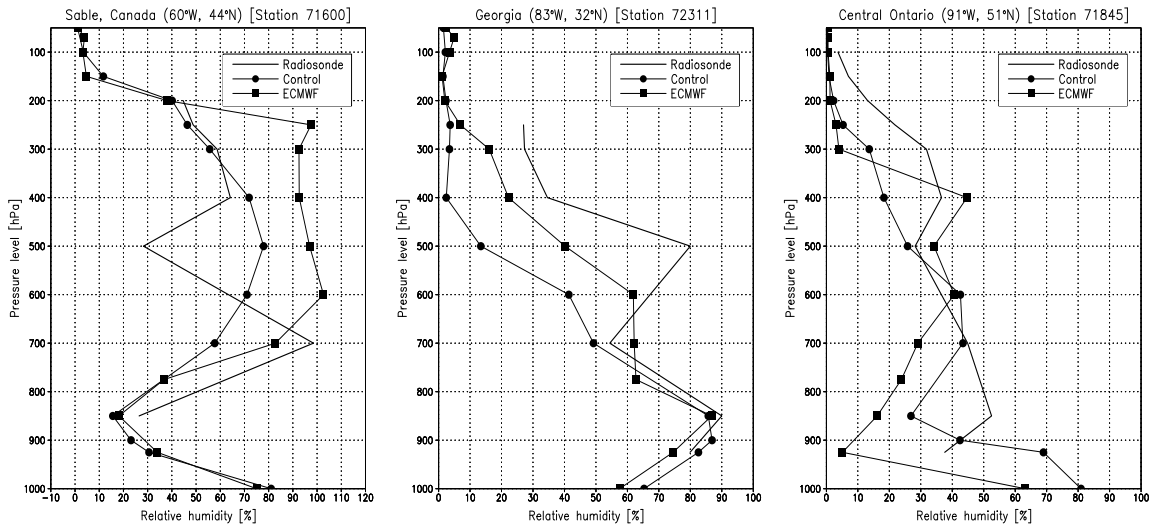


**Figure 4.11:** Comparison of vertical profiles of the relative humidity [%] at 00Z, 14th of March 1993 of ECHAM4 T106 (balls), ECMWF reanalysis (squares) and corresponding radiosonde measurements (solid line without markers).

The profiles indicate that neither the ECHAM4 simulation nor the ECMWF reanalysis corresponds to the radiosonde profiles. It is interesting to note that sometimes the adjusted model simulation is more similar to the radiosonde measurements than the reanalysis, although the observations are assimilated into the ECMWF forecast model. This again stresses the spin-up problem occurring in the reanalysis and supports the decision to avoid a validation using the reanalysis as the "truth". In the following comparisons radiosonde data is used.

In Figure 4.12 the relative humidity as simulated by the adjusted ECHAM4 simulation for different pressure levels at one time step during the blizzard case is compared with radiosonde measurements included as numbers. The vertical structure of the relative humidity is surprisingly well reproduced by the adjusted model simulation compared to the radiosonde profiles. In the main cloud regions the simulated relative humidities correspond to the observations within 10% at most locations. This stresses the importance of the dynamics in the determination of the 3D moisture distribution.

Differences occur outside of the main cloud regions. In the boundary layer behind the cold front the model appears to be too moist while it is too dry in parts of the middle and upper troposphere. The former could be caused either by too strong condensation in the boundary layer or, more likely, by suppressed vertical exchange of moisture. Processes which redistribute moisture in the troposphere are convection, diffusion and advection. The vertical diffusion moistens only the boundary layer. In deep convection two counteracting processes are active. Detrainment of convective cloud water and water vapour moistens higher levels of the troposphere, whereas convective precipitation is an efficient moisture sink. The net effect of deep convection is a removal of moisture. This is different for shallow, non-precipitating, convection, which transports moisture from the boundary layer to the free troposphere. However, the most important moisture sources for the middle troposphere are horizontal and vertical advection. Convection and vertical advection are usually linked in the way that convection provides the vertical velocity necessary for the large-scale transport of moisture.

This coupling of convection and vertical advection leads to a strong underestimation of the relative humidity in the middle troposphere when the convection is suppressed by other processes.

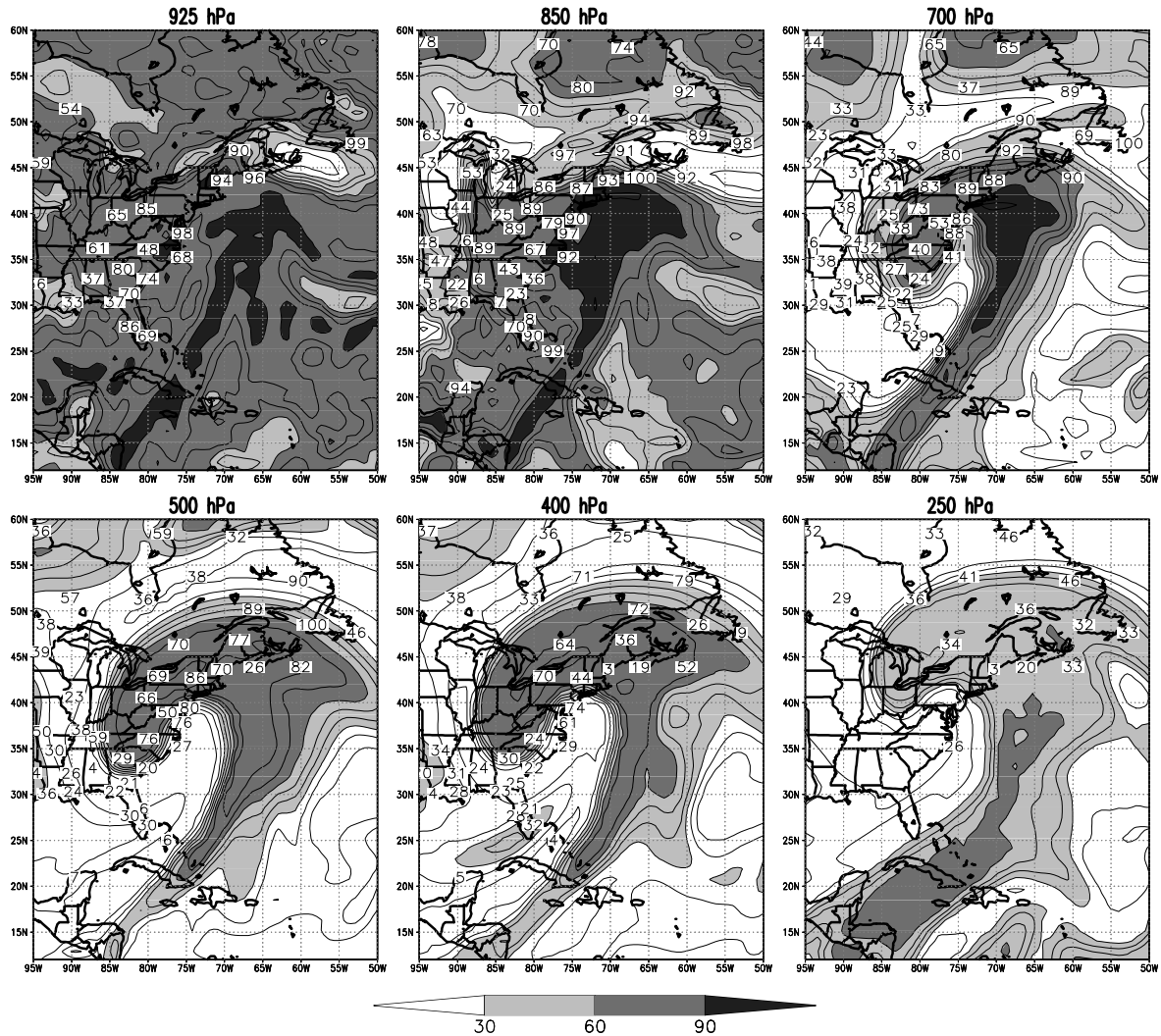


**Figure 4.12:** Relative humidity [%] at different tropospheric levels of the adjusted ECHAM4 T106 simulation. The numbers represent corresponding radiosonde measurements. [00Z, 14th of March 1993]

If the model, for example, simulates a too active cyclone with too strong vertical velocities in frontal regions, this implies too strong compensating subsidence in its environment (Figure 3.13). This strengthens the drying of the atmosphere and develops a stronger inversion at the top of the planetary boundary layer. A strong inversion suppresses the convective activity which could then not trigger the large-scale vertical advection of moisture. The result would be a strong decrease of the relative humidity above the planetary boundary layer, which prevents the development of clouds.

Figure 4.13 compares vertical profiles of temperature and relative humidity of Miami, Florida at 00Z, 14th of March 1993 of the model simulation with corresponding radiosonde profiles. It reveals a good agreement between the two temperature representations. Nevertheless, the mid-level relative humidity is underestimated by the model simulation. Therefore it is not surprising that the mid-level cloud cover is underestimated as well. Here a changed profile of the critical relative humidity with a lower value of  $r_0$  in the lower and middle troposphere might lead to a better description of clouds. This will be tested in a sensitivity study in the next chapter.

Walcek (1994) investigated the cloud cover and its relationship to the relative humidity during a springtime midlatitude cyclone. The only difference to the case examined here is that he investigated a cyclone developing over the continent. He found that, relative to other layers of

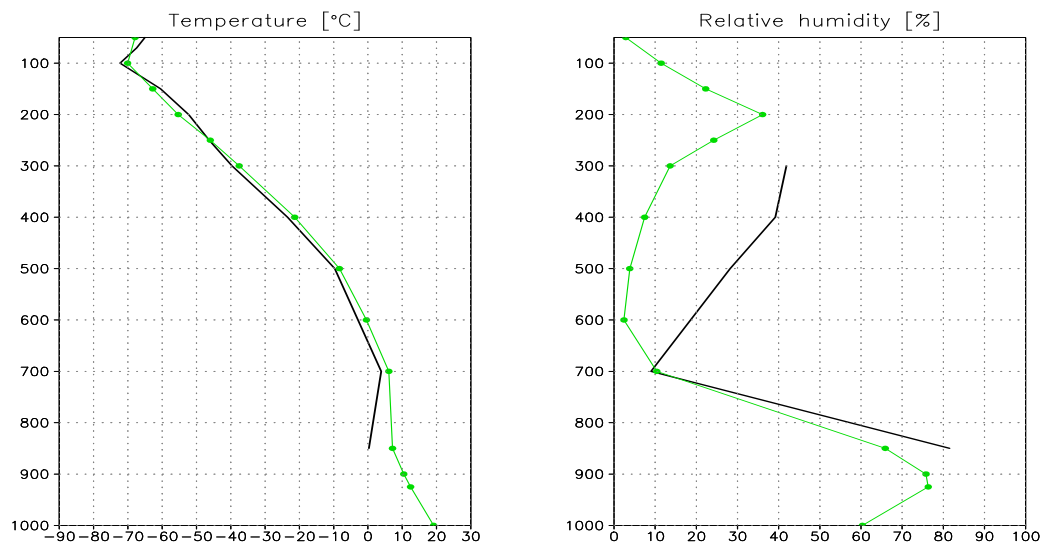


**Figure 4.13:** Temperature and humidity profiles of Miami [00Z 14th of March 1993] of the adjusted model simulation (filled circles) and corresponding radiosonde profiles (no marks).

the troposphere, the layer 2.5 to 5 km above the surface contains the highest cloud amounts at the lowest relative humidities with mean cloud amounts of 30 % at 50 % relative humidity and 650 hPa. This is not reproduced by ECHAM4, since the condensation threshold approach prevents the development of clouds below a critical relative humidity of 60% in middle and upper levels of the troposphere. The dry bias in the middle troposphere is also supported by [Lohmann et al. \(1995\)](#) who carried out a cloud study during the CEPEX period. They found additionally a dry bias in the lower troposphere and a wet bias in the upper troposphere. In the blizzard case the wet bias in the lower troposphere is not visible. In the upper troposphere a wet bias occurs in frontal regions, while the relative humidity is underestimated in surrounding areas, as for example over the cold continent. This difference is not surprising. In frontal regions moisture is transported to upper levels and then accumulated because of the underestimation of the sedimentation of ice crystals. Because of the missing moisture source this is not the case in undisturbed regions surrounding the developing cyclone. However, it is important to note that the density of observations in the upper troposphere is small even in the region of the developing cyclone.

Figure 4.14 compares the relative humidity of ECHAM4 and corresponding radiosonde profiles at 12Z, 19th of February 1993. As for the blizzard case, the relative humidity in the lowest levels of the troposphere is high nearly everywhere in the blocking situation. The relative humidity is in good agreement with radiosonde measurements in frontal regions surrounding the block. Unfortunately no measurements exist over the Atlantic in central regions of the anticyclone.

Apart from frontal regions a sharp decrease of the relative humidity occurs above the boundary layer. ECHAM4 simulates consistently low relative humidities in the central and eastern parts of the blocking high. Due to the critical relative humidity formulation, no clouds can exist at these low relative humidities, explaining the differences in total cloud cover compared to ISCCP satellite observations. Reasons for the strong moisture drop is an inversion at the top of the boundary layer (Figure 4.15) caused by large-scale subsidence. This stable stratification inhibits a distribution of moisture in deeper layers of the troposphere.

[Walcek \(1994\)](#) found that no critical relative humidity exists, below which the cloud cover is always zero, although it appears to decrease exponentially as humidity falls below 100%. For instance at humidities below 60-80 % many cloud cover formulations specify almost zero coverage while observations reveal 10 to 20 % coverage at relative humidities as low as 20 %. A typical



error which occurs when the relative humidity is used as the only indicator for cloud cover is 15-30% compared to observations. Furthermore a high degree of scatter is evident in the relationship of cloud cover and relative humidity (Walcek, 1994).

Other important quantities determining cloud amounts are vertical velocity, static stability and vertical shear of the horizontal wind. The former is very important because even small changes in vertical velocity can lead to large changes in the relative humidity. Another important factor is the horizontal resolution which determines the changes in cloud cover resulting from small-scale changes in the relative humidity.

### 4.3.3 Cloud top pressure

Further insight into differences between ECHAM4 and observations can be obtained by comparing cloud optical properties simulated by ECHAM4 with ISCCP observations. The most interesting quantities are cloud top pressure, investigated in this subsection, and cloud optical thickness which is described in the next subsection. For the comparison only those time steps are chosen, for which both satellite datasets, IR and VIS, are available. This enables a comparison of the model with satellite data as well as a comparison of the two satellite products.

In the model cloud top pressure is determined by scanning downward through the atmosphere. The highest layer with a cloud fraction larger than zero is transferred into pressure as the height coordinate, just as done with the satellite data. To be comparable to the satellite observation, it is necessary to neglect clouds with optical thicknesses lower than 0.2, since they are not correctly recognized by the satellites.

Figure 4.16 compares the cloud top pressure from the model and the two satellite datasets for three different time steps in the life-cycle of the developing cyclone representing the three major stages, namely developing, mature and dissipating stage of the development. In general ECHAM4 tends to overestimate cirrus clouds. This is clearly seen in all three stages. Furthermore, the model underestimates low and mid-level clouds. This is supported by results of Roeckner and LeTreut (1996), who found that the net-shortwave cloud forcing, which is mainly determined by low and mid-level clouds, is systematically underestimated over extratropical oceans. The systematic underestimation in the middle troposphere in the environment of the developing system is the result of a dry bias (Figure 4.12) likely caused by subsidence.

In the developing stage of the cyclone, the cloud height of the convective region over the Gulf of Mexico is underestimated. On the other hand, the area covered by high-level cirrus clouds is clearly overestimated above the eastern U.S.A. and the eastern Gulf of Mexico. In some regions, such as the western Atlantic ocean, the model simulates high-level clouds that are not observed by the satellite. In the mature stage the observed structure of the cyclone high-level clouds is simulated along the warm front, cold front and bent-back warm front. However, in regions of the strongest upward motion along the warm front and the cold front the cloud height is still underestimated. The same is true for the dissipating stage where the coarse structure is again reasonably represented but differences occur in detail. A reason for the too low cloud tops in frontal regions might be a too strong horizontal mixing, which redistributes the upper level clouds too quickly and prevents them from rising to the heights observed in the ISCCP observations. Furthermore this would explain the too large regions covered by cirrus anvils compared to the observation. Another explanation for this difference is the coarse vertical resolution in the model of  $\approx 2$  km at the cirrus level, which cannot resolve microphysical processes (Tompkins and Emanuel, 1999).

An interesting systematic difference occurs behind the cold front. The model simulates low-level boundary clouds, while ISCCP mainly observes mid-level clouds. Since clouds in this region are of convective nature, weaknesses in the convection scheme might be an important contributor to

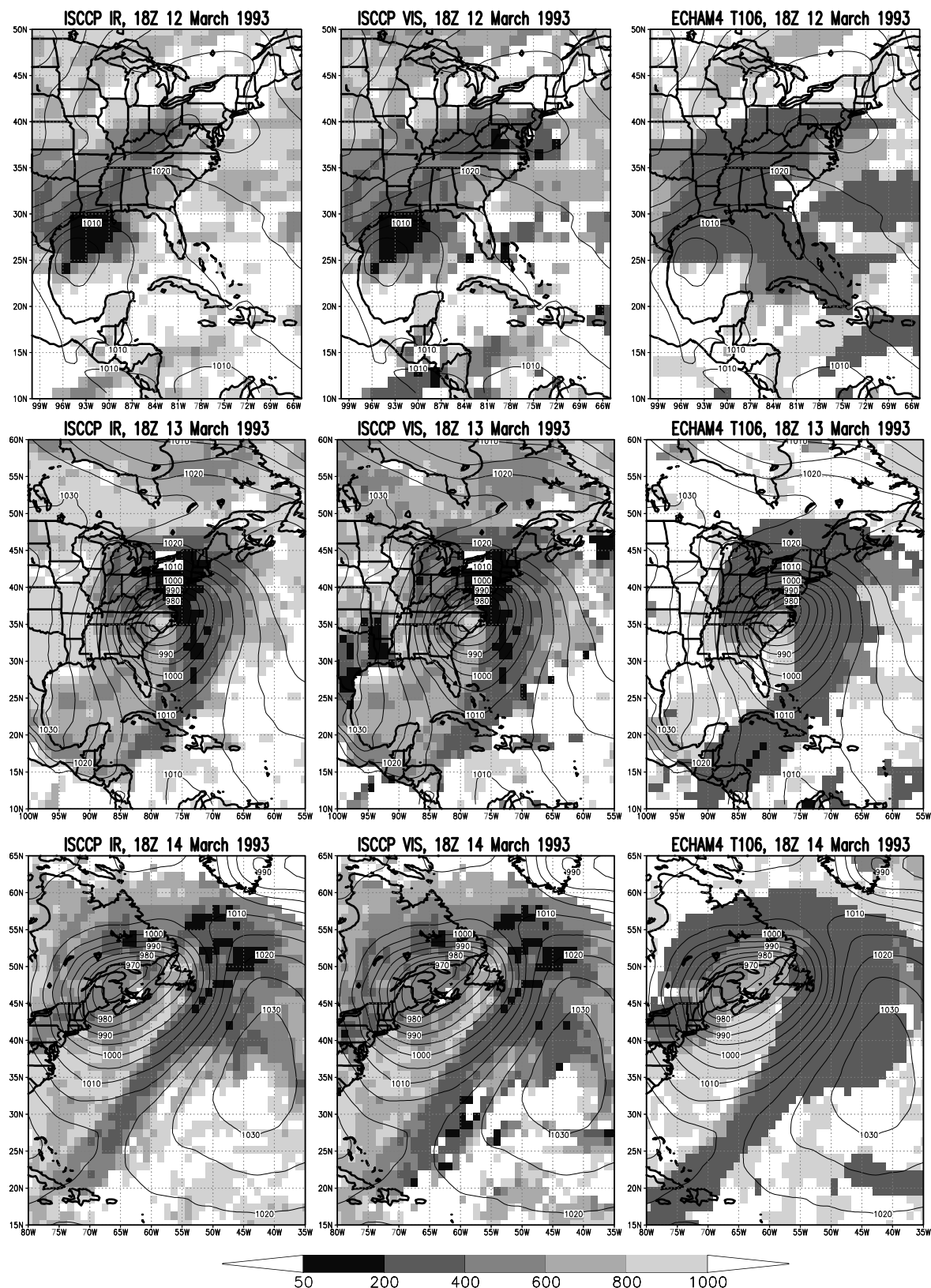


**Figure 4.16:** Comparison of the cloud top pressure [hPa] at three time steps representing the developing (top row), mature (middle row) and dissipating stage (bottom row) of the developing cyclone. The left column is the IR only satellite dataset, the middle one the VIS-adjusted observation and the right column represents the ECHAM4 simulation. The underlying mean sea level pressure [hPa] is for all plots the model calculated field.

this difference. Convection removes moisture from the troposphere as convective precipitation. At the same time detrainment of convective cloud water and water vapour acts as a moisture source for middle and upper levels of the troposphere. Therefore a too weak convection might be the reason for the too dry middle levels, which is then the reason for the underestimated cloud amounts. The convection scheme used in the ECHAM model distinguishes between penetrative, shallow and midlevel convection. Only one type of convection can occur in the grid box during one time step. The latter restriction could explain the too weak convective activity occurring behind the cold front. The simulated shallow convection excludes midlevel convection, which is probably necessary to transport large enough amounts of moisture to higher levels. Possible solutions for this problem are either a convection scheme which allows shallow as well as midlevel convection in the grid box during one time step, a changed order in which the prerequisites of the different convection types are checked (midlevel before shallow and penetrative) or a higher horizontal resolution which would generally increase the convective mass flux occurring in the grid box in regions with strong horizontal temperature gradients. The latter assumption is confirmed by a comparison of the convective mass flux of the T42 and T106 horizontal resolutions (Figure 4.17). Another reason for the suppressed convection could be a too strong subsidence in the dry slot behind the cold front as described in subsection 4.3.2.

Convection is usually associated with vertical advection, another important process, which transports moisture to higher levels. Thereby it provides the vertical velocity, which is necessary for the vertical advection of moisture. Other possible sources of moisture are evaporation of precipitation and horizontal advection. But they do not help behind the cold front, since no clouds occur at upper levels, which could precipitate and the middle troposphere in upwind regions over the U.S.A. is dry.

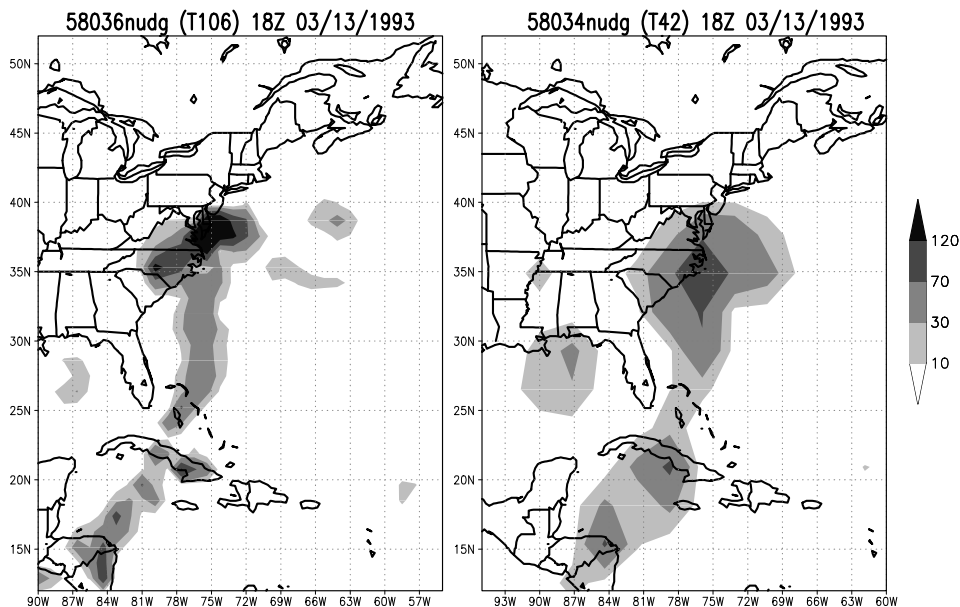


**Figure 4.17:** Comparison of the upward convective mass flux [ $gm^{-2}s^{-1}$ ] at model level 15 ( $\sim 850$  hPa) [18Z, 13th of March 1993] for ECHAM4 T106 (left) and ECHAM4 T42 (right).

The comparison of the two satellite datasets confirms that the IR observation misses some clouds. The largest differences occur in the mature stage. While the IR observation recognizes for example low-level clouds in the cold air over Texas, high-level clouds are detected by the more reliable VIS-adjusted observation due to the better performance of the cloud detection in the visible channel. However, in most regions the two datasets agree well.

Figure 4.18 compares the cloud top pressure for the blocking situation. Here two time steps in the mature stage of the system are investigated. Low-level clouds are the most prominent cloud

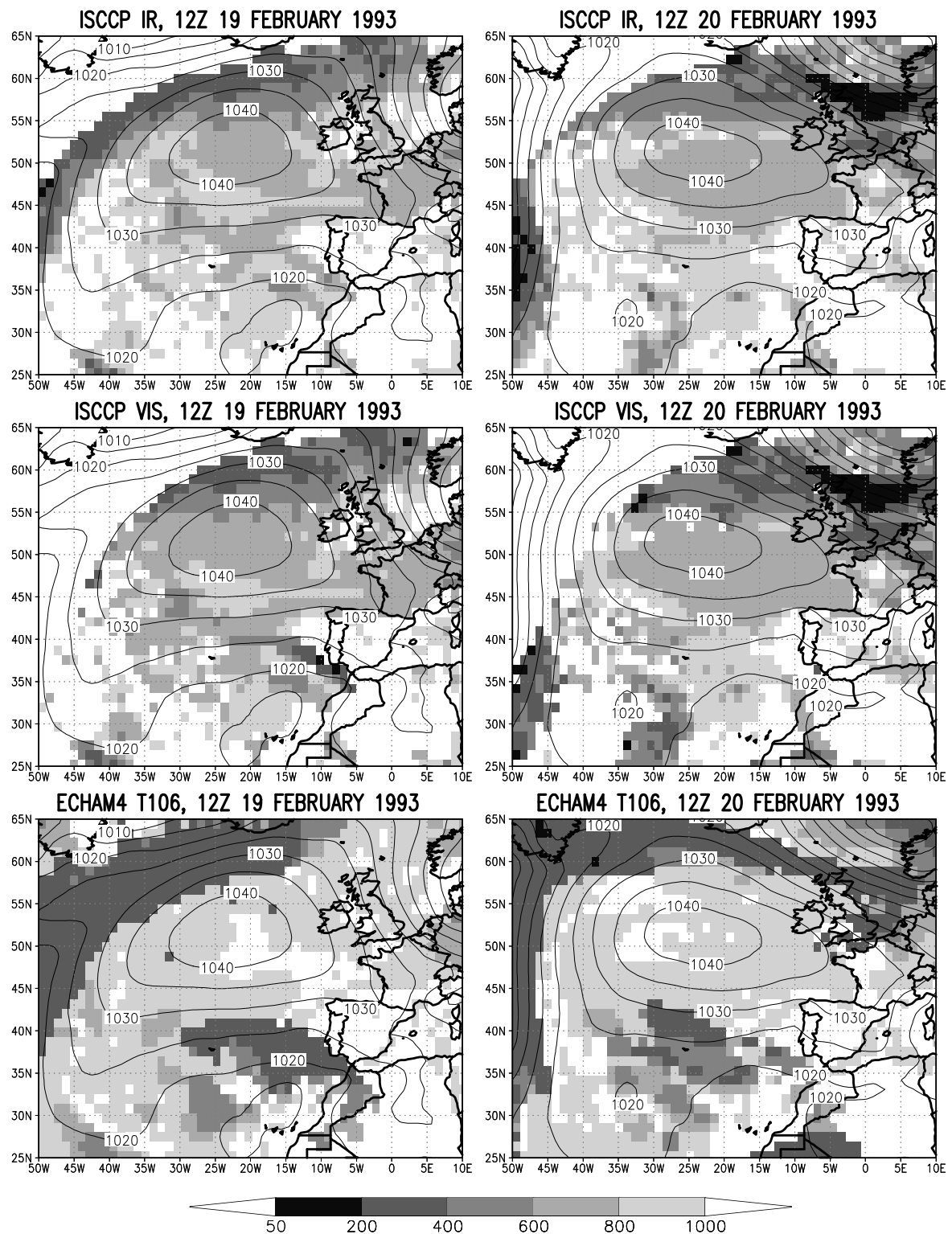


**Figure 4.18:** Same as Figure 4.16 but for two time steps of the blocking case. The upper row represents the IR only satellite observation, the middle row the VIS-adjusted observation and the bottom row the adjusted ECHAM4 simulation for 12Z 19th (left column) and 12Z 20th (right column) of February 1993.

type of blocking anticyclones. Similar as in the region behind the cold front in the blizzard case, the cloud top pressure is underestimated in the model simulation as compared to ISCCP observations. However, low-level boundary layer clouds are not convectively generated in the

model simulation in the blocking case. Instead, they are developed by the turbulence scheme and vertically constrained by an inversion layer, caused by subsidence from above (Brinkop and Roeckner, 1995).

The clouds occurring in southern regions of the anticyclone are dominated by high-level clouds in the model simulation but by low and mid-level clouds in the observations, indicating problems in the representation of the local cloud distribution. It is to be expected that these high-level clouds in ECHAM4 are the remnants of a dissipating cloud system, supporting the assumption that the dissipation of high-level clouds is too weak or too slow in the model simulation. The same is true for high-level clouds in the frontal systems surrounding the high. On the other hand, the cloud top pressure in the front to the northeast of the blocking high over the North sea between Scotland and Norway is underestimated, as similarly observed along the cold front in the blizzard case in the mature stage of the development.

To address the influence of the restriction to account only for clouds with optical thicknesses larger than 0.2, Figure 4.19 shows the cloud top pressure for one time step of the blizzard and the blocking case neglecting this restriction.

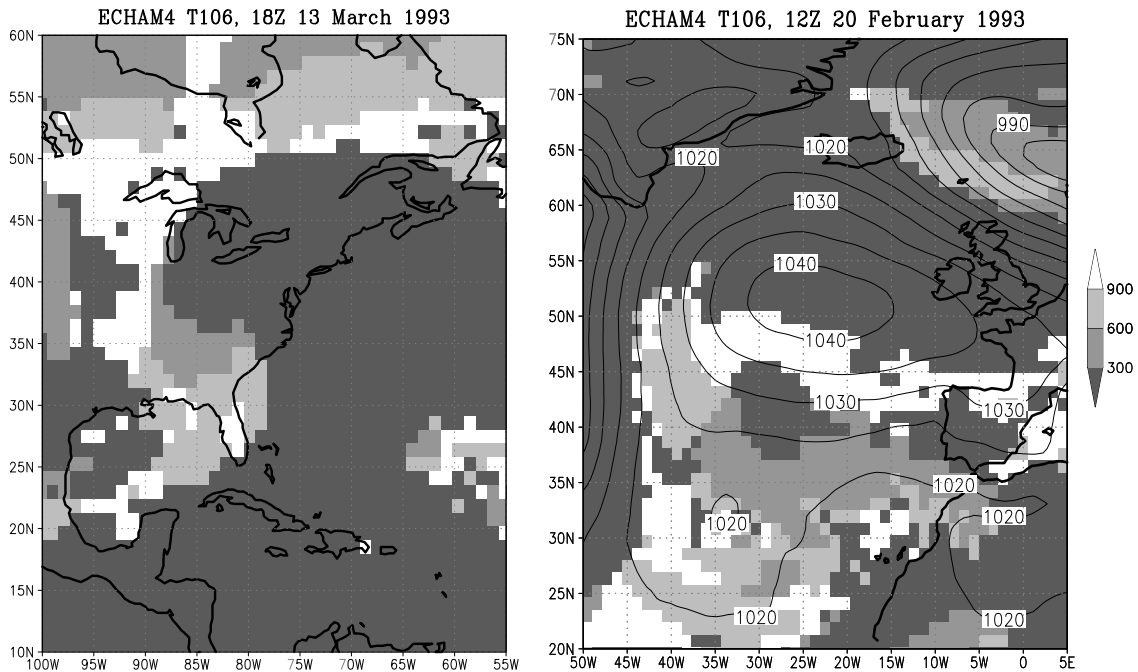


**Figure 4.19:** Cloud top pressure [hPa] of the adjusted ECHAM4 T106 simulation for one time step in the blizzard (left) and blocking case (right), neglecting the condition that the cloud optical thickness  $\tau$  has to be larger than 0.2.

Some systematic differences occur. Without the  $\tau > 0.2$  restriction, low and mid-level clouds appear to the north of the developing cyclone along the East Coast of the U.S.A., but they are still differently distributed compared to the observations (Figure 4.16). The area covered by high-level cirrus clouds is extended to the east. On the other hand no changes in cloud height occur in frontal regions of the cyclone, caused by the coarse vertical resolution or a dynamical mechanism, which efficiently distributes the clouds horizontally. No changes occur in the region behind the cold front, confirming that only low-level clouds are present. This is supported by the cross sections of cloud cover in subsection 4.2.1. To the south of the developing system in regions influenced by the upper tropospheric outflow from the ITCZ, additional clouds are detected higher up in the atmosphere.

In case of the blocking situation more high-level clouds are detected in large parts of the system where only low-level clouds have been detected with the “ $\tau > 0.2$  restriction”. In contrast to the

blizzard case, higher clouds are detected in large parts of the cloud band surrounding the block, in particular to the east of Greenland, where a region with stratospheric clouds is simulated (Figure 4.10).

As a general conclusion, this comparison illustrated that ECHAM4 seems to accumulate thin ice-clouds in undisturbed regions. In the developing stage or in active frontal regions, the changes, induced by the “ $\tau > 0.2$  restriction” are on the other hand much smaller.

#### 4.3.4 Cloud optical thickness

The cloud optical thickness in the ISCCP dataset is retrieved by comparing observed visible radiances with values pre-calculated from a visible radiation model covering the wavelength spectrum 0.55 to 0.7  $\mu m$ . In the D-series of the dataset near infrared radiances are used to additionally improve the retrievals over highly reflective snow and ice surfaces in polar regions. In the ECHAM4 model the cloud optical thickness is calculated for two bands in the visible and near infrared spectrum as described in section 2.1.3. To make the comparison as fair as possible only the first spectral band is included. However, the spectral bands of the observation and the model simulation are slightly different.

The comparison is done for the same time steps as for the cloud top pressure to enable the recognition of links between the different cloud optical properties. Figure 4.20 compares the cloud optical thickness simulated by the model with the satellite retrievals for the blizzard case.

In general, the coarse structure of the optical thickness field is well represented by the model. However, systematic differences as compared to the satellite observations occur. In the developing stage of the cyclone the absolute values of the cloud optical thickness as well as the area covered by large values is underestimated in the model simulation. This is true although the cloud top pressure comparison showed that the area covered by high-level clouds is overestimated in ECHAM4, indicating a different vertical distribution with larger amounts of high-level clouds and smaller amounts of low-level clouds in the model simulation as compared to ISCCP. The optical thickness is proportional to the liquid water path (LWP), which is strongly influenced by the convective activity. A strong convection induces strong vertical velocities associated with vertical advection of moisture and larger amounts of detraining cloud water. Furthermore stronger surface winds are induced, which enhance the evaporation from the warm ocean surface. The underestimated cloud optical thickness in the ECHAM4 simulation is therefore likely explained by an underestimated convective activity. On the other hand, larger cloud optical thicknesses are simulated over the eastern Gulf of Mexico and the position of the optical thickness maximum is shifted to the southwest as compared to the observations of ISCCP.

It is expected that the higher horizontal resolution of the “original” ISCCP dataset causes part of the differences. Although both, ECHAM4 and ISCCP, are used in T106 resolution, small-scale features may still be present in the interpolated satellite observation. To demonstrate the effect of the interpolation, Figure 4.21 compares the cloud optical thickness of ISCCP interpolated to the two different horizontal resolutions T106 and 0.5°. The main difference is, that the higher resolution dataset shows higher absolute values and more local phenomena. This is to be expected, because an interpolation reduces the gradients observed with a higher horizontal resolution. Nevertheless, some of the local features are represented in the T106 version of the observation, such as locally occurring large optical thicknesses, which represent small-scale convective events, over Georgia and along the cold front. However, the underestimation of low and mid-level clouds is probably the main reason for differences between model results and satellite data, as suggested by the cloud top pressure comparison.

In the mature stage the optical thickness is overestimated in central regions of the large-scale ascent to the northeast of the surface low. On the other hand the area covered by optically

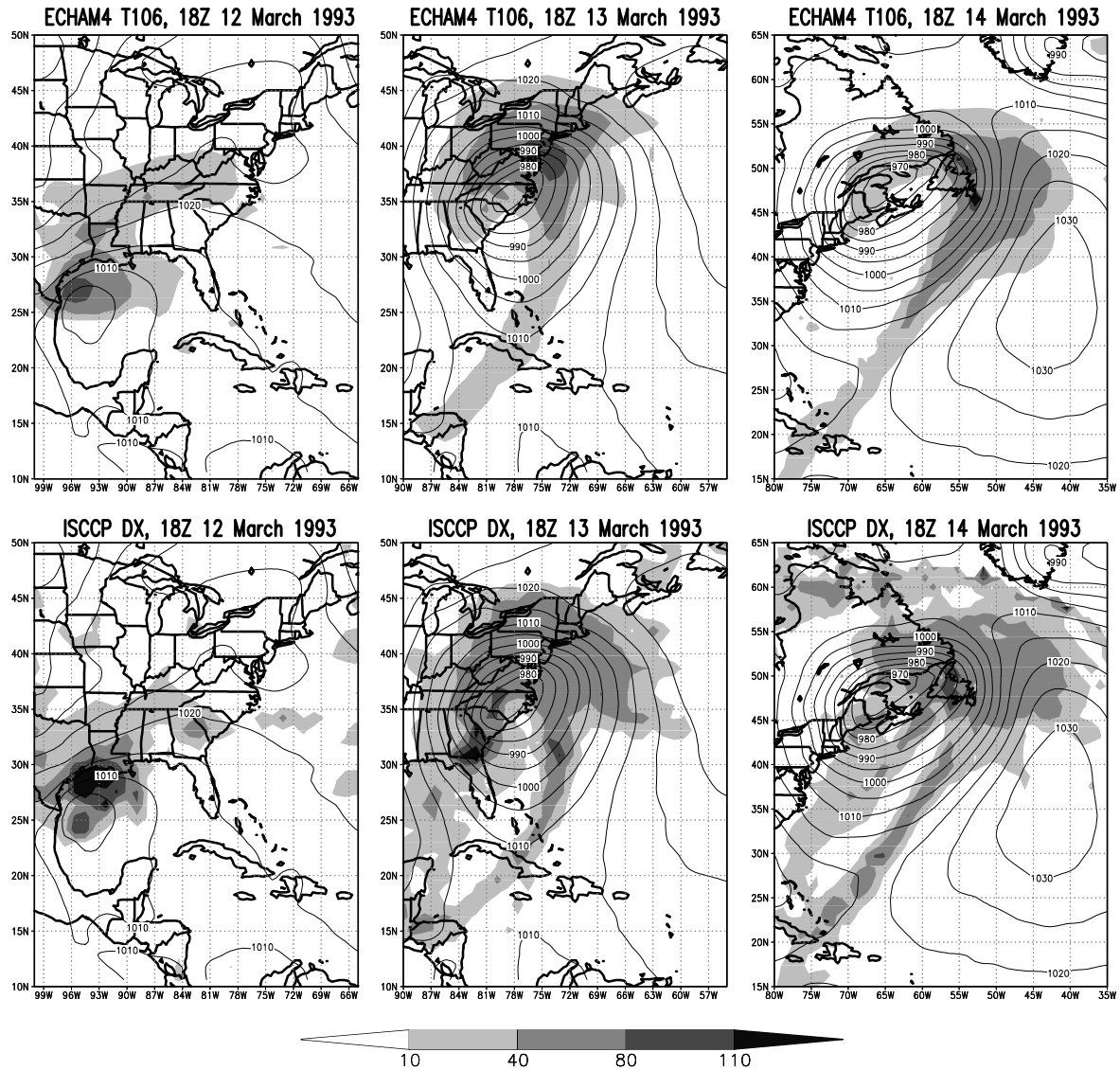


**Figure 4.20:** Comparison of the visible cloud optical thickness  $\tau$  for the model simulation (upper row) and the visibly corrected ISCCP DX dataset (interpolated to T106 resolution)(lower row). The mean sea level pressure [hPa] for all plots is the model calculated field.

thick clouds is underestimated compared to the satellite observations, particularly along the warm front in upwind regions of the strongest ascent. This supports the assumption of an underestimation of condensation in the stratiform cloud scheme in the lower troposphere. The changed profile of the critical relative humidity, investigated in a sensitivity experiment in the next chapter might partly remove this underestimation. Furthermore, the strong optical thickness maximum over Georgia is not represented in the model simulation, likely a result of the coarse horizontal resolution, which inhibits the simulation of this convectively induced maximum in the region of the largest temperature gradient and wind velocity. As a finer horizontal resolution is associated with stronger convection (Figure 4.17), this local phenomenon might be represented in a higher resolution model simulation. A possibility to check this is to perform a simulation with a regional model. However, this is beyond the scope of this thesis and remains for future projects. Along the cold front, absolute values of the cloud optical thickness are generally underestimated, indicating that a resolution of T106 is not able to reproduce the sharp frontal boundary.

In the dissipating stage, the main features are again well represented in the ECHAM4 simulation. The small-scale regions of large optical thickness at the land-ocean boundary of Newfoundland

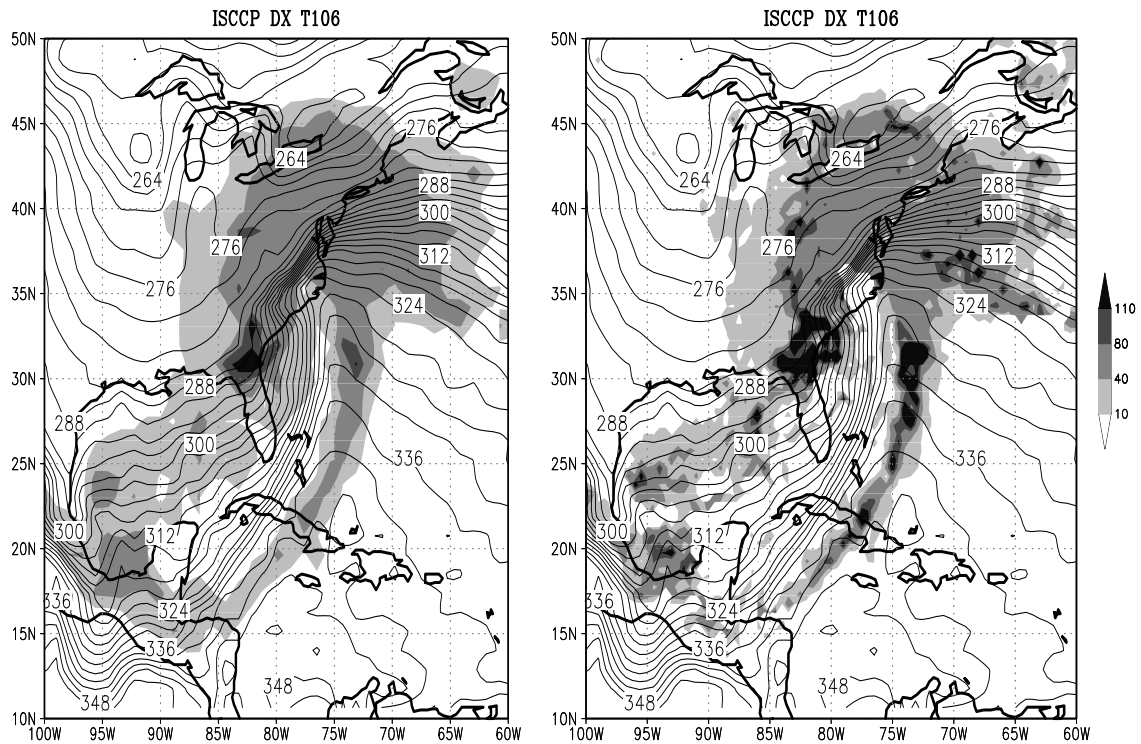


**Figure 4.21:** Near surface equivalent potential temperature [K] and cloud optical thickness  $\tau$  at 18Z 13th of March 1993 for two versions of the ISCCP DX dataset. **Left:** Interpolation to T106. **Right:** Interpolation to  $0.5^\circ$ .

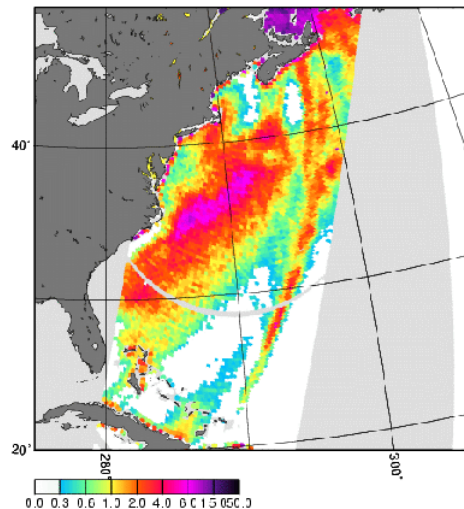


**Figure 4.22:** Precipitation rate as observed by SSM/I microwave measurements (NOAA-11).

and the Canadian mainland is stronger simulated in ECHAM4, as compared to ISCCP, suggesting that the model is very sensitive to the large temperature gradient when the air is saturated. In contrast to the mature stage, the area covered by large values of the optical thickness is extended and more similar in size to ISCCP. This indicates, that the amount of low and mid-level clouds, which are mainly responsible for larger values of the optical thickness, are better represented in later stages of the development. This difference between the mature and the dissipating stage could be caused by a too large value of the condensation threshold, which delays the development of clouds in earlier stages of the development.

As in the mature stage the cloud optical thickness is underestimated in the model simulation behind the cold front. Observations of typical cyclones [e.g. [Browning \(1985\)](#), [Houze \(1993\)](#)

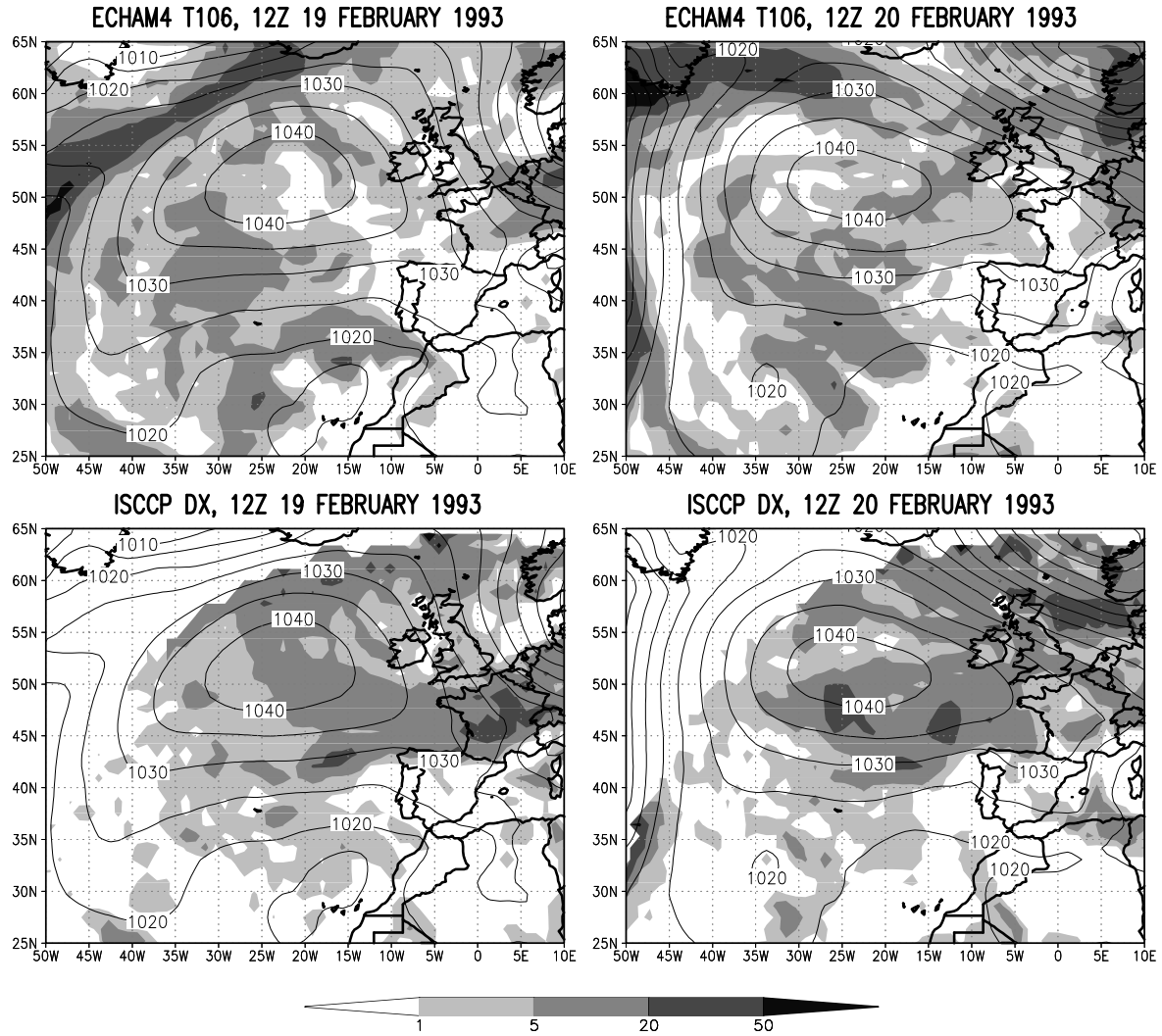


Figure 4.23: Same as Figure 4.20 but for the blocking case.

or Neiman and Shapiro (1993) and Neiman et al. (1993)] show that in those regions small to medium scale convective clouds follow a narrow belt of low cloudiness in the so-called post-frontal subsidence zone. Both features are visible in the satellite observed optical thicknesses, particularly in the dissipating stage (lower right panel of Figure 4.20).

In the model simulation the optical thickness is generally underestimated behind the cold front, because only thin low-level boundary layer clouds are simulated (Figure 4.9). The existence of higher clouds behind the cold front is also confirmed by SSM/I observations of precipitation rates. Figure 4.22 shows for example the descending picture of the 14th of March 1993.

Figure 4.23 compares the model and the observation for the two time steps during the blocking situation. As to be expected from the cloud top pressure comparison, the cloud optical thicknesses are underestimated by the model simulation in the central parts of the system. The strong drop of the relative humidity above the boundary layer and the strong dependence of the cloud cover to the relative humidity are the reasons for this difference. Furthermore, the large optical thicknesses, simulated by the model in southern and southeastern regions of the block, are not confirmed by the observations.

### 4.3.5 Cloud types

The World Meteorological Organization (WMO) classifies clouds into three main groups namely low-level, mid-level and high-level clouds (International Cloud Atlas, 1987). They are further subdivided into ten cloud types [e.g. Liljequist and Cehak (1994) or Barry and Chorley (1987)] illustrated in Figure 4.24.

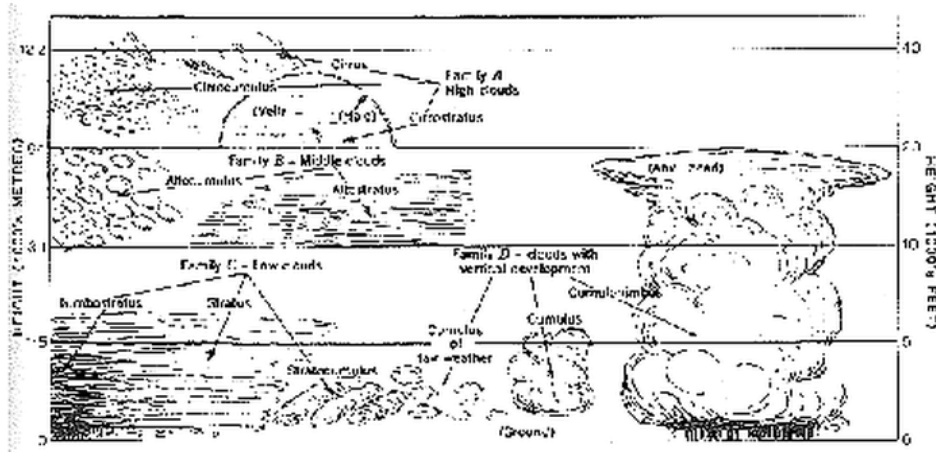


Figure 4.24: Ten basic cloud groups according to height and form (Barry and Chorley, 1987).

For the ISCCP cloud data products, 9 different cloud types are calculated with a classification algorithm that uses cloud top pressure and cloud optical thickness (Table 4.1). Since the cloud types are associated with the dynamics of the environment (Lau and Crane, 1995), this is another way of validating the representation of the dynamics in and around synoptic-scale systems.

cloud type	cloud top pressure [hPa]	cloud optical thickness []
cumulus	1000 ... 680	0 ... 3.6
stratocumulus	1000 ... 680	3.6 ... 23
stratus	1000 ... 680	23 ... 379
altocumulus	680 ... 440	0 ... 3.6
altostratus	680 ... 440	3.6 ... 23
nimbostratus	680 ... 440	23 ... 379
cirrus	440 ... 50	0 ... 3.6
cirrostratus	440 ... 50	3.6 ... 23
cumulonimbus	440 ... 50	23 ... 379

Table 4.1: Cloud types and associated values for cloud optical thickness [] and cloud top pressure [hPa] following ISCCP (Rossow et al., 1996b).

The major disadvantage of this algorithm is that it does not recognize multiple cloud layers, since no 3D information is available in the high-resolution DX dataset. This leads, for example, to large values of the cloud optical thickness and low values of the cloud top pressure being automatically classified as cumulonimbus, although it could also be a thick stratus cloud with an overlying thick cirrus. Another disadvantage is the necessity of the visible channel for the calculation, restricting the comparison to daytimes.

The cloud type information is critical for the radiation balance (Ockert-Bell and Hartmann, 1992). In regions where a single cloud type is dominant, such as stratus regions without overlying cirrus, the total cloud cover is able to explain variations in OLR<sup>4</sup> and albedo associated with

<sup>4</sup>OLR = Outgoing Longwave Radiation

clouds. On the other hand, in regions where clouds have more variable optical properties and structure, as in tropical convection regions or midlatitude storm tracks, cloud-type changes are essential in determining the day-to-day variations of the radiation budget. In midlatitudes and polar regions significant contributions to the zonal average longwave cloud forcing are provided by low and mid-level clouds (Hartmann et al., 1992).

The variation of net radiation is also dependent on the degree of cancellation between the effect of clouds on the albedo and the OLR. Highest clouds contribute most to the longwave cloud forcing, while the albedo is, on the other hand, primarily forced by low-level clouds with larger values of the optical thickness (e.g. marine stratus). The strong albedo forcing of high thick clouds is offset by their large OLR forcing, which results in only little contribution to the net cloud forcing (Hartmann et al., 1992).

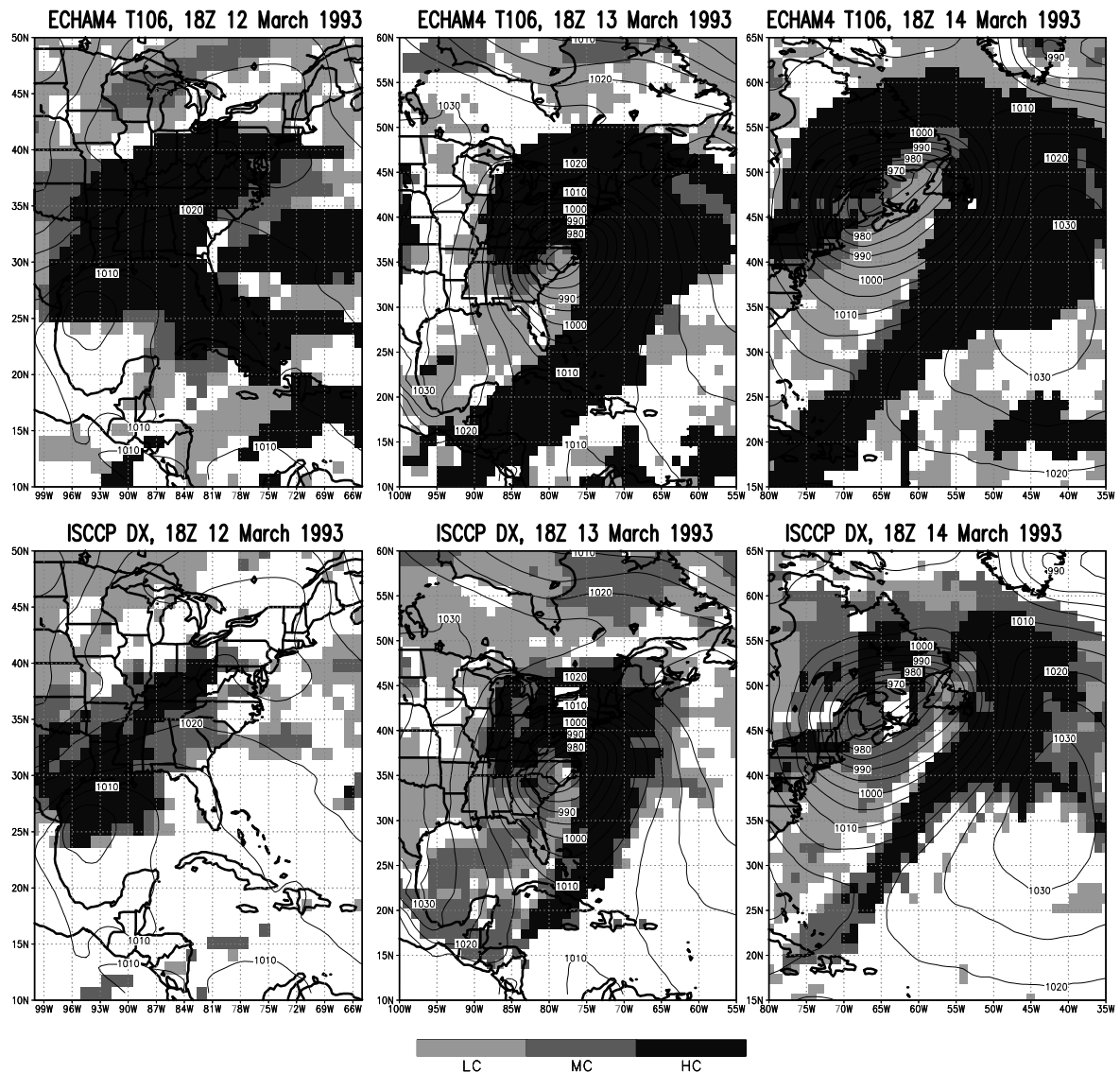


**Figure 4.25:** Comparison of the different cloud types calculated with the ISCCP cloud classification algorithm for the time steps used before [ECHAM4 T106 (upper row); ISCCP DX (lower row)]. The mean sea level pressure [hPa] is the model calculated field.

Figure 4.25 compares the cloud types calculated from the results of the ECHAM4 simulation with the corresponding values calculated from the cloud optical properties of ISCCP DX. The broad-scale features are reasonably simulated by the model as illustrated by the shape of the cumulonimbus regions. However, the model tends to overestimate high-level clouds, thick cumulonimbus as well as thin cirrus clouds, in pre-frontal regions where low to mid-level clouds

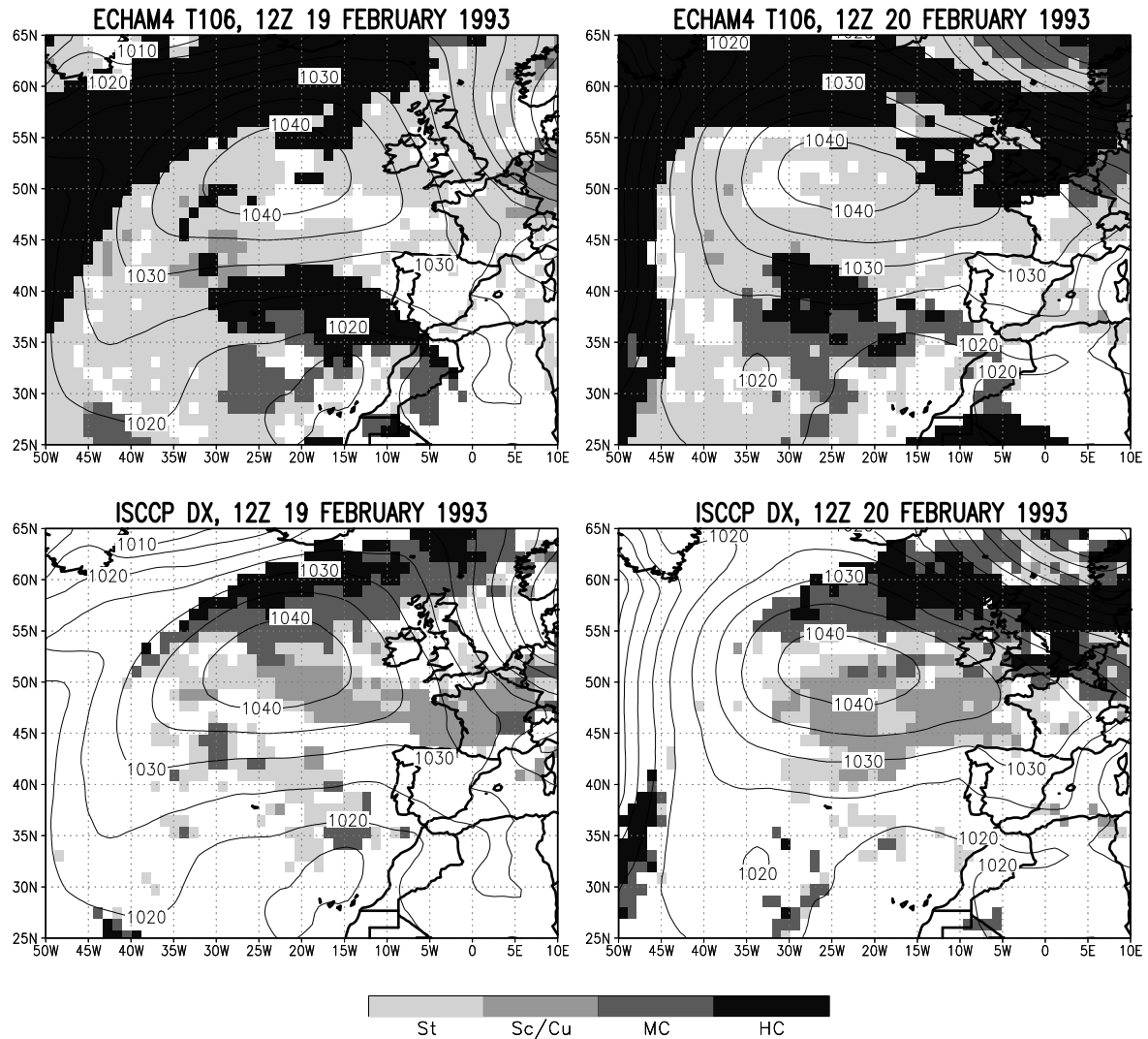


Figure 4.26: Same as Figure 4.25 but for the blocking case.

are dominant in the satellite observation. This is true for all three stages of the development and suggest a too slow removal of ice crystals from the upper troposphere. The main sink of ice crystals is the sedimentation. It is parameterized as a function of the ice water content, leading to a slower removal of thin cirrus clouds as compared to thicker ice clouds and therefore to a long lifetime and an accumulation of thin cirrus clouds. Another possible reason is a too weak detrainment of convective cloud water and/or water vapour in the middle troposphere. Stronger values would reduce the amount of convective cloud water detrained in the upper troposphere.

As for the comparison of cloud optical thickness and cloud top pressure the general underestimation of low and mid-level clouds, particularly in the environment of the developing system, is obvious. Most prominent is the region behind the cold front, where low and mid-level clouds follow a narrow belt of low cloudiness in the post-frontal subsidence. Here the model simulation is dominated by low-level clouds only. Reasons for this underestimation could be the sub-grid scale nature of clouds, typical for the post-frontal weather, for which even T106 is a too coarse horizontal resolution, the “uni-modality” of the convection scheme or a too strong subsidence behind the cold front, as described in subsection 4.2.3.

The development of the fronts is realistic although the area covered by cumulonimbus clouds is generally too large in the model simulation as well as in the ISCCP observation compared to what is expected from typical cyclones (Browning, 1985). However, this is, as mentioned above, a general weakness of the classification algorithm.

As suggested by the comparison of the cloud top pressure and the cloud optical thickness, the cloud height in the bent-back warm front decreases from the mature to the dissipating stage in the ISCCP observation associated with a transfer of high-thick cumulonimbus clouds to middle-thick Nimbostratus clouds. This can be explained by evaporation and re-condensation of precipitation developed at higher levels. In the stratiform cloud scheme of ECHAM4, evaporation of precipitation from higher levels occur in the cloud-free part of the grid box. It is included as a source term into the budget equation of water vapour in lower levels. A reason for the too dry middle troposphere could be an underestimation of this evaporation. Moreover, the too weak or slow removal of ice crystals, especially from thin ice clouds, explains the transfer from high-thick to high-thin clouds like cirrus or cirrostratus and therefore the overestimated cirrus anvils in the model simulation.

Figure 4.26 does the same comparison for the blocking case, revealing the same results as obtained from the blizzard case. The coarse distribution of high-level clouds in frontal regions surrounding the blocking high is well represented in the adjusted model simulation. However, the underestimation of mid-level and the overestimation of high-level clouds is clearly seen. The cloud system to the south of the anticyclone is not observed by ISCCP. In central regions of the high low-level stratus clouds with higher optical thicknesses are observed by the satellite.

#### 4.3.6 Brightness temperature

In this subsection the effect of clouds on the infrared part of radiation is discussed. It is expected that the systematic errors in the representation of clouds have a detrimental effect on the radiation budget simulated by the model.

Understanding the link between cloud formation/decay processes and the radiative balance depends on the examination of variations of individual radiative flux components together with changes in individual cloud properties. Such a study was recently performed by [Zhang and Rossow \(1995\)](#). Their key conclusion was that uncertainties in the calculated radiative fluxes are no longer dominated by uncertainties in cloud properties, except in polar regions. Rather, the remaining uncertainties are contributed in roughly equal parts by the properties of the surface, atmosphere and clouds. In particular the surface temperature and albedo and the low-level temperature in the atmosphere are important.

ECHAM4 has been developed as a climate model. Therefore the radiation scheme is tuned in a way that the global annual mean radiation budget is in accordance (to within the measuring accuracy) with ERBE satellite observations. However, because of this tuning the scheme might miss features which are important for the simulation of synoptic time scales.

The problem associated with the investigation of the radiative effects of clouds is to find observations which are comparable with the model results. The OLR provided by the model, which is integrated over the whole spectrum, is not directly comparable with the narrow-band brightness temperature measured by the satellite in the spectral band 10.5 to 12.5  $\mu m$ . The brightness temperature is a measure for the amount of radiation emitted from the top of the clouds and is therefore often used to determine the cloud height.

To ensure comparability the model output is reprocessed with a narrow-band radiation model ([Morcrette, 1991a](#)). This so-called "model-to-satellite" approach minimizes the uncertainties due to potentially different assumptions (e.g. for the cloud optical properties) in the cloud retrieval scheme and the model radiation scheme. It can be applied regardless of the horizontal resolution of the satellite observations and the model output ([Morcrette, 1991a](#)).

Another problem is introduced by the different horizontal resolutions of the datasets. The satellite brightness temperature is representative for an area of about 30  $km^2$  at nadir. It is transferred to T106 horizontal resolution to receive similar spatial resolutions for both satellite

and model results by simply averaging the observed data over the model grid. Typically such a grid box contains information from 4 to 20 pixels depending on the satellite viewing angle. With this simple averaging, it is implicitly assumed that the model brightness temperature computed from only one set of surface conditions and one atmospheric profile would be equal to the average brightness temperature calculated from a model with the resolution of the satellite observation, an assumption which cannot be validated (Morcrette, 1991a).

Furthermore, the interpolation to the model resolution is associated with an information loss (see Figure 4.21), in particular in a cloudy atmosphere, where a large range of brightness temperatures occurs. Nevertheless, the main features relevant for the validation of the model parameterization as the vertical structure, amplitude or diurnal cycle of the brightness temperature are satisfactorily retained (Morcrette, 1991a).

The narrow-band model is based on the approach by Rodgers and Walshaw (1966). The whole long-wave spectrum is divided into a number of spectral intervals. Here 10 lines around  $11.5 \mu m$  are used over which the spectral fluxes are calculated using a statistical band model (Morcrette, 1984). Over a given spectral interval, the infrared upward and downward fluxes are written as:

$$F^+(z) = [\pi B(s) - \pi B(0)] t(z, 0; r) + \pi B(z) - \int_0^z \pi \frac{dB}{dT}(z') \frac{dT}{dz}(z') t(z, z'; r) dz' \quad (4.1)$$

$$F^-(z) = [\pi B(Z) - \pi B(\infty)] t(Z, z; r) - \pi B(z) - \int_z^Z \pi \frac{dB}{dT}(z') \frac{dT}{dz}(z') t(z, z'; r) dz' \quad (4.2)$$

where  $\pi B$  is the frequency-integrated Planck function,  $Z$  the height of the upper limit of the atmosphere,  $s$  and  $0$  refer to the surface and the layer just above and  $(z, z'; r)$  is the transmission function of flux through a slab between  $z$  and  $z'$ .

Furthermore the absorptions of  $H_2O$ ,  $CH_4$  and  $N_2O$  are taken into account as well as the effect of the water vapour continuum over the entire spectrum. The validation of the narrow-band model has shown to give total fluxes within 1% of the result of the line-by-line model (Morcrette, 1984).

This model is used to calculate the IR brightness temperatures around the  $11.5 \mu m$  spectral band from the model variables temperature, specific humidity, cloud liquid water, cloud ice, surface pressure, surface temperature and partial cloud cover. For clear sky and cloudy sky, radiative fluxes  $F$  are determined by equations (4.1) and (4.2). Then the brightness temperatures are calculated using:

$$T_{Br} = h \cdot \frac{c}{k} \cdot \frac{P_k}{\ln \left( 1 + \frac{2hc^2}{F} \right)} \quad (4.3)$$

with the Planck constant  $h = 6.626 \cdot 10^{-34} Js$ , the Boltzmann constant  $k = 1.381 \cdot 10^{-23} JK^{-1}$ , the speed of light  $c = 299792458 m/s$  and the peak frequency  $P_k = 11.56 \mu m$ . From the model and the ISCCP data the radiative effect of the clouds is calculated by subtracting the cloudy sky brightness temperature from the clear sky value.

$$C_{eff} = T_{Br,clear} - T_{Br,cloudy} \quad (4.4)$$

Figure 4.27 and Figure 4.28 show the temporal development of  $C_{eff}$  for the blizzard case for the model simulation and the satellite observation.

The comparison reveals three main results:

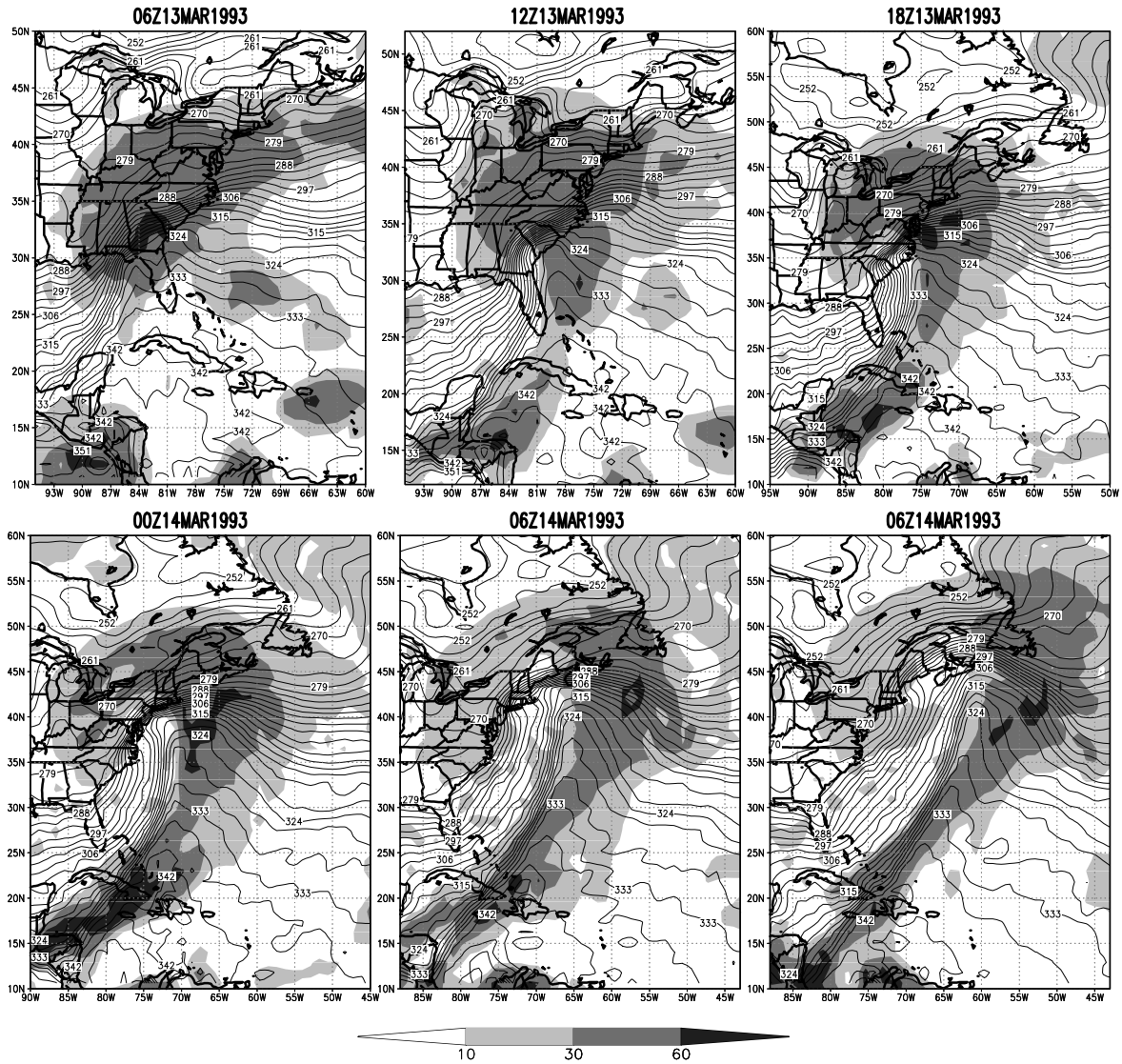


**Figure 4.27:** Temporal development of the equivalent potential temperature [K] (contour) (lowest model level) and the effect of clouds on the infrared brightness temperature field [K] (shaded) of the adjusted ECHAM4 simulation for the blizzard case between the 13th and 14th of March 1993.

- In the developing stage of the system the adjusted ECHAM4 simulation strongly underestimates the radiative effect of clouds along the cold front. Reason is an underestimated convective activity caused by the unimodal restriction of the convection scheme or the relatively coarse horizontal resolution.
- In the dissipating stage on the other hand the model overestimates the effect of clouds. This supports the assumption that the cloud dissipating mechanisms, as sedimentation of ice crystals or vertical mixing in the upper troposphere, are too weak or too slow in the model.
- The cloud effect on the brightness temperature in the cold air behind the cold front is systematically underestimated. While the model only simulates clouds in the boundary layer, the satellite observes clouds which extend into higher levels of the troposphere. This difference might be caused by too coarse horizontal as well as vertical resolutions, the unimodal nature of the convection scheme or a too strong subsidence.

The latter finding is also supported by SSM/I observations of precipitation (Figure 4.22). Even in the higher resolution T213, until recently used in the ECMWF operational analysis, the

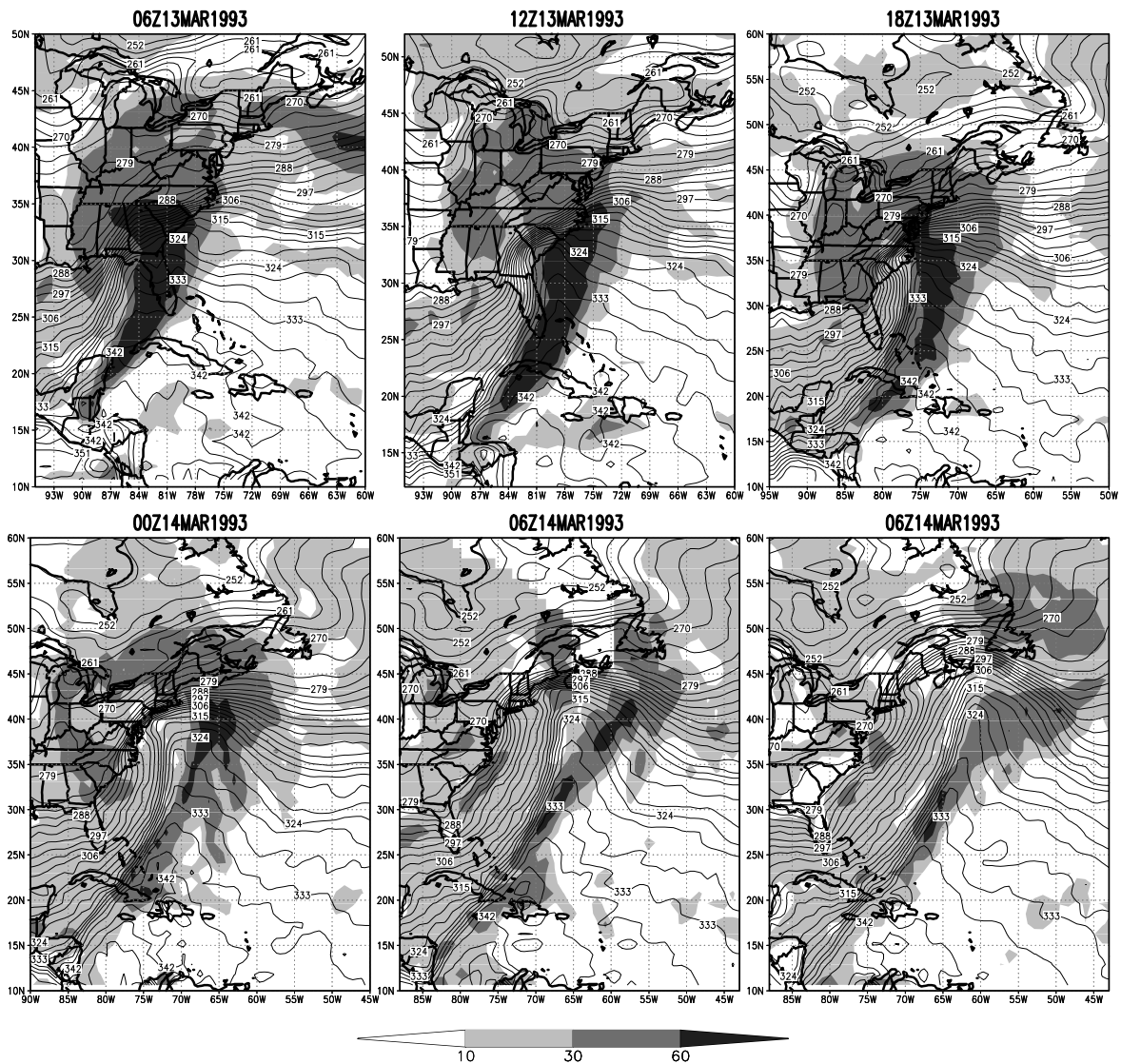


**Figure 4.28:** Same as Figure 4.27 but for ISCCP DX. The underlying equivalent potential temperature [K] is the model calculated field.

precipitation development behind the cold front is underestimated (Klepp, 1999).

Another way of analyzing the vertical distribution of clouds is to prepare histogram plots in a similar way as applied by Morcrette (1991a). Here two different types of histograms are presented. First, the occurrence of the brightness temperature within different temperature intervals for a distinct region and over a distinct time interval is summed up and plotted against the brightness temperature as the height coordinate. Second, the accumulation is only done over the area and plotted against time and brightness temperature in a so-called evolution histogram (Morcrette, 1991a).

ISCCP stores the data as integer values to save disk space. The values are re-converted into physical values using look-up tables. Therefore only distinct physical values occur. Since the brightness temperature bins in-between those distinct values stay empty, large scattering occur. To overcome this problem the ISCCP data is filtered by combining the information of neighbouring bins.

For the blizzard case data from the 12th of March 1993 00Z to the 15th of March 1993 21Z between 100°W to 30°W and between 10°N to 60°N is included in the histogram. In this case it is necessary to choose a large region to ensure that the whole life-cycle develops within the

region. For the blocking case, because of the stationarity of the system, only a small region is necessary. Here the region  $30^{\circ}\text{W}$  to  $5^{\circ}\text{W}$  and  $40^{\circ}\text{N}$  to  $55^{\circ}\text{N}$  and the period from the 19th of February 1993 00Z to the 21st of February 1993 21Z is summed up. The left panel of Figure 4.29 shows the results for the blizzard case while the right one represents the blocking case.

The main result is a good general agreement between satellite and model data indicating a well represented mean vertical cloud structure in the model simulation in the regions of interest. This is true although the moisture is not relaxed to the observed state. Nevertheless systematic differences occur.

This method has many advantages as mentioned above. However, disadvantages are that although the radiation scheme accounts for partial cloud cover, large cloud amounts in high levels of the troposphere can lead to shadowing of low-level clouds in the same column. Furthermore this method is not able to distinguish between information coming from the surface or the lowest cloud layer. Therefore the highest occurring brightness temperatures are mainly a representation of the surface temperature variability.

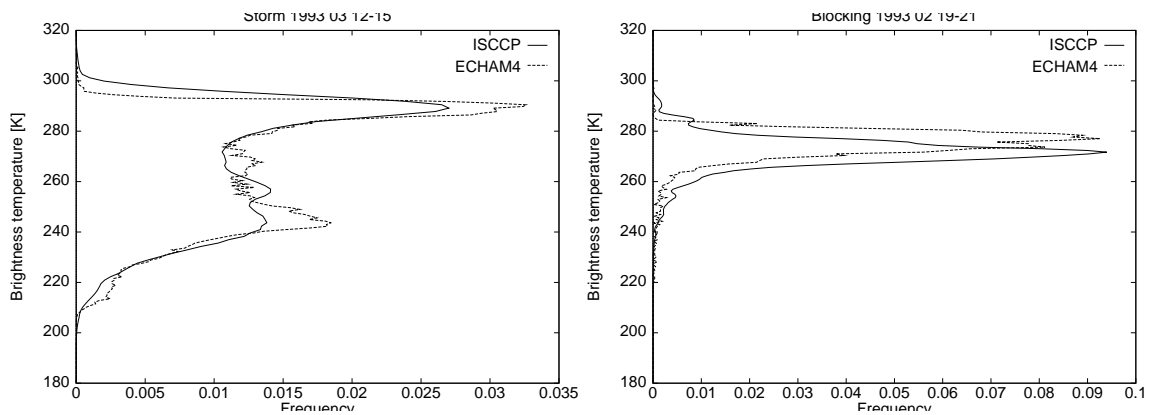


**Figure 4.29:** Histogram of the frequency of brightness temperature bins plotted against the brightness temperature [K] for the blizzard case (left) and the blocking case (right). The solid line represents the ISCCP observation and the dotted line the results of the model simulation.

Due to the large amount of landpoints in the region selected for the blizzard case, the variability of the surface temperature is larger and reflected by a broader distribution on the warm side of the histogram. As a consequence the frequency in each bin is lower compared to the blocking case, where few temperature bins are clearly favoured, reflecting small SST changes. This is true for the model simulation as well as the ISCCP observation. However, some differences between the two datasets in the blizzard case are obvious. On the warm side of the histogram ECHAM4 shows a stronger peak and a more rapid drop of the frequency to warmer temperatures. This is related to a more uniform surface temperature, caused by the coarser “original” horizontal resolution and by the way the surface temperature is calculated in the model. The satellite measures the skin temperature of ocean as well as land surfaces. In the model simulation, daily SSTs from the ECMWF reanalysis are used, while the temperature of land surfaces is calculated by the model.

The underestimated low-level cloud cover cannot be seen in such kind of plot because of the shadowing effect by higher-level clouds and the surface temperature variability. Interesting differences occur in the temperature range between 280 and 250 K. While the frequency is stronger on the warm side in the model simulation, the cold side of this range is favoured by the ISCCP observation, indicating different distributions of low and mid-level clouds, supported by the comparisons in former subsections.

Larger differences occur around 240 K. While ISCCP shows a broader distribution with smaller frequencies, the model simulation reveals a sharp peak of high frequencies at 240 K. This suggests

a more uniform cloud distribution with similar probabilities for the occurrence of clouds over a large height range in the ISCCP observations. Around 240 K clouds are overestimated in the model simulation. This is consistent with findings from the cloud top pressure comparison, that the model tends to overestimate the area coverage of high level clouds in a narrow height range due to the coarse vertical resolution, while highest clouds occur in the ISCCP observations.

The histogram of the blocking case shows a much smaller temperature range for the ECHAM4 simulation and the satellite observations, because the selected region is dominated by low-level clouds. The general shape and maximum frequency of the two representations are in good agreement. Nevertheless, the peak occurs at 280 K in the model simulation instead of 270 K in the observations. This difference is caused either by higher surface temperatures or by lower cloud heights in the model simulation. Since the temperature changes of the ocean surface are small, it is more likely, that the shift is caused by differences in the representation of clouds. This assumption is supported by the cloud top pressure comparison, where ISCCP systematically observed higher cloud tops.

In an evolution histogram of the brightness temperature  $T_{Br}$ , fractions of the total numbers of picture elements within each temperature class are plotted as a function of time (Morcrette, 1991a). Figure 4.30 compares the evolution histogram of the CLAUS observation with the adjusted model simulation for the blizzard case. The CLAUS data is used, because it avoids the problems caused by storing the data as integer counts.

Plotted is a logarithmic representation of the probability of the occurrence of clouds.

$$K = \frac{\log(thist)}{\log(2)} \quad (4.5)$$

with “*thist*” being the frequency distribution in the chosen region at one time step (as in Figure 4.29). Since the sum of the frequencies in all brightness temperature bins at one time step equals to 1 and  $\log(1) = 0$ , negative values occur. The scaling with  $\log(2)$  leads to a doubled probability with an increase by one unit.

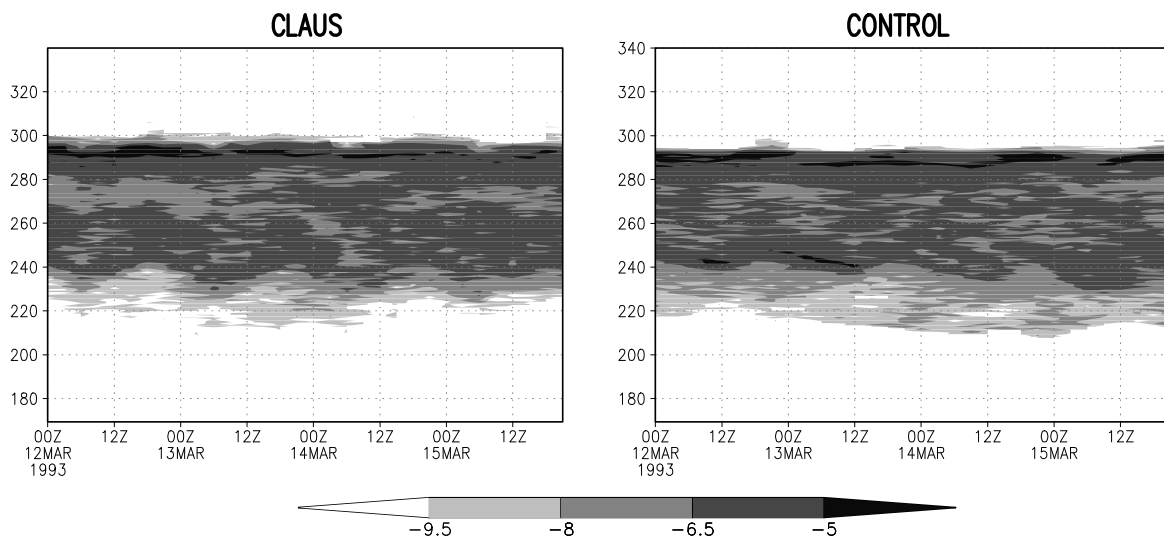


**Figure 4.30:** Evolution histogram of the brightness temperature  $T_{Br}$  [K] from the 12th to 15th of March 1993. The plotted unit is a measure of the probability of the occurrence of clouds in the temperature bin. An increase by one unit corresponds to a doubled occurrence probability.

The model results and the observations are similar, an encouraging result if one bears in mind that moisture is not adjusted in the ECHAM4 simulation. Both datasets show a large variability, temporally as well as in cloud height. The large values on the warm side of the histogram are

mainly the representation of the surface temperature variability, in which no diurnal cycle is visible. In the model simulation stronger noon peaks occur compared to the CLAUS dataset in later times of the observed period, either related to differences in the surface temperature variability or to a stronger diurnal cycle of low-level clouds with larger cloud amounts during daytime and smaller during night.

A second region of large cloud amounts in the model simulation and in the satellite observations is the upper troposphere in the  $T_{Br}$  region around 240 K. The development of the extratropical cyclone is associated with a strong diurnal cycle of upper-tropospheric clouds. It is well represented in the model simulation, although the amplitude is underestimated compared to the satellite observations. This is true for changes of the temperature as well as for the probability of the occurrence of clouds. The model clouds are more uniformly centred around 240 K and the diurnal changes of the probability are smaller. The latter supports the assumption that the sedimentation of ice crystals is underestimated in ECHAM4. This is also indicated by the occurrence of higher clouds in later stages of the development. In the observations on the other hand, the dissipation of the storm is clearly seen as decreasing probability of the occurrence of high-level clouds and a weakening diurnal cycle in the second half of the period, again not established in the model simulation

The occurring minimum and maximum temperatures are well simulated by the model indicating that the mean longwave impact of the model clouds is well captured. Nevertheless the model cloud cover in the lowest  $T_{Br}$  range is slightly higher, while the lowest absolute temperatures occur in the CLAUS dataset, especially in the mature stage of the development. This is consistent with the findings of the cloud top pressure comparison.

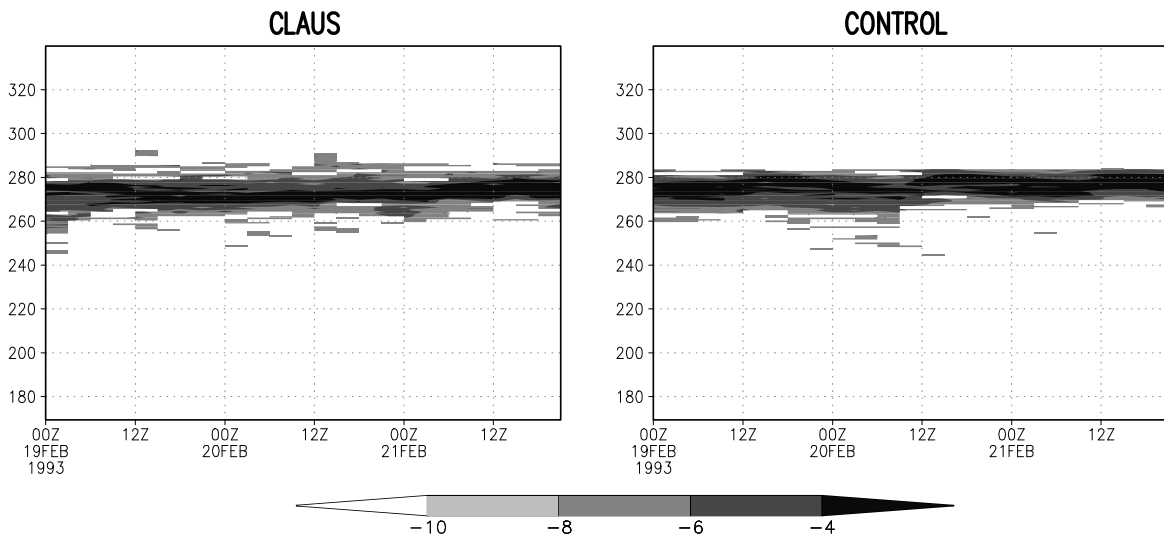


**Figure 4.31:** Same as Figure 4.30 but for the blocking case.

Figure 4.31 does the same comparison for the blocking case. Since the investigated region is much smaller and contains neither many land points nor many clouds in middle and upper levels, the histogram is dominated by a strong peak located between 280 and 260 K. This is true for the observation as well as the model simulation. However, differences between the two representations occur.

The observed temperature range is slightly larger in the CLAUS observation. The higher probabilities on the cold side of the histogram are the result of temporally occurring mid-level clouds, which are stronger represented in the observation than in the model simulation. At the same time CLAUS shows a larger scattering on the warm side of the broad peak, caused by the higher variability of the measured skin temperatures. Both differences lead to a stronger, more uniform peak in the model simulation. In addition, ECHAM4 shows a slightly stronger diurnal cycle

than observed. Since the variation of the surface temperature is small in the model simulation, this difference in  $T_{Br}$  is likely caused by differences in the representation of low-level clouds.

## 4.4 Summary of the cloud validation

In this section the representation of the 3D cloud distribution has been validated against observational data, mostly ISCCP DX satellite data. In contrast to the standard method of comparing monthly mean fields of cloud liquid water or cloud cover, the cloud properties for distinct synoptic situations have been compared. To enable the validation against single synoptic situations, the model dynamics are relaxed to ECMWF reanalysis fields using a dynamical adjustment based on the Newtonian relaxation technique (nudging). As case studies a blocking situation over the North Atlantic and the development of an extratropical cyclone along the East Coast of the U.S.A. have been selected for the validation. A third situation, convection in the tropical western Pacific, has been neglected since the used adjustment approach did not force the small-scale tropical circulation to the observed track.

In the following schematic illustration (Figure 4.32) the main differences between the model simulation and the ISCCP observations are presented together with possible causes for the model errors in the upper part of the Figure. The lower part contains possible changes in the physical parameterization schemes which might be able to reduce the model errors. This lower part of the schematic represents the line of approach for the next chapter in which sensitivity studies, including some of the changes, are performed to confirm or reject the suggested causes for the model errors.

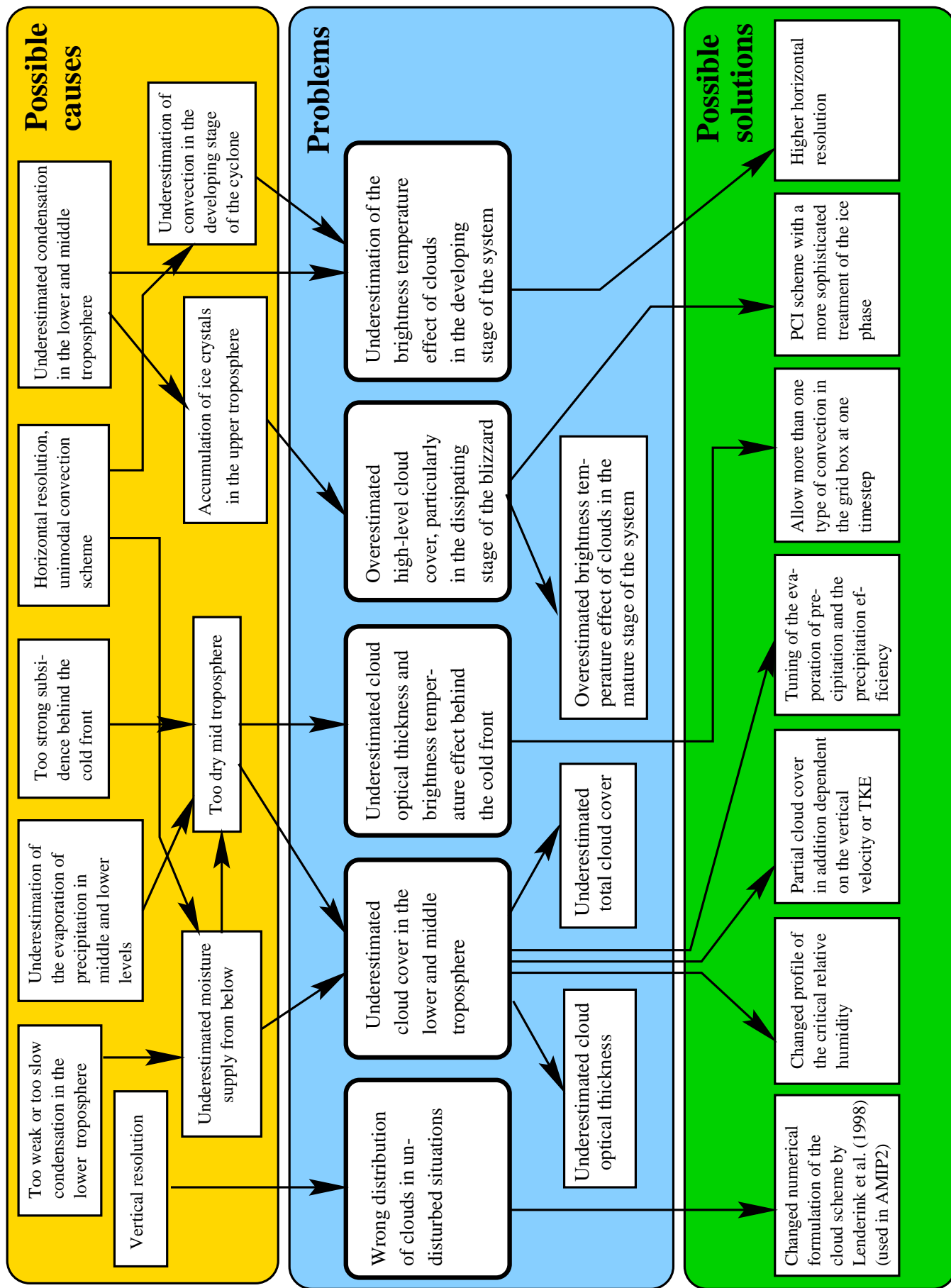


Figure 4.32: Schematic illustration of the results of the cloud validation.

# Chapter 5

## Sensitivity studies

### 5.1 Introductory remarks

The sensitivity studies, described in the following sections, are carried out to confirm or reject the suggestions for the causes of the model errors posed in the last section. Furthermore, some experiments contain changes, which will be included into the future model version ECHAM5, while another experiment could help to further improve certain aspects of the cloud parameterization.

In a first experiment the standard stratiform cloud scheme is replaced by the newer, more sophisticated scheme PCI, by [Lohmann and Roeckner \(1996a\)](#). It treats cloud liquid water and cloud ice with two different prognostic equations including more physical processes compared to the standard scheme. A developed version of the PCI scheme used here is part of the upcoming new model version ECHAM5.

In a second experiment the vertical profile of the "critical relative humidity" is changed in the standard stratiform cloud scheme. It determines the partial cloud cover within the grid box and therefore the onset of condensation. It is changed with the intention to increase the amounts of low and mid-level clouds and to impede condensation in the upper troposphere. This would lead to a better agreement with ISCCP observations.

In the third experiment the new advection scheme "SPITFIRE"<sup>1</sup> ([Rasch and Lawrence, 1997](#)) is tested, again an important component of the new model version ECHAM5. The fourth experiment is a simulation using the changes with respect to AMIP2<sup>2</sup>. Of the many changes included for that experiment, some directly influence the representation of clouds in the model.

Apart from SPITFIRE the experiments are carried out for the two investigated synoptic situations. For SPITFIRE only an experiment with the blizzard case has been carried out, because it is expected that the changed advection influences mainly regions with strong temperature and moisture gradients.

All investigations are carried out in the T106 horizontal resolution. Furthermore, they are started a few days in advance of the developing system, so that the atmosphere can reach the new balanced state. In section 5.2 the changes introduced by the experiments are described, while section 5.3 contains results of the comparisons with the CONTROL simulation.

To be able to illustrate the effects of the experiments on a variety of quantities for both synoptic systems, the comparison is restricted to one time step for the blocking case. This is no problem,

---

<sup>1</sup>SPITFIRE = SPlit Implementation of Transport using Flux Integral REpresentations

<sup>2</sup>AMIP2 = second Atmospheric Model Intercomparison Project

since the system remains stationary for several days. For the highly variable extratropical cyclone, investigated in the blizzard case, the information loss would be too large if only a single time step is used. Therefore the comparison is performed for the latter two time steps used for the validation of the CONTROL simulation in the last chapter, allowing a coarse assessment of changes in the temporal representation of the blizzard.

## 5.2 Description of the experiments

### 5.2.1 PCI - A new stratiform cloud scheme

The accurate distribution of liquid water and ice in clouds is very important, because water and ice interact differently with both longwave and shortwave radiation. Furthermore their precipitation efficiency is different. In addition, the condensed water content and how it is apportioned to droplets or ice crystals within clouds, governs the extent and nature of chemical reactions within clouds, and ultimately, how efficiently chemical species are removed from the atmosphere (Twohy et al., 1997).

In the standard ECHAM4 scheme cloud liquid water and cloud ice are calculated with one prognostic equation. The scheme was described in detail in section 2.1.2.. In the new parameterization (Lohmann and Roeckner, 1996a) two separate prognostic equations for cloud liquid water and cloud ice are used, avoiding the diagnostic separation between them.

$$\frac{\partial q_{cl}}{\partial t} = R(q_{cl}) + b \left( Q_{cnd}^c - Q_{aut}^c - Q_{racl}^c - Q_{sac}^c - Q_{frh}^c - Q_{frs}^c + Q_{mlt}^c \right) + (1 - b) Q_{cnd}^0 \quad (5.1)$$

$$\frac{\partial q_{ci}}{\partial t} = R(q_{ci}) + b \left( Q_{dep}^c - Q_{agg}^c - Q_{saci}^c + Q_{frh}^c + Q_{frs}^c - Q_{mlt}^c \right) + (1 - b) Q_{dep}^0 \quad (5.2)$$

The microphysical processes are:

- $Q_{cnd}^c$ : Condensation of water vapour and evaporation of cloud water.
- $Q_{aut}^c$ : Autoconversion of cloud droplets to rain.
- $Q_{racl}^c$ : Accretion of cloud droplets by rain.
- $Q_{sac}^c$ : Accretion of cloud droplets by snow.
- $Q_{frh}^c$ : Homogeneous freezing.
- $Q_{frs}^c$ : Heterogeneous freezing.
- $Q_{mlt}^c$ : Melting of ice crystals.
- $Q_{dep}^c$ : Deposition of water vapour onto ice crystals and sublimation of ice crystals.
- $Q_{agg}^c$ : Aggregation of ice crystals to snow flakes.
- $Q_{saci}^c$ : Accretion of ice crystals by snow.
- $Q_{cnd}^0$ : Evaporation of cloud water transported into the cloud-free part of the grid box.
- $Q_{dep}^0$ : Sublimation of cloud ice transported into the cloud-free part of the grid box.

In each case the superscript  $c$  represents the process in the cloudy part of the grid box, while 0 represents the process in the cloud-free part of the grid box.

The other main difference between the two schemes is that in the PCI scheme the autoconversion rate from cloud droplets to rain not only depends on the cloud liquid water but also on the number of cloud droplets  $N$  and the width of the droplet spectra. This allows a coupling of the cloud scheme with an aerosol scheme.

### 5.2.2 Vertical profile of the critical relative humidity

The critical relative humidity  $r_0$  is an important quantity used in the stratiform cloud scheme. It determines the partial cloud cover and therefore the condensation in a grid box. In the standard scheme it is an exponential profile depending on height and thermal stability of the atmosphere (see equations (2.18) to (2.20)).

The cloud validation has revealed that ECHAM4 simulates too little cloud amounts in the lower and middle troposphere and too large values in upper levels. To reduce these errors the standard exponential profile has been replaced by a third order polynomial profile following Geleyn (1980). It is calculated using the following equation.

$$r_0 = 1 - (a\sigma) \cdot (1 - \sigma) \cdot (1 + b(\sigma - 0.5)) \quad (5.3)$$

with  $\sigma = \frac{p}{p_s}$ ,  $p$  = level pressure,  $p_s$  = surface pressure and  $b = \sqrt{3}$ . While Geleyn (1980) used  $a = 2$  in his experiments it is changed to  $a = 3$  in this investigation to obtain a more extreme profile. The different profiles are illustrated in Figure 5.1.

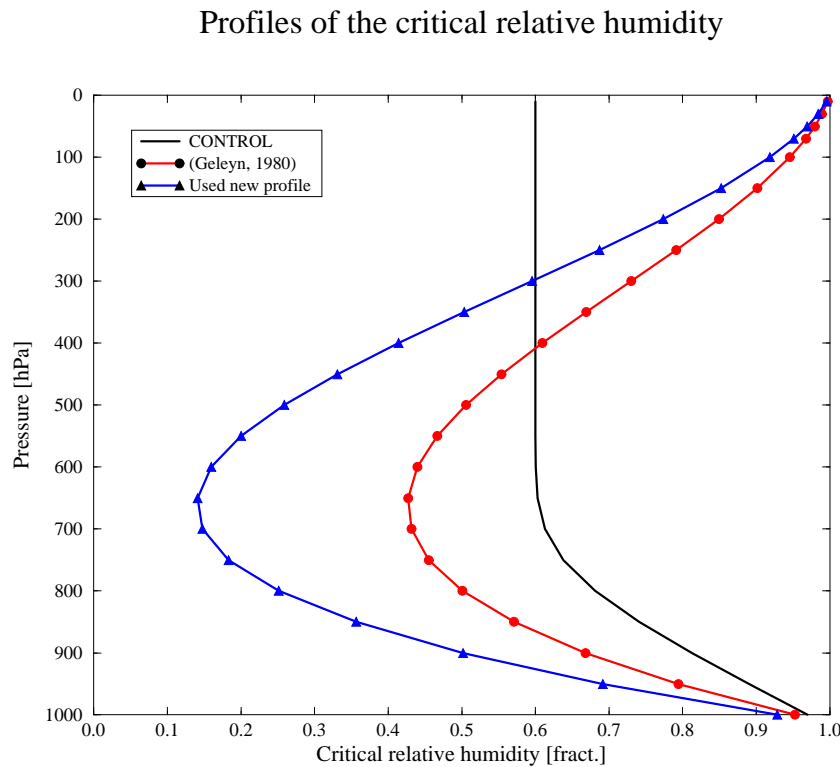


**Figure 5.1:** Vertical profiles of the critical relative humidity of the standard stratiform cloud scheme (no symbols), of the profile suggested by Geleyn (1980) (filled circles) and of the sensitivity study (filled triangles).

As the condensation threshold is reduced in the lower and middle troposphere and enhanced in upper levels, the new profile should lead to larger cloud amounts in lower and middle levels and lower values in the upper troposphere, more in accordance to observations of Walcek (1994). He found that largest cloud amounts at lowest relative humidities occur in the middle troposphere and that cloud amounts of 10 to 20% can occur at relative humidities as low as 20%.

### 5.2.3 Spitfire - A new advection scheme

For the simulation of the spatial and temporal distribution of tracers such as water vapour, cloud liquid water or chemical substances, which are marked by strong horizontal and vertical gradients, it is necessary to use an accurate numerical advection scheme.

Earlier explicit schemes suffered from the so-called "pole problem", namely the schemes become unstable in polar regions where the grid boxes are getting smaller. To stay numerically stable explicit schemes have to fulfill the so-called "Courant-Friedrich-Levy" (CFL) condition.

$$\frac{u \cdot \Delta t}{\Delta x} < 1 \quad (5.4)$$

It demands that during one time step an air parcel is passed through no more than one grid box. This requires short time steps in polar regions.

The spectral approach to transport the dynamical variables used in the older model version ECHAM3 is very good for approximating large-scale, global atmospheric dynamical motion. On the other hand, it has serious deficits in the advection of water vapour, liquid water and short-lived tracers due to occurring truncation errors, manifesting itself as negative mixing ratios (Feichter, 1997).

Furthermore trace gases vary by several orders of magnitude from the equator to the pole and from the surface to the upper troposphere/lower stratosphere. They are continuously forced on smallest scales by sub-grid scale processes in the model and large horizontal as well as vertical gradients occur (Williamson and Rasch, 1994).

For ECHAM4 the spectral method has been replaced by a shape-preserving semi-Lagrangian advection scheme together with a mass fixer, which ensures the conservation of mass during the advection process. Shape preservation provides a non-linear constraint on the scheme to accept and maintain large gradients without admitting over- and undershoots. The scheme has been described in detail in Williamson and Rasch (1989). It does not depend on the CFL condition, which enables the use of longer time steps.

The mass fixer works well for small errors in the mass conservation, but has serious problems to accurately represent tracers with strong vertical concentration gradients, particularly at the top and bottom of the model domain. There it increases the mass significantly, resulting in unrealistic tracer concentrations (Feichter, 1997).

The new "Spitfire" scheme (Rasch and Lawrence, 1997) represents a combination of different ideas to get a multi-dimensional flux form conservative scheme that is shape preserving. It works in the context of a tracer density  $\tilde{\rho} = \rho m$  with the air density  $\rho$  and the tracer mixing ratio  $m$  and is constructed by a series of one-dimensional updates of the conservation equation for the tracer density.

$$\frac{\partial \tilde{\rho}}{\partial t} = - \frac{\partial \tilde{\rho} u}{\partial a} \quad (5.5)$$

with  $a = x, y, z$ . The equation is solved by constructing a primitive function  $\Psi$  following Leonard et al. (1995).

$$\Psi(a) = \int_0^a \tilde{\rho}(a') da' \quad (5.6)$$

The integral is calculated assuming that  $\tilde{\rho}$  represents the mean value within a cell, so that the exact discrete integral at the cell walls  $a_{i+\frac{1}{2}}$  is given as:

$$\Psi\left(\rho, a_{i+\frac{1}{2}}\right) = \Psi\left(\rho, a_{i-\frac{1}{2}}\right) + \tilde{\rho}_i \Delta a_i \quad (5.7)$$

with  $\Psi\left(a_{\frac{1}{2}}\right) = 0$ . The departure point for a particle arriving at each cell wall is defined as

$$a_{i+\frac{1}{2}}^{dp} = a_{i+\frac{1}{2}} - v_{i+\frac{1}{2}} \Delta t \quad (5.8)$$

This allows the calculation of the flux of mass through a cell wall:

$$F(\rho)_{i+\frac{1}{2}} = \Psi\left(a_{i+\frac{1}{2}}^{dp}\right) - \Psi\left(a_{i+\frac{1}{2}}\right) \quad (5.9)$$

and leads finally to the discrete solution of equation (5.5)

$$\tilde{\rho}^n = \tilde{\rho}^o - \frac{\left(F(\rho)_{i+\frac{1}{2}} - F(\rho)_{i-\frac{1}{2}}\right)}{\Delta a_i} \quad (5.10)$$

Because the departure points are not located at the grid point, an interpolation is required.

This one-dimensional solution of the scheme is extended to multi-dimensions. The horizontal transport is obtained by toggling east-west and north-south updates at every other time step using the following three steps.

1. The fluxes in direction  $a$  are calculated using equation (5.9). Furthermore an advective update to the density is calculated that represents the solution of the advection equation (5.5) and neglects the divergence term.

$$\tilde{\rho}^x = \tilde{\rho}^o - \frac{\left(F(\rho)_{i+\frac{1}{2}} - F(\rho)_{i-\frac{1}{2}}\right)}{\Delta a_i} + \Delta t \rho^o \frac{u_{i+\frac{1}{2}} - u_{i-\frac{1}{2}}}{da} \quad (5.11)$$

2. Then the fluxes in the other direction  $b$  ( $G(\rho^x)$ ) are calculated using the provisional advection density  $\tilde{\rho}^x$ . These fluxes are called  $G(\rho^x)$ .
3. Finally the horizontal solution is updated with

$$\tilde{\rho}_{i,j}^n \Delta a_i \Delta b_j = \tilde{\rho}_{i,j}^o \Delta a_i \Delta b_j - \left[F(\rho^o)_{i+\frac{1}{2}} - F(\rho^o)_{i-\frac{1}{2}}\right] - \left[G(\rho^x)_{j+\frac{1}{2}} - G(\rho^x)_{j-\frac{1}{2}}\right] \quad (5.12)$$

where  $i, j$  are the indices in the direction  $a, b$  respectively.

Because of the operator splitting and the large time step solution the result is shape preserving, but not strictly monotonic. In practice this may result in problems occurring near the pole.

#### 5.2.4 AMIP2 - A step forward to the new model version ECHAM5

AMIP2 contains many changes compared to the standard ECHAM4 model. It is to be expected that many of them do not influence the representation of the systems investigated here. Such modifications are a changed calendar to a year with 365 days, included solar orbital parameters or new climatologies for ozone, sea ice and SST. More important are the following changes:

- Replacement of the explicit surface scheme by an implicit one (Schulz et al., 1999).
- Changed numerics in the large-scale condensation scheme by Lenderink et al. (1998).
- More accurate formulation of the saturation water vapour pressure (Sonntag, 1994).
- Changed values for some of the tuning parameters in the stratiform cloud scheme.
- Small changes in the convection scheme.

The new implicit surface scheme (Schulz et al., 1999) might induce a large influence on the simulations, but at least half a year is necessary for the model to reach a new balanced state of the surface parameters as for example ground water. Since the simulations used here are not longer than 3 months, it is to be expected that the influences of the implicit surface scheme are also small.

The changes in the stratiform condensation and in the convection scheme are the most important for this thesis and are described in more detail. The performance of the standard stratiform condensation scheme appears to be strongly dependent on the temporal and spatial resolution which is used. The cause for this behaviour can be traced back to the use of so-called “provisional values” (values at the previous time step updated with the increments due to vertical diffusion, advection and radiation) for the prognostic variables (Lenderink et al., 1998). They are used for the calculation of the cloud cover  $b$  and the changes in the saturation specific humidity  $\frac{\partial q_{sat}}{\partial t}$ , which are then used in the calculation of the large-scale condensation and evaporation. Even with relatively short time steps large differences can occur between the provisional values and the value at the previous time step, caused by large tendencies generated in the turbulence scheme, which are compensated by the condensation scheme (Lenderink et al., 1998).

The new approach by Lenderink et al. (1998) is based on the same formalism as used in the standard scheme, but includes three important modifications, mainly on the level of the numerical implementation of the scheme.

- The cloud cover  $b$  is now based on the consistent fields of the previous full time step.
- The change in saturation specific humidity is now calculated from a linearization around the consistent state of the previous full time step. Evaporation of cloud water  $C^e$  in clear air is also taken into account.
- No negative evaporation ( $C^e \leq 0$ ) in the cloud free part of the grid box is allowed.

According to Lenderink et al. (1998) those changes lead to the cloud cover being almost insensitive to the temporal as well as horizontal resolution, which leads to significant improvements in 3D simulations.

Other changes in the stratiform condensation scheme are a more accurate calculation of the saturation water vapour pressure (Sonntag, 1994) and different values for some of the tuning parameters. They influence the precipitation rate, the sedimentation of ice-crystals, the evaporation of precipitation and the profile of the “critical relative humidity”. The changes have strong influences on the representation of clouds in the tropics, whereas midlatitudes and polar regions are weaker influenced (Roeckner, 1999).

The effects of the changed tuning parameters are not confined to the stratiform cloud scheme. This is illustrated with the parameter “ $zrtc$ ”, which is the critical relative humidity in the upper troposphere. It is slightly increased from 0.6 to 0.7 for AMIP2, which slows down the development of clouds in the upper troposphere. A later development of convective clouds is associated with a stronger heating of the surface due to longer solar irradiance. Since the heating of land surfaces is much stronger as compared to ocean surfaces, the convection over tropical land surfaces is enhanced. This is associated with stronger compensating subsidence suppressing convection over tropical oceans. Thus, the small change of the critical relative humidity changes the distribution of the tropical convection persistently, more in accordance with observations (Roeckner, 1999).

In the convection scheme only small changes are included. An error has been fixed in the calculation of the evaporation of precipitation and two physical constants has been changed. One of them, the parameter which determines the minimum depth of a convective cloud required for the development of precipitation, has been doubled over land. Together with the implicit coupling

of the land-surface temperature and the changes of the tuning parameters in the stratiform condensation scheme, this leads to a much better represented monsoon circulation in the AMIP2 climate simulation. Furthermore the behaviour of detrainment is slightly changed. While in the standard ECHAM4 version only 10 % of the detraining mass reach the level above the detraining layer, this value is changed to 33 % for the AMIP2 simulation.

## 5.3 Results of the experiments

### 5.3.1 Introductory remarks

The experiments reveal virtually no changes on the representation of the large-scale dynamics. This is clearly seen by comparing the development of the equivalent potential temperature (not shown). On the other hand systematic differences occur in the representation of cloud related processes. In the following subsections the effects of the different sensitivity studies on cloud cover, cloud water path (CWP), cloud optical thickness, detrainment, precipitation efficiency and brightness temperature are discussed.

### 5.3.2 Cloud cover

Figures 5.2 and 5.3 compare the total cloud cover of the CONTROL simulation and the sensitivity experiments with ISCCP satellite observations. In general, the CONTROL simulation, as well as the sensitivity experiments, underestimate total cloud cover. Largest differences occur behind the cold front, where dry air from higher levels is mixed downward. Here the threshold approach for the calculation of the partial cloud cover (“critical relative humidity”), together with an underestimated convective activity and vertical advection of moisture, prevent a more realistic development of cloud cover. Another general feature is that all experiments are capable of simulating overcast sky in the region of the large-scale ascent in the mature stage of the development (upper row of Figures 5.2 and 5.3), while larger differences occur along the cold front. In the dissipating stage (lower row) on the other hand, the cold front is similarly simulated by the different experiments, whereas larger differences occur in pre-frontal regions in northern parts of the cold front and the large-scale ascent.

The best representation of frontal cloud cover compared to the observation is found in the AMIP2 simulation. Here persistent overcast sky is simulated along the fronts in both stages of the development. The only remarkable difference to ISCCP is again the dry slot behind the cold front. But even here indications for larger cloud amounts are found compared to the other experiments. Smallest differences occur between the CONTROL and the SPITFIRE simulation.

The RHCRIT and the PCI experiment simulate generally larger cloud amounts in regions not directly influenced by the developing cyclone, as for example to the east of the cold front in the warm sector of the system. At the same time the changes in frontal regions are smaller. This indicates a stronger development of clouds in lower levels of the troposphere and smaller effects at higher levels. In the upper troposphere no changes occur in the RHCRIT experiment, indicated by an unchanged representation of pre-frontal cirrus clouds, while they are clearly reduced in the PCI simulation. The former is remarkable, because the profile of the critical relative humidity has been changed in a way that it should reduce upper-level clouds.

Figure 5.4 shows the relative humidity in the CONTROL simulation and the differences to the RHCRIT experiment. It is clearly seen that no changes in upper-tropospheric relative humidity occur. Furthermore the values are lower than the critical relative humidity (Figure 5.1) and should actually lead to a dissipation of clouds. This suggests that the cloudiness in the upper troposphere is mainly influenced by the strength of the moisture sink, namely the sedimentation

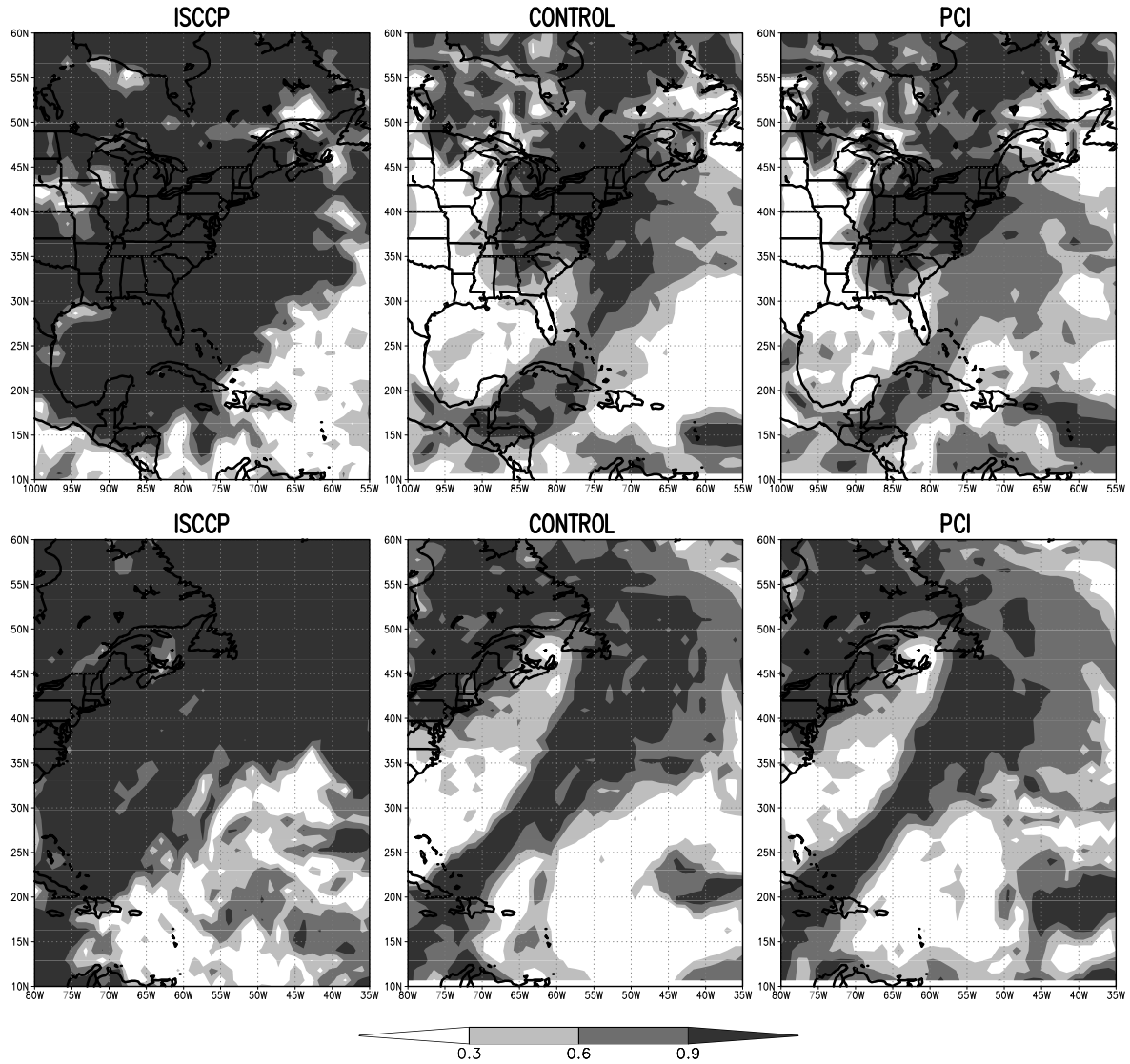


**Figure 5.2:** Total cloud cover [fract.] of the ISCCP observation, the CONTROL simulation and the PCI experiment for the mature (18Z, 13th of March 1993, upper row) and dissipating stage (18Z, 14th of March 1993, lower row) of the developing cyclone along the East Coast of the U.S.A..

of ice crystals, than by the condensation threshold. An underestimation of the sedimentation of ice crystals would therefore lead to an accumulation of ice and a slower removal of clouds in the upper troposphere despite the changed profile of the critical relative humidity.

The reduction of pre-frontal cloud amounts in the PCI simulation is particularly true in the dissipating stage of the development. There are two possible explanations for this behaviour. Firstly, the more sophisticated treatment of ice crystals might lead to a more efficient removal of cloud ice due to the larger amount of processes included. While the direct sedimentation is the main sink for ice crystals in the CONTROL simulation, this is achieved by a stronger precipitation development over the ice phase in the PCI scheme, where a direct sedimentation is not defined. Secondly, a stronger development of clouds or a stronger precipitation efficiency in lower and middle levels of the troposphere might remove the moisture before it reaches higher levels. The 3D distributions of clouds and moisture and its temporal characteristics, which will be investigated further below in this section, might clarify this point.

Figure 5.5 compares the representation of the total cloud cover for one time step during the blocking situation. No simulation of the blocking case with SPITFIRE has been performed,

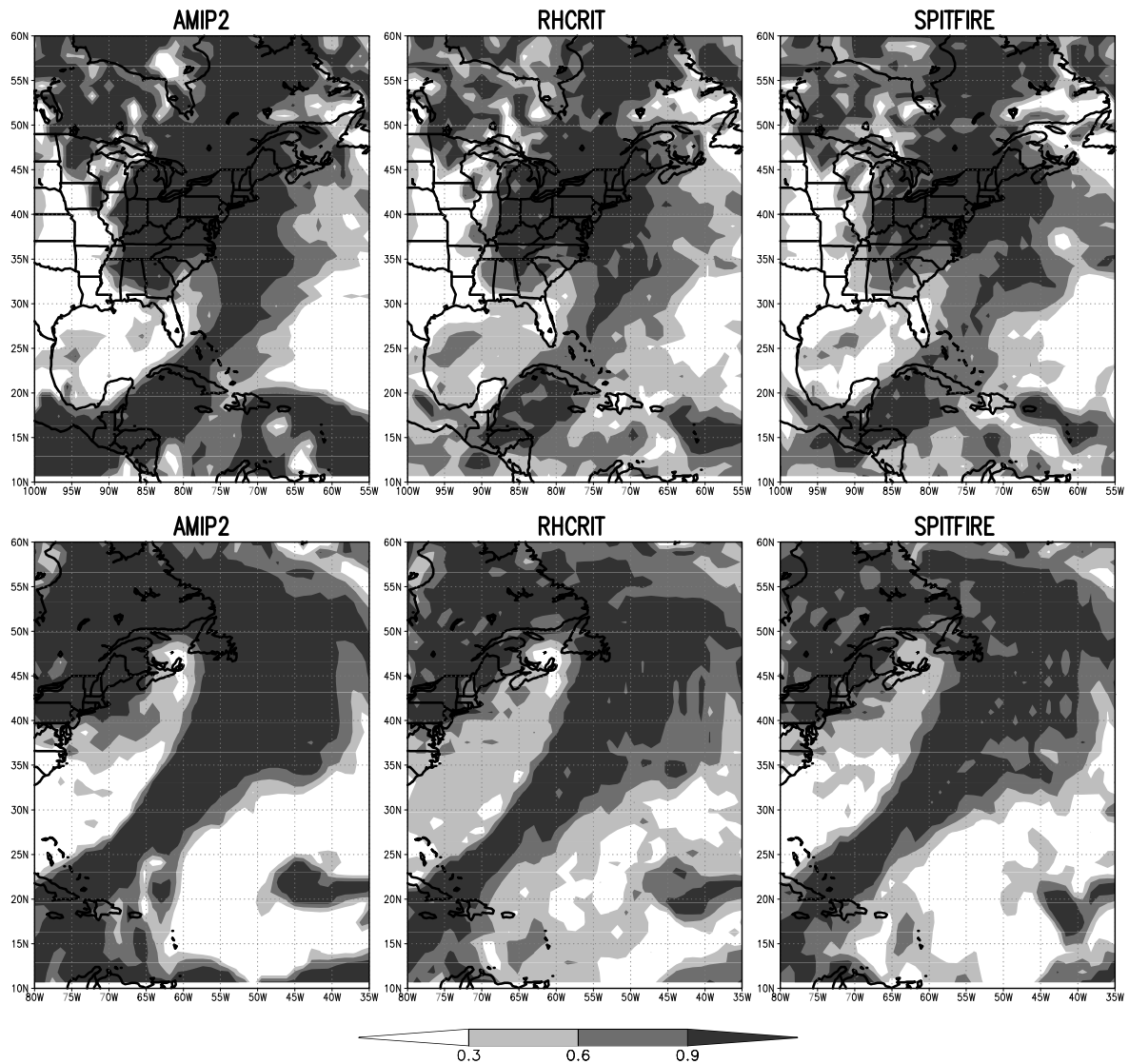


**Figure 5.3:** Same as Figure 5.2 but for the AMIP2, RHCRT and SPITFIRE experiment.

because the effect of the changed advection is expected to be small in this case of weaker gradients of temperature and moisture. The other three simulations improve the cloud distribution compared to the ISCCP observations. By far the best representation is found in the RHCRT experiment, where the overall cloud distribution is surprisingly well reproduced. Nevertheless, in the region with broken cloud cover to the west of the blocking high, the cloud amounts are overestimated, while the frontal structure over western Europe is more weakly represented in the RHCRT simulation as compared to ISCCP. Nevertheless, RHCRT shows the best represented front over western Europe of all simulations.

PCI and AMIP2 show larger deficits, although they also improve the representation compared to the CONTROL simulation. In the AMIP2 simulation the cloud band surrounding the block is well represented. However, as in the RHCRT simulation, the front over western Europe is underestimated. Furthermore, clear sky regions occur where the satellite has observed overcast sky. Possible causes are that stronger condensation in the surrounding front reduces the moisture in downwind regions, so that the threshold relative humidity is not exceeded or additionally induced downward motions. In the PCI simulation no such regions of strongly underestimated cloud cover are simulated, but the cloud amounts in the overcast region in central and eastern parts of the high and in the surrounding cloud band are underestimated.

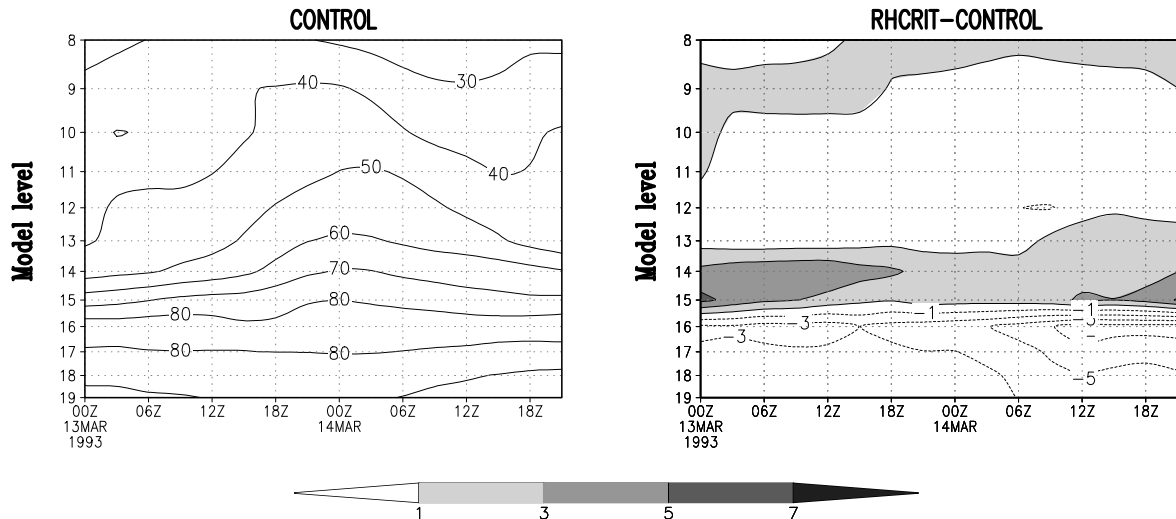


**Figure 5.4:** Time height section of the relative humidity [%] of the CONTROL simulation (left) and difference RHCRIIT-CONTROL (right). In shaded regions the relative humidity is higher in the sensitivity experiment while it is lower in contoured regions. Contours are drawn for: -7, -5, -3, -1, 1, 3, 5 and 7% [level 15  $\approx$  850 hPa; level 11  $\approx$  500 hPa; level 8  $\approx$  250 hPa]

Further insight into the effects of the different experiments on cloudiness is gained by a comparison of cloud amounts in the three different cloud layers of the troposphere. From the partial cloud amounts at the distinct model levels the layer cloud amounts are calculated using the same overlap assumption as used for the calculation of total cloud cover, namely maximum overlap for adjacent levels and random overlap in other cases. Table 5.1 compares the different cloud levels as they are defined in ECHAM4 and a meteorological textbook (Liljequist and Cehak, 1994). Figures 5.6 and 5.7 compare the cloudiness in the three layers for the different experiments.

Cloud layer	ECHAM4	Liljequist & Cehak
lower	- 750 hPa	- 2 km
middle	730 - 450 hPa	2 - 7 km
upper	440 - 50 hPa	7 - 13 km

**Table 5.1:** Definition of the three cloud layer in the ECHAM model and a definition taken from Liljequist and Cehak (1994).

It is important to note that this method misinterprets deep cumulus clouds (e.g. cumulonimbus). The WMO classification of the different cloud types into the three cloud layers is done by means of the height of the cloud base. Therefore, thick cumulus clouds are per definition low-level clouds. Here on the other hand, their contribution to the three cloud layers is calculated. Therefore it is not possible to compare the results to observations from surface stations. However, the cloudiness at the different cloud layers is calculated in the same way for each experiment, enabling a comparison of the model representations.

In general, low-level cloud amounts are enhanced along the fronts in all experiments. In addition, the PCI and the RHCRIIT experiment simulate larger cloud amounts in the lower troposphere in the warm sector of the cyclone compared to the CONTROL simulation and the other two sensitivity experiments. Over the cold continent to the north and west of the developing system, no changes occur in the PCI simulation, while cloud cover is increased in the RHCRIIT experiment. Since the condensation is the same in PCI and CONTROL, a reason for larger low-level cloud cover in undisturbed situations is a moister lower troposphere in the PCI simulation (Lohmann, 1999). This is confirmed by larger specific humidities as compared to the CONTROL simulation. Figure 5.8 shows Hovmöller diagrams of the vertical distribution of the specific humidity,

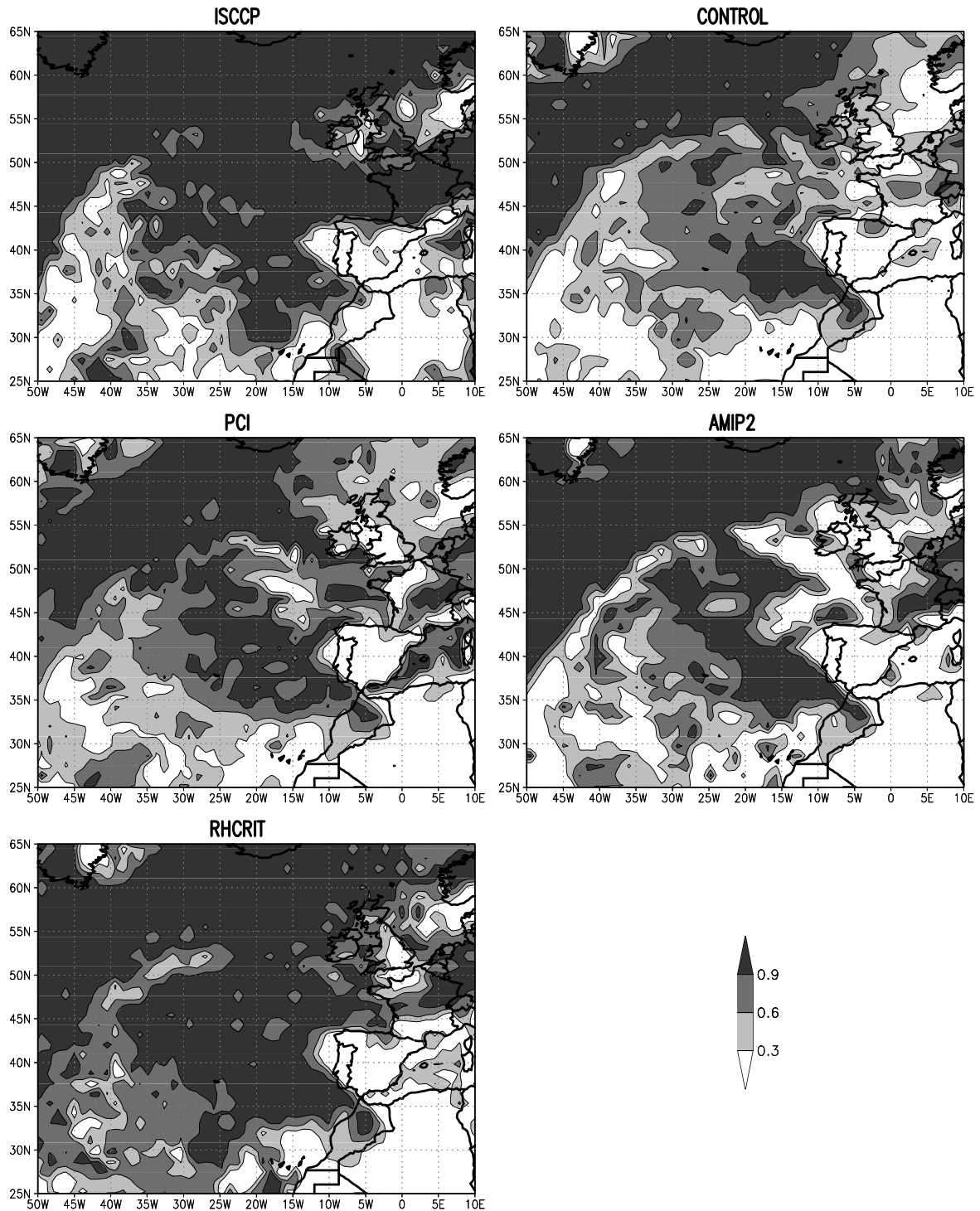


**Figure 5.5:** Same as Figure 5.2 but for one time step of the blocking case (12Z, 19th of February 1993).

average over a region  $20^\circ$  by  $20^\circ$ , in the blizzard case. While the boundary layer is generally moister in the PCI simulation, this is the case in the whole troposphere during the strongest development of the system.

Larger values of the specific humidity are associated with larger relative humidities, because the adjusted temperature does not change. This explains the larger cloud amounts in the lower troposphere in the PCI simulation. The presence of a moister atmosphere in which clouds are developed and evaporated more frequently without precipitating is furthermore supported by

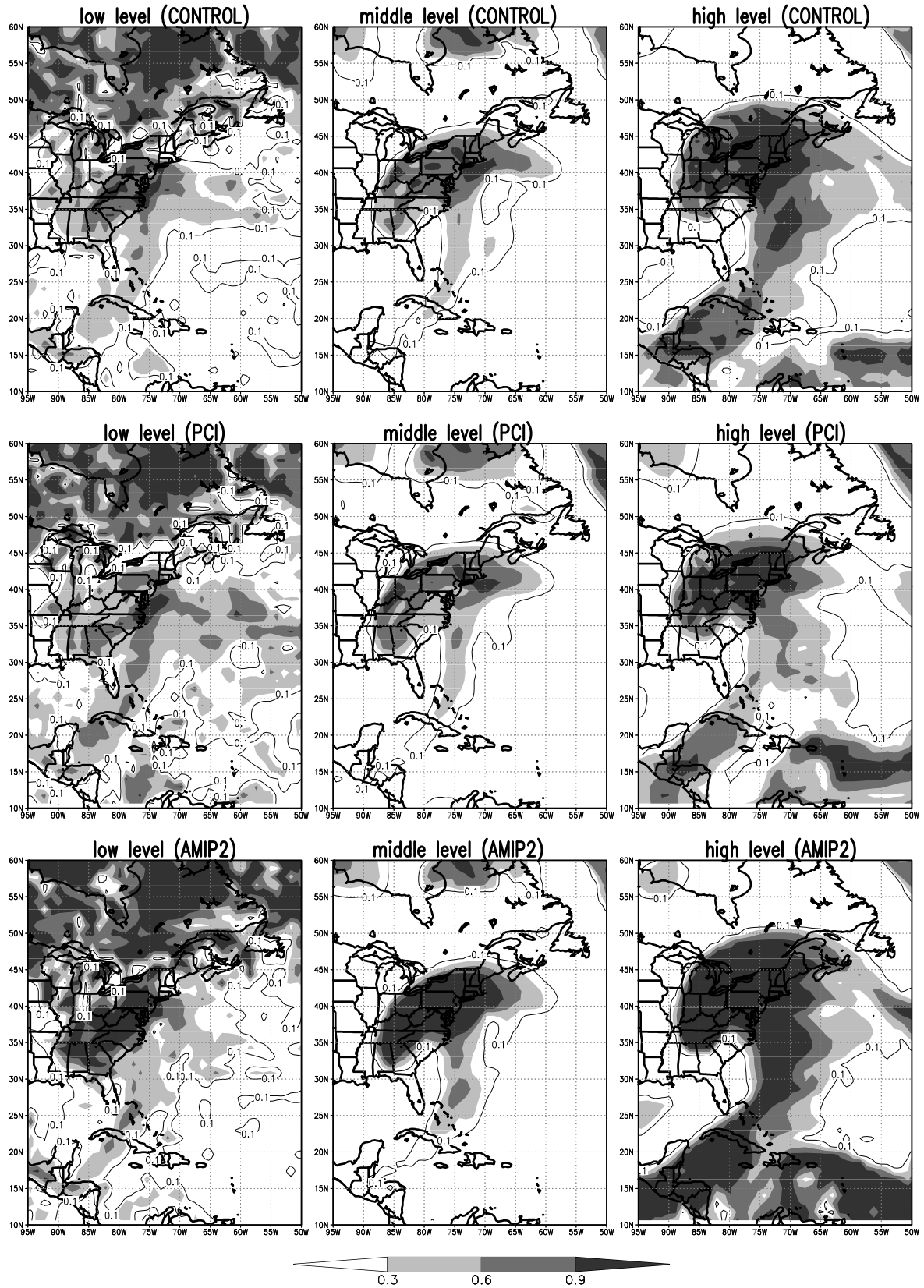


**Figure 5.6:** Cloud cover [fract.] in the three cloud layers of the troposphere of the CONTROL simulation (upper row), the PCI experiment (middle row) and the AMIP2 experiment (lower row). [00Z 14th of March 1993].

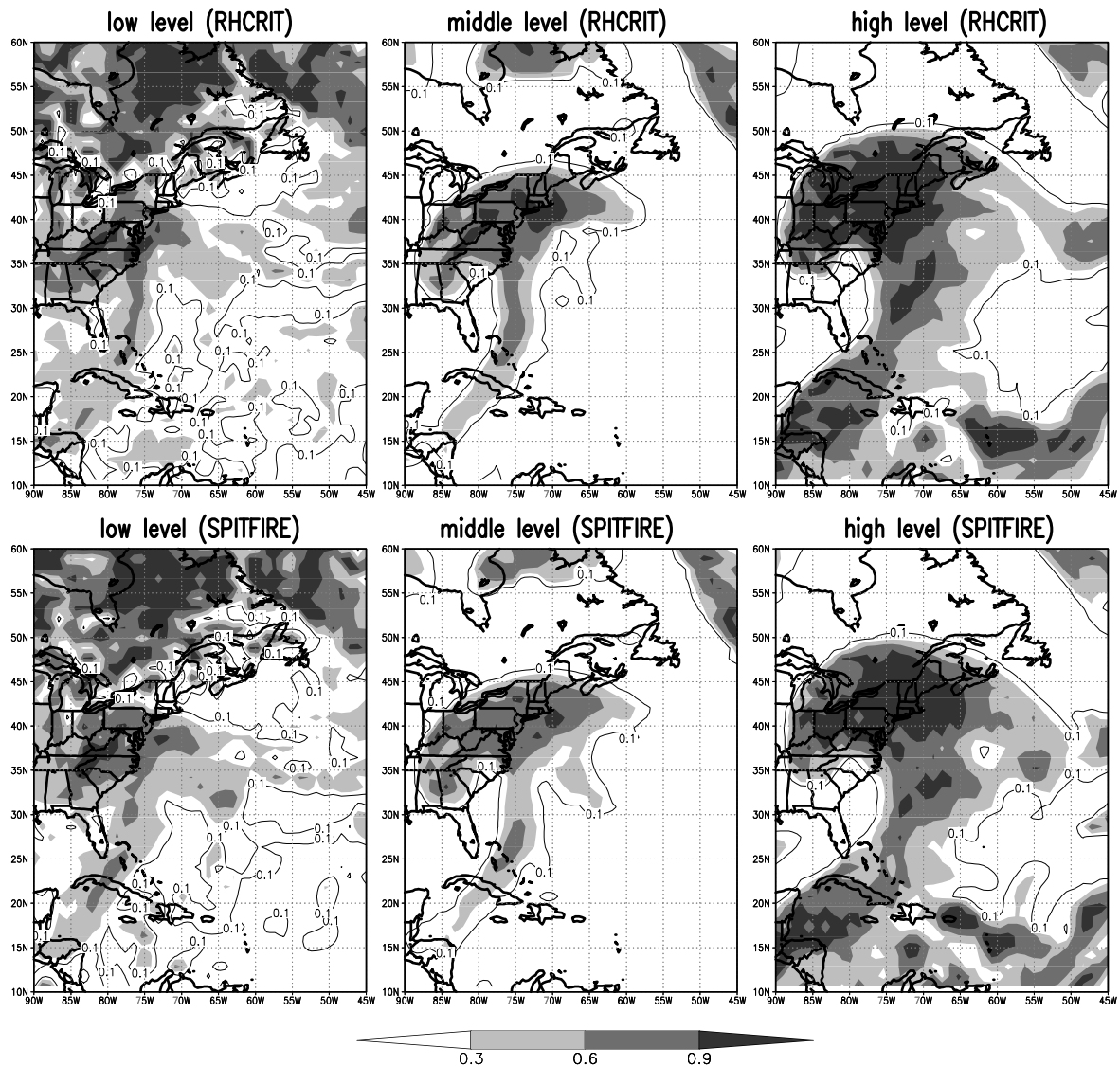


**Figure 5.7:** Same as Figure 5.6 but of the RHCrit (upper row) and the SPITFIRE (lower row) experiment.

larger amounts of cloud water at those levels (Figure 5.9). Another systematic difference of the PCI experiment is that it simulates a broader cold front in the lower troposphere as compared to the other simulations, again a consequence of the moister lower troposphere.

The stronger low-level cloud amounts even over the cold continent stress the more general changes induced by the modified profile of the critical relative humidity in the RHCrit experiment. Furthermore, a sharper cold front is simulated with a better represented reduction of the cloudiness in the post-frontal subsidence. In upwind regions of the large-scale ascent higher cloud amounts are simulated in the PCI and RHCrit experiments compared to the CONTROL simulation, SPITFIRE and AMIP2. This again underlines the stronger (faster) cloud development in lower levels in both experiments.

SPITFIRE and AMIP2 on the other hand simulate larger cloud amounts in frontal regions rather than in surrounding areas. The direct comparison between the two experiments reveals that SPITFIRE uniformly enhances the cloud amounts along the cold front, especially in the southern part, while AMIP2 strongly enhances the cloud amounts in the regions of the large-scale ascent over the cold continent. This illustrates that the changed advection is especially important in regions dominated by the convection scheme and supports the assumption that

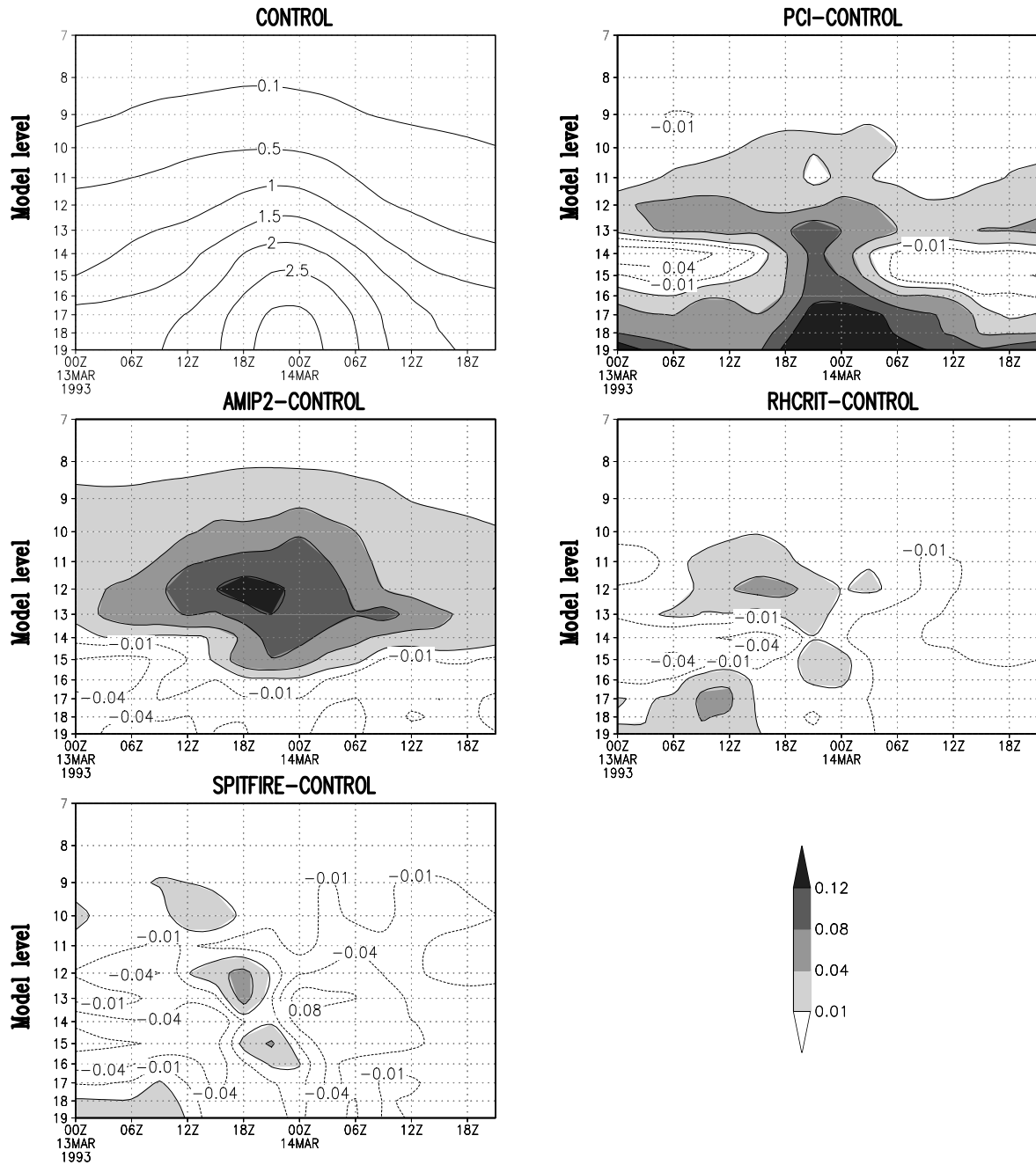


**Figure 5.8:** Height-time section of the spatially averaged specific humidity [ $gkg^{-1}$ ] in the blizzard case of the CONTROL simulation (upper left) and differences to the sensitivity studies. In shaded regions of the difference plots larger values occur, while lower values are simulated in contoured regions. Contours are drawn for  $-0.08$ ,  $-0.04$ ,  $-0.01$ ,  $0.01$ ,  $0.04$ ,  $0.08$  and  $0.12 gkg^{-1}$ . The region used for the average is  $85^{\circ}W$  to  $65^{\circ}W$  and  $35^{\circ}N$  to  $55^{\circ}N$ . [level 15  $\approx$  850 hPa; level 11  $\approx$  500 hPa; level 8  $\approx$  250 hPa]

SPITFIRE will only weakly influence the cloud development in the blocking case. AMIP2 on the other hand introduces numerical changes by Lenderink et al. (1998) into the stratiform condensation scheme. Due to the use of the prognostic variables at the previous full time step instead of the provisional values, larger cloud amounts in all three layers of the troposphere are simulated as compared to the CONTROL simulation. However, the changes are confined to frontal regions and the strongest effects occur over the continent, because the tendencies of vertical diffusion, radiation and advection, which are used to calculate the provisional values, are largest in these regions.

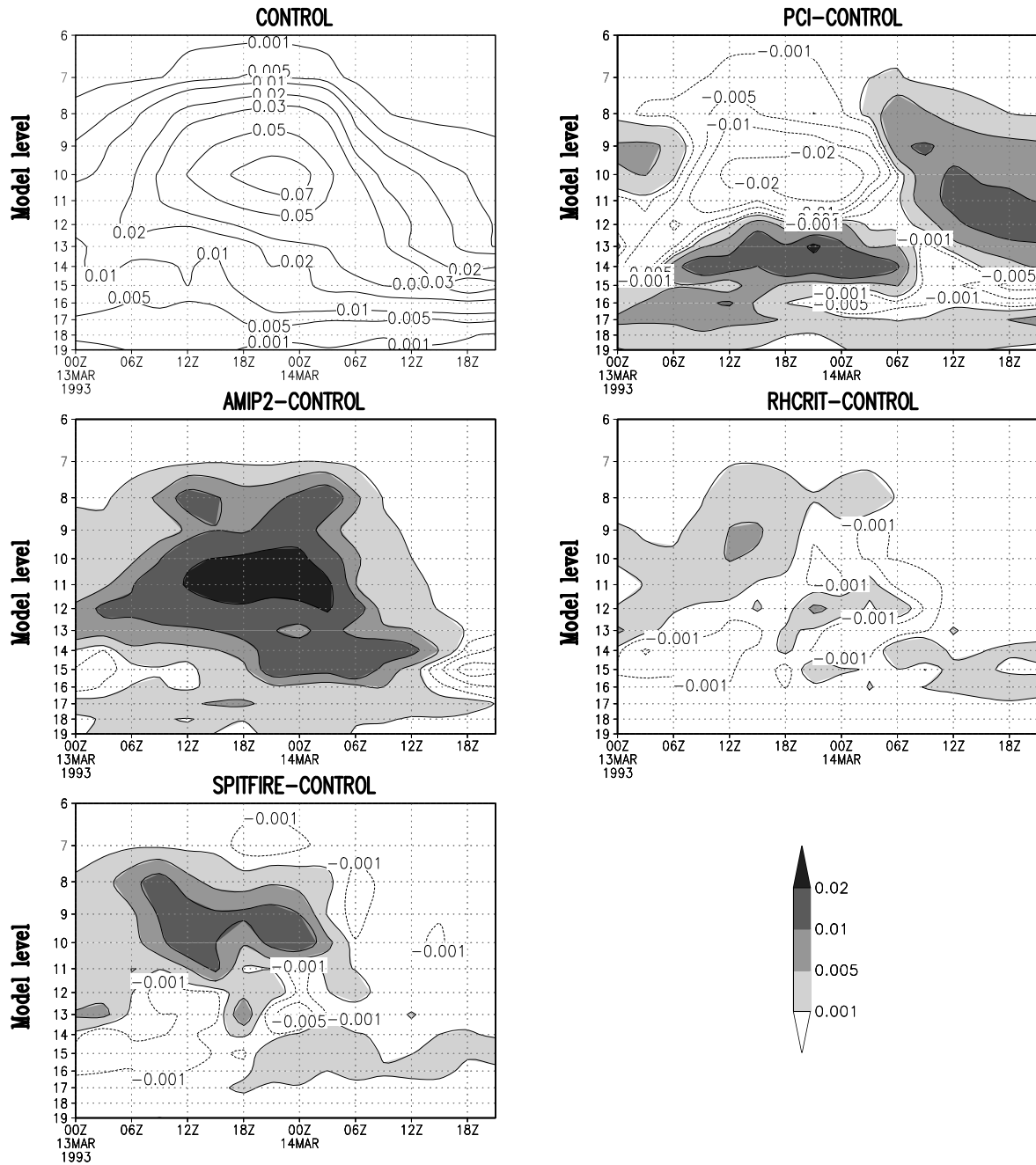


**Figure 5.9:** Same as Figure 5.8 but for the cloud water content [ $gkg^{-1}$ ]. Contours are drawn for -0.02, -0.01, -0.005, -0.001, 0.001, 0.005, 0.01 and 0.02  $gkg^{-1}$

Smallest cloud amounts as well as smallest differences between the experiments occur in the simulation of mid-level clouds. Furthermore, the effects are generally confined to frontal regions. The mid-level cloud cover, observed by ISCCP behind the cold front, is not reproduced in any of the experiments. This supports the assumption, posed in the last chapter, that weaknesses in the convection scheme or a too strong subsidence could be responsible for this error. A moisture transport into the middle troposphere by convection and vertical advection is necessary to exceed the threshold relative humidity required for the development of clouds. Another possible sources for larger relative humidities in middle levels are a stronger evaporation of precipitation or a horizontal advection of moisture. Both is not the case in the dry air behind the cold front, because no clouds occur in the upper troposphere and the air in middle levels over the cold continent is dry.

While PCI and AMIP2 induce only slight changes into the representation of clouds along the cold front, especially in the southern part, RHCRT and SPITFIRE clearly extend the region covered by mid-level clouds to the south, more in accordance to ISCCP observations of the cloud optical thickness. This similar reaction of SPITFIRE and RHCRT is likely caused by different mechanisms. While RHCRT generally leads to enhanced condensation due to the lowered condensation threshold, SPITFIRE transports sharper gradients, which enhances the vertical advection and therefore the upward transport of moisture along the cold front. This is demonstrated in Figure 5.10, in which the specific humidity transported by the vertical velocity at 850 hPa is compared for the different experiments and the CONTROL simulation. It shows that the strongest upward transport of moisture is confined to a sharper front in the SPITFIRE simulation. Furthermore, the southern part of the cold front is slightly shifted to the west as compared to the CONTROL simulation.

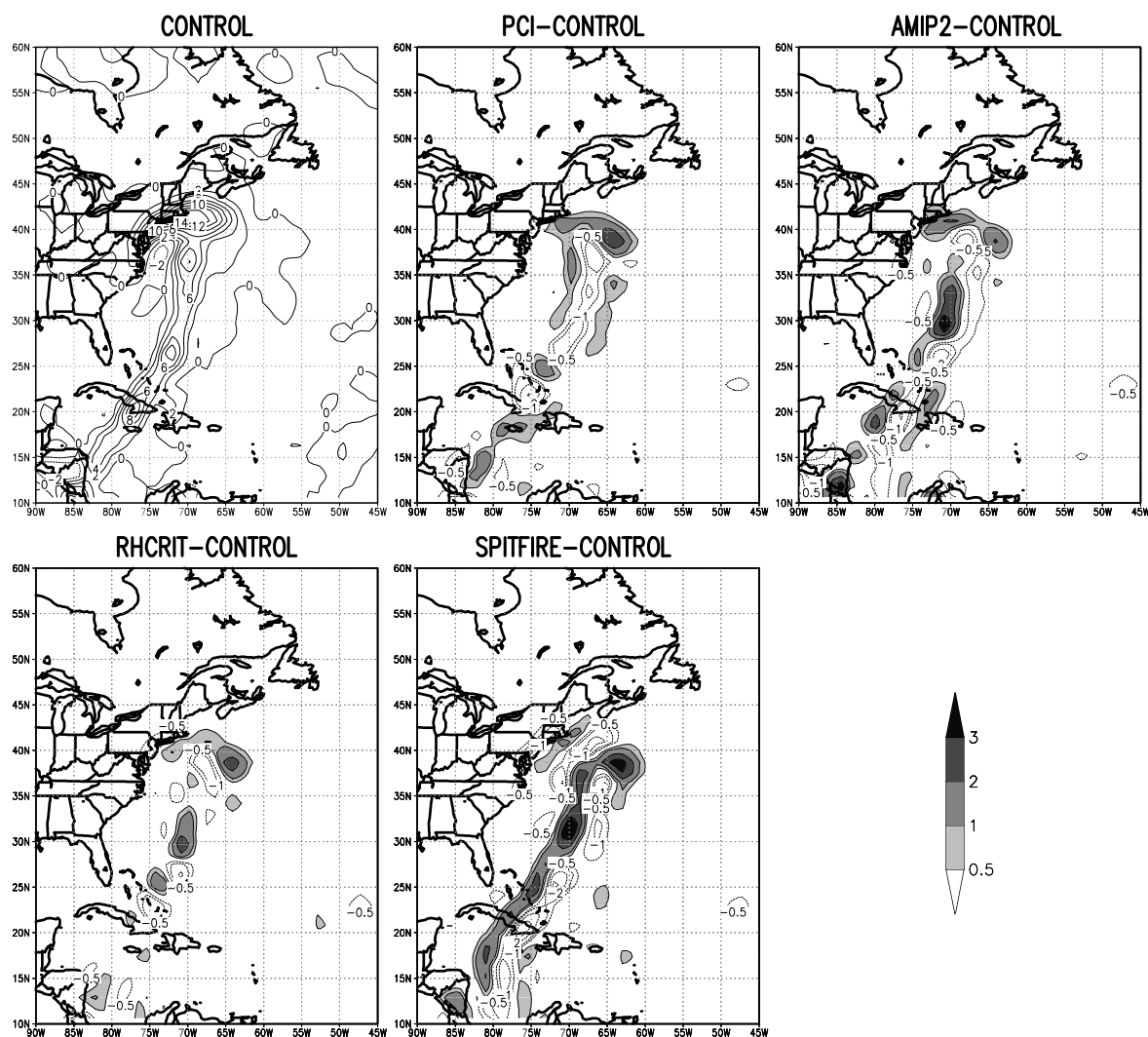


**Figure 5.10:** Specific humidity transported by the vertical velocity [ $kgkg^{-1} \cdot Pas^{-1}$ ] at model level 15 ( $\sim 850$  hPa) of the CONTROL simulation (contoured, upper left panel) and differences to the sensitivity studies at 00Z, 14th of March 1993. Shaded regions in the difference plots denote regions where the sensitivity study transport larger amounts of moisture. Contours are drawn for: -3, -2, -1, -0.5, 0.5, 1, 2 and 3 [ $kgkg^{-1} \cdot Pas^{-1}$ ].

While RHCRT leads to stronger cloud cover along both the warm and the cold front, strongest enhancements are confined to the cold front in the SPITFIRE simulation, supporting the assumption posed above, that the changed advection is especially important in regions influenced by convection. While AMIP2 strongly enhances mid-level cloud amounts in the large-scale ascent

and the northern part of the cold front, only small differences occur between the other experiments and the CONTROL simulation. This is consistent to the moister middle troposphere simulated by AMIP2 (Figure 5.8).

While in the SPITFIRE and the RHCRIT experiments only small changes occur in the upper troposphere, the AMIP2 experiment simulates clearly larger upper-level cloud amounts in frontal regions. In addition to the changes included by Lenderink et al. (1998) this might be caused by the larger amount of convective cloud water detraining into the level above the main detrainment layer. The area extent of the cirrus anvils in pre-frontal regions is on the other hand not changed compared to the CONTROL simulation. This is caused by a stronger sedimentation of ice crystals which is parameterized in terms of the ice water content. In the PCI experiment on the other hand, the upper-level cirrus anvils in pre-frontal regions of the cold and the warm front are clearly reduced.

Figure 5.8 and 5.9 show that PCI simulates a moister troposphere as compared to the CONTROL simulation during the strongest development of the system. At the same time larger amounts of liquid water are only simulated in the middle and lower troposphere, while they are clearly lower in the upper troposphere. This suggests either that the lower cloud amounts in the upper troposphere are caused by a stronger precipitation efficiency in the middle troposphere or by a stronger removal of ice crystals from the upper troposphere. The investigation of the temporal development of the 3D cloud structure and an investigation of the autoconversion rate (precipitation efficiency) further below in this chapter might favour one of the two explanations.

In contrast to what is expected, no changes in the upper-level cloud cover occur in the RHCRIT experiment, although the profile of the critical relative humidity has been changed with respect to a more suppressed condensation. This resistance against a changed condensation profile indicates that the upper levels of the midlatitudes are insensitive to changes of the condensation threshold. The transition from an enhanced to a suppressed condensation in the new profile compared to the standard profile happens at about 300 hPa. This might be too high to effect the development of clouds in midlatitudes. In the tropics on the other hand, where clouds grows to levels of 150 hPa or higher, a much larger effect is expected. (Roeckner, 1999).

For the blocking situation nearly no changes occur in the upper two cloud layers (not shown) in the experiments. This is to be expected, since low-level clouds are the major cloud types occurring in blocking anticyclones. The low-level cloud cover is enhanced in the PCI and the RHCRIT experiments, while the changes are small in AMIP2. This suggests that the error included by the use of the provisional values for the prognostic variables is especially large in frontal regions, while only small changes are induced in undisturbed situations like the blocking case. This is an unexpected result, because Lenderink et al. (1998) introduced the changes to achieve a better representation of stratocumulus which does not occur in this case. As observed during the comparison of total cloud cover, regions of clear sky occur, where the satellite has observed overcast sky. The strongest improvements occur in the RHCRIT experiment, leading to the best representation of low-level cloud cover. It is encouraging to note that limited changes as included for the RHCRIT experiment, lead to a better representation of the cloud distribution in the blocking situation than more significant changes, such as the PCI or the AMIP2 experiment. Furthermore it becomes apparent from the comparison, as expected, that the convection scheme plays only a minor role for the representation of clouds occurring in the blocking situation, since, apart from AMIP2, no changes have been introduced into the convection scheme.

To investigate the temporal changes of the vertical cloud structure, Hovmöller diagrams of the partial cloud cover, averaged over a region  $20^\circ$  by  $20^\circ$ , are plotted for the blizzard as well as the blocking case (Figures 5.12 and 5.13). They illustrate differences between the sensitivity experiments and the different synoptic situations.

For the blizzard case a region has been chosen, which contains major parts of the warm front, cold front and bent-back warm front at 00Z, 14th of March 1993. A general feature of all experiments

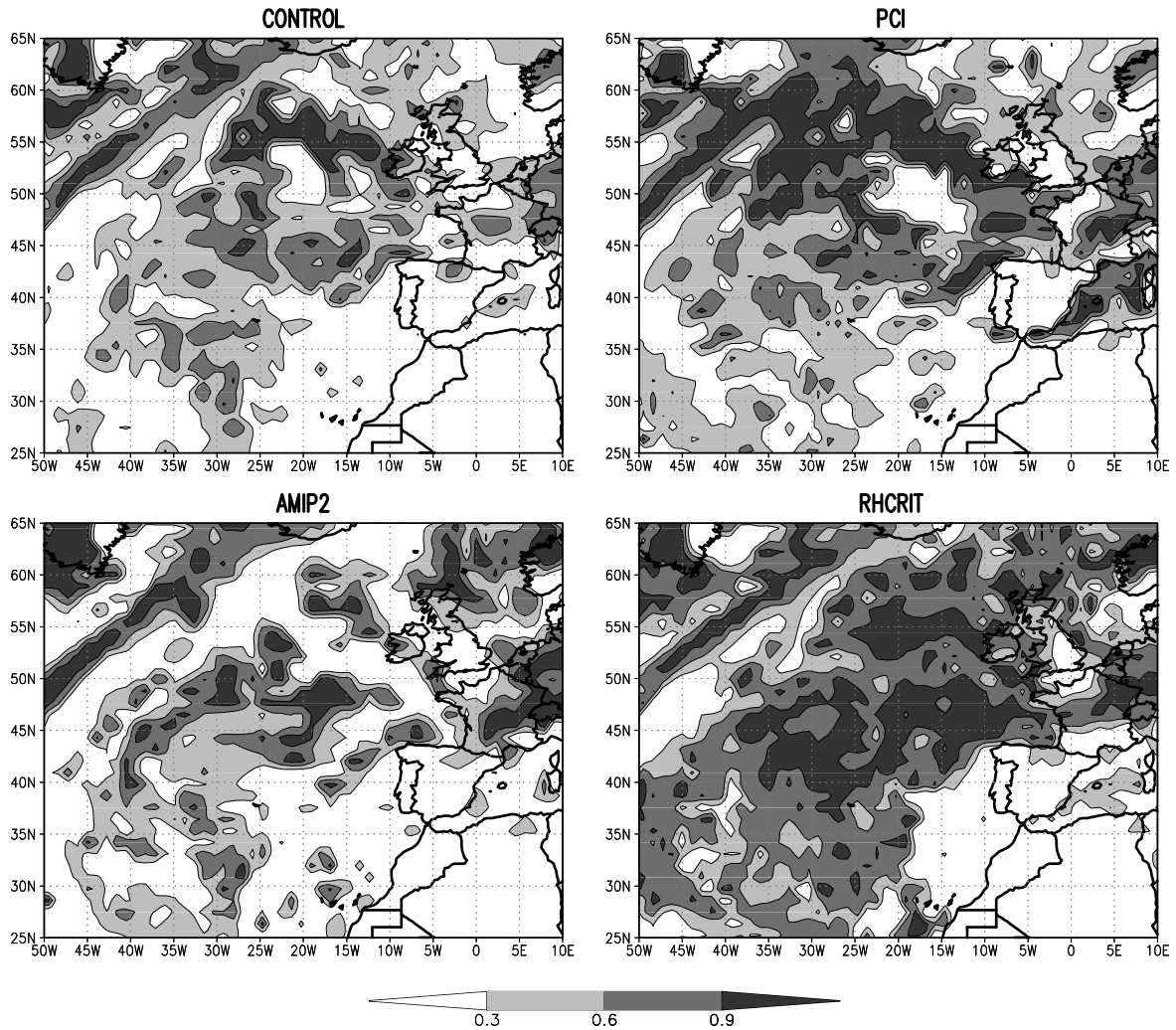


**Figure 5.11:** Same as Figure 5.6 but for the low-level cloud cover for one time step of the blocking situation (12Z, 19th February 1993).

is a higher cloud top at the time of the strongest development of the system with lower values occurring before and afterwards. Furthermore, largest cloud amounts occur consistently in the upper troposphere during the development of the system.

The smallest upper tropospheric cloud amounts are simulated in the PCI simulation. However, height and time at which the maximum occurs remain the same as in the other simulations. On the other hand cloud dissipation in the upper troposphere is weaker or slower in the PCI simulation, suggested by the largest upper-tropospheric cloud amounts being simulated at the end of the observed period. Therefore the lower cloud amounts in the upper troposphere are not caused by a stronger removal of ice crystals, because they precipitate slower. The smaller cloud amounts are the result of a reduced development of clouds in the upper troposphere or a reduced upward transport of moisture from below. In the PCI experiment a moister troposphere is simulated at the time of the strongest development (Figure 5.8). Furthermore larger amounts of liquid water occur in the lower and middle troposphere (Figure 5.9). Since the conversion of cloud water to precipitation (autoconversion rate) is a function of the mixing ratio of cloud liquid water in the cloudy part of the grid box, the larger liquid water content is associated with stronger precipitation development. This is an efficient process, removing moisture from the atmosphere, which could otherwise be transported into higher levels.

The slower dissipation of clouds in the PCI experiment is explained by different ice phase processes. While in the CONTROL simulation the precipitation flux in the upper troposphere is

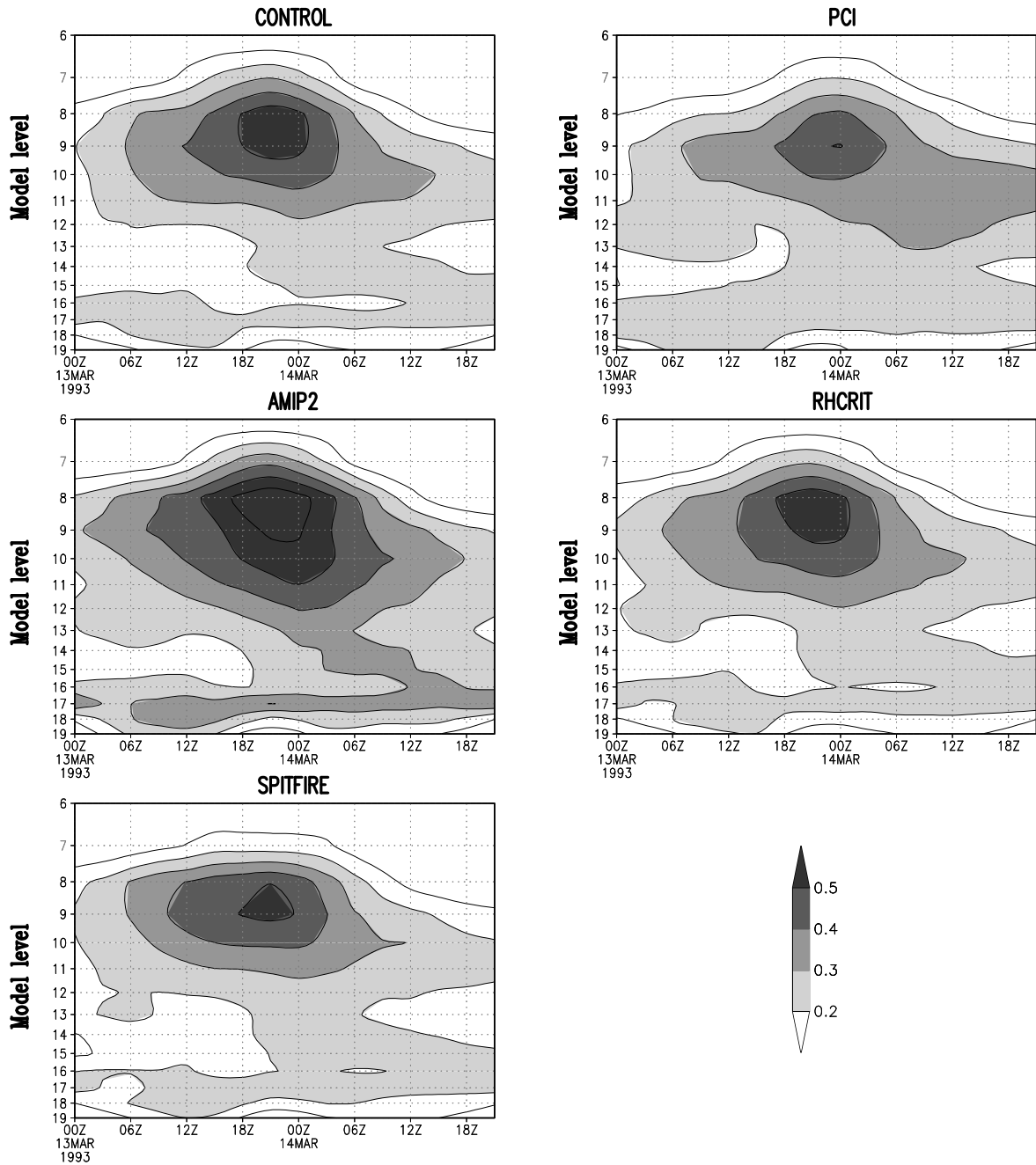


**Figure 5.12:** Height-time section of the spatially averaged cloud fraction [fract.] in the blizzard case. The region used for the average is  $85^{\circ}\text{W}$  to  $65^{\circ}\text{W}$  and  $35^{\circ}\text{N}$  to  $55^{\circ}\text{N}$ . Contour lines are: 0.1, 0.2, 0.3, 0.4, 0.5 and 0.6. [level 15  $\approx$  850 hPa; level 11  $\approx$  500 hPa; level 8  $\approx$  250 hPa]

parameterized in terms of the sedimentation flux of ice crystals, in PCI ice crystals are assumed to have no terminal velocity, but aggregate to snow flakes which further remove ice crystals by accretion. The aggregation rate of ice crystals in PCI increases faster with increasing cloud ice than the sedimentation flux in CONTROL does. Therefore the ice phase precipitation is faster at high cloud ice mixing ratios and slower at small cloud ice mixing ratios (Lohmann and Roeckner, 1996b). This leads to a stronger development of snow in lower and middle levels of the troposphere, while ice crystals in the upper troposphere are accumulated, especially in midlatitudes and polar regions, explaining the slower dissipation of clouds. Furthermore, PCI is the only simulation in which the precipitation efficiency in middle levels of the troposphere in the region of the large-scale ascent is larger than in the CONTROL simulation although lower amounts of cloud liquid water are simulated. In the other simulations larger autoconversion

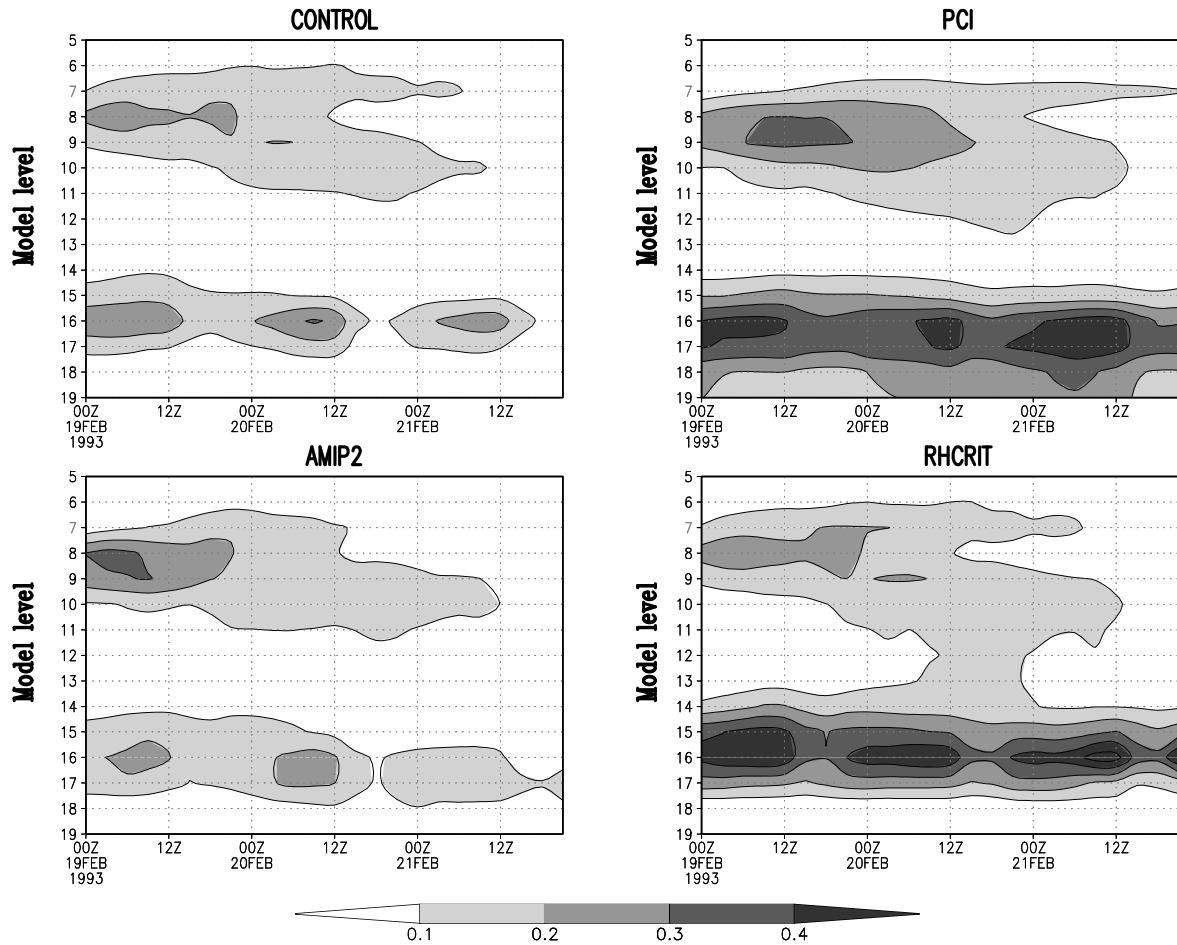


**Figure 5.13:** Same as Figure 5.12 but for the blocking situation. Here the region  $35^{\circ}\text{W}$  to  $15^{\circ}\text{W}$  and  $35^{\circ}\text{n}$  to  $55^{\circ}\text{N}$  is used for the averaging.

rates are consistently associated with larger values of the cloud liquid water. This difference is probably caused by the autoconversion rate being additionally dependent on the number of cloud droplets in the PCI simulation. The stronger precipitation development over the ice as well as over the liquid phase in middle levels of the troposphere removes moisture more efficiently than in the other simulations and impedes the development of clouds in the upper troposphere (Figure 5.9).

As expected from the horizontal comparisons, AMIP2 simulates the largest cloud amounts. This is true for the whole troposphere with particularly strong values occurring in upper and lower parts, consistent with higher specific humidities and larger amounts of liquid water compared to the CONTROL simulation (Figures 5.8 and 5.9). Since the “shape” of the cloudiness in the Hovmöller diagram is the same as in the other experiments, but with higher absolute values, the AMIP2 experiment seems to respond faster to the forcing from the environment in the blizzard case (i.e. clouds are developed and dissipated faster).

Larger cloud amounts in the middle troposphere are simulated in AMIP2 and PCI, while SPIT-FIRE and RHCRIT only slightly change the cloud distribution compared to the CONTROL simulation. The reason for larger mid-tropospheric cloud amounts in AMIP2 and PCI is the moister lower and middle troposphere as indicated by higher specific humidities as well as larger amounts of liquid water than in the CONTROL simulation during the strongest development of the cyclone (Figures 5.8 and 5.9).

In the blocking case smallest changes compared to the CONTROL simulation occur in the AMIP2 experiment. This is surprising, since it induced the largest changes in the blizzard case,

suggesting that the changes introduced for AMIP2 mainly influence disturbed situations, such as frontal regions, while undisturbed situations are only weakly affected. This is true although the strongest changes in the vertical distribution of the specific humidity occur, underlining the low relative humidities in the middle troposphere in the blocking high.

PCI as well as RHCRT simulate higher cloud amounts in the lower troposphere than the CONTROL simulation as suggested by the comparison of geographic distributions of cloud cover (Figure 5.11). Major difference between RHCRT and PCI is that in the RHCRT experiment, larger cloud amounts are restricted to levels around the top of the planetary boundary layer, while clouds are extended to the ground in the PCI simulation. As suggested by Figure 5.14 this is caused by a moister lower troposphere in the PCI simulation. At the same time larger cloud amounts and specific humidities are simulated in the upper troposphere, confirming the reduced removal of ice crystals in the PCI simulation. RHCRT on the other hand simulates a drier lowest troposphere compared to the CONTROL simulation preventing the development of clouds in the boundary layer.

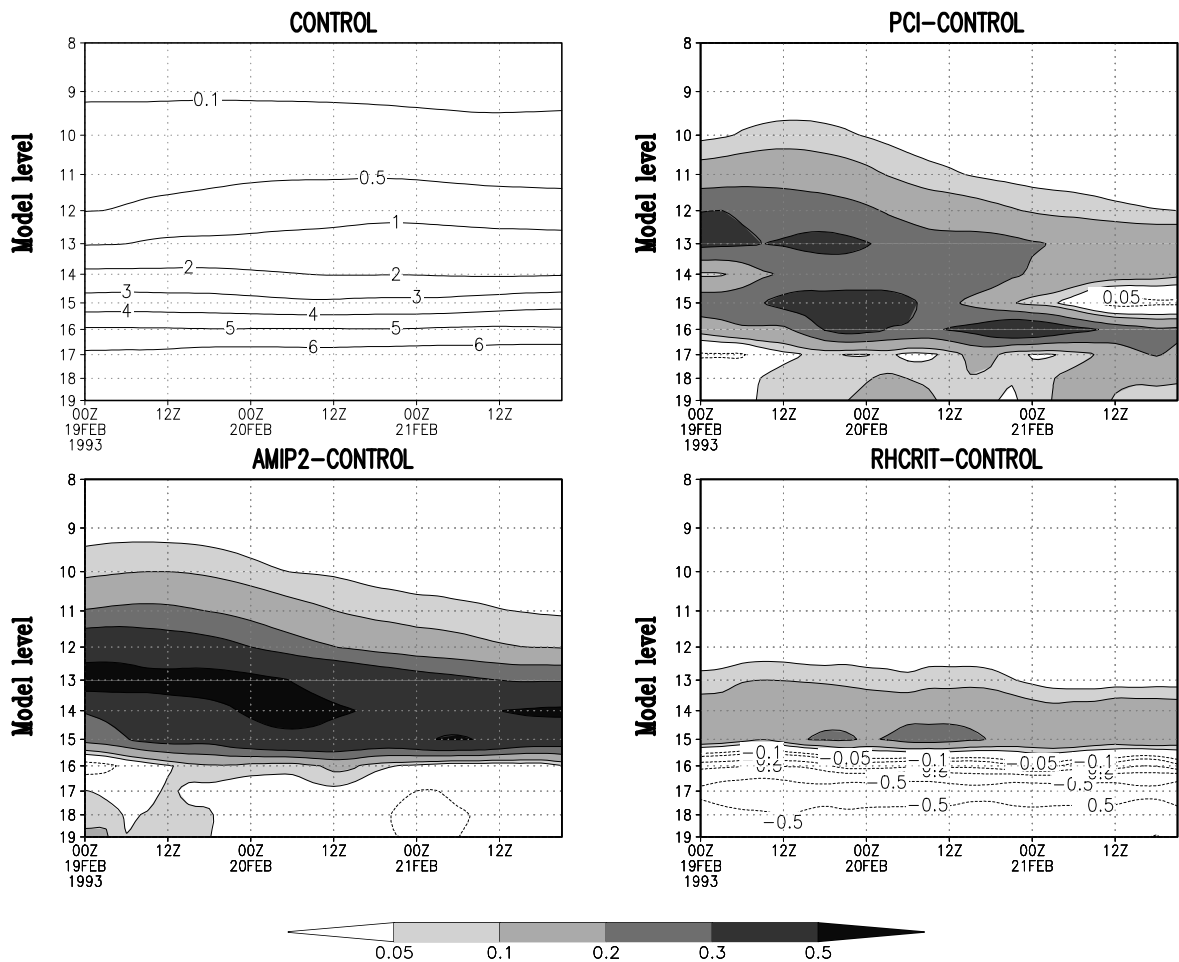


**Figure 5.14:** Height-time section of the spatially averaged specific humidity [ $gkg^{-1}$ ] in the blocking case of the CONTROL simulation (upper left) and differences to the sensitivity experiments. The region used for the average is  $55^{\circ}W$  to  $35^{\circ}W$  and  $35^{\circ}N$  to  $55^{\circ}N$ . In shaded regions the experiments simulate a moister atmosphere with drier conditions in contoured regions. Contours are drawn for  $-0.5, -0.3, -0.2, -0.1, -0.05, 0.05, 0.1, 0.2, 0.3$  and  $0.5 gkg^{-1}$ . [level 15  $\approx$  850 hPa; level 11  $\approx$  500 hPa; level 8  $\approx$  250 hPa]

All experiments and the CONTROL simulation show a clearly developed diurnal cycle of low-level cloudiness, especially pronounced in RHCRT. The latter indicates the strongest respond to the radiative forcing with the changed profile of the critical relative humidity. This is not

surprising, since the lower condensation threshold is easier exceeded by the daily developing turbulent exchange of moisture.

### 5.3.3 Cloud water path (CWP)

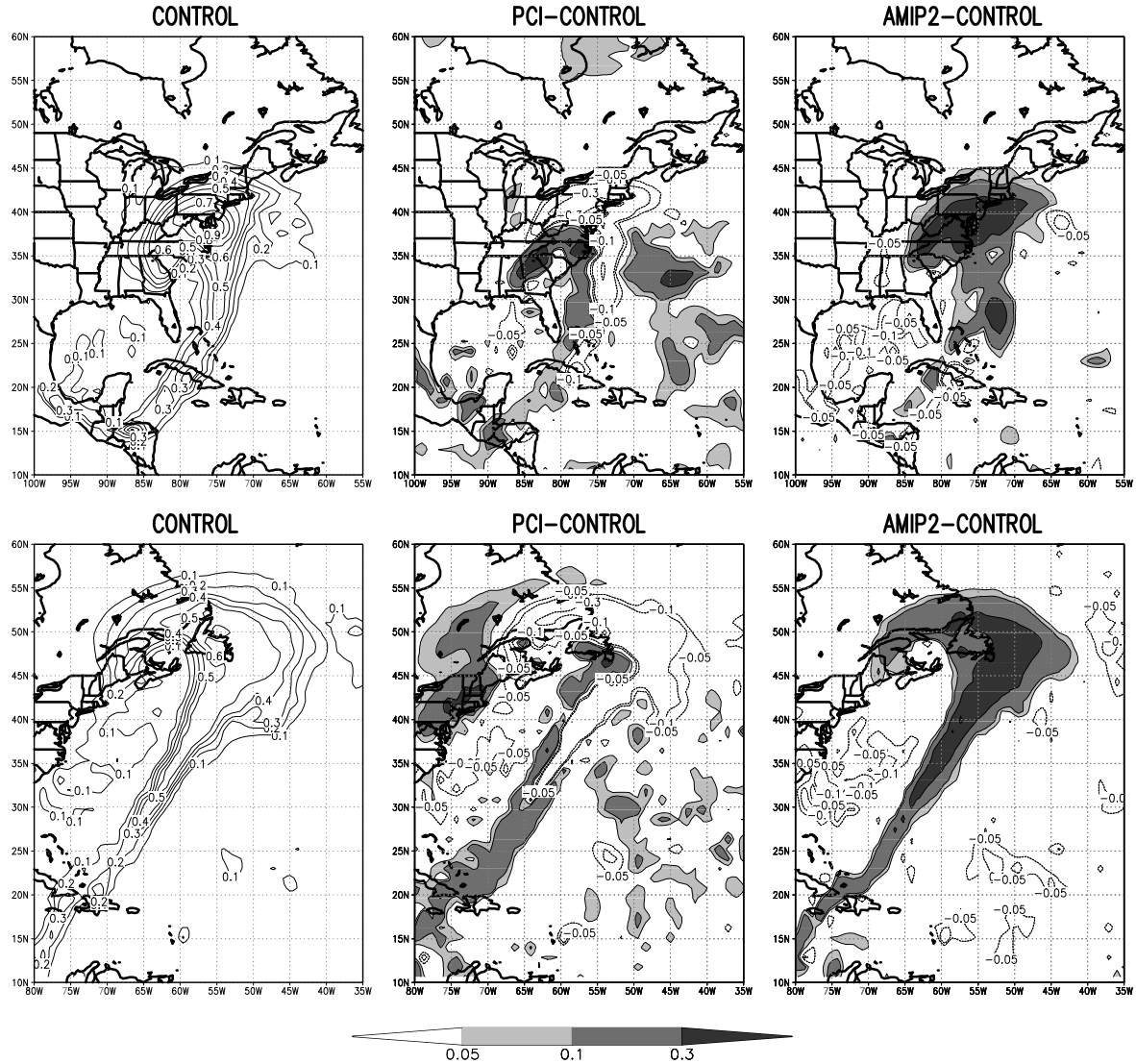


**Figure 5.15:** Cloud water path (CWP) [ $kgm^{-2}$ ] of the CONTROL simulation (left column, total values contoured) and differences PCI-CONTROL (middle column) and AMIP2-CONTROL (right column) for the mature (18Z, 13th of March 1993, upper row) and dissipating (18Z, 14th of March 1993, lower row) stage in the blizzard case. Shaded areas in the difference plots mark regions where the experiments simulate larger CWPs, whereas smaller values are simulated in contoured regions. Contours are drawn for  $-0.3$ ,  $-0.1$ ,  $-0.05$ ,  $0.05$ ,  $0.1$  and  $0.3$   $kgm^{-2}$ .

Figures 5.15 and 5.16 compare the cloud water path (hereafter referred to as CWP) simulated by the CONTROL simulation and the sensitivity experiments. In addition, Figure 5.9 shows time-height sections of the spatially averaged cloud water distribution for the CONTROL simulation and the sensitivity experiments. Largest changes occur in the AMIP2 simulation, which strongly enhances CWP in frontal regions. Especially strong changes occur in the region of the large-scale ascent along the warm front, corresponding to large cloud amounts simulated by AMIP2 in this region. A comparison of the two stages of development shows that the enhancements are strongest in the region of the large-scale ascent in the mature stage of the development, while strongest enhancements occur along the cold front in the dissipating stage of the development.

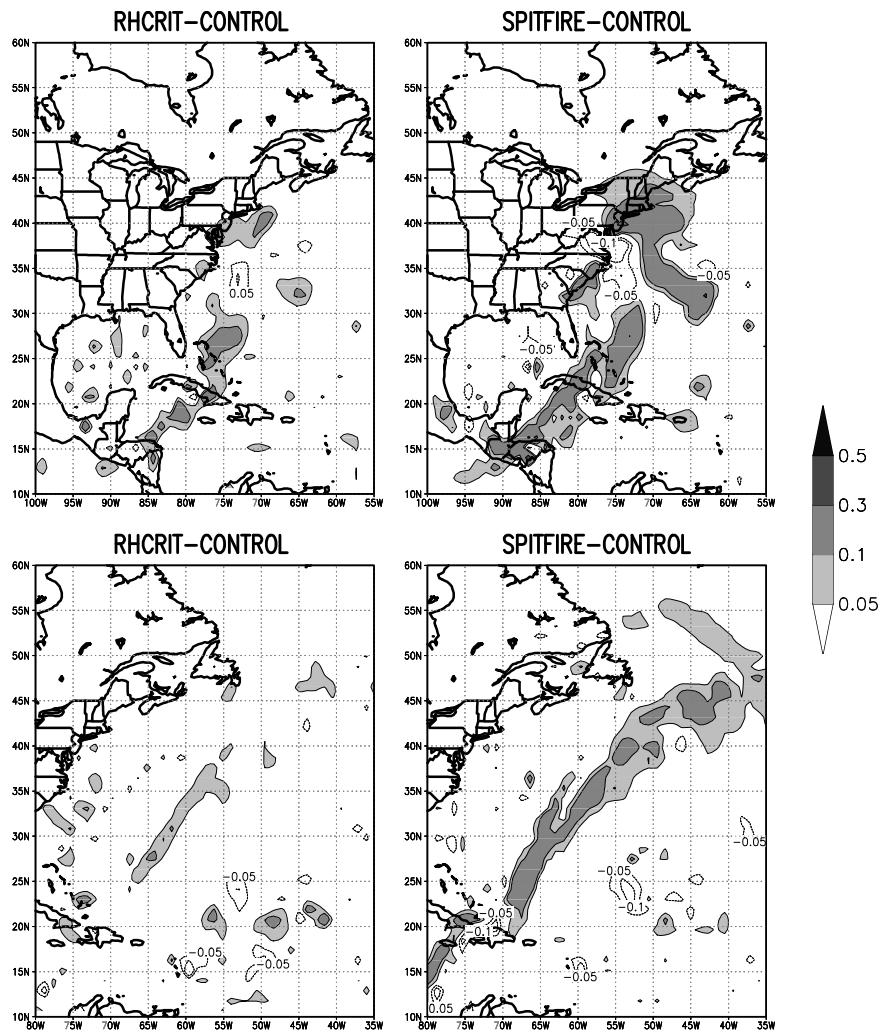


**Figure 5.16:** Same as Figure 5.15 but for the differences RHCrit-CONTROL (left column) and SPITFIRE-CONTROL (right column).

This is caused by an accumulation of cloud water in middle and upper levels of the troposphere in frontal regions (Figure 5.9). On the other hand CWP in the environment of the system, in pre- as well as in post-frontal regions, is systematically reduced compared to the CONTROL simulation.

A different behaviour occurs in the PCI simulation. While the other experiments simulate consistently higher CWPs along the fronts, upwind and downwind regions are differently simulated in the PCI simulation. Lower values of the CWP are simulated in the region of large-scale ascent and in pre-frontal parts of the cold front, consistent with lower cloud amounts in the upper-tropospheric frontal outflow. The vertical distribution is presented in Figure 5.9. Larger amounts of cloud water are simulated in lower and middle levels of the troposphere, while lower values occur in the upper troposphere. This suggests a stronger precipitation efficiency in middle levels in the PCI simulation, removing efficiently liquid water from the atmosphere. In downwind parts of the large-scale ascent and rear parts of the cold front, on the other hand, larger values are simulated. This is true for rear parts of the cold front as well as for the bent-back warm front. The generally larger CWPs in the warm sector of the cyclone and the stronger developed cold front in the dissipating stage in the PCI simulation as compared to the CONTROL simulation are caused by a moister lower troposphere, in which clouds are developed and evaporated more frequently without being precipitated (Lohmann, 1999). Larger CWPs in upwind regions of the

Appalachian mountain range indicate furthermore a stronger sensitivity of the PCI scheme to orography. This is again caused by the moister lower troposphere, leading to a faster response of condensation to orographic forcing. The mentioned changes lead to frontal boundaries being more pronounced in the PCI simulation. On the other hand smaller CWP are simulated behind the cold front compared to the CONTROL simulation, not in accordance with optical thickness observations of ISCCP.

The smallest changes occur in the RHCRT experiment. In contrast to the PCI simulation the spatial patterns of the CWP remain constant, indicating that the cloud dissipation is enhanced together with the condensation. Higher CWPs are only simulated in the region of the cold front, while virtually no changes occur in the large-scale ascent along the warm front and the bent-back warm front. Reason for this behaviour might be that the new profile makes an impact only where condensation has already occurred, and not in the sub-cloud layer. Along the cold front this is associated with the largest improvements occurring in regions where largest differences to ISCCP observations of cloud optical thickness occur. The larger CWPs result in sharper horizontal gradients along the cold front and therefore a more pronounced frontal boundary. However, the changes in the CWP are small as compared to the effects on the cloudiness. The differences in the warm sector of the developing system are relatively small, supporting the assumption that the temporal characteristics of condensation has not changed in the RHCRT experiment. Slightly larger cloud amounts have been observed in this region (Figure 5.7), indicating that only shallow clouds with low CWPs are developed in addition to the CONTROL simulation. Another encouraging result is the slightly larger CWP behind the cold front in the RHCRT experiment as compared to the CONTROL simulation indicating an improved representation of clouds compared to ISCCP observations, although the cloudiness is still underestimated.

As the RHCRT experiment, SPITFIRE simulates larger CWPs as compared to the CONTROL simulation. In contrast to RHCRT, they occur in upwind regions of the fronts as well, indicating a stronger condensation and a broadening of the fronts. On the other hand, the strongest upward transport of moisture is confined to a sharper front than in the CONTROL simulation (Figure 5.10). Along the northern part of the cold front as well as in the region of the large-scale ascent, larger CWPs occur only in upwind regions of the fronts, while in southern parts of the cold front they are enhanced in central parts as well. This indicates a stronger sensitivity of the SPITFIRE scheme to temperature, since an enhancement of CWP occur exclusively over the warm ocean. The larger CWPs are the result of a stronger vertical advection of moisture in fronts. This is caused by the SPITFIRE scheme being less diffusive than the semi-Lagrangian scheme used in the CONTROL simulation, allowing the transport of sharper gradients of water vapour, distributing larger amounts of moisture within a deeper layer. The strongest enhancements occur on the warm side of the front, because the warm air in the lower troposphere contains large amounts of moisture. Behind the cold front, in contrast to the RHCRT experiment, no changes of the CWP occur despite the strong turbulent mixing in the cold air streaming over the warm ocean surface.

Figure 5.17 compares the CWP in the CONTROL simulation and the sensitivity experiments for one time step of the blocking situation. Here absolute values are compared, because the occurring gradients are smaller. As in the blizzard case AMIP2 simulates much larger CWPs in frontal regions surrounding the block, while the amounts of cloud water in undisturbed regions of the blocking high remain nearly unchanged or are even slightly reduced compared to the CONTROL simulation.

RHCRT and PCI on the other hand simulate larger CWPs. The comparison of the two simulations reveals larger values in the PCI simulation, although larger low-level as well as total cloud amounts are simulated in the RHCRT experiment (Figures 5.5 and 5.11). In the PCI simulation a moister lower troposphere is simulated (Figure 5.14 and 5.18). Therefore lower amounts of liquid water can re-evaporate compared to the RHCRT experiment, in which the

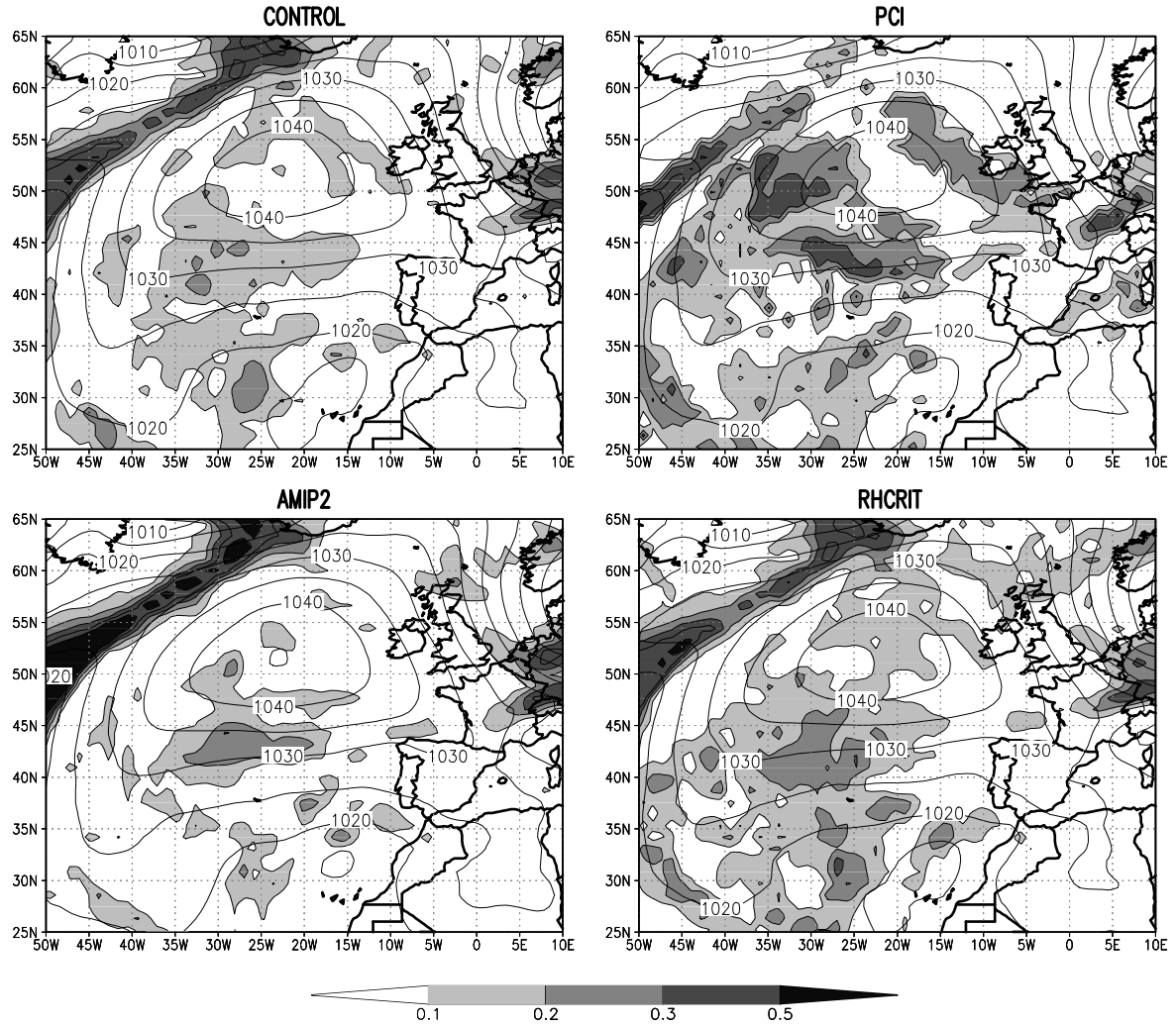


**Figure 5.17:** Mean sea level pressure [hPa] and CWP [ $kgm^{-2}$ ] for one time step of the blocking situation (12Z, 19th of February 1993).

boundary layer is drier as compared to the CONTROL simulation and therefore clearly drier than the lower troposphere in the PCI simulation. Furthermore, the critical relative humidity is lower in the lower troposphere, leading to a stronger development of clouds at identical relative humidities. The concentration of larger amounts of moisture at the top of the boundary layer leads to larger cloud amounts at the top of the boundary layer in the RHCRT experiment. On the other hand deeper clouds are simulated in the PCI simulation (Figure 5.13).

### 5.3.4 Cloud optical thickness

Figures 5.19 and 5.20 compare the distributions of the cloud optical thickness in ISCCP and the different model simulations.

In the blizzard case the coarse structure and the order of magnitude of the cloud optical thicknesses are well represented by the different model simulations. The exception is the PCI simulation, which systematically underestimates the cloud optical thickness. One reason for this difference is the clearly larger effective radius of ice crystals used in this simulation, leading to lower optical thicknesses for identical amounts of cloud ice. In addition, lower CWP are simulated by PCI, caused by a stronger precipitation efficiency in the middle troposphere, which additionally reduces the cloud optical thickness.

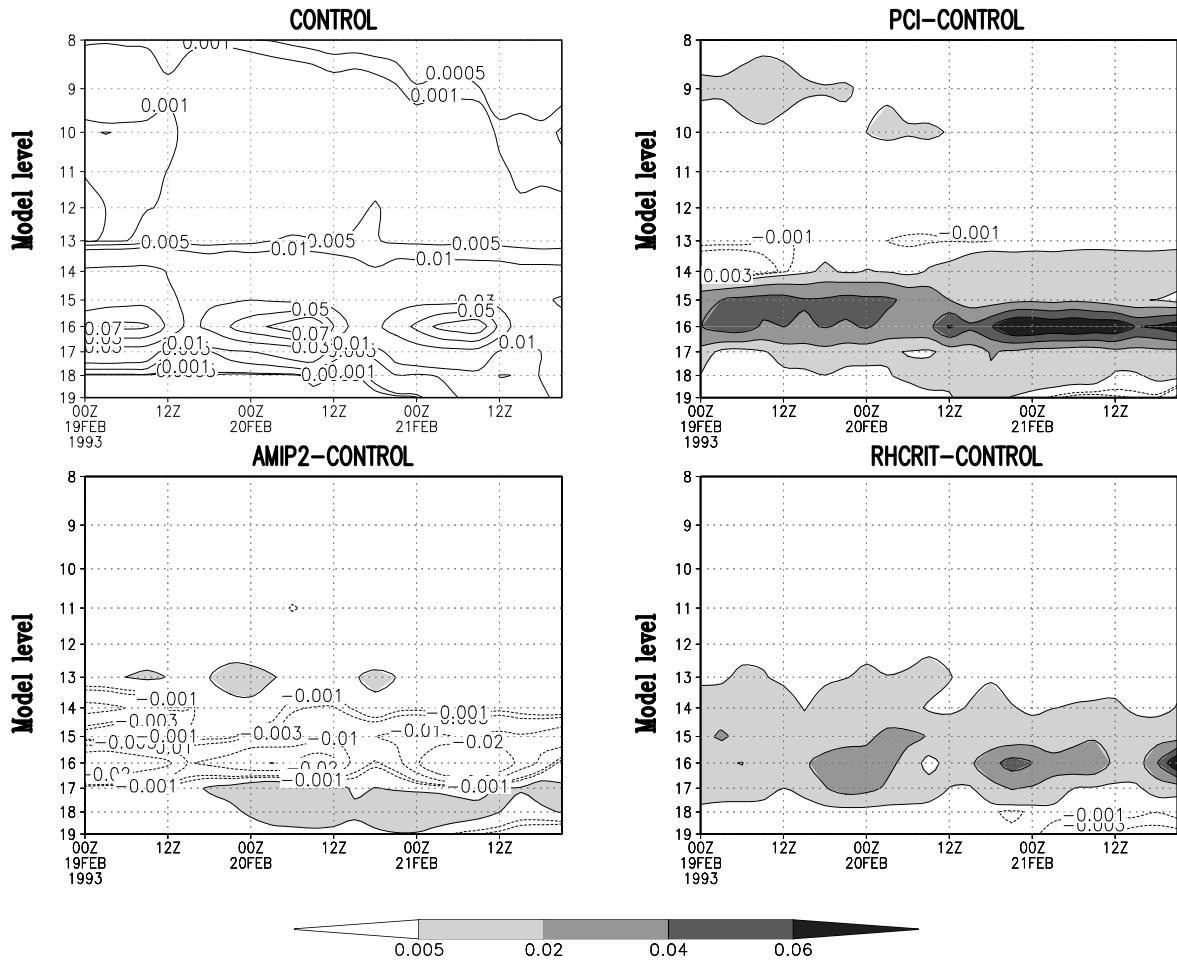


**Figure 5.18:** Height-time section of the spatially averaged cloud water content [ $gkg^{-1}$ ] for the blocking case of the CONTROL simulation (upper left) and differences to the sensitivity experiments. The region used for the average is  $55^{\circ}W$  to  $35^{\circ}W$  and  $35^{\circ}N$  to  $55^{\circ}N$ . In shaded regions the experiments simulate larger cloud water contents with lower amounts in contoured regions. Contours are:  $-0.02$ ,  $-0.01$ ,  $-0.003$ ,  $-0.001$ ,  $0.005$ ,  $0.02$ ,  $0.04$  and  $0.06$   $gkg^{-1}$ . [level 15  $\approx$  850 hPa; level 11  $\approx$  500 hPa; level 8  $\approx$  250 hPa]

Apart from the PCI simulation the sensitivity experiments as well as the CONTROL simulation tend to overestimate the cloud optical thickness in the region of the largest ascent to the north of the surface low in the mature stage of the system. Furthermore, the region covered by optically thick clouds is underestimated in all model simulations in upwind regions of the large-scale ascent. This indicates a too weak condensation in lower levels in the model simulations. However, this is not reduced by the RHCRIT experiment, indicating that other processes in addition to the profile of the critical relative humidity contribute to this bias. This difference is clearly reduced in the dissipating stage of the development in each experiment.

All experiments underestimate the cloud optical thickness in southern parts of the cold front in the dissipating stage, indicating that, although the front is present, the convective transports are too small to maintain larger cloud optical thicknesses. One reason is the coarse horizontal resolution, smoothing the temperature and moisture gradients. This reduces the convective activity, the detrainment of convective cloud water and water vapour and the advection of moisture into the middle troposphere. Furthermore the evaporation of precipitation could be too weak. The weaknesses lead to low relative humidities in middle levels in southern regions of the cold front preventing the development of clouds. Another feature that is common to all model simulations is an underestimation of the optical thickness behind the cold front in the mature

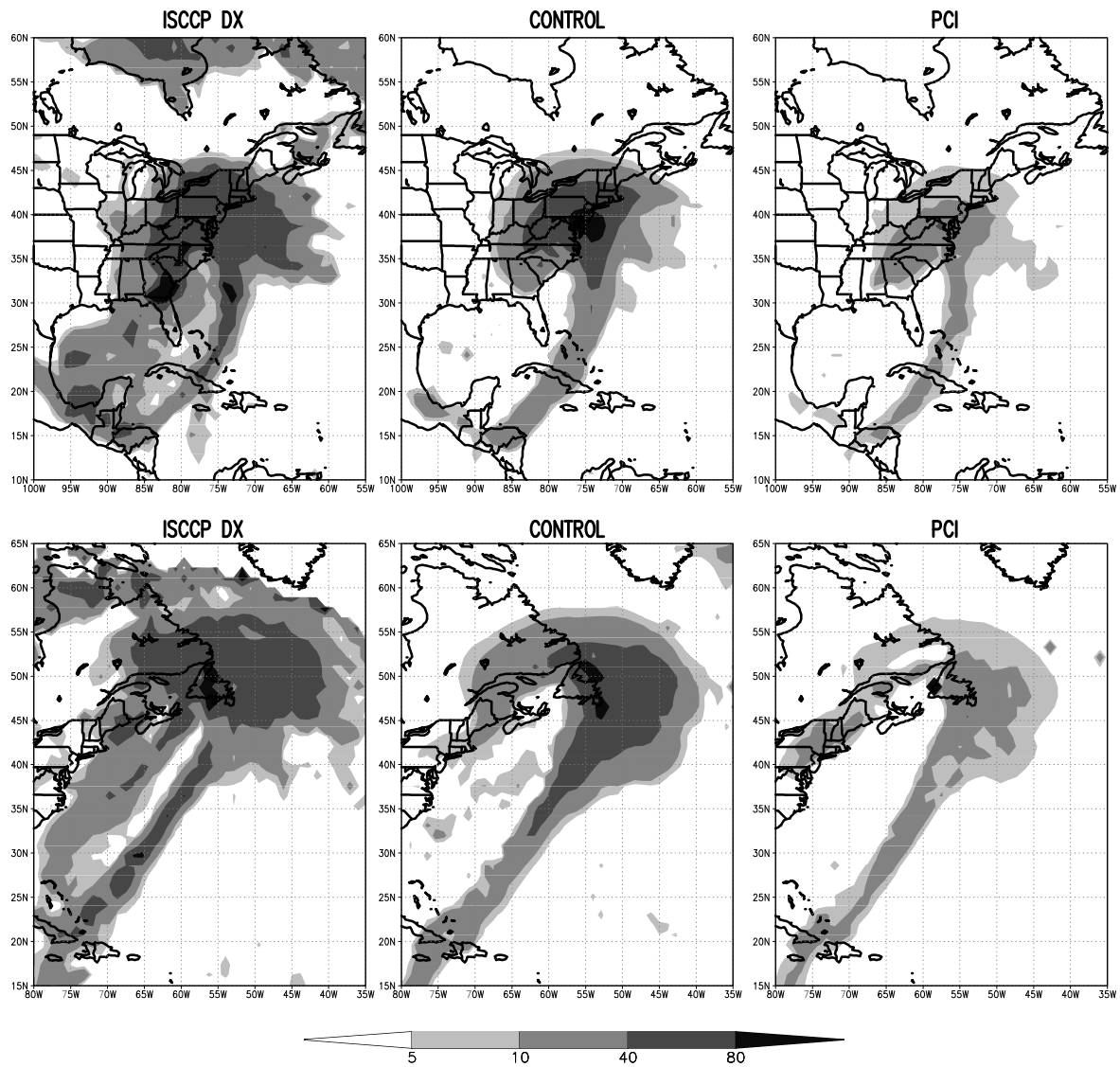


**Figure 5.19:** Cloud optical thickness  $\tau$  for the mature (18Z, 13th of March 1993, upper row) and dissipating (18Z, 14th of March 1993, lower row) stage in the blizzard case of ISCCP DX (left column), the CONTROL simulation (middle column) and the PCI experiment (right column).

as well as the dissipating stage of the development, supporting the suggested underestimation of convective activity in the cold air behind the cold front. Reasons could be, as suggested above, either a too strong subsidence or weaknesses in the convection scheme.

Due to larger amounts of liquid water in the AMIP2 simulation the cloud optical thickness is overestimated compared to ISCCP observations. This is true for the mature as well as the dissipating stage. In the mature stage, larger values occur in the large-scale ascent along the warm front and the bent-back warm front, while the largest overestimation occurs in the northern part of the cold front in the dissipating stage. From an optical thickness point of view, the clouds behind the cold front are more poorly represented than in the CONTROL simulation, although, at least in the dissipating stage, slightly larger cloud amounts are simulated in the AMIP2 experiment. This discrepancy is explained by optically thinner clouds occurring in the AMIP2 simulation as compared to the CONTROL simulation behind the cold front.

Although the representations are very similar in the CONTROL and RHCRIT simulations, the best distribution in both stages of the development is again simulated in the RHCRIT experiment. In the mature stage, larger optical thicknesses are simulated along the cold front,

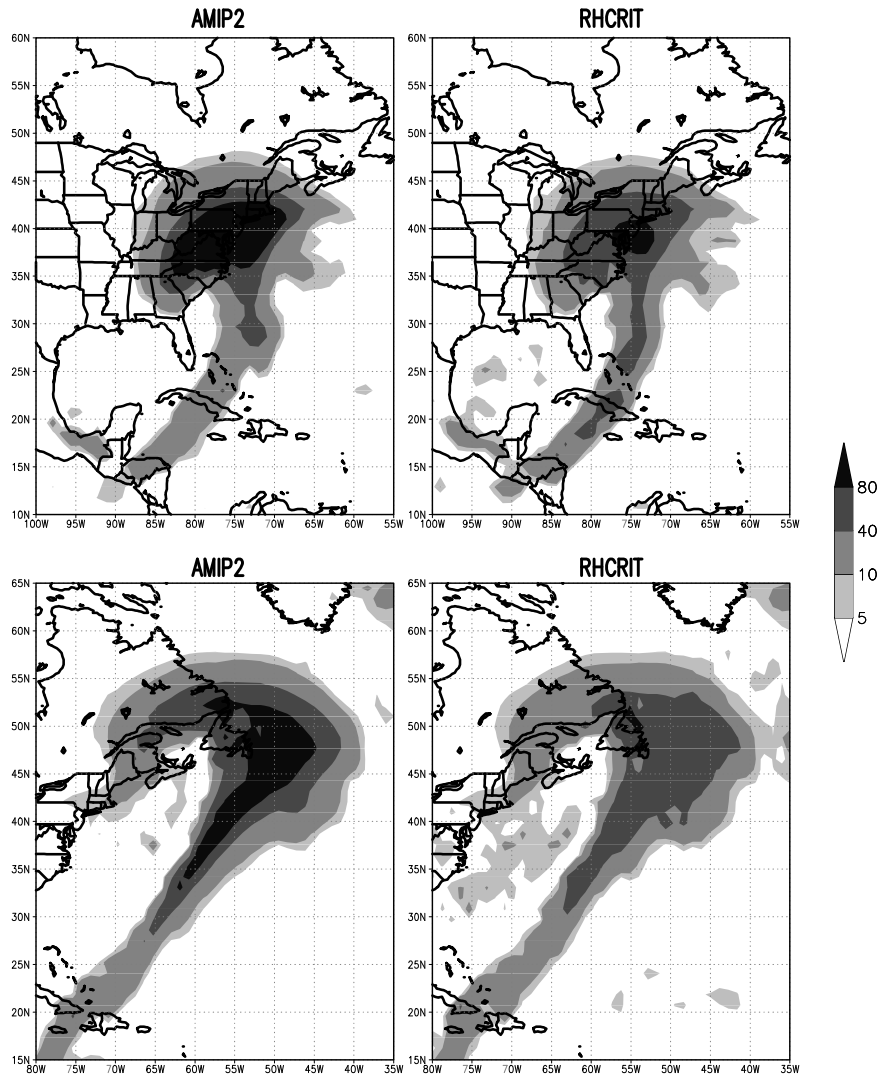


**Figure 5.20:** Same as Figure 5.19 but of the AMIP2 (left column) and the RHCRT (right column) experiment.

corresponding best to the ISCCP observation. In the dissipating stage the post-frontal subsidence and the cloudiness behind the front are represented better than in the other simulations. Nevertheless, the optical thickness behind the cold front in the post-frontal subsidence is still underestimated compared to the observations. It is an encouraging and surprising result that the best representation of cloudiness is simulated with the experiment using the smallest modifications as compared to the CONTROL simulation. It underlines furthermore the potential for model improvements possible by accurately tuning the physical constants.

Figure 5.21 shows the same comparison for the blocking situation. The general structure of the cloud optical thickness is similarly represented in all model simulations. The order of magnitude of the simulated cloud optical thickness is in good agreement with ISCCP for all experiments apart from the PCI simulation, which overestimates the cloud optical thickness associated with the larger amounts of liquid water present in the lower troposphere. However, in contrast to the blizzard case, the clouds are distributed differently as compared to ISCCP observations. Optically thicker clouds are observed in central and eastern parts of the anticyclone, whereas the model simulates higher values in southern and southwestern regions of the system. This difference suggests model errors in the representation of low-level boundary layer clouds, in agreement with findings of [Chen and Roeckner \(1997\)](#), who validated the representation of clouds in a climatological sense. They concluded that total cloud cover is systematically underestimated

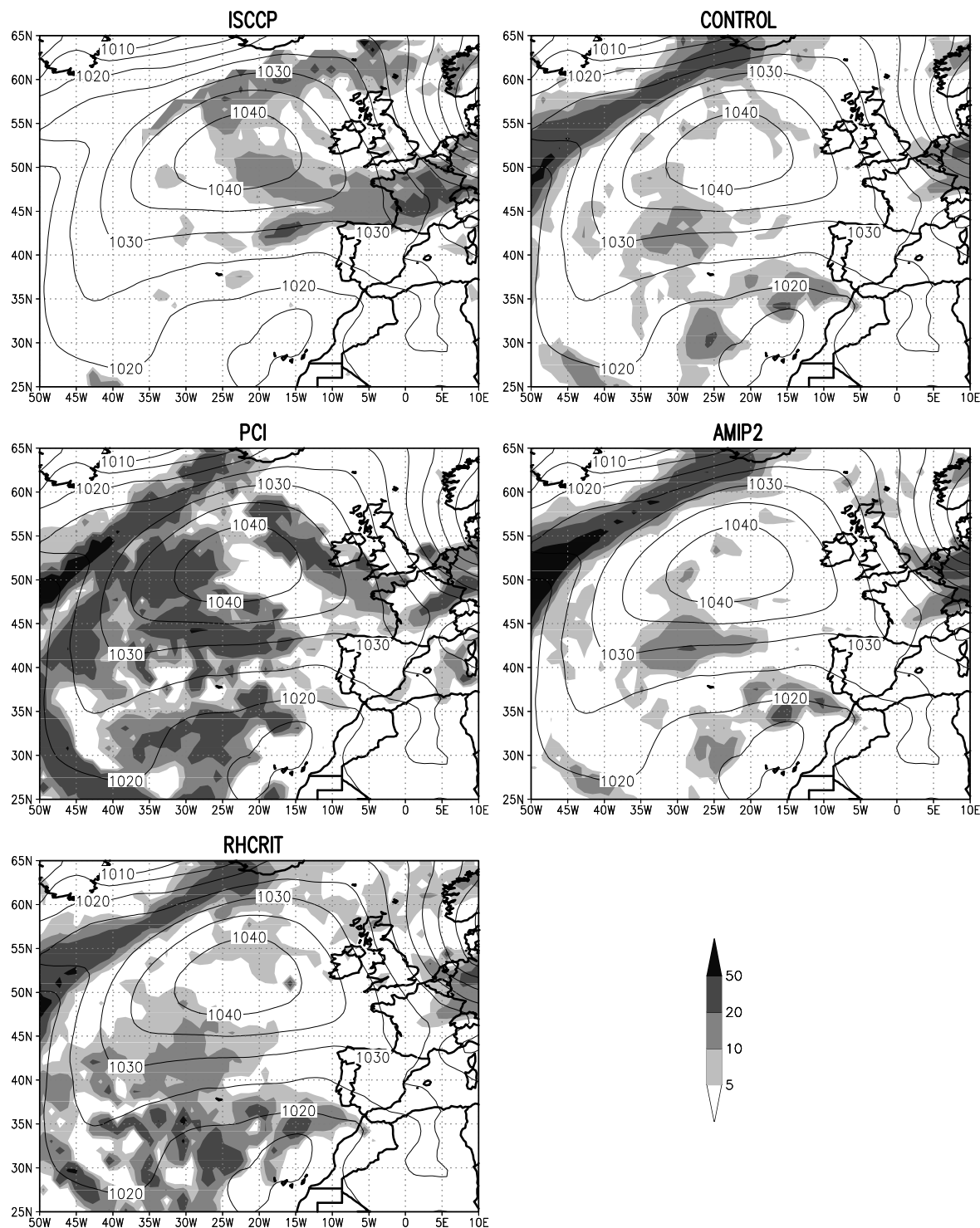


**Figure 5.21:** Same as Figure 5.19 but for one time step during the blocking case [12Z, 19th February 1993].

by ECHAM4 T42 over midlatitude oceans and in subtropical subsidence regions over eastern ocean basins.

### 5.3.5 Detrainment and precipitation efficiency

The effect of the different experiments on the cloud evolution is demonstrated with two quantities, namely the precipitation efficiency and the detrainment of convective cloud water, at one

time step during the development of the East Coast storm. The precipitation efficiency represents the amount of cloud liquid water and cloud ice which is transformed to precipitation during a specified time interval. The detrainment, on the other hand, i.e. the amount of convective cloud water released into the large-scale environment, is an important moistening mechanism which favours the development of stratiform clouds.

Figure 5.22 and 5.23 compare the precipitation efficiency of the CONTROL simulation and the different sensitivity studies at model level 12 ( $\sim 600$  hPa) in the middle troposphere and at model level 8 ( $\sim 250$  hPa) in the upper troposphere, respectively.

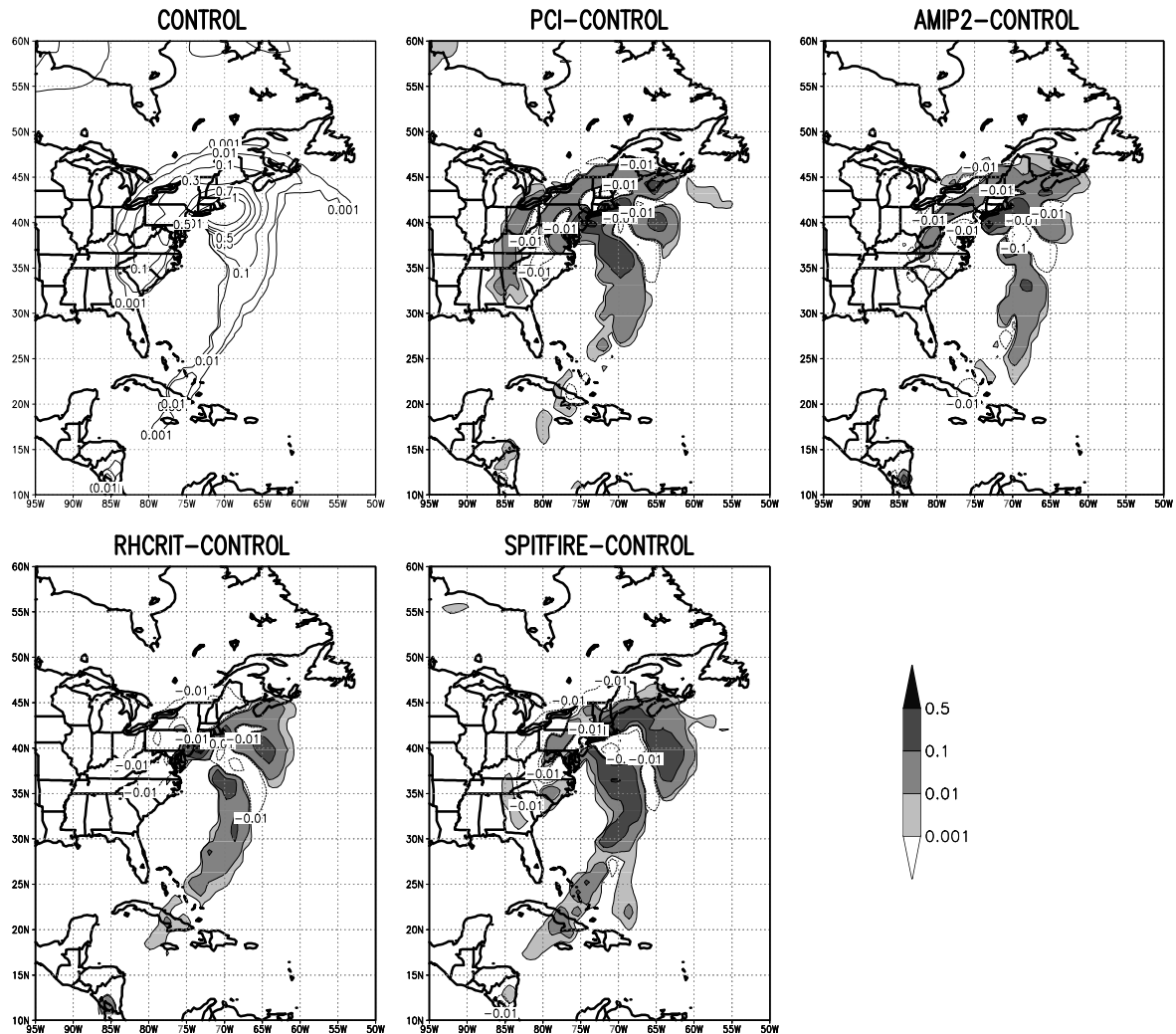


**Figure 5.22:** Precipitation efficiency [ $gh^{-1}$ ] at model level 12 ( $\sim 600$  hPa) of the CONTROL simulation (contoured total values) and differences to the different sensitivity experiments at 00Z, 14th of March 1993. In the difference plots, shaded regions denote stronger precipitation efficiencies in the experiments, while smaller values are found in contoured regions. Contour lines are plotted for  $-0.1, -0.01, 0.01, 0.001, 0.01, 0.1, 0.5 gh^{-1}$ .

All experiments simulate larger precipitation efficiencies in large parts of the fronts compared to the CONTROL simulation. This is not surprising, because it is determined by the cloud water content (liquid + ice). The coarse features of the differences to the CONTROL simulation are similar in the different model simulations. All experiments simulate a reduction of the precipitation efficiency in the northern part of the cold front, probably caused by the following mechanism. According to the “conveyor belt” model of cyclogenesis [e.g. Carlson (1980), Browning (1985) or Browning and Roberts (1996)] warm air rises along the cold front from south to north. Thereby it steadily loses moisture due to condensation and precipitation. Since

precipitation efficiency is coupled with the cloud water content and stronger precipitation efficiency occurs along the cold front in the sensitivity experiments, the moisture is faster removed from the atmosphere, leading to smaller precipitation efficiencies as compared to the CONTROL simulation in downwind parts of the cold front. The region further to the north is on the other hand supplied by rising motion along the warm front containing large amounts of cloud water.

In the PCI simulation differences are largest over the cold continent, in relation to the other experiments, because the precipitation efficiency depends, in addition to the cloud water content, on the number of cloud droplets:  $N (Q_{aut} \sim \frac{LWC^{4.7}}{N^{3.3}})$ . Therefore stronger values occur in regions with lower numbers of cloud droplets.  $N$  is larger over land than over the ocean resulting in a stronger precipitation efficiency over the ocean as compared to the atmosphere over the continent. The stronger precipitation efficiencies over the cold continent in the regions of the warm front and bent-back warm front are caused by larger amounts of cloud water in the middle troposphere (Figure 5.9). Furthermore, the moist air over the eastern U.S.A. is of maritime origin, containing low numbers of cloud droplets.

On the other hand, reduced cloud cover and CWP in pre-frontal regions in the upper troposphere confirm the stronger conversion of cloud water to precipitation in the PCI simulation. This is true for precipitation development over the ice phase and the liquid phase, efficiently removing moisture from the middle troposphere, which is then no longer available for the development of clouds in the upper troposphere.

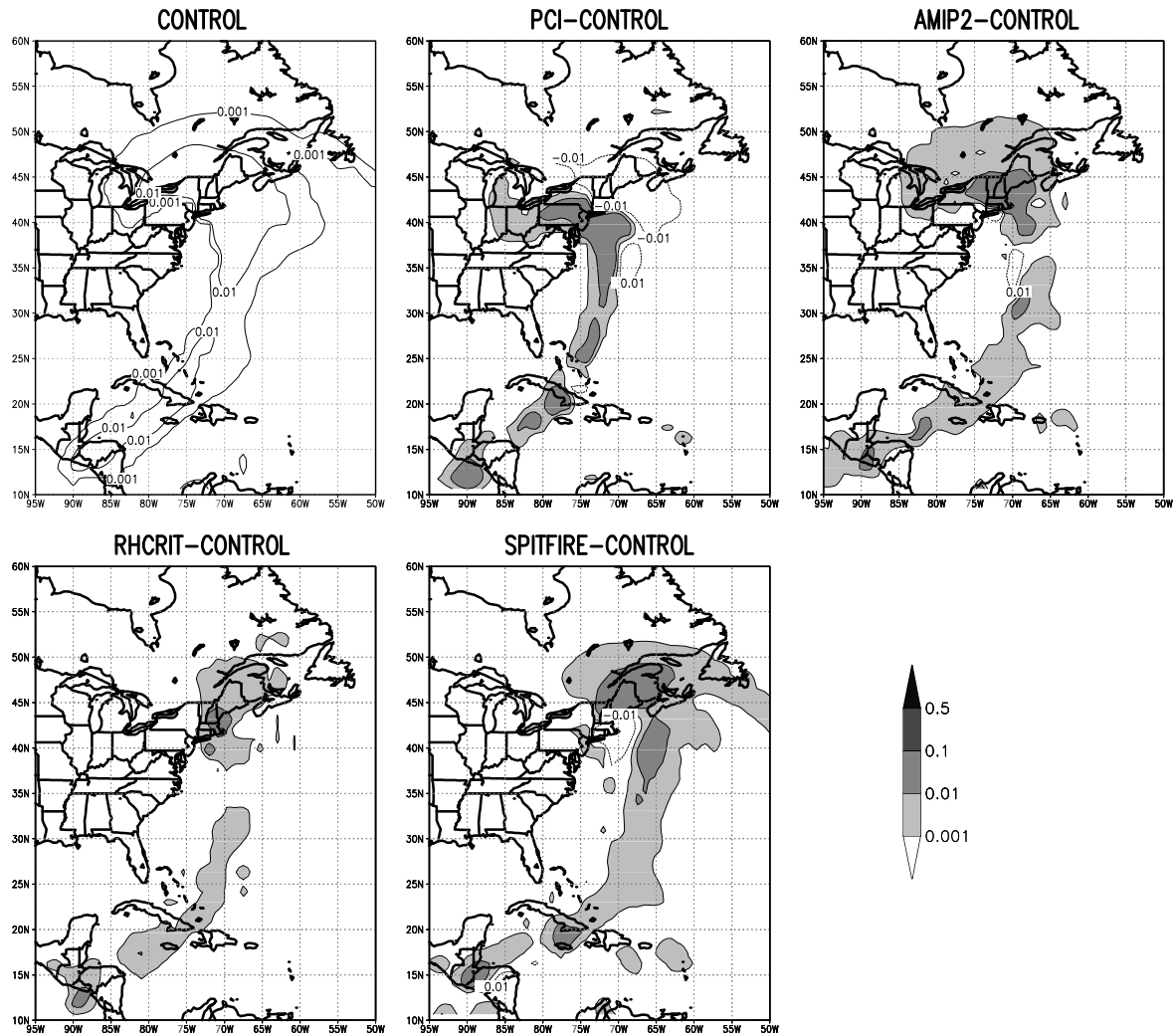


Figure 5.23: Same as Figure 5.22 but at model level 8 (~250 hPa).

Similarly enhanced precipitation efficiencies as in the PCI experiment are simulated by the other experiments. However, in the AMIP2 simulation, it is not as strongly enhanced as the condensation rate. The latter is therefore not balanced by a higher precipitation efficiency, explaining the large cloud amounts and CWP. This is consistent to higher specific humidities and larger amounts of cloud water present in the middle and upper troposphere as compared to the CONTROL simulation (Figures 5.8 and 5.9). In the RHCRIT experiment larger precipitation efficiencies and larger CWP are mostly confined to frontal regions over the warm ocean. Over the cold continent the precipitation efficiency has not changed or is even slightly reduced compared to the CONTROL simulation. The largest precipitation efficiencies in northern parts of the cold front and the large-scale ascent along the warm front occur in the SPITFIRE simulation, illustrating that the changed advection scheme maintains the balance between enhanced condensation and enhanced precipitation development.

In the upper troposphere (Figure 5.23) larger differences to the CONTROL simulation and between the different experiments occur. While changes in the same order of magnitude as the absolute values appear in the middle troposphere, the experiments simulate precipitation efficiencies which are one order of magnitude larger in some regions in the upper troposphere, especially in northern parts of the cold front and in central parts of the large-scale ascent along the warm front. This is explained by larger amounts of cloud water being simulated by the sensitivity studies in the middle and upper troposphere (Figure 5.9). The strongest precipitation efficiencies in the PCI experiment occur in rear parts of the fronts, associated with large amounts of cloud ice being simulated in these confined regions. As in the middle troposphere, strong precipitation efficiencies are simulated in the PCI experiment as compared to the other simulations, confirming its strongest precipitation efficiency in relation to the other experiments even in the upper troposphere. On the other hand, consistent with lower CWPs, the precipitation efficiencies are reduced in pre-frontal regions of the northern cold front and the warm front.

The changes induced by RHCRIT, AMIP2 and SPITFIRE are more similar to each other with stronger precipitation efficiencies occurring along the cold front and in the region of the large-scale ascent. Smallest changes occur in the RHCRIT experiment, associated with smaller amounts of cloud water in the upper troposphere (Figure 5.9).

The changes in the precipitation efficiency lead to large changes in the represented precipitation patterns (not shown). Especially in the northern part of the cold front and in the large-scale ascent along the warm front strong enhancements of large-scale precipitation, with values up to  $1 \text{ mmh}^{-1}$ , occur. On the other hand, the convective precipitation does not reveal systematic tendencies due to the small-scale nature of convection which is only weakly influenced by the adjustment process.

Figure 5.24 and 5.25 compare the detrainment of convective cloud water at the same levels in the middle and upper troposphere. Here larger differences between the experiments occur. The introduced changes along the cold front are attributed to large scattering caused by the small-scale nature of convection which is not forced to the observed state by the adjustment procedure. Therefore no systematic changes occur. The opposite is true in the northern part of the cold front and the large-scale ascent, where the influences of large-scale processes are more important.

In the PCI simulation, compared to the other experiments, the scattering is largest in the region of the large-scale ascent, while more systematic changes occur in the southern part of the cold front, where larger amounts of liquid water are detrained into the large-scale environment. Furthermore, a systematically lower detrainment occurs in the northern part of the cold front. This is also visible in the other experiments, but not as pronounced as in the PCI simulation.

AMIP2, RHCRIT and SPITFIRE generally enhance the detrainment of cloud water in the region of the large-scale ascent and in the northern part of the cold front apart from a region

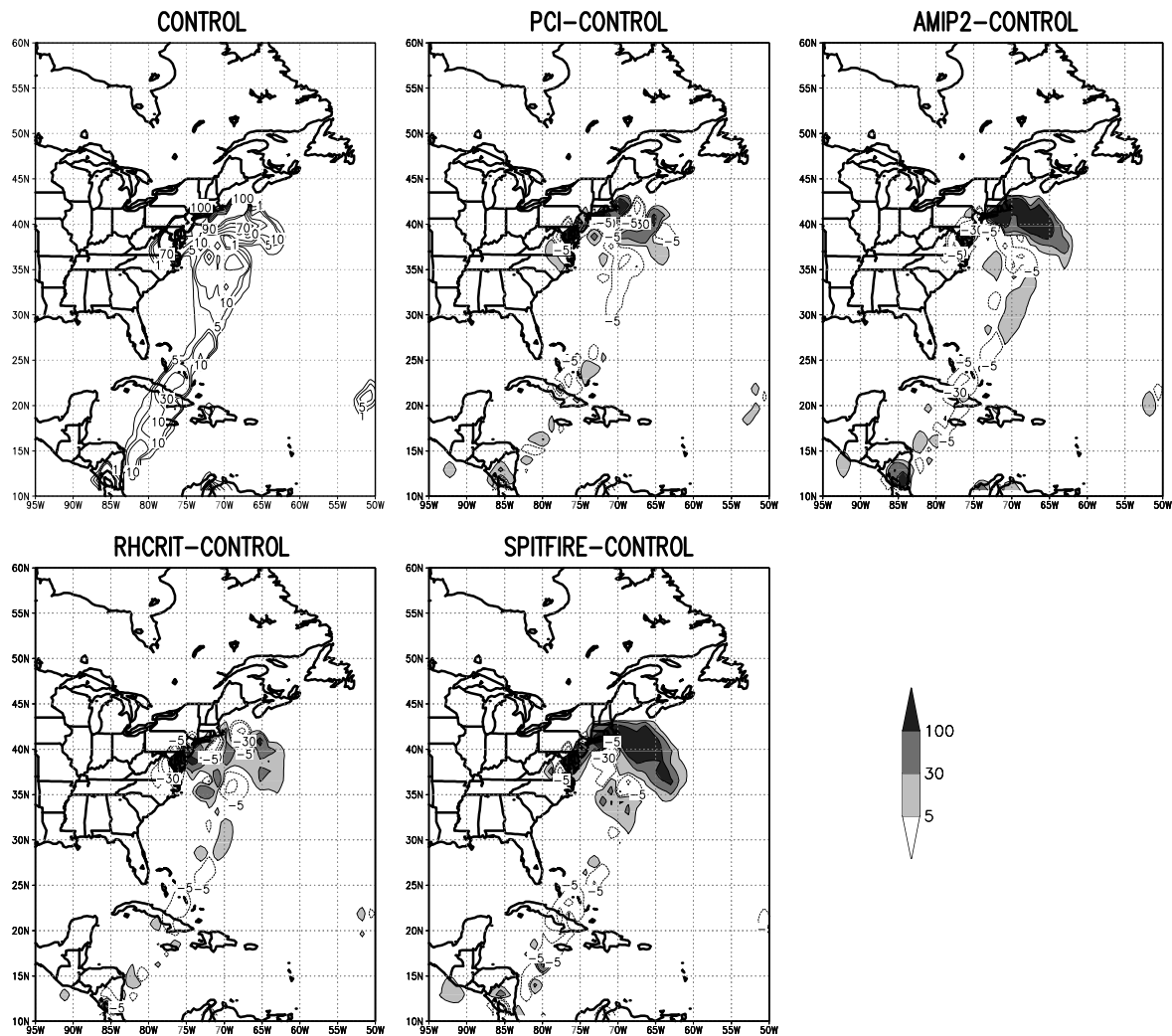


**Figure 5.24:** Detrainment of convective cloud water [ $gh^{-1}$ ] of the CONTROL simulation (upper left plot) and differences to the sensitivity studies at model level 12 ( $\sim 600$  hPa) [00Z, 14th of March 1993]. In the difference plots, shaded regions denote stronger detrainment in the experiments, while smaller values are found in contoured regions. Contours are plotted for -100, -30, -5, 5, 30 and 100  $gh^{-1}$ .

with reduced values between cold and warm front similar to the tendency observed during the comparison of the precipitation efficiency. The absolute changes are similar in the AMIP2 and the SPITFIRE experiment, although the condensation is stronger in the AMIP2 experiment. As the precipitation efficiency in SPITFIRE is larger than in AMIP2 (Figure 5.22), larger amounts of moisture are transported to higher levels of the troposphere in the AMIP2 simulation (Figure 5.8). The changes introduced by RHCRT are smaller than in AMIP2 and SPITFIRE.

In the upper troposphere smaller changes occur, except in the AMIP2 experiment. Here stronger detrainment of convective cloud water occurs in the region of the large-scale ascent and, different to the situation in middle levels of the troposphere, also along the cold front. The stronger detrainment along the warm front is caused by a stronger upward transport of moisture and larger amounts of cloud water being simulated in the upper troposphere. The enhancement along the cold front is caused mainly by a changed tuning parameter in the convection scheme. The constant controlling the amount of detrained convective cloud water reaching the model level above the main detrainment layer is changed from 0.1 to 0.33, leading to larger amounts of cloud water in higher levels.

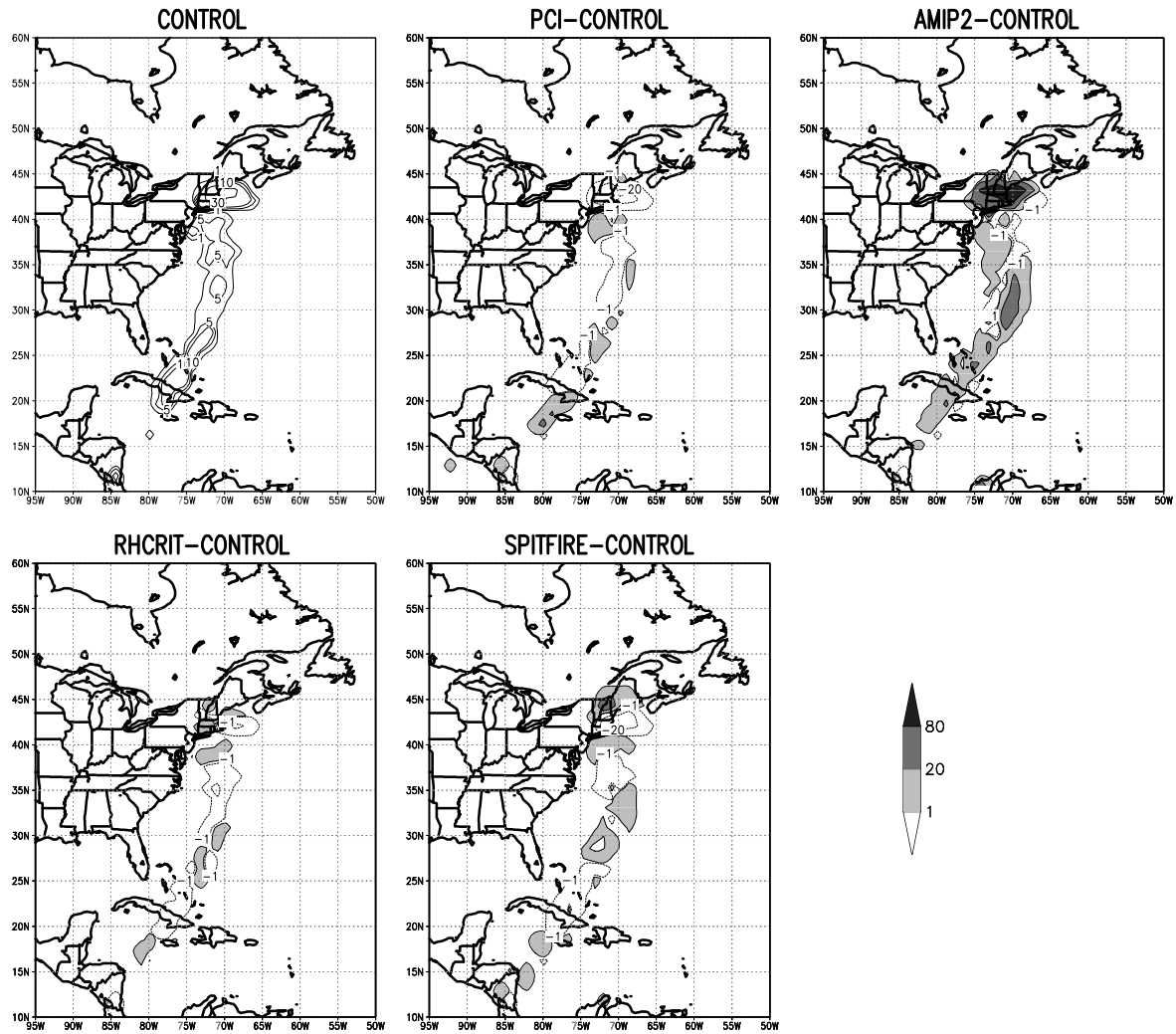
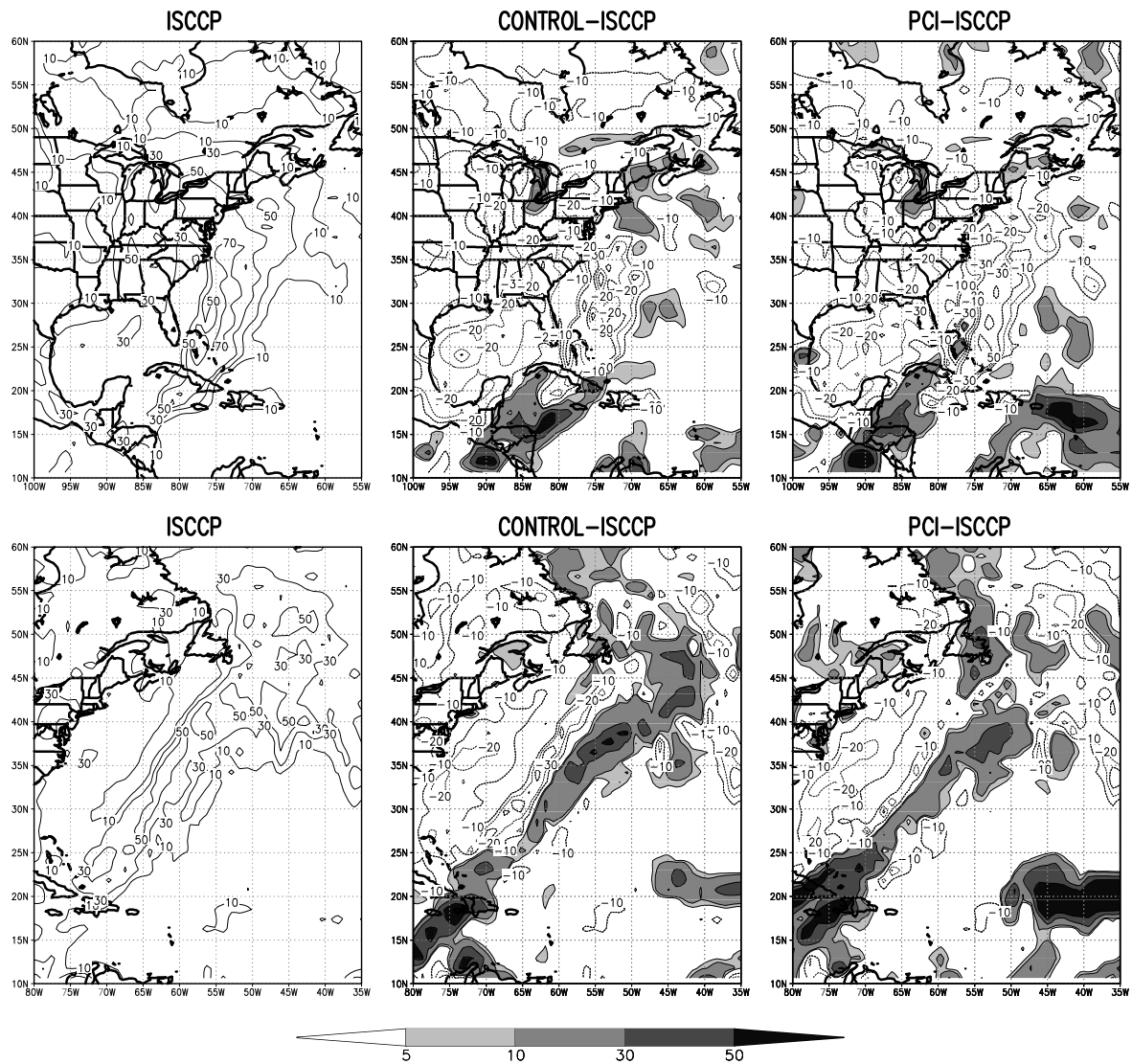


Figure 5.25: Same as Figure 5.24 but at model level 8 ( $\sim 250$  hPa).

### 5.3.6 Brightness temperature

To investigate how the differences in cloudiness influence the infrared part of the radiation in the different experiments, Figures 5.26 and 5.27 show the brightness temperature effect of clouds, defined in equation (4.4), for the ISCCP satellite observation and differences to the CONTROL simulation and the sensitivity experiments for the mature and dissipating stage of the development in the blizzard case.

Some general differences between the model simulations and the observation are obvious. The model tends to overestimate the effect of clouds in southern parts of the cold front indicating the simulation of higher clouds. This is true for the mature as well as the dissipating stage and the bias has similar values in each experiment. However, the optical thickness is underestimated in the dissipating stage as compared to satellite observations (Figures 5.19 and 5.20), suggesting that cirrus clouds are overestimated, while low and mid-level clouds are underestimated in the model simulations. Apart from its southern part, the cloud effect is systematically underestimated along the cold front in the mature stage of the development, indicating that the cloud tops are lower in the model simulation, caused by insufficient convective activity. The effect of clouds is overestimated in the pre-frontal regions of the cold and warm front in the dissipating stage. This systematic difference occurs with similar strength in each experiment and is explained by the overestimated pre-frontal cirrus clouds. Large differences between the



**Figure 5.26:** IR brightness temperature effect [ $K$ ] of ISCCP DX (left column, contours are: 10, 30, 50 and 70  $K$ ) and differences CONTROL-ISCCP (middle column) and PCI-ISCCP (right column) for the mature (18Z, 13th of March 1993, upper row) and dissipating (18Z, 14th of March 1993, lower row) stage in the blizzard case. In shaded regions of the difference plots the model overestimates the brightness temperature effect, while an underestimation occurs in contoured regions. Contours are drawn for: -50, -30, -20, -10, 5, 10, 30 and 50  $K$ .

sensitivity experiments occur in the representation of the large-scale ascent in the mature stage. Conversely, in rear parts of the fronts and in the cold air behind the cold front, the cloud effect is systematically underestimated. The underestimation in rear parts of the cold front indicates a misplacement of the strongest convective activity in the model simulations, caused by the relatively coarse horizontal resolution. The underestimated brightness temperature effect in the cold air behind the cold front is consistent with the underestimated convective activity suggested during the comparison of the cloud optical thickness. None of this biases is changed significantly by any of the simulations, although some differences between the experiments occur.

In the large-scale ascent along the warm front and in pre-frontal regions of the cold front, the cloud effect is smaller in the PCI experiment as compared to the CONTROL simulation. This is true in the mature as well as in the dissipating stage of the development. This difference is caused by smaller amounts of high-level clouds in pre-frontal regions and reduces the positive bias as compared to the satellite observation. On the other hand a stronger effect of clouds is simulated in rear parts of the cold front compared to the CONTROL simulation, reducing the negative

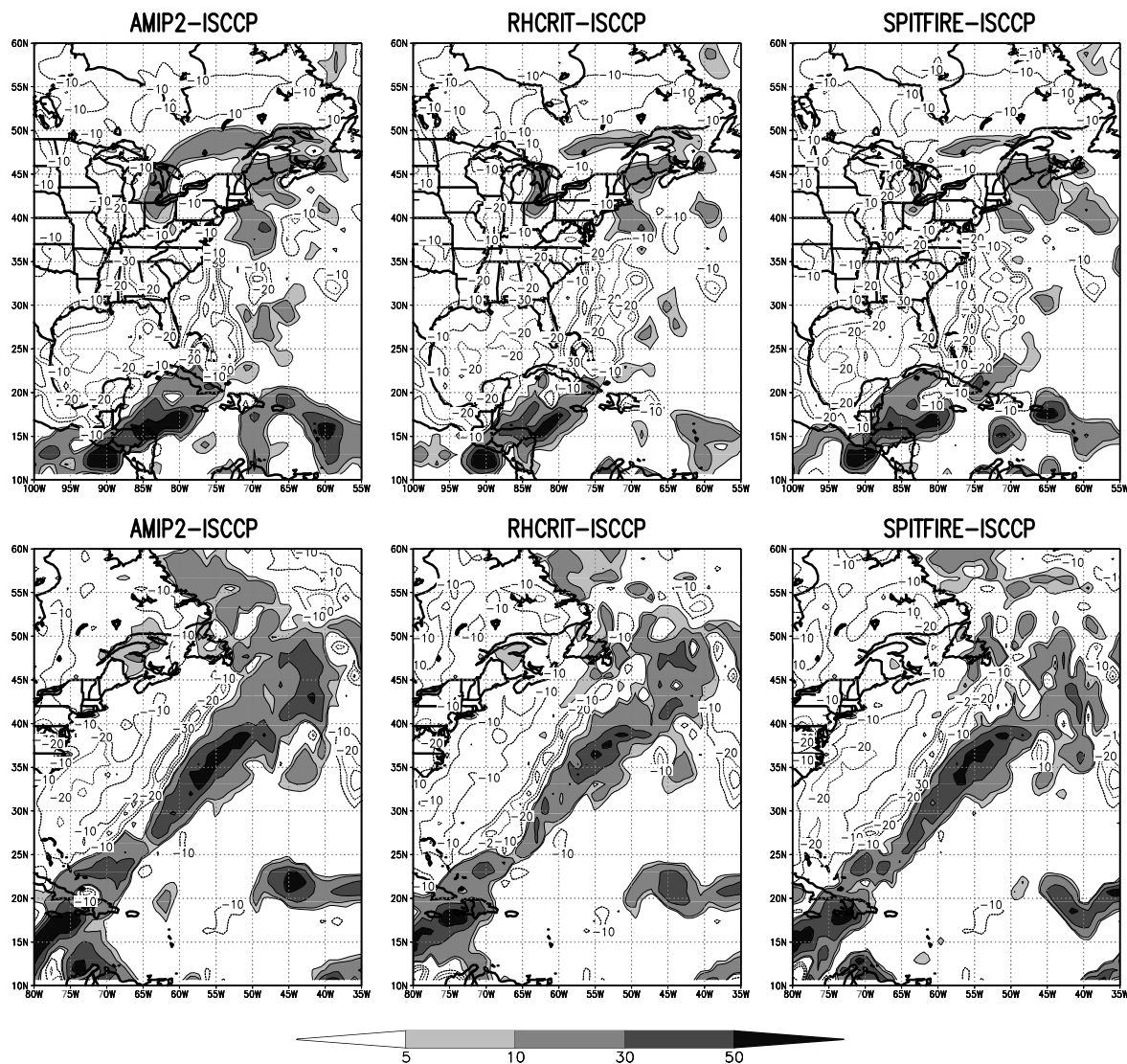


**Figure 5.27:** Same as Figure 5.26 but for the differences AMIP2-ISCCP (left column), RHCRIIT-ISCCP (middle column) and SPITFIRE-ISCCP (right column).

bias compared to ISCCP. However, the brightness temperature effect is still underestimated. Reduced cloud effects in pre-frontal regions and stronger effects in rear parts lead to more pronounced fronts with stronger gradients to its environment.

Compared to the CONTROL simulation the effect of clouds is generally enhanced in the AMIP2 experiment in large regions along the fronts in the mature stage of the development, indicating higher clouds in those regions. This reduces the difference to the observations along the cold front but enlarges the overestimation of the cloud effect in the region of the large-scale ascent. The same is true for the dissipating stage, where the positive bias of the cloud effect in pre-frontal regions of the cold front and in upwind regions of the warm front are even stronger than in the CONTROL simulation.

The changes induced by RHCRIIT are small compared to the CONTROL simulation and contain no systematic behaviour apart from slightly higher cloud effects along the cold front in both stages of the development and behind the cold front in the dissipating stage. SPITFIRE enhances the cloud effect compared to the CONTROL simulation in pre-frontal regions of the cold front and in upwind regions of the large-scale ascent. While the enhancements along the cold front are confined to southern parts in the mature stage, a generally enhanced cloud effect in pre-frontal regions of the cold front occurs in the dissipating stage.

As in the validation section evolution histograms are compared for the model simulations and the CLAUS dataset. This is done in Figure 5.28 for the blizzard case and in Figure 5.29 for the blocking case. In general the evolution histograms of the different experiments are similar for the blizzard as well as the blocking case. Apart from the strong peak on the warm side of the histogram representing the variability of the surface temperature and the effect of the low-level clouds, a second peak occurs in the upper troposphere around 240 K in the histogram for the blizzard case, strongest in the first half of the observed period, representing upper level clouds developing in the blizzard case.

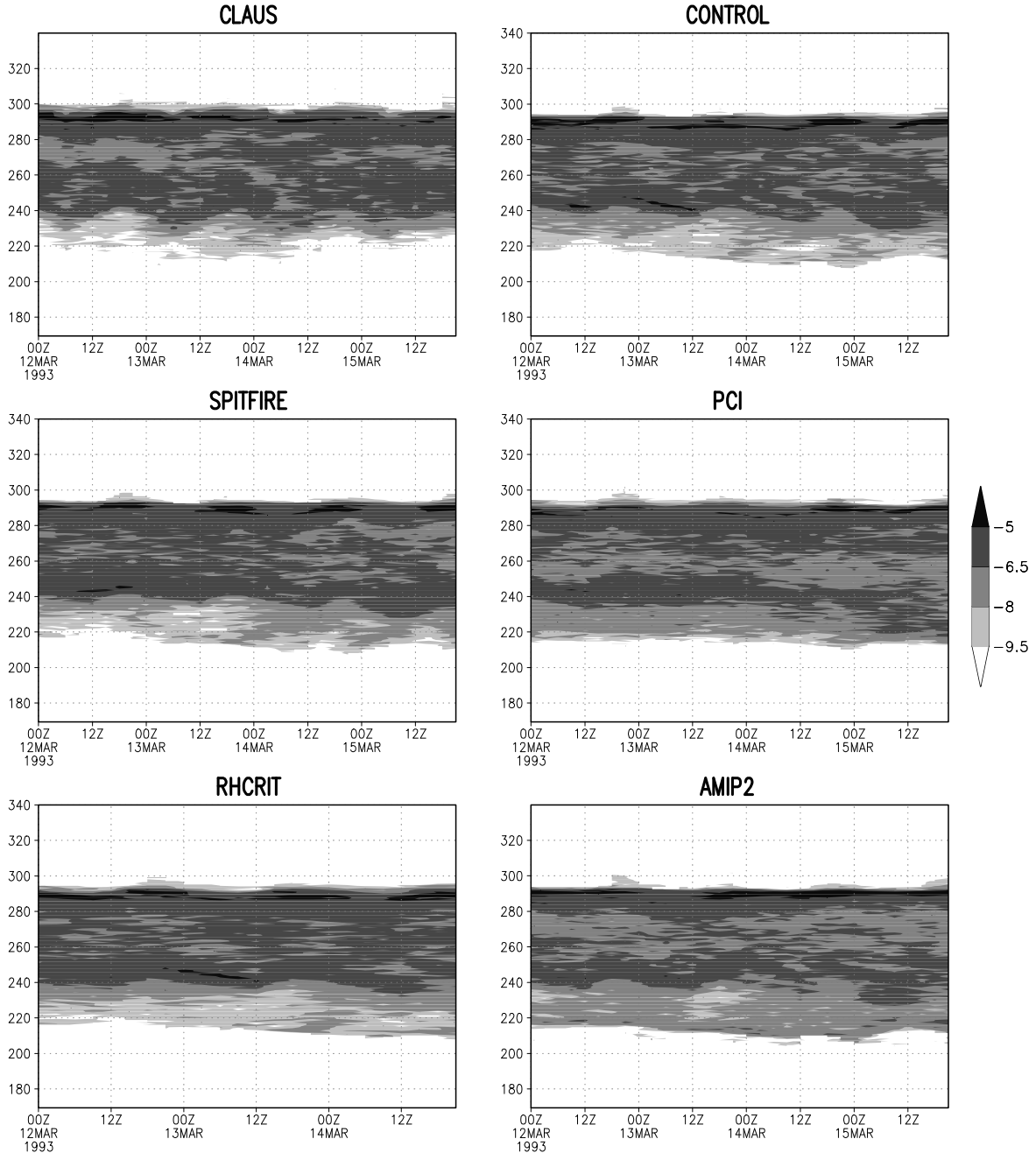


**Figure 5.28:** Evolution histogram of the IR brightness temperature  $T_{Br}$  of the ISCCP observation, the CONTROL experiment and the sensitivity studies for the blizzard case. An increase by one unit corresponds to a doubled occurrence probability.

Surface temperatures are calculated in the same way in all experiments except for AMIP2, where a new implicit formulation is introduced, so that differences on the warm side of the histogram are mainly caused by differences in low-level cloudiness. As the implicit surface scheme needs

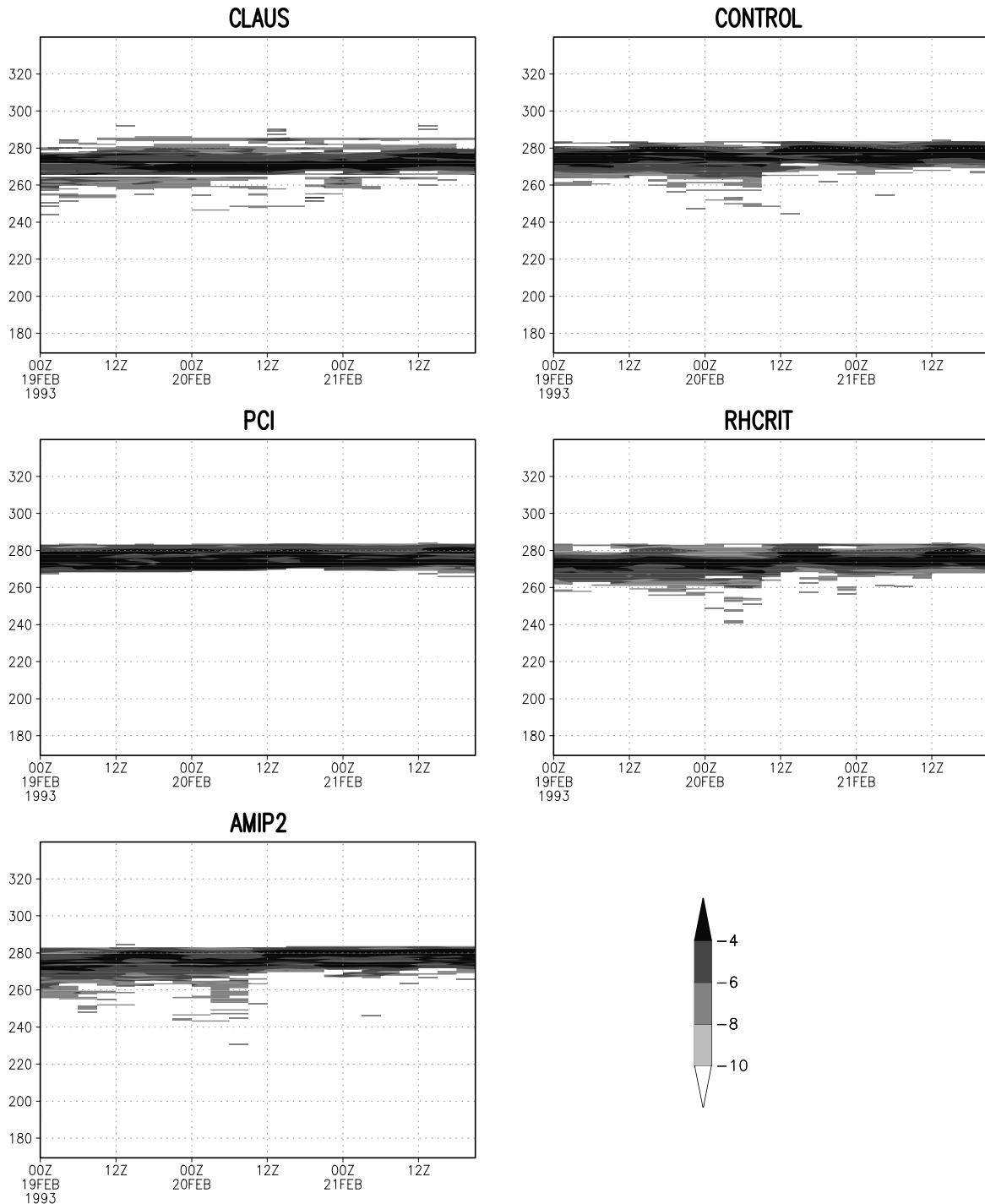


**Figure 5.29:** Same as Figure 5.28 but for the blocking case.

at least half a year to reach its new balanced state, the same is true for the AMIP2 simulation.

The largest difference in the lower troposphere is the more pronounced diurnal cycle in the SPITFIRE experiment. The afternoon maxima are separated better as compared to the other experiments and the CONTROL simulation. This shows the effect of a stronger vertical advection leading to larger low-level cloud amounts during periods of stronger turbulent exchange and indicates a stronger response to the radiative forcing. RHCRT shows a similar diurnal cycle, although low-level cloud amounts are generally higher. The same is true for AMIP2 especially in the second half of the observation period. In the PCI simulation the amount of low-level clouds is reduced during the strongest development with larger values occurring before and af-

terwards. This is probably explained by a more frequent occurrence of cloud in higher levels of the troposphere.

Differences also occur in mid-level cloud cover. PCI and AMIP2 simulate smaller cloud amounts as compared to the other simulations. Lowest probabilities occur in the second half of the observation period between 12Z 14th of March and 00Z 15th of March 1993 in the PCI simulation. This is probably caused by the stronger precipitation efficiency in relation to the other experiments. SPITFIRE clearly enhances mid-level cloudiness in the first half of the observation period during the development of the East Coast storm with lower values in the second part. The opposite signal is found in the CLAUS (and ISCCP) observations, indicating a more even vertical distribution during the development of the cyclone. Compared to the other experiments RHCRIT simulates larger cloud amounts in middle levels of the troposphere because of the reduced condensation threshold.

The diurnal cycle of upper tropospheric cloudiness in the different simulations and the CLAUS observation is anti-correlated with the diurnal cycle in the lower troposphere. The strongest oscillation is found in the CLAUS observation. From all the model simulations, the diurnal cycle is best reproduced in the CONTROL simulation, although the amplitude is weaker than observed. The SPITFIRE and the AMIP2 experiment reproduce the phase of the oscillation, whereas the amplitude is clearly underestimated compared to the observations, caused by the reduced sedimentation of ice crystals. The RHCRIT experiment shows a longer period as well as a reduced amplitude of the oscillation, while no diurnal cycle of the upper level cloudiness is reproduced in the PCI simulation. The latter is caused by the slowest removal of ice crystals in the upper troposphere as compared to the other experiments (Figure 5.13).

Another systematic difference of the experiments compared to the CLAUS observation is the lower variability of high-level clouds during the observed period. ECHAM4 tends to overestimate high-level cirrus clouds around 240 K, caused by the coarse vertical resolution of 1.5 to 2 km in the upper troposphere, indicating an underestimated removal of ice crystals in the model simulations. The lowest variability occurs in the PCI experiment, where the cloud top temperature remains constant at 220 K during the whole period because of the slow removal of ice crystals.

In the histogram of the blocking situation the largest scattering on the warm side of the strongest peak is found in the CLAUS observation, caused by the variability of the measured skin temperature. Differences between the CONTROL simulation and the sensitivity experiments are on the other hand caused by differences in the representation of low-level cloudiness.

The CONTROL simulation and the AMIP2 experiment show similar distributions, with small variations on the warm side of the histogram and an indication of a diurnal cycle in low-level cloudiness. The largest difference between the two experiments is a slightly larger probability for the occurrence of mid- and high-level clouds in the AMIP2 experiment. PCI, as in the blizzard case, simulates the most uniform cloud distribution with the lowest variability on the warm as well as the cold side of the histogram. However, an indication of a diurnal cycle is reproduced. RHCRIT experiences the strongest variability on the warm side of the histogram and the strongest diurnal cycle. This is consistent with the results revealed by the Hovmöller diagram (Figure 5.13) of the cloud distribution. Both a stronger diurnal cycle, as well as a larger near surface variability, support the assumption of a stronger response of the condensation to the changed conditions in the lower model troposphere in the RHCRIT experiment.

# Chapter 6

## Conclusions

### 6.1 Discussion of the results

In this thesis the representation of synoptic scale cloud systems in the ECHAM4 model has been investigated. Instead of looking at monthly mean values of cloud cover and cloud properties, as it is usually done for the validation of a climate model, the development of such systems in a higher temporal and horizontal resolution has been investigated. Important tasks are the validation of the 3D structure of the cloud fields and finding the answer to the question of whether the reasonable climatological representation of clouds is the result of realistically reproduced cloudiness in the synoptic scale - or more generally: **Is the well reproduced climate in the model the result of well reproduced weather phenomena ?**

There are two possible approaches to cope with the tasks mentioned above. First, the systems evolving in the model (if present) can be investigated in detail and their characteristic features can be compared with observations in typical systems. However, synoptic systems occurring on Earth show a wide variety of different features. Even one type of system occurring in different regions on the globe experiences differences. A possible solution is to calculate an average system from an ensemble of synoptic systems of one type in a distinct region on the globe. The characteristic features of this averaged system can then be compared with the features occurring in reality. This approach has been chosen by [Lau and Crane \(1995\)](#) and [Chen and Roeckner \(1999\)](#). However, this approach does not answer the question of whether the model is able to reproduce single synoptic systems and their temporal development in a realistic way.

To be able to compare the model simulation with observations from single synoptic systems in a higher temporal resolution, it is necessary to force the model to the observed state. In weather forecast models this is done with a data assimilation scheme which is not yet available for the ECHAM model.

Here a dynamical adjustment approach has been chosen based on the Newtonian relaxation technique (nudging) [e.g. [Anthes \(1974\)](#), [Hoke and Anthes \(1976\)](#) or [Krishnamurti et al. \(1991\)](#)]. It adds a non-physical relaxation term to the model equations at every time step to force the model dynamics to the observed track. As suggested by earlier investigations [e.g. [Kuo and Guo \(1989\)](#), [Brill et al. \(1991\)](#) or [Jeuken et al. \(1996\)](#)] the quantities which have been forced are vorticity, divergence, temperature and the logarithm of surface pressure. As “observations”, 6 hourly fields of the ECMWF reanalysis have been used. They are linearly interpolated to get the necessary data for the time steps in between two “observations”. The moisture has not been forced, because the purpose of this thesis was to emphasize the dynamical processes. Furthermore, large spin-up errors occur in the moisture field of the ECMWF reanalysis. Since the purpose of this thesis is to validate the model parameterizations, the forcing should influence the model physics as little as possible. The strength of the forcing is determined by an adjustment

time scale for every variable. Here values suggested by [Jeuken et al. \(1996\)](#) were used. They are large enough to force the model dynamics to the observed state within a few days, but too small to remove errors produced by the physical parameterization schemes. The main advantage of the adjustment procedure as compared to standard data assimilation schemes is the more gradual forcing to the observed state, which reduces the amount of meteorological noise introduced into the model.

For the investigation three different synoptic situations in the period February and March 1993 were chosen. The choice was guided by the purpose to cover a large range of situations. As an example of midlatitude cyclones, an extraordinary strong cyclone, which developed between the 12th and 14th of March 1993 along the East Coast of the U.S.A. was investigated in detail. East Coast storms are one of the main weather concerns of that region developing regularly between December and April, triggered by strong temperature gradients between the warm ocean and the cold continent.

Midlatitude and subtropical anticyclones were represented by an Atlantic blocking situation. Such events are climatologically very important because of its large influence on local and hemispheric flow patterns ([Tibaldi et al., 1997](#)) and occur frequently in regions of the storm tracks over the Pacific and Atlantic ocean. Although they can occur in all seasons, the strongest systems with the longest durations occur during winter. Here a typical situation was chosen, which developed between the 15th and 23rd of February 1993 over the North Atlantic.

As a third situation tropical convection in the western Pacific warm pool region was chosen. As a heat and moisture source for the upper troposphere it is an important engine for the tropical circulation. It has for example a strong influence on the “tropical easterly jet”, the upper tropospheric “return flow” of the northern hemispheric summer monsoon ([Dümenil and Bauer, 1998](#)). Furthermore the moisture transported into the upper troposphere and the convective cloud water detrained into the large-scale environment strongly influence the radiation budget. Here a situation, which developed during the TOGA-COARE experiment was chosen.

A synoptic validation confirmed that the adjustment approach does a good job in forcing the model to the observed state for the two midlatitude systems. For tropical convection on the other hand this is not the case. The reason is a much stronger dependence of convection on local conditions like SST or surface heat fluxes rather than the large-scale circulation. Furthermore the ECMWF reanalysis, used as a surrogate for in-situ observations, is partly a model product, depending on the amount of observations which are assimilated into the forecast model. In the tropics only few observations are available. Therefore the forcing files used as input for the adjustment are more or less pure model products. Since the observed cloud systems cannot be reproduced by the adjusted simulation, the third situation was neglected for the validation.

Together with the synoptic validation, an investigation was conducted to see whether an AMIP simulation, which is not forced to the observed state, is able to reproduce the investigated systems. During the course of this investigation it was found, that the cyclone development along the East Coast of the U.S.A. is reasonably well reproduced in the AMIP simulation. For blocking situations this was shown by [Tibaldi et al. \(1997\)](#) for the older model version ECHAM3 and by [Tschuck \(1998\)](#) and [D’Andrea et al. \(1998\)](#) for ECHAM4, whereas tropical convection was investigated by [Lohmann et al. \(1995\)](#). They confirmed that the main features of tropical convection are well reproduced in the model.

The richest source of observations for the cloud validation is provided by the ISCCP DX dataset. It contains observations of cloud cover, brightness temperature in the thermal-infrared window (10.5 - 12.5  $\mu\text{m}$ ), cloud top pressure and cloud optical thickness. These quantities are either directly provided by the model or can be calculated from the model output. Furthermore ISCCP provides an algorithm, which translates a value of the cloud optical thickness and cloud top pressure into one of 9 cloud types. This is important, because the influence on the radiation

budget depends on cloud type (Hartmann, 1993). For the relative humidity no observations by ISCCP are available. Therefore radiosonde profiles have been used for the validation.

In the cloud cover validation the ECMWF reanalysis has been included as an alternative model product to investigate the effect of different cloud cover descriptions. While the cloud cover is diagnostically calculated from the relative humidity in the ECHAM4 model, a prognostic approach is used in the ECMWF reanalysis, taking the transport of cloud area, the formation of cloud area by convection, stratiform condensation and turbulence and the evaporation of cloud area into account. In spite of these different approaches, the cloud cover is similar in the two model simulations with large differences occurring compared to the observations (van Meijgaard et al., 1999). This demonstrates that the reanalysis should not be used for the validation of clouds.

Although the model is able to capture the coarse structure of the cloudiness, the horizontal distribution as well as the 3D structure, systematic differences to ISCCP observations occur. They are listed in the following enumeration.

- Underestimation of total cloud cover.
- Underestimation of low- and mid-level cloud amounts.
- Underestimation of the cloud optical thickness in large parts of the large-scale ascent in the mature stage of the system.
- Underestimation of the IR brightness temperature effect in the developing stage of the cyclone.
- Overestimation of the IR brightness temperature effect in the dissipating stage of the cyclone.
- ECHAM4 cannot reproduce the observed cloud distribution in the blocking situation.
- ECHAM4 underestimates cloudiness in the convectively influenced region behind the cold front.

In the following possible causes for the errors are summarized before suggestions are given how the biases could possibly be reduced.

The underestimation of total cloud cover is caused by an underestimation of low and mid-level cloud amounts. The latter are underestimated because of a too dry middle troposphere leading to the condensation threshold not being exceeded. Reasons are either too weak vertical advection of moisture, an underestimated evaporation of precipitation and/or an underestimated horizontal advection of moisture into the grid box. The differences occurring behind the cold front could be caused by weaknesses in the convection scheme. Only one type of convection is possible in a grid box during one time step, leading to underestimated convective mass fluxes when shallow instead of midlevel convection is switched on. The mentioned underestimation of mid-level clouds could also be caused by weaknesses in the representation of the model dynamics. A too strong subsidence reduces the height of the planetary boundary layer and sharpens the inversion occurring at its top. This is important in central regions of the blocking high. Furthermore, the subsidence suppresses the convective activity, which is important behind the cold front. Moreover, the too coarse horizontal resolution might contribute to the bias, because it reduces convective fluxes in this region of sharp lower tropospheric temperature gradients.

The dissipation of clouds at relative humidities below a threshold value does not correspond to observations in the atmosphere. Walcek (1994) found that no clear value of the critical relative humidity can be defined below which clouds dissipate completely. Nevertheless, this approach

is used in many climate models and leads to an underestimation of cloud cover particularly in middle levels of the troposphere, where largest cloud amounts occur at lowest values of the relative humidity.

The different cloud distributions in the model simulation and the ISCCP observation might be caused by the coarse vertical resolution, smoothing the sharp temperature and moisture gradient at the top of the boundary layer, or by a too strong subsidence above the boundary layer, which would lower the cloud top, corresponding to the results of the cloud top pressure comparison with ISCCP observations.

The underestimation of the IR brightness temperature effect in the developing stage of the system is caused by an underestimation of convective activity, a problem which might be caused to a large part by the relatively coarse horizontal resolution of  $\sim 100 \times 100$  km, smoothing the sharp gradients of temperature and moisture, occurring at the boundary between cold air over the continent and warm air over the Gulf of Mexico. The overestimation in the dissipating stage on the other hand results from an overestimation of cirrus clouds caused by a too weak or too slow removal of ice crystals. The sedimentation rate is parameterized as a function of the ice water content and is tuned to reasonably reproduce global mean ERBE radiation measurements, leading to an underestimated sedimentation for single synoptic situations.

The underestimated total cloud cover could be enhanced by improving the representation of clouds in lower and middle levels troposphere. In ECHAM4 the partial cloud amount at a model level is calculated diagnostically from the relative humidity and the stability of the atmosphere. Here a more sophisticated diagnostic (e.g. by including the dependence on additional predictors such as vertical velocity or turbulent mixing) or even a prognostic calculation (e.g. on the basis of statistical considerations) might help to reduce the difference. Furthermore a reduced condensation threshold or a stronger transport of moisture can lead to an improved representation of clouds in the lower and middle troposphere. A reduced condensation threshold is achieved by using a changed profile of the “critical relative humidity”, with smaller threshold values in lower and middle levels of the troposphere. The stronger transport of moisture into the middle troposphere could be achieved by stronger advection of moisture (horizontally as well as vertically) or by stronger detrainment of cloud water and water vapour from convective clouds. Both could result from a higher horizontal resolution due to the strengthened gradients of temperature and moisture. They would enhance convective mass fluxes, which would provide the vertical velocity necessary for larger vertical advection of moisture.

The underestimated boundary layer cloudiness could be improved by a higher vertical resolution in the boundary layer. This is confirmed by [Bushell and Martin \(1999\)](#), although they note that the cloudiness is still underestimated even with a higher vertical resolution. The overestimated cloudiness in the upper troposphere due to the accumulation of ice crystals could be reduced by an enhanced sedimentation rate. One possibility to achieve this is for example the introduction of a temporal dissipation term, which remove the ice within 5 to 10 hours, which is the observed average lifetime of cirrus anvils in tropical cloud clusters ([Danielsen, 1982](#)).

Sensitivity studies were also conducted for three reasons.

- To confirm or reject the suggested causes for the model errors.
- To test changes, which will be introduced into the upcoming model version ECHAM5, individually from a cloud point of view in order to isolate as much as possible their effects on the representation of the model physics.
- To examine small changes, which might lead to a better description of clouds in the model.

In detail, the following experiments have been carried out:

In the **PCI** experiment, the standard stratiform condensation scheme has been replaced by a more sophisticated one developed by [Lohmann and Roeckner \(1996a\)](#), which treats cloud liquid water and cloud ice with separate prognostic equations. This is associated with a larger number of physical processes being introduced into the model. They lead to a stronger precipitation efficiency, removing moisture from the troposphere more efficiently than in the CONTROL simulation. Therefore, cloud amounts in the upper-tropospheric pre-frontal outflow are reduced, weakening the bias of the overestimated cloud effect in later development stages of the extratropical cyclone. An intensification of the precipitation efficiency in the middle troposphere is therefore a feasible method to reduce the overestimation of cirrus in the upper troposphere. Furthermore, it simulates a moister lower troposphere, strongly improving the representation of clouds in the blocking case. On the other hand, the larger effective radius of ice crystals used in the PCI scheme as compare to the CONTROL simulation leads, together with the reduced CWP, to an underestimated cloud optical thickness as compared to ISCCP observations.

In the **RHCRIT** experiment, the vertical profile of the condensation threshold (“critical relative humidity”) has been changed from an exponential to a polynomial profile following an approach by [Geleyn \(1980\)](#) with smaller values of the condensation threshold in lower and middle levels and larger values in the upper troposphere. It was the intention to force larger cloud amounts in lower and middle levels of the troposphere and smaller values in the upper troposphere as compared to the CONTROL simulation. This small change, compared to the other experiments, leads to the best cloud distribution in the blocking case. At the same time, the fastest reaction to the forcing from the environment is introduced by developing the strongest diurnal cycle in the representation of low-level clouds. This is not surprising, because smaller changes of the relative humidity are necessary to cause changes in cloud cover. In the blizzard case frontal regions are more pronounced, in accordance with cloud optical thickness observations of ISCCP. Furthermore, it is the only experiment, which slightly improves the representation of clouds behind the cold front. This demonstrates, that midlatitude cloudiness in lower and middle levels of the troposphere is very sensitive to the condensation profile and that the profile used in CONTROL simulation might be the cause for the erroneous cloudiness. On the other hand, the changed profile does not reduce the overestimated cloudiness in the upper troposphere, indicating that it is stronger influenced by other processes such as for example the sedimentation of ice crystals. However, the influence is larger in the tropics ([Roeckner, 1999](#)). On the other hand it demonstrates that a changed condensation profile is not a panacea since the underestimated cloud optical thickness in upwind regions of the large-scale ascent is not changed in the mature stage.

In the **AMIP2** experiment, the effects of changes introduced for the AMIP2 experiments on the representation of clouds are tested. A large part of the introduced changes is expected to have no influence on the investigated systems, either due to the too short integration time or due to a small influence in midlatitudes. Of particular importance are a changed numerical implementation of parts of the stratiform cloud scheme ([Lenderink et al., 1998](#)), a more accurate calculation of the saturation water vapour pressure ([Sonntag, 1994](#)), a stronger detrainment of convective cloud water into the level above the main detrainment layer and different values for some of the tuning parameters used in the stratiform cloud scheme. AMIP2 simulates a moister middle and upper troposphere in frontal regions. Therefore, clearly larger cloud amounts are simulated in the three cloud layers, especially along the warm front and the bent-back warm front of the developing cyclone. This leads to well represented cloudiness along the fronts with consistent overcast sky. The modified description of the detrainment of convective cloud water leads to higher cloud tops along the cold front during the life-cycle of the extratropical cyclone and reduces the underestimation of the brightness temperature effect in the developing and mature stage. On the other hand, it increases its overestimation in the dissipating stage of the development, since even larger amounts of ice are accumulated in higher levels of the atmosphere. Furthermore, AMIP2 induces the smallest changes into the cloud distribution in the blocking

situation. This is a surprising result, because [Lenderink et al. \(1998\)](#) have been introduced the numerical changes to improve the representation of stratocumulus clouds.

**SPITFIRE** ([Rasch and Lawrence, 1997](#)) is a new advection scheme, which will replace the semi-Lagrangian scheme ([Williamson and Rasch, 1989](#)) in the upcoming model version ECHAM5. It is less diffusive than the standard semi-Lagrangian scheme, allowing the transport of sharper gradients. This leads to a stronger vertical advection of moisture. As a result the condensation threshold is exceeded earlier with subsequent earlier development of clouds. This induces positive effects on the representation of the cloudiness in lower and middle levels of the troposphere and sharpens frontal boundaries. At the same time the precipitation efficiency is enhanced, so that the temporal characteristics of condensation and precipitation remain nearly unchanged. Therefore the biases in the representation of the brightness temperature effect are not changed.

In addition to the four experiments a new adjustment approach, the so-called “slow normal mode insertion” (NMI) ([Machenhauer and Kirchner, 1999](#)) has been tested. It replaces the slow modes of the model with the corresponding modes of the ECMWF reanalysis, while modes faster than 24h are developed by the model itself. A cut-off time of 24h is used, because modes with periods up to that value have been found to be well balanced in primitive equation models like ECHAM ([Machenhauer, 1977](#)). Since fast modes are the main source of gravity waves, the excitation of gravity waves is strongly reduced by this approach, leading to reduced adjustment tendencies as compared to the standard method ([Jeuken et al., 1996](#)) used in this thesis. But it also raises the question of whether a model, using this kind of adjustment, is able to capture fast meteorological phenomena as rapidly developing extratropical cyclones. Therefore a short simulation of the blizzard case has been performed. Main result is, that the NMI approach is able to force the model dynamics to the observed state even for such fast systems. Encouraging is furthermore, that the distributions of low-level cloudiness and CWP are slightly better represented compared to cloud optical thickness observations of ISCCP, with a sharper development of the post-frontal subsidence and larger cloud amounts behind this dry band as compared to the CONTROL experiment (not shown).

The main results of this thesis are that in addition to a climatological validation, detailed investigations of synoptic situations are necessary to attribute model errors to their causes. By using the dynamical adjustment the model is able to reproduce synoptic-scale cloud systems, although systematic differences to the observations of ISCCP occur. The method is easy to use and enables an efficient testing of modifications of the parameterization schemes within short times, provided that the necessary forcing files are available. For example a test with a changed parameterization for one synoptic situation could easily be performed within one day in the lower horizontal resolution of T42 including post-processing and visualization of the model output. However, it is important to note that the use of this method is restricted to synoptic-scale systems in midlatitudes, since tropical systems depend mainly on the local forcing from the SST and the surface fluxes.

## 6.2 Future work

The work presented here could be extended in many directions. One important task is to test whether ECHAM4 is able to reproduce tropical systems that are more strongly influenced by the large-scale circulation than single convective events. Such phenomena are for example tropical cyclones, monsoon depressions in the Ganges valley or the whole monsoon circulation. Also, the adjustment to observed rain rates should be investigated. [Krishnamurti et al. \(1993\)](#) have shown, that an initialization of a forecast model with observed rain rates strongly improves tropical forecasts even in “difficult” situations like a triple cyclone case over the Pacific. This

approach would enable more detailed validations of parameterization schemes important for the representation of the tropical circulation.

To investigate the influence of a higher horizontal resolution, the calculations could be repeated with a regional model using a clearly finer grid compared to the relatively coarse resolution of T106 (for example REMO with 14 km horizontal resolution). Special interest could be focused on the representation of meso-scale phenomena like rain bands or convectively generated cloudiness behind the cold front.

With the recently developed possibility to produce forcing files from an adjusted simulation, a more detailed investigation of the effects of the introduced changes is possible. In experiments adjusted with the results of the CONTROL simulation, the effects of a changed parameterization could be isolated by preparing differences. Furthermore, this enables a more detailed investigation of the errors caused by the adjustment, when the simulation forced with the reanalysis is compared with a simulation forced by an adjusted CONTROL simulation.

Another interesting extension of this work would be to use the output of a more realistic “cloud resolving model” or from a “large eddy simulation” as a surrogate for in-situ observations. This would enable a more detailed validation of the 3D representation of clouds and cloud microphysical processes in the model.

In this work forecast experiments have only been used to confirm that the adjusted model simulation represents a nearly balanced state, by comparing short forecasts with the adjusted simulation. On the other hand longer forecasts, initialized with a restart file of the adjusted simulation, can be performed. They would allow a more detailed investigation of the “drifting characteristics” of the model.

Last but not least, much more experiments are conceivable, either with other changes in the physical parameterization schemes, or with other synoptic situations.

- Changed cloud overlap assumption.
- Changed method for the calculation of the partial cloud cover at distinct model levels.
- Changed description of the sedimentation rate of ice crystals.
- ECHAM5.
- More efficient evaporation of precipitation.
- Parameterization of cloud cover
- Lee cyclogenesis
- Tropical cyclones
- Monsoon depressions
- ...

**Acknowledgments:**

In particular I am thankful to Prof. Dr. Lennart Bengtsson who enabled me the preparation of this interesting thesis at the Max Planck Institute. His never ending enthusiasm in our long and fruitful scientific discussions and his expert advice were highly motivating.

I am very grateful to Prof. Dr. Hartmut Graßl for his interest in the subject and willingness to examining the thesis.

Many thanks to Erich Roeckner. His profound knowledge of the ECHAM4 model and his calm and thoughtful way of discussing scientific topics were always a great help.

Johann Feichter, Martin Stendel, Ingo Kirchner, Ulrike Lohmann, Adrian Tompkins and Andreas Rhodin are acknowledged for all their suggestions brought in. I am furthermore grateful to Johann Feichter, Martin Stendel and Ingo Kirchner for their help in the preparation and debugging of the model for the simulations and for making available the necessary forcing files; to Andreas Rhodin for the supply of the brightness temperature data; to Ulrike Lohmann for kindly providing the climatologies of cloud cover, CLWP and precipitable water; to Christian Klepp for the preparation of some figures of SSM/I observations and to Norbert Noreiks for kindly serving me with the figures of the energy cycle and the hydrological cycle for the introduction.

In addition, Adrian Tompkins and Ulrike Lohmann are thanked for carefully reading the manuscript. They not only improve grammar and spelling, but also gave useful comments on the scientific content. I am furthermore grateful to Stefan Hagemann for critically reviewing the contents of the CD-ROM.

I am indebted to the UCAR Joint Office for Science Support and to the NASA Langley Research Center EOSDIS Distributed Active Archive Center. From the former I obtained the COMET data, while the latter provided the ISCCP DX observations.

Furthermore Uwe Schulzweida, Luis Kornblueh and Reinhard Budich are thanked for their tireless computational assistance and Michael Böttinger from the German Climate Computing Centre (DKRZ) for his help with the 3D visualization of the data.

Phillip Rasch from NCAR is acknowledged for all his efforts to furnish me with the GEMPAK meteorological package, which enabled the use of the COMET data.

Last but not least thanks to my family for their unbroken patience and encouragement during the preparation of this thesis.

# Bibliography

- Anderson, J. L., 1993: The climatology of blocking in a numerical forecast model. *J. Climate*, **6**, 1041–1056.
- Anthes, R. A., 1974: Data assimilation and initialization of hurricane prediction models. *J. Atmos. Sci.*, **31**, 702–719.
- Barkstrom, B., E. Harrison and R. Lee III, 1990: Earth Radiation Budget Experiment. *EOS*, **71**, 297–305.
- Barry, R. G. and R. J. Chorley, 1987: *Atmosphere, Weather and Climate*. Routledge, New York, 5th edition. 460pp.
- Baumgartner, A. and E. Reichel, 1975: *The world water balance*. Elsevier, Amsterdam, The Netherlands. 179pp.
- Bengtsson, L., 1991a: Advances and prospects in numerical weather forecasting. *Quart. J. Roy. Meteor. Soc.*, **117**, 855–902.
- Bengtsson, L., 1991b: Numerical prediction of atmospheric blocking - a case study. *Tellus*, **33**, 235–269.
- Bergeron, T., 1970: Mesometeorological studies of precipitation. IV: Orographic and convective rainfall patterns. Report No. 20, Department of Meteorology, Uppsala, Sweden.
- Bjerknes, J., 1919: On the structure of moving cyclones. *Geophys. Publ.*, **1**, 1–8.
- Bjerknes, J., 1951: Extratropical cyclones. In: *Compendium of Meteorology*, T. Malone, ed., pp. 577–598. American Meteorological Society, Boston, Massachusetts.
- Bjerknes, J. and H. Solberg, 1922: Life cycle of cyclones and the polar front theory of atmospheric circulation. *Geophys. Publ.*, **3**, 1–18.
- Brest, C. L. and W. B. Rossow, 1992: Radiometric calibration and monitoring of NOAA AVHRR data for ISCCP. *Int. J. Remote Sens.*, **13**, 235–273.
- Brill, K. F., L. W. Uccellini, J. Manobianco, P. J. Kocin and J. H. Hohman, 1991: The use of successive, dynamic initialization by nudging to simulate cyclogenesis during GALE IOP 1. *Meteorol. Atmos. Phys.*, **45**, 15–40.
- Brinkop, S. and E. Roeckner, 1995: Sensitivity of a general circulation model to parameterizations of cloud-turbulence interactions in the atmospheric boundary layer. *Tellus*, **47A**, 197–220.
- Bromwich, D. H., 1990: Estimates of Antarctic precipitation. *Nature*, **343**, 627–629.
- Browning, K. A., 1985: Conceptual models of precipitating systems. *Meteor. Mag.*, **114**, 293–316.

- Browning, K. A. and N. M. Roberts, 1996: Variation of frontal and precipitation structure along a cold front. *Quart. J. Roy. Meteor. Soc.*, **122**, 1845–1872.
- Bushell, A. C. and G. M. Martin, 1999: The impact of vertical resolution upon GCM simulations of marine stratocumulus. *Clim. Dyn.*, **15**, 293–318.
- Carlson, T. N., 1980: Air-flow through mid-latitude cyclones and the comma cloud pattern. *Mon. Wea. Rev.*, **108**, 1498–1509.
- Cess, R. D., M. H. Zhang, W. J. Ingram, G. L. Potter, V. Alekseev, H. W. Barker, E. Cohen-Solal, R. A. Coleman, D. A. Dazlich, A. D. DelGenio, M. R. Dix, V. Dymnikov, M. Esch, L. D. Fowler, J. R. Fraser, V. Galin, W. L. Gates, J. J. Hack, J. T. Kiehl, H. L. Treut, K. K.-W. Lo, B. J. McAvaney, V. P. Meleshko, J.-J. Morcrette, D. A. Randall, E. Roeckner, J. F. Royer, M. E. Schlesinger, P. V. Sporyshev, B. Timbal, E. M. Volodin, K. E. Taylor, W. Wang and R. T. Wetherald, 1996: Cloud feedback in atmospheric general circulation models: An update. *J. Geophys. Res.*, **101**, 12791–12794.
- Cess, R. D., M. H. Zhang, P. Minnis, L. Corsetti, E. G. Dutton, B. W. Forgan, D. P. Garber, W. L. Gates, J. J. Hack, E. F. Harrison, X. Jing, J. T. Kiehl, C. N. Long, J.-J. Morcrette, G. L. Potter, V. Ramanathan, B. Subalisar, C. H. Whitlock, D. F. Young and Y. Zhou, 1995: Absorption of solar radiation by clouds: observations versus models. *Science*, **267**, 496–499.
- Cess, R. D., M. H. Zhang, G. L. Potter, H. W. Barker, R. A. Colman, D. A. Dazlich, M. Esch, J. R. Fraser, V. Galin, W. L. Gates, J. J. Hack, W. J. Ingram, J. T. Kiehl, A. A. Lacis, H. L. Treut, Z. X. Li, X. Z. Liang, J. F. Mahfouf, B. J. McAvaney, V. P. Meleshko, J.-J. Morcrette, D. A. Randall, E. Roeckner, J. F. Royer, A. P. Sokolov, P. V. Sporyshev, K. E. Taylor, W. C. Wang and I. Yanai, 1993: Uncertainties in carbon dioxide radiative forcing in atmospheric general circulation models. *Science*, **262**, 1252–1255.
- Chahine, M., 1992: The hydrological cycle and its influence on climate. *Nature*, **359**, 373–380.
- Chen, C.-T. and E. Roeckner, 1996a: A comparison of satellite observations and model simulations of column-integrated moisture and upper-tropospheric humidity. *J. Climate*, **9**, 1561–1585.
- Chen, C. T. and E. Roeckner, 1996b: Validation of the Earth radiation budget as simulated by the Max Planck Institute for Meteorology general circulation model ECHAM4 using satellite observations of the Earth Radiation Budget Experiment (ERBE). *J. Geophys. Res.*, **101**, 4269–4287.
- Chen, C.-T. and E. Roeckner, 1997: Cloud simulations with the Max Planck Institute for Meteorology general circulation model ECHAM4 and comparison with observations. *J. Geophys. Res.*, **102**, 9325–9350.
- Chen, C.-T. and E. Roeckner, 1999: Evaluation of cloud simulations in a general circulation model from a cloud system approach. Part I: midlatitude cyclone. Manuscript in preparation.
- Cione, J. J., S. Raman and L. J. Pietrafesa, 1993: The effect of Gulf Stream-induced baroclinicity on U.S. East Coast winter cyclones. *Mon. Wea. Rev.*, **121**, 421–430.
- Collins, W. D., W. C. Conant and V. Ramanathan, 1994: Earth radiation budget, clouds and climate sensitivity. In: *The chemistry of the atmosphere: Its impact on global change*, pp. 207–215. J. G. Calvert, Oxford, UK.
- D’Andrea, F., S. Tibaldi, M. Blackburn, G. Boer, M. Deque, M. R. Dix, B. Dugas, L. Ferranti, T. Iwasaki, A. Kitoh, V. Pope, D. Randall, E. Roeckner, D. Strauss, W. Stern, H. van den Dool and D. Williamson, 1998: Northern hemispheric blocking as simulated by 15 atmospheric general circulation models in the period 1979–1988. *Clim. Dyn.*, **14**, 385–407.

- Danielsen, E. F., 1982: A dehydration mechanism for the stratosphere. *Geophys. Res. Letters*, **9**, 605–608.
- Dickinson, M. J., L. F. Bosart, W. E. Bracken, G. J. Hakim, D. M. Schultz, M. A. Bredrick and K. R. Tyle, 1997: The March 1993 superstorm cyclogenesis: Incipient phase, synoptic- and convective-scale flow interaction and model performance. *Mon. Wea. Rev.*, **125**, 3041–3072.
- Dirks, R. A., J. P. Kuettner and J. A. Moore, 1988: Genesis of Atlantic Lows Experiment (GALE). An overview. *Bull. Amer. Meteor. Soc.*, **69**, 148–160.
- Dümenil, L. and H.-S. Bauer, 1998: The tropical easterly jet in a hierarchy of general circulation models and reanalyses. MPI Report 247, Max Planck Institute for Meteorology, Hamburg, Germany.
- Dümenil, L. and E. Todini, 1992: A rainfall-runoff scheme for use in the Hamburg climate model. In: *Advances in Theoretical Hydrology, A tribute to James Dooge*, J. P. O’Kane, ed., pp. 129–157. Elsevier Press, Amsterdam, The Netherlands.
- Feichter, J., 1997: Performance of the NCAR semi-Lagrangian transport scheme in the MPI GCM, ECHAM. In: *Contributions to the MPI workshop on conservative transport schemes*, B. Machenhauer, ed., pp. 5–9. Max Planck Institute for Meteorology, Hamburg, Germany.
- Forbes, G. S., R. M. Blackburn and P. L. Taylor, 1993: "Blizzard of the century" - The storm of the 12-14 March 1993 over the eastern United States. *Meteorol. Magazine*, **122**, 153–162.
- Fouquart, Y. and B. Bonnel, 1980: Computation of solar heating of the Earth’s atmosphere: A new parameterization. *Beitr. Phys. Atmos.*, **53**, 35–62.
- Gates, W. L., 1992: AMIP: The Atmospheric Model Intercomparison Project. *Bull. Amer. Meteor. Soc.*, **73**, 1962–1970.
- Geleyn, J.-F., 1980: Some diagnostics of cloud-radiation interaction in the ECMWF forecasting model. In: *Proceedings of the ECMWF Workshop on radiation and cloud-radiation interaction in numerical modelling*. European Centre for Medium Range Weather Forecasting, Reading, UK.
- Gibson, J. K., P. Källberg, S. Uppala, A. Hernandez, A. Nomura and E. Serrano, 1997: The ECMWF Re-Analysis (ERA). 1. ERA description. ECMWF Re-Analysis Project Report Series 1, European Centre for Medium Range Weather Forecasting, Reading, UK.
- Gilchrist, A., 1971: An example of synoptic development in a general circulation model. *Quart. J. Roy. Meteor. Soc.*, **97**, 340–347.
- Gilhousen, D. B., 1994: The value of NDBC observations during March 1993’s "Storm of the Century". *Weather and Forecasting*, **9**, 255–264.
- Giorgetta, M. and M. Wild, 1995: The water vapour continuum and its representation in ECHAM4. MPI Report 162, Max Planck Institute for Meteorology, Hamburg, Germany.
- Greenwaldt, T. J., G. L. Stephens, T. H. V. Haar and D. L. Jackson, 1993: A physical retrieval of cloud liquid water over the global oceans using Special Sensor Microwave/Imager (SSM/I) observations. *J. Geophys. Res.*, **98**, 18471–18488.
- Gregory, D., R. Kershaw and P. M. Inness, 1997: Parameterization of momentum transport by convection. Part II: Tests in single-column and general circulation models. *Quart. J. Roy. Meteor. Soc.*, **123**, 1153–1183.

- Hadlock, R. and C. W. Kreitzberg, 1988: Experiment on Rapidly Intensifying Cyclones over the Atlantic (ERICA): field study, objectives and plans. *Bull. Amer. Meteor. Soc.*, **69**, 1309–1320.
- Hahn, C. J., S. G. Warren and J. London, 1994a: *Climatology data for clouds over the globe from surface observation, 1982-1991: The total cloud edition*, volume NDP-026A. The Carbon Dioxide Information Analysis Center, Oak Ridge National Laboratory, Oak Ridge.
- Hahn, C. J., S. G. Warren and J. London, 1994b: *Edited synoptic cloud reports from ships and land stations over the globe, 1982-1991*, volume NDP-026B. Carbon Dioxide Information Analysis Center, Oak Ridge National Laboratory, Oak Ridge.
- Hartmann, D. L., 1993: Radiative effects of clouds on Earth's climate. In: *Aerosol-cloud-climate interactions*, P. V. Hobbs, ed., pp. 151–173. Academic Press, New York, U.S.A.
- Hartmann, D. L., M. E. Ockert-Bell and M. L. Michelsen, 1992: The effect of cloud type on Earth's energy balance: Global analysis. *J. Climate*, **5**, 1281–1304.
- Heysmsfield, A. J., 1977: Precipitation development in stratiform ice clouds. A microphysical and dynamical study. *J. Atmos. Sci.*, **34**, 367–381.
- Hoke, J. E. and R. A. Anthes, 1976: The initialization of numerical models by a dynamic-initialization technique. *Mon. Wea. Rev.*, **104**, 1551–1556.
- Holton, J. R., 1992: *An introduction to dynamic meteorology*, volume 48 of *International Geophysics Series*. Academic Press, New York, 3rd edition. 511pp.
- Hoskins, B. J., M. E. McIntyre and A. W. Robertson, 1985: On the use and significance of isentropic potential vorticity maps. *Quart. J. Roy. Meteor. Soc.*, **111**, 877–946.
- Houze, R. A., 1993: *Cloud Dynamics*, volume 53 of *International Geophysics Series*. Academic Press, San Diego. 573pp.
- Huo, Z., D.-L. Zhang, J. Gyakum and A. Staniforth, 1995: A diagnostic analysis of the super-storm of March 1993. *Mon. Wea. Rev.*, **123**, 1740–1761.
- International Cloud Atlas, 1987: volume 2. World Meteorological Organization, Geneva, Switzerland. 212pp.
- Jeuken, A. B. M., P. C. Siegmung, L. C. Heijboer, J. Feichter and L. Bengtsson, 1996: On the potential of assimilating meteorological analysis in a global climate model for the purpose of model validation. *J. Geophys. Res.*, **101**, 16939–16950.
- Joly, A., D. Jorgensen, M. A. Shapiro, A. Thorpe, P. Bessemoulin, K. A. Browning, J.-P. Cammas, J.-P. Chalon, S. A. Clough, K. A. Emanuel, L. Eymard, R. Gall, P. H. Hildebrand, R. H. Langland, Y. Lemaitre, P. Lynch, J. A. Moore, P. Ola, G. Persson, C. Snyder and R. M. Wakimoto, 1997: The Fronts and Atlantic Storm-Track EXperiment (FASTEX): Scientific objectives and experimental design. *Bull. Amer. Meteorol. Soc.*, **78**, 1917–1940.
- Kershaw, R. and D. Gregory, 1997: Parameterization of momentum transport by convection. Part I: Theory and cloud modelling results. *Quart. J. Roy. Meteor. Soc.*, **123**, 1133–1152.
- Kidwell, K. B., 1995: NOAA Polar Orbiter Data Users Guide (TIROS-N, NOAA-6, NOAA-7, NOAA-8, NOAA-9, NOAA-10, NOAA-11, NOAA-13 and NOAA-14). Technical Report 304, National Oceanic and Atmospheric Administration, National Environmental Satellite, Data and Information Service, Washington, DC.
- Kiehl, J. T. and K. E. Trenberth, 1997: Earth's annual global mean energy budget. *Bull. Amer. Meteor. Soc.*, **78**, 197–208.

- Kirchner, I., 1999: personal communication.
- Klepp, C., 1999: personal communication.
- Kocin, P. J., P. N. Schumacher, R. F. M. Jr and L. W. Uccellini, 1995: Overview of the 12-14 March 1993 superstorm. *Bull. Amer. Meteor. Soc.*, **76**, 165–182.
- Kocin, P. J. and L. W. Uccellini, 1990: *Snowstorms along the northeastern coast of the United States: 1955 to 1985*. American Meteorological Society, Boston, Massachusetts. 280pp.
- Kondratyev, K. Y., V. I. Binenko and I. N. Melinkova, 1998: Absorption of solar radiation by clouds and aerosols in the visible wavelength region. *Meteorol. Atmos. Phys.*, **65**, 1–10.
- Krishnamurti, T. N., H. S. Bedi and K. Ingles, 1993: Physical initialization using SSM/I rain rates. *Tellus*, **45A**, 247–269.
- Krishnamurti, T. N., J. Xue, H. S. Bedi, K. Ingles and D. Oosterhof, 1991: Physical initialization for numerical weather prediction over the tropics. *Tellus*, **43AB**, 53–81.
- Kuo, Y. H. and Y. R. Guo, 1989: Dynamic initialization using observations from a network of profilers and its impact on short-range numerical weather prediction. *Mon. Wea. Rev.*, **117**, 1975–1998.
- Kurz, M., 1990: *Synoptische Meteorologie. Leitfäden für die Ausbildung im Deutschen Wetterdienst 8*, Deutscher Wetterdienst, Offenbach am Main, Germany. 197pp.
- Lau, N.-C. and M. W. Crane, 1995: A satellite view of the synoptic-scale organization of cloud properties in mid-latitude and tropical circulation systems. *Mon. Wea. Rev.*, **123**, 1984–2006.
- Lau, N.-C. and M. W. Crane, 1997: Comparing satellite and surface observations of cloud patterns in synoptic-scale circulation systems. *Mon. Wea. Rev.*, **125**, 3172–3189.
- Lejenäs, H. and R. A. Madden, 1992: Travelling planetary waves and blocking. *Mon. Wea. Rev.*, **120**, 2821–2830.
- Lejenäs, H. and H. Okland, 1983: Characteristics of northern hemispheric blocking as determined from a long-time series of observational data. *Tellus*, **35A**, 350–362.
- Lenderink, G., E. van Meijgaard and A. A. M. Holtslag, 1998: Evaluation of the ECHAM4 cloud-turbulence scheme for stratocumulus. Preprints 98-13, KNMI, De Bilt, The Netherlands. Submitted to Contributions to Atmospheric Physics.
- Leonard, B. P., A. P. Lock and M. K. MacVean, 1995: The NIRVANA scheme applied to one-dimensional advection. *Int. J. Numer.*, **5**, 341–377.
- Liljequist, G. H. and K. Cehak, 1994: *Allgemeine Meteorologie*. Vieweg, Braunschweig, 3rd edition. 412 pp.
- Liu, G. and J. A. Curry, 1993: Determination of characteristic features of cloud liquid water from satellite microwave measurements. *J. Geophys. Res.*, **98**, 5069–5092.
- Lohmann, U., 1999: personal communication.
- Lohmann, U., N. McFarlane, L. Levkov, K. Abdella and F. Albers, 1999: Comparing different cloud schemes of a single column model by using mesoscale forcing and nudging technique. *J. Climate*, **12**, 438–461.
- Lohmann, U. and E. Roeckner, 1996a: Design and performance of a new cloud microphysics scheme developed for the ECHAM general circulation model. *Clim. Dyn.*, **12**, 557–572.

- Lohmann, U. and E. Roeckner, 1996b: Influence of different parameterizations of ice clouds on climate sensitivity in a general circulation model. In: *Proceedings of the 12th International Conference on Clouds and Precipitation*, pp. 1228–1231. Zürich, Switzerland.
- Lohmann, U., E. Roeckner, W. D. Collins, A. J. Heymsfield, G. M. McFarquhar and T. P. Barnett, 1995: The role of water vapour and convection during the Central Equatorial Pacific Experiment (CEPEX) from observations and model simulations. *J. Geophys. Res.*, **100**, 26229–26245.
- Lupo, A. R. and P. J. Smith, 1994: Climatological features of blocking anticyclones in the Northern Hemisphere. *Tellus*, **47A**, 439–456.
- Machenhauer, B., 1977: On the dynamics of gravity oscillations in a shallow water model, with applications to nonlinear normal mode initialization. *Beitr. Phys. Atm.*, **50**, 253–271.
- Machenhauer, B. and I. Kirchner, 1999: Assimilation of ERA data in ECHAM - New “Slow Normal Mode” assimilation and revision of the preprocessing of the ERA data. Abstract available on: <http://www.mpimet.mpg.de/kirchner.ingo/Salzau99/abstract.html>.
- Matveev, L. T., 1984: *Cloud dynamics*. Atmospheric Science Library. D. Reidel Publishing Company, Dordrecht. 340pp.
- McFarlane, N. A., G. J. Boer, J.-P. Blanchet and M. Lazare, 1992: The Canadian Climate Center second-generation general circulation model and its equilibrium climate. *J. Climate*, **5**, 1013–1044.
- Michelangeli, P.-A. and R. Vautard, 1998: The dynamics of Euro-Atlantic blocking onsets. *Quart. J. Roy. Meteor. Soc.*, **124**, 1045–1070.
- Miller, M. J., T. N. Palmer and R. Swinbank, 1989: Parameterization and influence of sub-grid scale orography in general circulation and numerical weather prediction models. *Met. Atmos. Phys.*, **40**, 84–109.
- Moncrieff, M. W., 1995: Mesoscale convection from a large-scale perspective. *Atmos. Res.*, **35**, 87–112.
- Morcrette, J.-J., 1984: Sur la paramétrisation du rayonnement dans les modèles de la circulation générale atmosphérique. Thèse de doctorat, Université des Sciences et Techniques de Lille. 373pp.
- Morcrette, J.-J., 1991a: Evaluation of model-generated cloudiness: satellite-observed and model-generated diurnal variability of brightness temperature. *Mon. Wea. Rev.*, **119**, 1205–1224.
- Morcrette, J.-J., 1991b: Radiation and cloud radiative processes in the European Centre for Medium Range Weather Forecasts forecasting system. *J. Geophys. Res.*, **96**, 9121–9132.
- Neiman, P. J. and M. A. Shapiro, 1993: The life cycle of an extratropical marine cyclone. Part I: Frontal-cyclone evolution and thermodynamic air-sea interaction. *Mon. Wea. Rev.*, **121**, 2153–2176.
- Neiman, P. J., M. A. Shapiro and L. S. Fedor, 1993: The life cycle of an extratropical marine cyclone. Part II: Mesoscale structure and diagnostics. *Mon. Wea. Rev.*, **121**, 2177–2199.
- Nordeng, T. E., 1994: Extended version of the convective parameterization scheme at ECMWF and their impact on the mean and transient activity of the model in the tropics. Tech. Memo 206, European Centre for Medium Range Weather Forecasting, Reading, UK.

- Ockert-Bell, M. E. and D. L. Hartmann, 1992: The effect of cloud type on Earth's energy balance: Results from selected regions. *J. Climate*, **5**, 1157–1171.
- Ohmura, A. and H. Gilgen, 1993: Re-evaluation of the global energy balance. In: *Geophys. Monograph, 75, IUGG Volume 5*, pp. 93–110.
- Palmer, T. N., G. J. Shutts and R. Swinbank, 1986: Alleviation of a systematic westerly bias in general circulation and numerical weather prediction models through an orographic gravity wave drag parameterization. *Quart. J. Roy. Meteor. Soc.*, **112**, 1001–1031.
- Petch, J. C. and J. M. Edwards, 1999: Off-line radiation calculation using a LEM simulation of TOGA-COARE. Part 1: Investigation of cloud-overlap assumption used in the UM. Atmospheric Process Research, TDN 254, UK Met. Office, Bracknell, Berkshire.
- Ramanathan, V. and A. M. Vogelmann, 1997: Greenhouse effect, atmospheric solar absorption and the Earth's radiation budget: From the Arrhenius-Langley era to the 1990s. *Ambio*, **26**, 1, 38–46.
- Randall, D. A., J. A. Coagley, C. W. F. Jr, R. A. Kropfli and D. H. Lenschow, 1984: Outlook for research on subtropical marine stratiform clouds. *Bull. Amer. Meteor. Soc.*, **65**, 1290–1301.
- Rasch, P. J. and M. Lawrence, 1997: Recent developments in transport methods at NCAR. In: *Contributions to the MPI workshop on conservative transport schemes*, B. Machenhauer, ed. Max Planck Institute for Meteorology, Hamburg, Germany.
- Rockel, B., E. Raschke. and W. Weyres, 1991: A parameterization of broad-band radiative transfer properties of water, ice and mixed clouds. *Beitr. Phys. Atmos.*, **64**, 1–12.
- Rodgers, C. D. and C. D. Walshaw, 1966: The computation of infrared cooling rate in planetary atmospheres. *ibid*, **92**, 67–92.
- Roeckner, E., 1999: personal communication.
- Roeckner, E., K. Arpe, L. Bengtsson, S. Brinkop, L. D. M. Esch, F. Lunkeit, M. Ponater, B. Rockel, R. Sausen, U. Schlese, S. Schubert and M. Windelband, 1992: Simulation of the present-day climate with the ECHAM model: Impact of the model physics and resolution. MPI Report 93, Max-Planck-Institute for Meteorology, Bundesstrasse 55, 20146 Hamburg, Germany.
- Roeckner, E., K. Arpe, L. Bengtsson, M. Christoph, M. Claussen, L. Dümenil, M. Giorgetta, U. Schlese and U. Schulzweida, 1996: The atmospheric general circulation model ECHAM4: Model description and simulation of the present-day climate. MPI Report 218, Max Planck Institute for Meteorology, Hamburg, Germany.
- Roeckner, E. and H. LeTreut, 1996: GCM studies and parameterization. In: *NATO ASI Series*, P. J. Crutzen and V. Ramanathan, eds., volume I 35, pp. 109–133. Springer Verlag, Berlin Heidelberg.
- Rossow, W. B. and L. C. Garder, 1993a: Cloud detection using satellite measurements of infrared and visible radiances for ISCCP. *J. Climate*, **6**, 2341–2369.
- Rossow, W. B. and L. C. Garder, 1993b: Validation of ISCCP cloud detections. *J. Climate*, **6**, 2370–2393.
- Rossow, W. B. and R. A. Schiffer, 1991: ISCCP cloud data products. *Bull. Amer. Meteor. Soc.*, **72**, 2–20. Postscript version at: <http://isccp.giss.nasa.gov/documents.html>.

- Rossow, W. B., A. Walker and M. Roiter, 1996a: International Satellite Cloud Climatology Project (ISCCP): Description of reduced resolution radiance data. WMO/TD-No. 58, World Meteorological Organization, Geneva, Switzerland. 163 pp. Postscript version at: <http://isccp.giss.nasa.gov/documents.html>.
- Rossow, W. B., A. W. Walker, D. E. Beuschel and M. D. Roiter, 1996b: International Satellite Cloud Climatology Project (ISCCP): Documentation of new cloud datasets. WMO/TD-No. 737, World Meteorological Organization, Geneva, Switzerland. 115pp. Postscript version at: <http://isccp.giss.nasa.gov/documents.html>.
- Rossow, W. B., A. W. Walker and L. C. Garder, 1993: Comparison of ISCCP and other cloud amounts. *J. Climate*, **6**, 2394–2417.
- Sanders, F. and L. F. Bosart, 1985: Mesoscale structure in the megalopolitan snowstorm of 11–12 February 1983, Part 1: Frontogenetical forcing and symmetric instability. *J. Atmos. Sci.*, **42**, 1050–1061.
- Schultz, D. M., W. E. Bracken, F. Bosart, G. J. Hakim, M. A. Bedrick, M. J. Dickinson and K. R. Tyle, 1997: The 1993 superstorm cold surge: Frontal structure, gap flow and tropical impact. *Mon. Wea. Rev.*, **125**, 5–39.
- Schulz, J.-P., L. Dümenil and J. Polcher, 1999: The impact of two different land-surface coupling techniques in a single column version of the ECHAM4 atmospheric model. MPI Report 297, Max Planck Institute for Meteorology, Hamburg, Germany.
- Shapiro, M. and D. Keyser, 1990: Fronts, jet streams and the tropopause. In: *Extratropical cyclones: The Erik Palmén Memorial Volume*, C. W. Newton and E. Holopainen, eds., pp. 167–191. American Meteorological Society.
- Slingo, J. M., 1987: The development and validation of a cloud cover prediction scheme for the ECMWF model. *Quart. J. Roy. Meteor. Soc.*, **113**, 899–927.
- Smith, R. N. B., 1990: A scheme for predicting layer clouds and their water content in a general circulation model. *Quart. J. Roy. Meteor. Soc.*, **116**, 435–460.
- Sonntag, D., 1994: Advancements in the field of hygrometry. *Meteorol. Zeitschrift*, **N.F. 3**, 51–66.
- Sundqvist, H., 1978: A parameterization scheme for non-convective condensation including prediction of cloud water content. *Quart. J. Roy. Meteor. Soc.*, **104**, 677–690.
- Sundqvist, H., E. Berge and J. E. Kristjanson, 1989: Condensation and cloud parameterization studies with a mesoscale numerical weather prediction model. *Mon. Wea. Rev.*, **117**, 1641–1657.
- Tibaldi, S., F. DAndrea, E. Toshi and E. Roeckner, 1997: Climatology of Northern Hemisphere blocking in the ECHAM model. *Clim. Dyn.*, **13**, 649–666.
- Tiedtke, M., 1989: A comprehensive mass flux scheme for cumulus parameterization in large-scale models. *Mon. Wea. Rev.*, **117**, 1779–1800.
- Tiedtke, M., 1993: Representation of clouds in large-scale models. *Mon. Wea. Rev.*, **121**, 3040–3061.
- Tompkins, A. M. and K. A. Emanuel, 1999: The vertical resolution sensitivity of simulated equilibrium tropical temperature and water vapour profiles. *Quart. J. Roy. Meteor. Soc.* in press.

- Tschuck, P., 1998: Blocking anticyclones in the ECHAM general circulation model. Ph.D. thesis, Eidgenössische Hochschule Zürich. 120pp.
- Tsou, C. H. and P. J. Smith, 1990a: The role of synoptic/planetary-scale interactions during the development of a blocking anticyclone. *Tellus*, **42A**, 174–193.
- Tsou, C. H. and P. J. Smith, 1990b: The importance of non-quasigeostrophic forcing during the development of a blocking anticyclone. *Tellus*, **42A**, 328–342.
- Twohy, C. H., A. J. Schanot, W. A. Cooper and H. Gerber, 1997: Measurement of condensed water content in liquid and ice clouds using an airborne Counterflow Virtual Impactor. *J. Atmos. Océ. Tech.*, **14**, 197–202.
- Uccellini, L. W. and D. R. Johnson, 1979: Coupling of upper and lower tropospheric jet streaks and implications for the development of severe convective storms. *Mon. Wea. Rev.*, **107**, 682–703.
- Uccellini, L. W. and P. J. Kocin, 1987: The interaction of jet streak circulations during heavy snow events along the East Coast of the United States. *Weather and Forecasting*, **2**, 289–308.
- van Meijgaard, E., J. A. Konings, A. J. Feijt and A. C. A. P. van Lammern, 1999: Comparison of model predicted cloud cover profiles with observations from ground and satellite. Preprints 99-5, KNMI, De Bilt, The Netherlands. Submitted to Contributions to Atmospheric Physics.
- Walcek, C. J., 1994: Cloud cover and its relationship to relative humidity during a springtime midlatitude cyclone. *Mon. Wea. Rev.*, **122**, 1021–1035.
- Warren, S. G., C. J. Hahn, J. London, R. M. Chervin and R. L. Jenne, 1986: Global distribution of total cloud cover and cloud type amounts over land. NCAR Tech. Note TN-273, National Centre for Atmospheric Research, Boulder, CO, U.S.A.
- Webster, P. J. and R. Lukas, 1992: TOGA-COARE: The Coupled Ocean-Atmosphere Response Experiment. *Bull. Amer. Meteor. Soc.*, **73**, 1377–1416.
- Weng, F. and N. C. Grody, 1994: Retrieval of cloud liquid water using the Special Sensor Microwave Imager (SSM/I). *J. Geophys. Res.*, **99**, 25535–25551.
- Williamson, D. L. and P. J. Rasch, 1989: Two-dimensional semi-Lagrangian transport with shape preserving interpolation. *Mon. Wea. Rev.*, **117**, 102–129.
- Williamson, D. L. and P. J. Rasch, 1994: Water vapour transport in the NCAR CCM2. *Tellus*, **46A**, 34–51.
- Xu, K. M. and S. K. Kruger, 1991: Evaluation of cloudiness parameterizations using a cumulus ensemble model. *Mon. Wea. Rev.*, **119**, 342–367.
- Zhang, Y.-C. and W. B. Rossow, 1995: Calculation of surface and top of the atmosphere radiative fluxes from physical quantities based on ISCCP data sets. 1: Method and sensitivity to input data uncertainties. *J. Geophys. Res.*, **100**, 1149–1165.